NORTHWESTERN UNIVERSITY

Dynamic Mechanisms of Metabotropic Glutamate Receptor Activation and Modulation

A DISSERTATION

SUBMITTED TO THE GRADUATE SCHOOL

IN PARTIAL FULFILLMENT OF THE REQUIREMENTS

for the degree

DOCTOR OF PHILOSOPHY

Field of Interdisciplinary Biological Sciences

By

Brandon Wey-Hung Liauw

EVANSTON, ILLINOIS

December 2022

Abstract

G protein-coupled receptors (GPCRs) are the largest family of membrane receptors in humans and play a role in nearly all physiological processes. Among GPCRs, metabotropic glutamate receptors (mGluRs) are a structurally distinct family of synaptic receptors that are essential in regulating neurotransmission and synaptic plasticity. Due to their important regulatory role in the central nervous system, mGluRs have emerged as promising targets for treating a range of neurological and psychiatric disorders. The overall objective of this thesis dissertation is to characterize the mechanisms of mGluR activation and modulation.

mGluRs function as constitutive dimers and possess large extracellular domains composed of a ligand binding Venus flytrap (VFT) domain and a linker cysteine-rich domain (CRD). In addition, the highly conserved 7 transmembrane (7TM) domain forms an allosteric pocket that can be targeted by synthetic modulators. Thus, mGluR function is dependent on a complex and coordinated transmission of conformational dynamics among three structural domains and two ligand-binding sites. At the beginning of this thesis work, our understanding of mGluR conformational dynamics was fragmented and incomplete. Moreover, how the spatially separated domains and ligand binding sites were conformationally coupled was unclear.

Here, we used a combination of single-molecule fluorescence resonance energy transfer (smFRET), cell-based FRET, and functional calcium imaging to quantify the conformational dynamics underlying mGluR2 activation and modulation. During mGluR2 activation, we show that CRDs are in dynamic equilibrium among four distinct conformations, two of which were previously unknown, and that transitions between the conformations occur in an ordered and sequential manner. The intermediate states were identified to act as critical checkpoints for

receptor activation. Finally, comparing the VFT domain rearrangement during activation with that of the CRD and 7TM domain revealed dramatically different structural dynamics, providing direct evidence for loose coupling in mGluRs

Our four-state activation model provided us with a framework to interpret and describe the effects of both synthetic and endogenous allosteric modulators on mGluR2 conformational dynamics. We identified novel mechanisms for positive and negative allosteric modulation that are dependent on the intrinsic dynamics of the CRD and the two intermediate states. Furthermore, examination of the VFT domain, CRD, and 7TM domain demonstrated that the allosteric modulators tested affect the overall dimeric rearrangement of mGluR2. Lastly, we show that solubilizing agents strongly influence the structural and dynamic properties of mGluRs, emphasizing the importance in optimizing components of the hydrophobic scaffold.

Collectively, the findings presented in this thesis established and refined a dynamic framework for mGluR2 activation and modulation that likely extends to other mGluRs and other dimeric multidomain membrane receptors.

Acknowledgments

I first want to thank my advisor, Prof. Reza Vafabakhsh, for taking a risk on me back in the summer of 2017 and guiding me to where I am today. We have gone through a lot together and I am proud of what the lab has become. Looking back now, while highly motivated, I was rough around the edges and had a lot to learn. Fortunately for me, Reza showed extraordinary patience as a mentor, and for that I am eternally grateful. Whether it was conducting experiments, analyzing data, making figures, or composing a scientific narrative, Reza always made himself available for questions and provided thoughtful advice. I believe this is something many people inside the department and out can attest to as well. I also thank Reza for teaching me to be more creative, developing my scientific intuition, and just making me a more confident and critical scientist. While the road was not always smooth, I appreciate Reza always being straightforward about things and seeing me as both a scientist-in-training and a human being. God bless Prof. Reza.

Next, I would like to thank my lab mates who have provided me with good times, support, and mentorship throughout the years. First, a big thank you to my roommate and lab twin, Dr. Michael Schamber. As an old man, you have been able to share a lot of science and life wisdom while helping me keep my eyes on the bigger picture, and for that I am grateful. A big thank you also goes out to our former head-of-chemistry, Dr. Hamid Afsari. While we did not always agree with one another, I am grateful for all the chemistry and obsessive behavior you taught me because that ultimately made me a much better scientist. Thank you, soon to be doctor Ashley for being the best desk make and my emotional support rabbit when times were tough. Thank you Dr. Arash Foroutan for being a really organized collaborator and patient with me when I got really stressed out. Thank you Deanna Badong and Denny May for helping RezaLab get organized and rolling

back in the day. We were recently joined by Drs. An Pham, Chiranjib Banerjee, and Kristina Cechova and Yiren Tu who all brought their own unique personalities and wisdom to the lab and it has been a treat getting to know you all. I would also like to thank a former rotation student, Weifeng Lu, whose work was essential for the completion of my last paper.

I would next like to thank my friends in and out of graduate school. The friends I made at Northwestern have greatly enriched my experience through a combination of scientific conversations and just random fun times. My time here would not be the same without them. Thank you to Miranda Jacobs, Vas Dumrongprechachan, Gabe Cavin-Meza, and Chris Koo for coffee breaks, food adventures, gyming, bouldering, cat play dates, and just being there when I needed someone to talk to. I would also like to thank Soo Ro and Shuya Wang for being excellent mentors during my first year of graduate school and always trying to pump me up.

Next, I want to thank my friends outside of academia who have kept me grounded and sane over the years. Thank you to all my Rosemead and UCLA friends, Jane Tam, Michael Dinh, Jenny Cam, Melanie Chhem, Viet Vo, Parkson Hua, Brian Huynh, Pisacha Wichianchan, Liane Hung, Stanley Lin, Jason Kong, Nakin Bhandari, and Jun Li for checking in on me throughout the years and making it a point to see me whenever I am back in town. I know it is not always easy to listen to me rant, so I really appreciate you all. I also want to give a special thank you to Lillian Lai. You were my number one supporter for a long time, and I could not have made it without you. You now have half a PhD.

Lastly, I would like to thank my parents and brothers. My parents have always put me and my brothers before anything else. Everything I am able to do and accomplish is thanks to them. Even though they did not always have the answers or even understand the challenges I faced, they were

always encouraging and pushed me to reach beyond what I thought I could achieve. I really owe my drive and motivation to them. I also want to thank my older brothers for looking after me as a kid and even now. I could only be young and dumb and chase my dreams because they took care of much of the hard work behind the scenes, and for that I am grateful.

Thank you to all the mentors, peers, family, and friends that have been a part of my journey and supporting me throughout the years. I could not have done this without you all.

For my parents

Table of Contents

List of Figures

List of Tables

Chapter 1: Introduction

The ability of a cell to rapidly sense and respond to environmental cues is a central tenet of biology and is vital for cellular survival, homeostasis, and propagation of genetic material (Smock & Gierasch, 2009). In vertebrates, G protein-coupled receptors (GPCRs) are the largest family of membrane receptors, with over 800 members, and are central to the sensory-response process in effectively all tissues and organ systems (Regard et al., 2008). Based on their sequence and structure homology, GPCRs are divided into six classes, designated A-F. Metabotropic glutamate receptors (mGluRs) and the class C GPCRs in general, are unique members of the GPCR superfamily as they possess large extracellular domains and function as obligate dimers (Niswender & Conn, 2010). mGluRs are integral in regulating neuronal excitability in the central nervous system in response to glutamate. While mGluRs represent a promising target for treating a range of neurological and psychiatric disorders, lack of knowledge about their activation mechanism has been a roadblock in drug development. To address these shortcomings, the work in this thesis focuses on characterizing and identifying mechanisms underlying mGluR activation and modulation in response to both endogenous and exogenous ligand.

1.1 G protein-coupled receptors

GPCRs are responsible for detecting a range of stimuli that includes light, mechanical force, peptides, amino acids, lipids, and ions. Upon stimulation, GPCRs couple to and activate heterotrimeric G proteins by functioning as nucleotide exchange factors, initiating the exchange of GDP for GTP. Subsequently, activated G proteins regulate the levels of secondary messengers, cyclic adenosine monophosphate (cAMP) and calcium, as well as the activity of other proteins such as ion channels to induce a physiological response. (Wootten et al., 2018). The role of GPCRs in nearly all physiological processes, their wide expression patterns, and accessibility on cellular membranes has led to their emergence as the most sought-after therapeutic target, currently serving as targets for nearly 30% of all clinically approved pharmaceuticals (Hauser et al., 2017).

GPCRs are characterized by a highly conserved seven α-helical domain structure linked by three extracellular (ECL) and three intracellular (ICL) loops and are subdivided into six classes based on sequence homology (Ciancetta et al., 2015). The different classes include the class A – rhodopsin-like receptors, class B – secretin and adhesion family of receptors, class C – metabotropic receptors, class D – fungal mating receptors, class E – cAMP receptors, and class F – frizzled and smoothened receptors (Lee et al., 2018). Among the six classes, the rhodopsin-like (class A) receptors are the best studied and largest subset.

Class A GPCR activation is dependent on ligand binding at the cognate binding site located within the 7 transmembrane (7TM) domain bundle. Ligand binding initiates an outward shift of the cytosolic side of helix 6, enabling heterotrimeric G protein coupling and nucleotide exchange (Rasmussen et al., 2011). Using a combination of structural, computational, and functional analysis, a conserved activation mechanism for class A GPCRs, that linked key structural motifs

and placed them in the broader context of receptor activation, was established (Flock et al., 2015; Zhou et al., 2019). However, GPCRs are structurally diverse, possess a highly variable N-terminal domains, and employ distinct ligand-binding modalities, hence limiting the mechanism to class A receptors (Basith et al., 2018).

Class C receptors are the most structurally distinct members of the GPCR superfamily as they function as obligate dimers and possess large extracellular domains that are composed of ~500 amino acids and contain the ligand binding sites (Niswender & Conn, 2010). Thus, class C GPCR activation requires a combination of localized structural changes and global conformational coupling of domains. The class C receptors consist of mGluRs along with the $GABA_B$ receptor, calcium sensing receptor (CaSR), several taste receptors, and a few orphan receptors.

1.2 Metabotropic glutamate receptors

1.2.1 Discovery of mGluRs

L-glutamic acid is the primary excitatory neurotransmitter in the mammalian central nervous system and is essential for initiating fast postsynaptic action potentials through the activation of ionotropic glutamate receptors (iGluRs) (Boulter et al., 1990; Moriyoshi et al., 1991; Hollmann et al., 1989). In addition to activating ligand-gated ion channels, glutamate was also found to stimulate inositol phospholipid metabolism, resulting in the formation of inositol 1,4,5-triphosphate (IP_3) and intracellular calcium mobilization (Nicoletti et al., 1986; Sladeczek et al., 1985; Sugiyama et al., 1987). Intracellular IP_3 and calcium levels demonstrated a GTP-dependence, suggesting that glutamate may be acting through an unknown GPCR. The gene of this putative protein was cloned from *Xenopus laevis* oocytes and encoded for a heptahelical

domain-containing protein, identifying it as a GPCR (Houamed et al., 1991). Interestingly, the receptor lacked sequence homology with other known GPCRs, suggesting it belonged to a new class of GPCRs. Furthermore, this receptor had 1199 amino acids which was substantially larger than other known GPCRs, and had a unique topology, with the 7TM domain flanked by large amino- and carboxyl-terminal domains. Subsequent work cloned an additional seven genes, resulting in the identification of eight mGluRs in total (Abe et al., 1992; Duvoisin et al., 1995; Nakanishi, 1992; Okamoto et al., 1994; Tanabe et al., 1992). mGluRs are predominantly synaptic proteins in the central nervous system, where they are essential for regulating neurotransmission, except for mGluR6, which is primarily found in the retina where it mediates transmission between photoreceptor cells and bipolar cells (Niswender & Conn, 2010; Nakajima et al., 1993).

1.2.2 Physiology of mGluRs

mGluRs are subdivided into three groups, groups I (mGluR1/5), II (mGluR2/3), and III (mGluR4/6/7/8), based on sequence homology and G protein-coupling (Niswender & Conn, 2010). Group I mGluRs primarily localize to post-synapses where they couple to $G\alpha_{q/11}$ to activate phospholipase C, resulting in the hydrolysis of phosphoinositides. In contrast, group II and III mGluRs are primarily localized to pre-synapses where they couple to $G\alpha_{i/o}$, resulting in the inhibition of adenylyl cyclase and reduction of cAMP levels. Group II and III mGluRs can also directly regulate activity of some ion channels such as G protein inward rectifying potassium channels (GIRKs), via the release of $G_{\beta\gamma}$ subunits of the G protein. Interestingly, it is now recognized that mGluRs can signal through non-canonical transducers such as β-arrestins (Abreu et al., 2021; Eng et al., 2016) and several types of G proteins in a tissue and cell-type dependent

manner (Hermans & Challiss, 2001; Iacovelli et al., 2002), resulting in a far more complex signaling profile than initially perceived.

Dimeric organization of mGluRs and diversity in subtypes enable an expanded array of potential signaling modalities. In addition to forming homodimers, mGluRs can also form heterodimers between group I receptors and between group II and III receptors, resulting in a total of 11 possible heterodimer combinations (Doumazane et al., 2011). Although mGluR heterodimer physiology is still an area of active research, work thus far has suggested that heterodimerization functions as a biological mechanism to diversify receptor signaling. Heterodimeric mGluRs demonstrate unique properties such as basal activity, transactivation, and altered glutamate sensitivity that were absent in their homodimeric counterparts (Habrian et al., 2019; Levitz et al., 2016; Liu et al., 2017). Furthermore, mGluRs homodimers themselves demonstrate a broad range of glutamate sensitivity, ranging from nanomolar to tens of millimolar, enabling glutamate detection in different biological context.

Taken together, mGluR physiology is highly complex due to receptor subtype diversity, dimerization, and ability to couple to multiple transducers. To effectively leverage the therapeutic potential of mGluRs, we ultimately must develop a more comprehensive understanding of their physiology that accounts for these factors.

1.3 Structure and dynamics of metabotropic glutamate receptors

mGluRs are structurally distinct GPCRs that possess large extracellular domains and function as obligate dimers (Figure 1.1) (Niswender & Conn, 2010). The extracellular domain is composed of the Venus flytrap (VFT) domain which has the glutamate binding site, and the cysteine-rich

domain (CRD) that functions to propagate ligand-induced structural changes from the VFT domain to the 7TM domain. In addition to G protein-coupling, the 7TM domain also contains the allosteric ligand binding site (Lindsley et al., 2016). mGluR function thus requires complex and coordinated conformational coupling of three distinct structural domains.

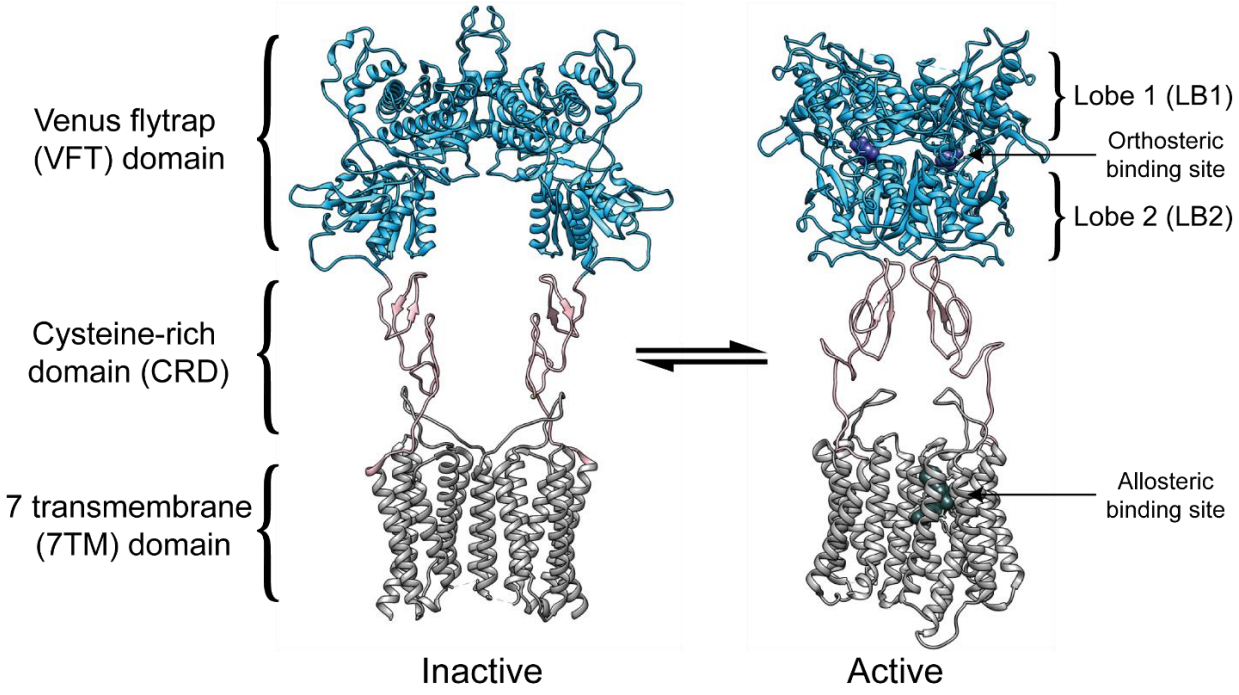

Figure 1.1 Schematic of mGluR structure
mGluRs are obligate dimeric GPCRs that possess large extracellular domains. The extracellular domain is composed of a bilobate (LB1 and LB2) Venus flytrap (VFT) domain (blue) that contains the glutamate binding site, and a cysteine-rich domain (CRD; pink) which serves as a structural linker. The 7 transmembrane (7TM) domain (gray) functions as the G protein-coupling domain and contains an allosteric ligand binding site within the transmembrane bundle. Upon receptor activation, the VFT domains close and reorient themselves, resulting in a general compaction and reorientation of the CRDs and 7TM domains. Inactive mGluR2 (PDB:7EPA). Active mGluR2 (PDB:7E9G).

1.3.1 Venus flytrap (VFT) domain

After the discovery of the mGluR genes, sequence analysis revealed that the extracellular amino-terminus shared significant homology with the bilobate bacterial periplasmic binding proteins that are responsible for binding and scavenging for amino acids (O'Hara et al., 1993). This domain was named as the Venus flytrap (VFT) domain. To verify that mGluR VFT domains contained the cognate ligand binding site, a subsequent study examined glutamate binding on soluble and truncated forms of the domain, and confirmed the VFT domain was necessary and sufficient for glutamate binding (Okamoto et al., 1998). Mutagenesis studies showed that glutamate binding is dependent on polar interactions, predominantly hydrogen bonds, with residues from both the upper (LB1) and lower (LB2) lobes (Figure 1.2A) (O'Hara et al., 1993; Hampson et al., 1999; Kunishima et al., 2000; Mølck et al., 2014). Specifically, residues Y74, R78, S165, T188, and D318 at the LB1-LB2 interface of mGluR1 were shown to be essential, as alanine mutations severely reduced glutamate affinity (Figure 1.2B).

mGluR dimerization is predominantly mediated by a conserved intermolecular disulfide bridge (Ray & Hauschild, 2000; Romano et al., 2001; Romano et al., 1996; Tsuji et al., 2000), C140 in mGluR1 (Figure 1.3, pink), and hydrophobic interactions at the LB1-LB1 interface (Levitz et al., 2016). Upon glutamate binding, the VFT domains undergoes two key conformational changes (Kunishima et al., 2000). First, glutamate binding triggers closure of the VFT domains, resulting in the LB2s coming closer into proximity. Potential conformations from this rearrangement include “open/open” (o/o), “open/closed” (o/c), and “closed/closed” (c/c) (Vafabakhsh et al., 2015). Second, the VFT domains undergo a 70° rotation on an axis perpendicular to the LB1 dimer interface (Kunishima et al., 2000). The inactive unrotated conformation is indicated as “Relaxed”

(R) and the rotated active conformation is indicated as “Active” (A). These two conformational changes can occur independent of each other and are the first steps in mGluR activation. In addition, the closure of both VFT domains is required for full mGluR activation (Kniazeff, Bessis, Maurel, Ansanay, Prézeau, et al., 2004).

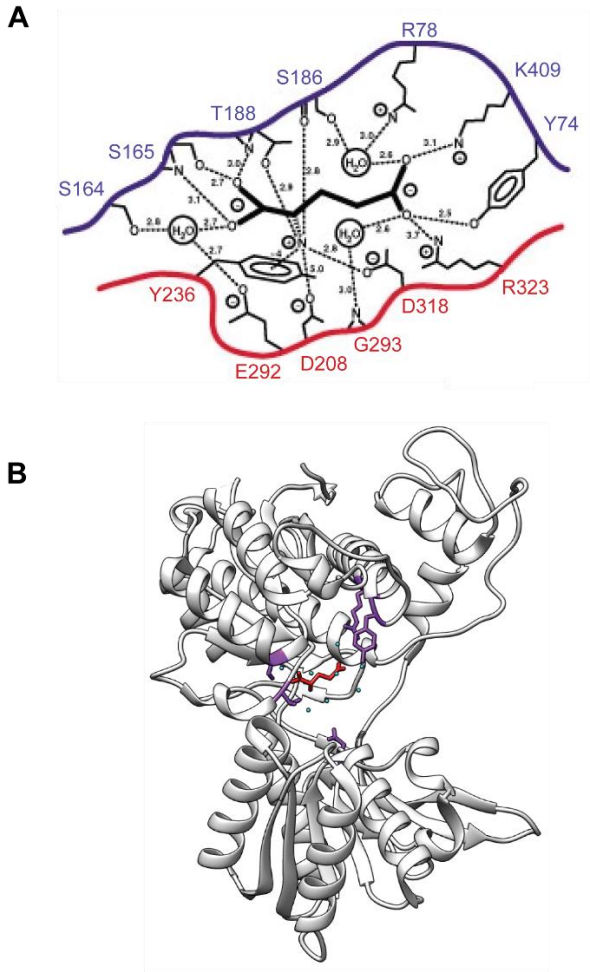

Figure 1.2 Key residues involved in glutamate binding at the orthosteric site
(A) Schematic of key residues interacting with glutamate at cognate binding site. Residues labeled in blue and red indicate location in LB1 and LB2, respectively. Glutamate binding is achieved predominantly through hydrogen bonding interactions. (figure created by Kunishima, N. et al. 2000) **(B)** Crystal structure (mGluR1; PDB:1EWK) of glutamate-bound VFT domain subunit. Purple residues indicate residues essential for glutamate binding. Glutamate is shown in red.

1.3.2 Cysteine-rich domain (CRD)

The CRD is a common structural domain of all class C GPCRs (except for the $GABA_B$ receptor). The CRD contains nine conserved cysteine residues and is primarily composed of six β-hairpins flanked by flexible unstructured regions (Figure 1.3, gold) (Liu et al., 2004; Muto et al., 2007a). The CRD is C-terminal to the VFT domain and is linked to LB2 by a disulfide bond between C254 and C543 in mGluR1 (Figure 1.3, cyan). This disulfide bond is an essential structural feature in mGluRs, serving as a fulcrum and enabling ligand-induced structural changes at the VFT domain to be propagated to the CRD and 7TM domain (Rondard et al., 2006). Importantly, conformational change of the CRD in response to ligand-binding is dependent on the ability of the VFT domains to not only close, but to reorientate to the active interface (Doumazane et al., 2013a). The remaining eight cysteines form intradomain disulfide bonds, providing some rigidity to the CRD (Figure 1.3, gold) (Muto et al., 2007a). Mutation of any of the cysteine residues in the CRD precludes receptor activation and illustrates the importance of this compact structural linker.

The first mGluR CRD structure in addition to molecular modeling analysis suggested that the VFT domains initiate receptor activation by bringing the 7TM domains into closer proximity via the CRDs (Muto et al., 2007a). This hypothesis was proven correct by the first full-length mGluR structure (Koehl et al., 2019a). However, the simple translation of the 7TM domains by the CRDs alone is not sufficient for receptor activation. Crosslinking studies revealed that a specific arrangement of the CRDs relative to one another, is essential for receptor activation (S. Huang et al., 2011). This finding suggests that in addition to the general translation of the 7TM domain, the CRD is essential for establishing a specific signaling competent dimeric arrangement necessary for G protein-coupling.

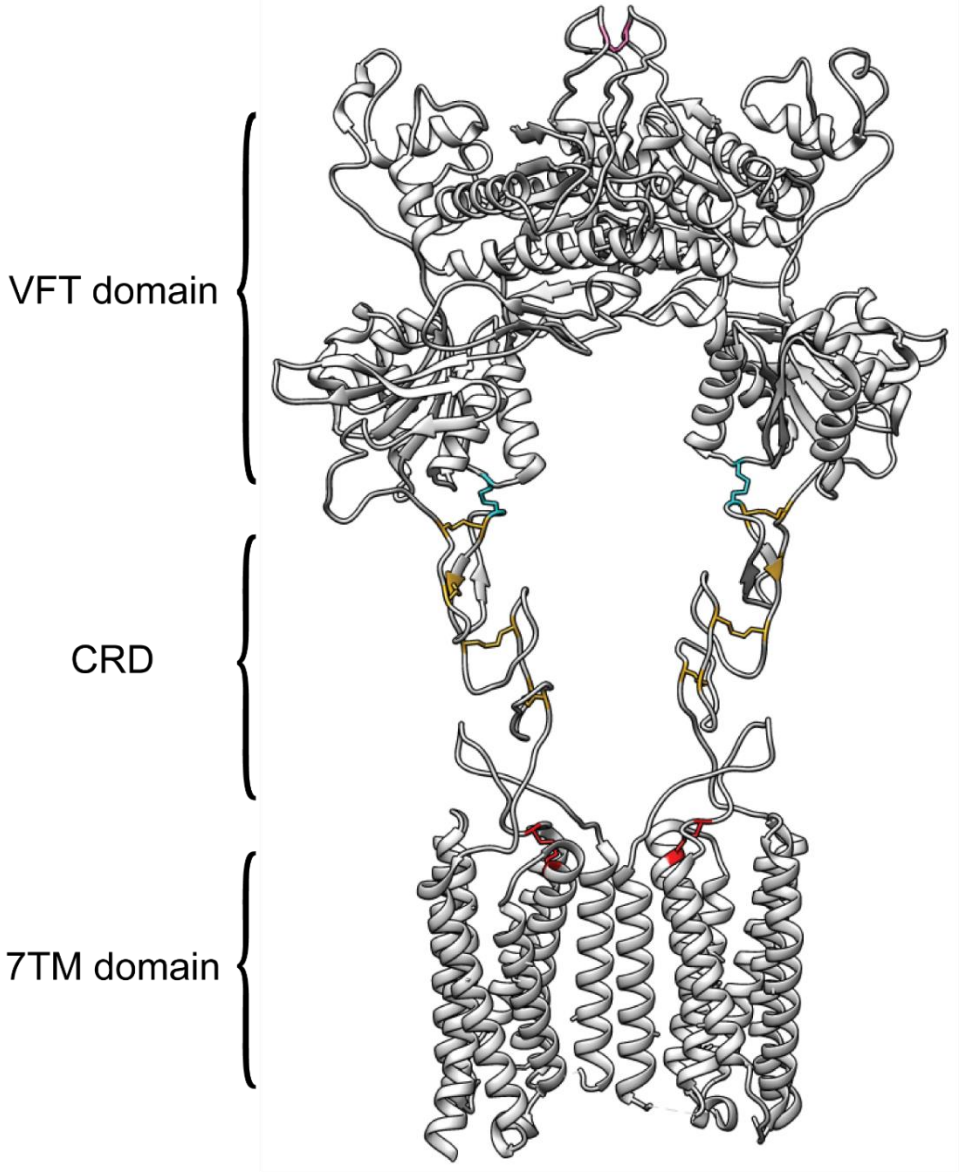

Figure 1.3 mGluR structure highlighting key disulfide bonds
Disulfide bonds in mGluRs are essential for maintaining receptor structural integrity and structurally linking the three domains. The intermolecular disulfide bond mediating dimerization is shown in pink and is located in the flexible loop at the LB1 interface. The disulfide bonds linking LB2s and the CRDs are colored in cyan. Disulfide bonds necessary to maintain structural integrity of the CRDs are colored in yellow. The disulfide bonds linking the CRDs and the 7TM domains are shown in red. (mGluR2; PDB:7EPA)

1.3.3 7 transmembrane (7TM) domain

7TM domain compaction and reorientation upon receptor activation was first quantified directly in live-cells using fluorescence resonance energy transfer (FRET) (Tateyama et al., 2004). Intermolecular conformational sensors reported structural changes when fluorescent reporters were placed within intracellular loops 2 (ICL2), but not at the C-terminal tails of mGluR1, suggesting that a general rearrangement of the 7TM domain core was occurring. Based on the first crystal structures of truncated dimeric 7TM domains, extracellular loop 2 (ECL2) was hypothesized to be a key structural link between the extracellular domains and the 7TM domains due to its outward extension towards the extracellular space (Wu et al., 2014; Doré et al., 2014). Although most of the extracellular domain of the receptor was truncated, ECL2 still formed a strong interaction with the C-terminus of the CRD via a network of backbone and side-chain hydrogen bonds. These structures also revealed that ECL2 is covalently anchored to the top of helix 3 through a disulfide bond, helping establish a more rigid allosteric link between the CRD and 7TM domain (Figure 1.3, red). Interestingly, this anchor point was shown to be important in initiating activation in class A GPCRs as well (Xu et al., 2011). Structure determination of the first full-length mGluR (mGluR5) revealed an almost identical conformation for ECL2 and provided a more complete picture of its role in interdomain linkage (Koehl et al., 2019a). Two primary interaction interfaces were determined. The first interface involves hydrophobic interactions between residues 729-731 of ECL2 and 568-571 of the CRD. The second interface involves ionic or cation-π interaction between a composite interface of the CRD composed of Glu539 and Trp557 and the apical loop region of ECL2 composed of residues 725-727.

The 7TM domain dimer interface varies among mGluRs and a growing body of evidence is emerging that links this variation to signaling modulation. In the full-length mGluR5 structure, the 7TM domains were well separated and a symmetric TM5-TM5 inactive interface was observed (Koehl et al., 2019a). In contrast, in the full-length mGluR2 structure, the 7TM domains were minimally separated and showed an asymmetric inactive TM3-TM4 interface (Seven et al., 2021). Minimal separation of the 7TM domains was also observed for mGluR7 which showed a TM3-TM3 and TM5-TM5 inactive interface (Du et al., 2021). Live-cell FRET studies on group II mGluRs revealed that TM4 was essential in modulating dimerization propensity, orthosteric and allosteric activation, and basal activity in the receptors (Thibado et al., 2021). Interestingly, in crosslinking experiments on mGluR2, the inactive interface was identified to be either TM4-TM4 or TM5-TM5, contrary to the asymmetric TM3-TM4 interface from structures (Xue et al., 2015a). Compared to the inactive receptors, the activated mGluRs (mGluR2/4/5) showed a consistent TM6-TM6 interface that may suggest a conserved mechanism necessary for G protein-coupling (Koehl et al., 2019a; Seven et al., 2021; Lin et al., 2021).

1.3.4 G protein interactions

Since the discovery of mGluRs, their lack of sequence homology with other GPCRs and dimeric structure have raised questions regarding their G protein-coupling mechanism. Rhodopsin-like GPCRs possess a conserved aspartate-arginine-tyrosine (DRY) tripeptide at the N-termini of ICL2 (Franke et al., 1990; Ohyama et al., 1992) and long, highly variable ICL3s (Cotecchia et al., 1992; Kobilka et al., 1988) that are essential for G protein-coupling and specificity, respectively. In contrast, mGluRs lack DRY motifs and have short and highly conserved ICL3s. A mGluR1 mutagenesis study revealed that conserved residues in ICL2 and ICL3 were necessary for G protein

signaling and selectivity (Francesconi & Duvoisin, 1998; Gomeza et al., 1996). Specifically, residues K690, T695, K697, P698, and S702 in ICL2 were important for G protein signaling while R775 and F781 in ICL3 played a role in G protein specificity. Thus, despite the distinct sequence homology of mGluR cytosolic regions, the intracellular loops still play an integral role in G protein-coupling.

The hallmark of class A and B GPCR activation is the outward movement of the cytoplasmic end of TM6 and the subsequent insertion of α5 helix from the Gα subunit into the cleft between TM3, TM5, and TM6 (Rasmussen et al., 2011). However, this outward shift of TM6 is absent in full-length structures of active mGluRs (Koehl et al., 2019a; Seven et al., 2021; Lin et al., 2021). Recently, several full-length mGluR structures with a single heterotrimeric G protein bound have been solved, verifying the lack of an outward shift in TM6 and highlighting novel G protein interactions with ICL2, ICL3, as well as the C-terminal tail of the receptor (Seven et al., 2021; Lin et al., 2021). In these structures, the α5 helix of Gα is stabilized in a pocket formed by TM3, ICL2, ICL3, and the C-terminal tail (Figure 1.4). ICL2 and the cytoplasmic tip of TM3 form half of the pocket and stabilize the α5 helix through various hydrophobic interactions and a polar interaction between R670 (mGluR2) and D350 (Gα). Opposite to ICL2, H828 and R829 of the C-terminal tail forms polar interactions with D341, Y320, and E318 of Gα. F756 on ICL3 forms a hydrophobic interaction with F354 on the Gα C-terminal. Comparison of the G protein-bound and -unbound subunits suggests that ICL3 is essential in initiating pocket formation. Specifically, an upward shift in TM6 results in a rearrangement of the hydrophobic residues in ICL3, which initiates hydrophobic packing with TM3, ICL2, and the C-terminus.

Aside from heterotrimeric G protein binding to a single monomer, these full-length mGluR structures highlight more subtle aspects of dimer asymmetry central to receptor activation (Seven et al., 2021; Lin et al., 2021). A notable difference between the G protein-bound and -unbound subunits is the orientation of W697 in TM4 and H723 in ECL2 in mGluR2 (Seven et al., 2021). In the G protein-bound subunit, W697 faces outward, while in the unbound subunit W697 projects into the 7TM domain core and interacts with H723. This W697-H723 interaction in the unbound subunit keeps TM5 and TM6 in closer proximity, reducing the size of the allosteric pocket and providing an explanation for why the positive allosteric modulator, ADX55164 (Addex Therapeutics), is bound to only a single monomer (Figure 1.4). Asymmetry is also apparent at the ECL2s. In the G protein-bound subunit, E712 and R714 in ECL2 point towards ECL3 while ECL2 is unresolved in the unbound subunit. Subsequent mutagenesis analysis of these residues confirmed their importance in propagating conformational change from the VFT domain to the 7TM domain. Currently, whether this asymmetric structure is established prior to or is the consequence of G protein coupling is still unclear.

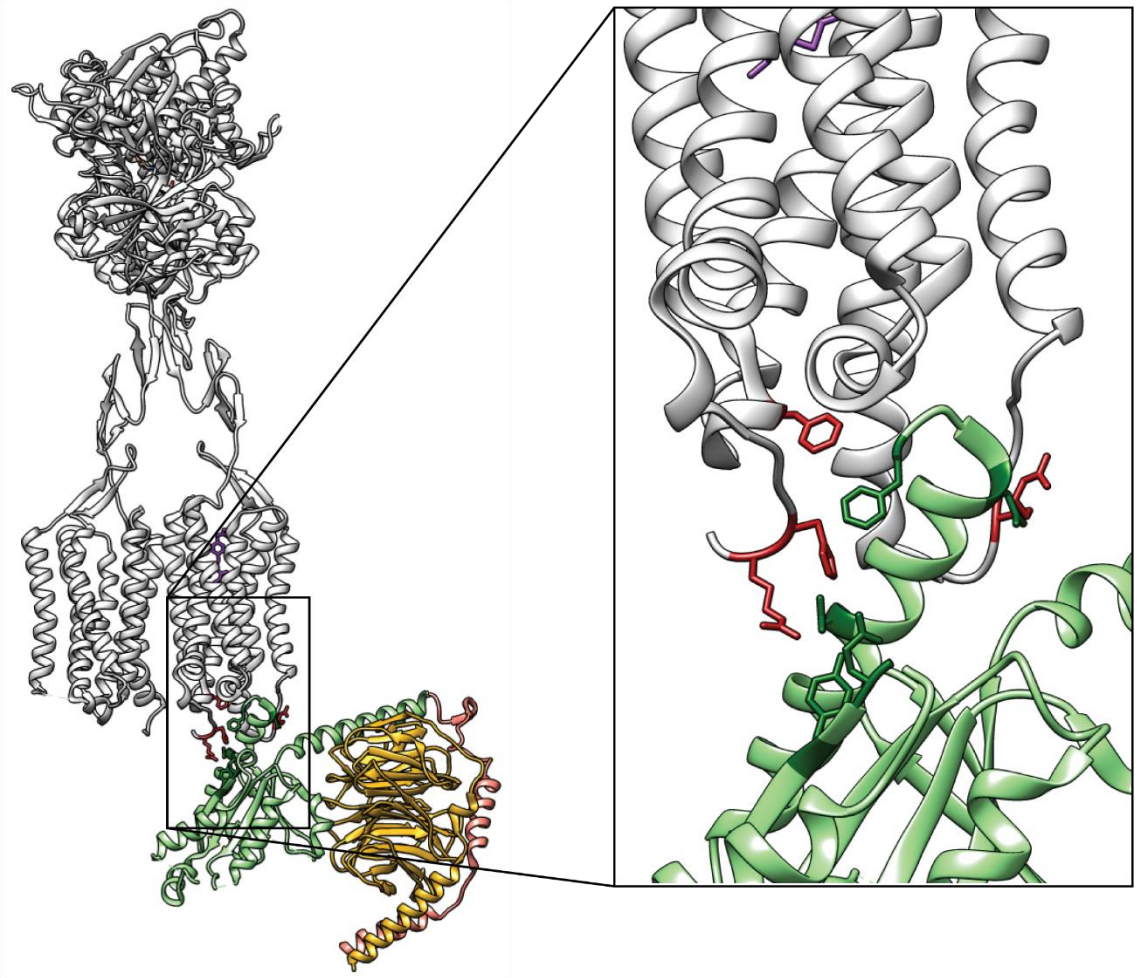

Figure 1.4 mGluR-G protein coupling interface
mGluR-G protein-coupling occurs using a mechanism distinct from rhodopsin-like GPCRs. Instead of the α5 helix of Gα inserting into the transmembrane bundle, the α5 helix is stabilized by a pocket formed by TM3, ICL2, ICL3, and the C-terminal tail. ICL3 is thought to initiate pocket formation via hydrophobic packing interactions. mGluR-G protein complex structure determination confirms mGluR coupling to individual heterotrimeric G proteins. mGluR2 shown in white, Gα in light green, G_β in yellow, G_γ in pink, interacting mGluR2 residues in red, and interacting α5 helix residues in dark green. (PDB:7MTS)

1.3.5 Structural dynamics and conformational coupling of domains

The recent influx of full-length mGluR structures has been invaluable in our understanding of the mGluR active conformation and G protein-coupling mechanism. However, it is accepted that mGluR activation and modulation are highly dynamic processes that static representations alone cannot sufficiently describe. Fortunately, there is a growing body of work utilizing FRET in both the cellular and single-molecule context to dissect mGluR structural dynamics.

Structural analysis of mGluRs revealed that the VFT domains undergo two major rearrangements: (1) closure of VFT domains and (2) rotation of VFT domains at the LB1 interface (Doumazane et al., 2013a). Both of these structural rearrangements are necessary to bring the LB2s together and initiate compaction of the CRDs and 7TM domains for receptor activation. Examination of group II mGluRs by single-molecule FRET (smFRET) led to the identification of three distinct VFT domain conformations (Vafabakhsh et al., 2015). These conformations were defined as relaxed-open/open (R/o/o), relaxed-open/closed (R/o/c), and active-closed/closed (A/c/c). The R/o/c conformation represented a transient intermediate step towards activation. Activation was determined to require the closure of both VFT domains and their subsequent rotation to the active interface, however, spontaneous closure of VFT domains could result in basal activation. The VFT domain was found to occupy four conformations when examined using fluorescence correlation spectroscopy (FCS), a method with sub-millisecond time resolution (Cao et al., 2021; Olofsson et al., 2014). However, the additional conformational state is not present in structural data, nor does it significantly change occupancy upon receptor stimulation, casting doubt on its physiological relevance.

VFT domain structural dynamics are an accurate metric of both orthosteric and allosteric ligand efficacy despite its distal location from the G protein-coupling interface. Specifically, stability or dwell-time of the VFT domain active conformation is an accurate predictor of agonist efficacy (Vafabakhsh et al., 2015). Furthermore, VFT domain stability demonstrates strong positive correlation with allosteric modulators' ability to regulate glutamate efficacy (Cao et al., 2021). While VFT domain dynamics have demonstrated strong predictive power in regard to ligand efficacy, whether VFT stability underlies ligand efficacy or is a mere byproduct of ligand-binding is unknown. Moreover, how pharmacological properties of compounds are represented at the CRD or 7TM domain is unclear.

Single-molecule FRET (smFRET) has proven to be a powerful tool for dissecting the different contributions of the dimer interface on mGluR cooperativity and structure. The advantage of smFRET over traditional ensemble FRET is that by analyzing proteins one at a time, one can detect rare and brief conformational states and the time-ordering of transitions. mGluR dimerization is mediated primarily by hydrophobic interactions and an intermolecular disulfide bond in LB1. In a smFRET study of group II mGluRs, the hydrophobic interactions were found to preferentially stabilize the receptor in the R/o/o configuration (Levitz et al., 2016). In contrast, the intermolecular disulfide bond functioned in stabilizing the A/c/c conformation of the dimeric receptor and enabled cooperativity between monomers. Collectively, these findings suggest that interactions at the dimer interface may function to tune receptor activation.

smFRET analyses on mGluR heterodimers have begun to reveal how functional diversity is enabled by heterodimerization. mGluR2/3 heterodimers demonstrated glutamate potency that was intermediate to their homodimeric constituents (Levitz et al., 2016). Furthermore, the presence of

a mGluR3 monomer in the heterodimer introduced moderate basal activity that was ~60% of the mGluR3 homodimer. While mGluR2/3 heterodimerization results in a receptor with physiological properties that are the average of its constituent components, this is not always the case. Interestingly, heterodimerization of mGluR2 and mGluR7 which have micromolar and millimolar glutamate potency, respectively, result in a hypersensitive receptor with sub-micromolar sensitivity in addition to basal activity (Habrian et al., 2019). The mGluR2/7 heterodimer also utilizes a novel activation pathway in which dimer reorientation occurs prior to closure of both VFT domains. Despite the wealth of information on the VFT domain provided by smFRET studies thus far, we have only begun to scratch the surface.

Establishing an active TM6-TM6 interface between the 7TM domains require both translation and reorientation of individual subunits (Koehl et al., 2019a; Tateyama et al., 2004). However, the convolution of intramolecular and intermolecular conformational changes at the 7TM domain have obfuscated the steps towards an active interface. Fortunately, novel tools for selecting heterodimeric receptors and generating intramolecular FRET sensors have helped shed light on the activation process at the 7TM domain (Hlavackova et al., 2012; Maurel et al., 2008). Live-cell FRET studies revealed that activation at the 7TM domain requires at least two steps, first an interdomain translation, followed by an intradomain rearrangement (Hlavackova et al., 2012). Application of synchronous receptor stimulation and data acquisition strategies revealed that the intermolecular and intramolecular rearrangement of the 7TM domains occurs within ~1ms and ~20ms, respectively (Grushevskyi et al., 2019). These studies also suggest that activation and deactivation follow a cyclic pathway with at least two metastable intermediate states. However,

due to the limitations of ensemble measurements, the identities of these intermediates are currently unknown.

The conformational dynamics of the CRD, the key structure linking the ligand-binding and G protein-coupling domains, are poorly understood relative to the VFT domain and 7TM domain. This is due in part to the compact and flexible nature of the CRD, making it technically challenging to site-specifically label without perturbing its native structure. However, its medial location relative to the orthosteric and allosteric ligand binding sites make it a promising candidate to probe both mGluR activation and modulation. A major goal of the thesis work presented herein is to develop tools to probe CRD structural changes and characterize conformational dynamics that underlie receptor activation and modulation.

1.4 Metabotropic glutamate receptor pharmacology

GPCRs currently represent the most sought-after family of drug targets, with about 30% of all clinically approved pharmaceuticals acting upon them (Santos et al., 2017). However, these ~500 therapeutic agents act on ~100 GPCRs, only a quarter of all the non-olfactory GPCRs (Hauser et al., 2017; Congreve et al., 2020). Furthermore, these compounds predominantly target the class A rhodopsin family of GPCRs, resulting in a saturated druggable space. mGluRs are major components of the glutamatergic pathway in the brain and thus represent a highly underutilized resource based on their potential for treating a range of neurological and psychiatric disorders (Lindsley et al., 2016; Conn & Jones, 2009; Conn, Lindsley, et al., 2009) that include Parkinson's disease (Abd-Elrahman et al., 2020; Kumar et al., 2015; Hopkins et al., 2009; Renner et al., 2010), Autism (Aguilar-Valles et al., 2015), Fragile-X syndrome (Stoppel et al., 2021), Huntington's

disease (Li et al., 2021), schizophrenia (Griebel et al., 2016), depression (Joffe et al., 2020), multiple sclerosis (Woo et al., 2021), and neuro-developmental disorders (Fisher et al., 2018; Palazzo et al., 2016), in addition to cancer (Pereira et al., 2017), congenital stationary night blindness (Varin et al., 2021), and pain (Mazzitelli et al., 2018). Underutilization of mGluRs stems in part from their unique architecture and complex activation mechanism. Thus, a central goal of this thesis is to develop mechanistic insight on mGluR activation and modulation by various therapeutic compounds.

1.4.1 Orthosteric ligand binding site

Initial drug development efforts for mGluRs focused on the orthosteric or cognate ligand-binding site (Niswender & Conn, 2010; Bräuner-Osborne et al., 2007). The development of subgroup specific ligands targeting the cognate site showed reasonable success due to the unique shape and bitopic nature among mGluR subgroups (Goudet et al., 2012). Group I mGluRs can form a unique π-π interaction using W100 and hydrogen bonds with Y64, K396, and R310 (mGluR5 residues) (Mølck et al., 2014). These interactions are absent in group II and III mGluRs, enabling group I specificity. In group II mGluRs, R64 (mGluR3 residue) in LB1 forms hydrogen bonds with carbonyl carbons in LB2, leading to a shift in lobes and expansion of the orthosteric site, allowing glutamate and other group II specific ligand to penetrate more deeply into the cavity (Mølck et al., 2014). Lastly, group III mGluRs, like group II receptors, possess a deeper orthosteric pocket. However, group III receptors also possess distinct residues deeper in the pocket, enabling group III specific ligands to be designed (Niswender & Conn, 2010; Mølck et al., 2014; Bräuner-Osborne et al., 2007). While group selectivity can be achieved by targeting these divergent structural features in the cognate ligand binding pocket, full conservation of the cognate site among some

group members precludes the subtype specificity needed to leverage these sites for clinical application. To achieve subtype specificity, targeting the less conserved allosteric site became of interest.

1.4.2 Allosteric ligand binding site

The separation of the cognate binding site from the 7TM domain has removed the evolutionary constraints on the allosteric pocket, resulting in an increase in subtype specific contacts (Niswender & Conn, 2010; Wootten et al., 2013). Currently, there are no known native ligands that bind within the allosteric pocket, leaving it available for external manipulation.

Residues forming contact sites within the allosteric pocket have been identified through structural and mutagenesis studies. The first mGluR 7TM domain structures were solved in the presence of negative allosteric modulators (NAMs) and demonstrated a similar ligand-binding modality as orthosteric ligand in rhodopsin-like GPCRs (Wu et al., 2014; Doré et al., 2014). The importance of the NAM-interacting residues, which are distributed across all 7TM domain helices, were verified in subsequent mutagenesis studies for mGluR2 employing high throughput functional screening (Figure 1.5) (Farinha et al., 2015; Lundström et al., 2011). Specifically, F780, H723, R636, and V798 were shown to be important for NAM function, while S688, G689, N735, F776, and L639 were found to be important for positive allosteric modulator (PAM) function. Interestingly, R635, F643, L732 were shown to be vital for mediating both PAM and NAM effects. An influx of new full-length mGluR structures further shed light on the residues that formed the PAM (PDB:7MTR, 7MTS, 7E9G) (Seven et al., 2021; Lin et al., 2021) and NAM binding pocket (PDB:7EPE, 7EPF) (Du et al., 2021). Many of the same residues were found to make contact with both PAMs and NAMs. The overlap of PAM and NAM binding sites suggests mGluR modulation

may involve subtle regulation of receptor structure that may facilitate or hinder entry into an active conformation (Figure 1.5).

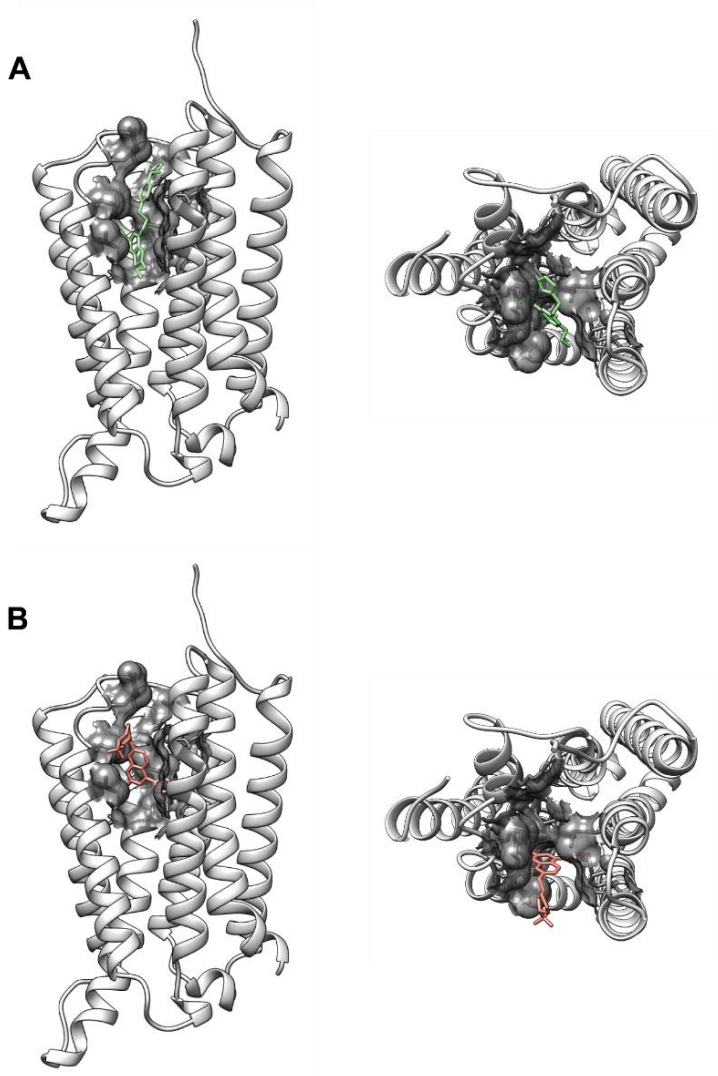

Figure 1.5 mGluR allosteric ligand binding site
Positive (PAM) and negative (NAM) allosteric modulators bind the mGluR allosteric site using conserved residues. mGluR2 residues found to interact with modulators via structural or mutagenesis studies are shown as surface representations (PDB:7MTS). A PAM (PDB:7MTS) **(A)** and NAM (PDB:7EPE) **(B)** solved in complex with mGluR2 show a similar topology within the binding site.

1.4.3 Allosteric modulators as therapeutics

Allosteric modulators possess broad functionality and subtype specificity, making them versatile therapeutic agents (Wootten et al., 2013; Feng et al., 2015; Thal et al., 2018; Urwyler, 2011). In contrast to orthosteric ligand that function by directly stimulating or inhibiting receptor activation, allosteric modulators can be designed to have no intrinsic effect when applied alone (Foster & Conn, 2017; Harpsøe et al., 2015). These so called "pure" modulators conserve the native spatiotemporal profile of receptors and have minimal overdose potential. In addition, allosteric modulators can also be engineered to have intrinsic agonist activity (ago-PAMs) (Conn, Lindsley, et al., 2009) or no activity (silent allosteric modulators; SAMs) (Gregory et al., 2015), making them useful tools to study the allosteric site.

Despite the therapeutic potential of mGluRs, technical advantages of allosteric modulators, and sustained drug discovery efforts for over 25 years, there are currently no clinically approved pharmaceuticals targeting mGluRs (Urwyler, 2011; Annoura et al., 1996). While many candidates have progressed to clinical trials, none demonstrated significant efficacy in humans (https://clinicaltrials.gov/). This contrasts with the substantial pre-clinical success of mGluR allosteric modulators (Urwyler, 2011). The failure in clinical translation of mGluR allosteric modulators stems from an incomplete understanding of both mGluR signaling complexity and the structural basis for mGluR allosteric modulation.

Improvements in tools for quantifying GPCR activation have shown mGluR signaling to be far more complex than previously anticipated, prompting the need for a more nuanced understanding of mGluR pharmacology (Sengmany et al., 2019; Sengmany et al., 2020; Sengmany et al., 2017). Specifically, mGluRs are now known to couple to multiple G proteins (Hermans & Challiss, 2001;

Iacovelli et al., 2002) and differentially interact with β-arrestin (Abreu et al., 2021; Eng et al., 2016). In a recent study, group I mGluRs demonstrated a unique ability to mediate synaptic plasticity in both a β-arrestin2- and $G\alpha_{q/11}$-dependent manner (Eng et al., 2016). While in a more general examination of mGluR subtypes, differential β-arrestin-mediated desensitization and internalization was observed among the family of receptors (Abreu et al., 2021). Furthermore, separate studies directly examining allosteric modulator effects on mGluR signaling demonstrated the potential for preferential pathway modulation (Sengmany et al., 2017). Collectively, these findings highlight the need for more comprehensive functional characterization of mGluR allosteric modulators.

Crystallographic and cryo-EM structures of mGluRs have been invaluable in defining allosteric ligand binding modalities and visualizing modulator-induced conformations (Wu et al., 2014; Doré et al., 2014; Seven et al., 2021; Du et al., 2021; Lin et al., 2021). However, these structures represent only a small subset of the potential mGluR-modulator combinations. Futhermore, static structural representations of mGluRs do not provide information on receptor dynamics which are central to mGluR function. Thus, establishing a dynamic structural framework for interpretting mGluR function is an essential step towards the development of allosteric drugs.

1.5 Metabotropic glutamate receptors in the lipid bilayer

1.5.1 Lipid bilayer modulates membrane receptor activity

Biological membranes are heterogenous and dynamic mosaics of lipids and proteins that provide the physiochemical environment necessary for GPCR function. Cholesterol is a unique lipid bilayer constituent that has demonstrated the ability to regulate GPCR function by altering the bulk

biophysical properties of the bilayer (Song et al., 2014; Allende et al., 2004; Anishkin et al., 2014) and through direct interactions (Song et al., 2014; Chini & Parenti, 2009; Gimpl, 2016).

The plasma membrane contains diverse topologies and microdomains such as lipid rafts enriched with sphingolipids and cholesterol (Lingwood & Simons, 2010; Brown, 2006; Elson et al., 2010). These rafts are densely packed and thicker structures (Mouritsen & Bloom, 1984; Lundbaek et al., 2003) with reduced elasticity (Rawicz et al., 2000; Needham & Nunn, 1990) and resistance to detergent solubilization (Allende et al., 2004; Gandhavadi et al., 2002; Brown & London, 2000) and are hypothesized to serve as signaling platforms, consolidating necessary machinery for GPCR signal transduction. These microdomains are highly transient nanoscopic structures and their mechanism for assembly is poorly understood. However, GPCR recruitment to these domains have shown dependency on cholesterol binding motifs such as the cholesterol consensus motif (CCM) (Hanson et al., 2008), the cholesterol recognition/interaction amino acid consensus (CRAC) motif, and the inverted CRAC (CARC) motif (Sarkar & Chattopadhyay, 2020). One goal of this thesis is to understand how cholesterol regulates mGluR conformational dynamics and function.

1.5.2 Cholesterol and mGluR function

mGluR recruitment to lipid rafts and activation have been directly linked to plasma membrane cholesterol. Studies on group I mGluRs (Kumari et al., 2013) and the *drosophila* mGluR homologue (dmGluR) (Eroglu et al., 2003) showed cholesterol dependence in glutamate binding affinity and receptor activation. In group I mGluRs specifically, disruption of lipid rafts by chemical or pharmacological approaches or mutation of the CRAC motif reduced mGluR signaling (Kumari et al., 2013). Similarly, cholesterol was also shown to directly interact and upregulate dmGluR glutamate affinity via chemical crosslinking studies (Eroglu et al., 2003). Collectively,

these findings suggest cholesterol functions as a PAM and is important for the recruitment of mGluRs to lipid raft signaling modules.

Computational studies have also been conducted on mGluR2 to identify cholesterol binding sites (Kurth et al., 2020). These studies suggested that there are 2 to 7 cholesterol interaction sites on the exterior of the mGluR2 7TM domain that rely on surface matching interactions. *In silico* analyses of group I mGluRs revealed that cholesterol may preferentially locate to shallow pockets formed by protein ridges and do not generally localize to CRAC motifs (Lee, 2019; Sejdiu & Tieleman, 2020). These simulations indicate that cholesterol does not form stable contacts with mGluRs, which is aligned with a lack of cholesterol in any full-length mGluR structure. Similar cholesterol interactions with the exterior of the 7TM domain have also been observed for non-class C GPCRs (Chini & Parenti, 2009; Gimpl, 2016; Sarkar & Chattopadhyay, 2020; Sejdiu & Tieleman, 2020).

1.5.3 Cholesterol and phospholipids in mGluR structures

The first crystal structure of the mGluR 7TM domain revealed cholesterol bound at the dimer interface (Wu et al., 2014). Specifically, six cholesterol molecules were found to interact with hydrophobic residues in TM1 of each monomer and were essential for 7TM domain crystallization. Whether this interface represents a biologically relevant inactive, active, or intermediate interface is unclear as the 7TM domains were truncated. Aside from mGluR1, cholesterol has also been identified in full-length structures of GPR158, another class C GPCR (Jeong et al., 2021; Patil et al., 2022). Interestingly, in these structures cholesterol not only binds at the dimer interface, leading to a more compact receptor, but also forms stable interactions with the exterior of the 7TM domain bundle.

In addition to cholesterol, phospholipids have also appeared to play a structural role in class C GPCRs. In both $GABA_B$ (Papasergi-Scott et al., 2020; Yang et al., 2022) and GPR158 receptors (Jeong et al., 2021; Patil et al., 2022), phospholipids were found deep within the 7TM domain bundle. In the case of the $GABA_B$ receptor, phosphatidylethanolamine was found to interact with ECL2, suggesting the phospholipid may serve as a key structural component to propagate conformational changes from the VFT domain to the 7TM domain.

1.5.4 Detergents

Detergents are indispensable tools for the isolation and purification of membrane proteins from biological membranes (Lin & Guidotti, 2009). Solubilization by detergents enabled membrane proteins to be studied using a range of physiochemical and kinetic methods *in vitro* (le Maire et al., 2000). However, detergents in many ways neglect the physicochemical complexity of the lipid bilayer that is necessary to maintain membrane protein structure and function (Charalambous et al., 2008). In this thesis, I will examine the effect of solubilizing detergents with diverse chemical structures on mGluR2 conformational dynamics – specifically focusing on n-Dodecyl-β-D-Maltopyranoside (DDM), laurel maltose-neopentyl glycol (LMNG), and glycol-diosgenin (GDN). The synthesis and application of DDM and its derivatives revolutionized the field of membrane protein biology, enabling efficient isolation of a broad range of membrane proteins (VanAken et al., 1986). DDM is composed of a maltose hydrophilic headgroup and a 12-carbon alkyl hydrophobic tail. DDM is characterized as a non-ionic and mild detergent and was integral in the initial purification and structure determination process of rhodopsin-like GPCRs (Newstead et al., 2008).

A new class of non-ionic detergents containing maltose-neopentyl glycols (MNGs) in the hydrophilic region have shown great promise in maintaining structure and function of a broader array of membrane proteins as compared to DDM (Chae et al., 2010). LMNG specifically, is the double hydrocarbon tail counterpart of DDM. Based on molecular dynamics simulation studies, the larger size of LMNG results in a lower rate of tumbling and diffusion in solution. This reduced diffusion is hypothesized to result in more effective shielding of the hydrophobic domains from water penetration, improved membrane protein stability, and reduced protein denaturation (Lee et al., 2020; S. Lee et al., 2016).

Over time, amphiphiles incorporating non-aliphatic structural elements in the hydrophobic region were synthesized and applied to membrane protein studies. The digitonin derivative, GDN, composed of a rigid steroid-based lipophilic group and a di-maltose hydrophilic headgroup has shown the ability to effectively solubilize membrane proteins from biological membranes and maintain protein function in a range of environmental conditions (Chae et al., 2012). This new class of detergent functions as a promising alternative to more traditional surfactants and may serve as a precursor to other amphiphiles employing a steroidal hydrophobic group.

1.5.5 Membrane mimetics

Membrane mimetics are essential for protein-lipid interaction studies in an *in vitro* context. The use of several lipid scaffolds have been shown to be useful for conserving membrane protein integrity and dynamics (Frey et al., 2017; Warschawski et al., 2011). Each scaffold type has unique strengths and limitations, and the choice depends on the question at hand.

Liposomes (Akbarzadeh et al., 2013), bicelles (Dürr et al., 2012), and nanodiscs (Bayburt et al., 2002; Denisov et al., 2004) enable tight control of scaffold components, allowing lipid

composition, cholesterol content, and other specific bilayer-centric questions to be addressed. However, these scaffolds require the time-consuming process of membrane protein purification and reconstitution. In addition to these processes, the use of these scaffolds requires the pre-solubilization of proteins in detergent before insertion into lipid particles, which may contribute to protein denaturation.

Hydrophobically associating polymers are novel tools for membrane protein extraction and solubilization that circumvent the challenges intrinsic to traditional membrane mimetic platforms (Knowles et al., 2009; Tonge & Tighe, 2001). The co-polymer styrene maleic acid (SMA) specifically has been shown to effectively extract and solubilize membrane proteins directly from biological membranes into SMA lipid particles (SMALPs), precluding the need for protein pre-solubilization, purification, and reconstitution (S. C. Lee et al., 2016). Furthermore, the synthesis of these polymers is straightforward and amenable to change, enabling them to be adapted for different applications (Kopf et al., 2022; Yasuhara et al., 2017). In this thesis, I will examine SMALP-solubilized mGluR2 structural dynamics, facilitating comparison between lipid- and detergent-solubilized receptors.

1.6 Single-molecule fluorescence resonance energy transfer (smFRET) microscopy

mGluRs are large membrane bound proteins whose function is dependent on the complex conformational coupling of three distinct structural domains. Studying mGluR conformational dynamics using traditional biophysical methods such as nuclear magnetic resonance (NMR) and double electron-electron resonance (DEER) spectroscopy would be technically challenging due to

the large amount of protein required for these approaches. Furthermore, these ensemble measurements do not provide information on temporal ordering of conformations or transient intermediates. To overcome these weaknesses, the work in this thesis applies single-molecule fluorescence resonance energy transfer (smFRET) microscopy to study mGluR2 conformational dynamics.

1.6.1 Fluorescence resonance energy transfer (FRET)

Resonance energy transfer (RET), or more specifically fluorescence resonance energy transfer (FRET), is an optical process in which excess energy from one molecule, donor, is transferred to another molecule, acceptor (Figure 1.6A) (Cleg, 2006; Jones & Bradshaw, 2019). This energy is derived from the relaxation of an electron from a higher energy state to a lower energy state, with the excess energy being transferred to the acceptor as non-radiative energy in the form of virtual photons. This form of energy transfer was theorized to occur through dipole interactions and was posited by J. Perrin (Perrin, 1932). This theoretical interpretation was expanded upon by Förster, who found the two main parameters governing this energy transfer to be (1) spectral overlap and (2) intermolecular distance between donor and acceptor (Förster, 1948, 1965). The famous R^{-6} distance relation in FRET efficiency calculations

$$E = \frac{1}{1 + (\frac{R}{R_0})^6}$$

was verified by S.A. Latt (Latt et al., 1965), and ultimately applied to the concept of a "spectroscopic ruler" (Sahoo, 2011; Stryer & Haugland, 1967).

smFRET is a powerful technique for studying the conformational distribution and dynamics of biological molecules (Figure 1.6A). By examining single particles, the need to synchronize

molecules can be bypassed and rare and transient conformations can be visualized (Figure 1.6B) (Gopich & Szabo, 2010; Ha, 2001; Schuler, 2013). Furthermore, smFRET allows for detailed quantification of kinetic rates of individual molecules. Conformational distribution can also be effectively approximated by the summation of FRET efficiency histograms estimated as Gaussian distributions (Figure 1.6C) (Gopich & Szabo, 2010).

The first smFRET experiment was conducted by T. Ha, which demonstrated that fluorescence from single donor-acceptor pairs could be measured (Ha et al., 1996). Since its inception, smFRET has been adapted for solution based studies, providing high resolution mechanistic insight on a wide range of biological phenomena that include DNA replication, recombination, transcription, translation, RNA folding and catalysis, non-canonical DNA dynamics, protein folding and conformational changes, various motor proteins, membrane fusions proteins, ion channels, and signal transduction to name just a few (Michalet et al., 2006; Sasmal et al., 2016; Seidel & Dekker, 2007; Smiley & Hammes, 2006; Weiss, 1999; Zhuang, 2005). Furthermore, as smFRET became more widespread, detailed instructions and tutorials have become available to guide individuals in microscope builds and smFRET experimental design and data analysis (Ha, 2001; Joo & Ha, 2012; Lerner et al., 2021; Roy et al., 2008).

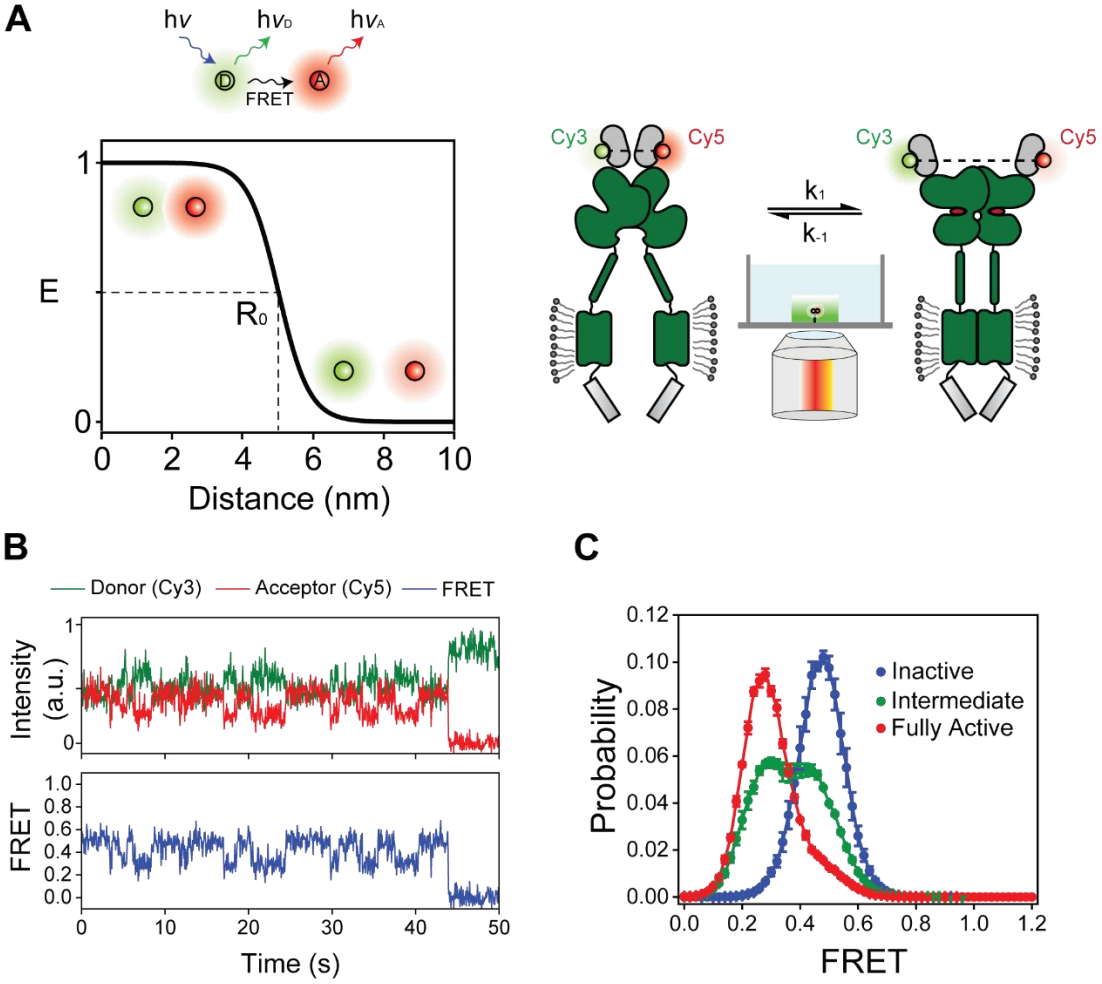

Figure 1.6 Single-molecule fluorescence resonance energy transfer (smFRET)
Fluorescence resonance energy transfer (FRET) between donor and acceptor molecules is a distance-dependent phenomenon and useful tool for probing structural changes in biomolecules. (A) FRET has a linear range, where R_0 represents the distance at which energy transfer is 50%. smFRET experiments conducted in this thesis specifically utilize an objective-based system. (B) Donor, acceptor, and corresponding FRET signal can be captured for individual receptors with up to millisecond time resolution, enabling kinetic analysis to be conducted. (C) Aggregation of data from many individual molecules can be used to generate FRET histograms that highlight the most common conformations of the protein of interest.

1.6.2 Fluorescent reporters, oxygen scavenging systems, and bioconjugation strategies

The choice of fluorescent reporter is central to all smFRET experiments (Roy et al., 2008). Generally, an ideal reporter is bright, possessing an extinction coefficient (ε) > 50,000 $M^{-1}cm^{-1}$ and quantum yield (QY) > 0.1, and photostable, showing minimal response to photophysical or chemical aggregation (Roy et al., 2008). In addition, an ideal FRET pair should have (1) large spectral separation between donor and acceptor emissions, (2) possess similar quantum yields, and (3) be small and water soluble with multiple options for bio-conjugation chemistries.

Fluorescent proteins have been applied to smFRET studies, however, their poor photostability have hindered their broader application (Brasselet et al., 2000). In contrast, semiconductor quantum dots (QDs) demonstrate good photostability, but lack monovalent conjugation schemes and are limited due to their large size (> 20nm in diameter) (Hohng & Ha, 2004, 2005). Thus, the most popular smFRET fluorophores have been and remain small organic dyes (< 1nm) (Kapanidis & Weiss, 2002). Although Cy3 and Cy5 remain the favorite FRET pair, alternatives to Cy3 with similar quality are available (Roy et al., 2008). Improvements in near infrared dyes such as Cy5.5 and Cy7 have also provided new ways to conduct 3-color FRET experiments (Hohng et al., 2004). Lastly, the recent invention of cell-permeable organic dyes has helped streamline the workflow for labeling intracellular proteins and protein domains (Grimm et al., 2017).

Reactive oxygen species in imaging buffer results in reduced photostability and increased photobleaching (Hübner et al., 2001). The oxygen scavenging system traditionally used to address this employ a mix of glucose oxidase, catalase, and β-D-glucose (Benesch & Benesch, 1953). However, an alternative option has emerged over time that uses protecatechuic acid and protocatechuate-3,4-dioxygenase, which has shown a ~40% improvement over the glucose

oxidase system (Aitken et al., 2008). Furthermore, the vitamin E derivative Trolox is now commonly used as an additive, functioning as an excellent quencher of unfavorable triplet states in fluorophores (Rasnik et al., 2006).

In conformational FRET sensor design, tag location and conjugation method are the most important considerations. Fluorescent tags should be in locations that stay within a 2-8nm proximity throughout the biological process of interest and ideally transition through the R_0 value (Wu & Brand, 1994). This is the linear range of FRET between Cy3 and Cy5 and will provide the greatest dynamic range in signal. There are various options for conjugating FRET pairs onto proteins of interest, each with their own distinct drawbacks. Large genetic tags such as HALO-, SNAP-, and CLIP-tags result in efficient labeling but are typically limited to the termini of proteins due to their size (~25KDa) (Cole, 2013; Los et al., 2008). Enzyme catalyzed reactions such as those by the acyl carrier protein (ACP) (Johnsson et al., 2005) or bacterial sortase (Guimaraes et al., 2013) use smaller genetic tags (~10KDa) but require the site of interest to be accessible to enzymes to catalyze the conjugation of the fluorescent substrate. Cysteine-labeling by maleimide-based reactions is a popular choice as the low occurrence of cysteines in proteins make them ideal for specific labeling (Braman, 2002; Higuchi et al., 1988). However, the function and stability of some proteins, such as mGluRs, are dependent on the presence of cysteines and corresponding disulfide bridges. Thus, cysteine-maleimide reactions are limited to certain proteins with minimal native cysteines present.

Unnatural amino acid (UAA) incorporation into proteins is a versatile approach to introduce a range of novel chemical groups into the protein of interest, enabling bio-orthogonal labeling reactions to occur (Lang & Chin, 2014). This strategy relies on the use of engineered translational

machinery composed of tRNA and complementary tRNA-synthetase to incorporate UAAs. The primary weakness of UAA-incorporation is the reduction in protein expression. However, through optimization of translational machinery, cell-lines, and expression schemes, expression of UAA-containing proteins has been greatly improved (Elsässer et al., 2016). In the work presented herein, I use UAA incorporation to generate novel mGluR2 conformational sensors to probe receptor activation and modulation (Huber et al., 2013a; Noren, Anthony-Cahill, et al., 1989; Serfling & Coin, 2016).

1.6.3 smFRET experimental setup and data analysis

Total internal reflection (TIR) microscopy creates an evanescent field that extends 100-200nm from the imaging interface which greatly reduces potential background (Axelrod, 1990; Axelrod, 2003). There are two types of TIR, the prism-type (PTIR) and the objective-type (OTIR). PTIR uses an inverted microscope and is dependent on a prism fused above the sample, while OTIR is reliant on a high numerical aperture oil objective to create and capture the evanescent field. OTIR has the advantage of not requiring expensive quartz slides and opens up extra space above the microscope setup enabling more commercial options all while achieving comparable signal-to-noise as PTIR. All TIR microscopy data presented here was acquired using an OTIR microscope. The microscope should be coupled to a 532nm solid-state laser, which is appropriate for the Cy3-Cy5 FRET pair, along with a 640nm laser to excite acceptors to confirm single donor-acceptor labeling of sample (Roy et al., 2008). TIR microscopy has gained popularity due to the emergence of electron-multiplying charge-coupled device (EM-CCD) cameras that are highly sensitive and enable fast detection (Michalet et al., 2007). These devices have extremely high quantum efficiency in the visible spectrum (85-95%) and low readout noise. Collectively these tools enable

large areas to be imaged (~0.05mm^2) resulting in the acquisition of hundreds of fluorescent signals in parallel.

For smFRET protein studies, minimizing unspecific protein adsorption on the imaging surface is imperative. To prevent non-specific protein binding, a passivating agent is used, with polyethylene glycol (PEG) being the most popular and effective choice (Sofia et al., 1998). PEG passivated imaging surfaces are prepared by treating a surface-activated slide or coverslip with aminosilane then conjugating PEG via a N-hydroxysuccinimide (NHS) ester reaction (Ha, 2001). Small amounts of biotinylated-PEG can be added during surface conjugation to enable specific tethering of antibodies to the surface via a streptavidin (or neutravidin)-biotin interaction allowing for immune-purification of protein of interest during the experiment. Several methods to improve surface passivation have been developed (Cai & Wind, 2016; Heyes et al., 2007; Heyes et al., 2004; Pan et al., 2015). In addition, the process of chamber assembly and regeneration as well as general considerations for experimental corrections have been thoroughly outlined (Roy et al., 2008; Hellenkamp et al., 2018; Paul & Myong, 2022).

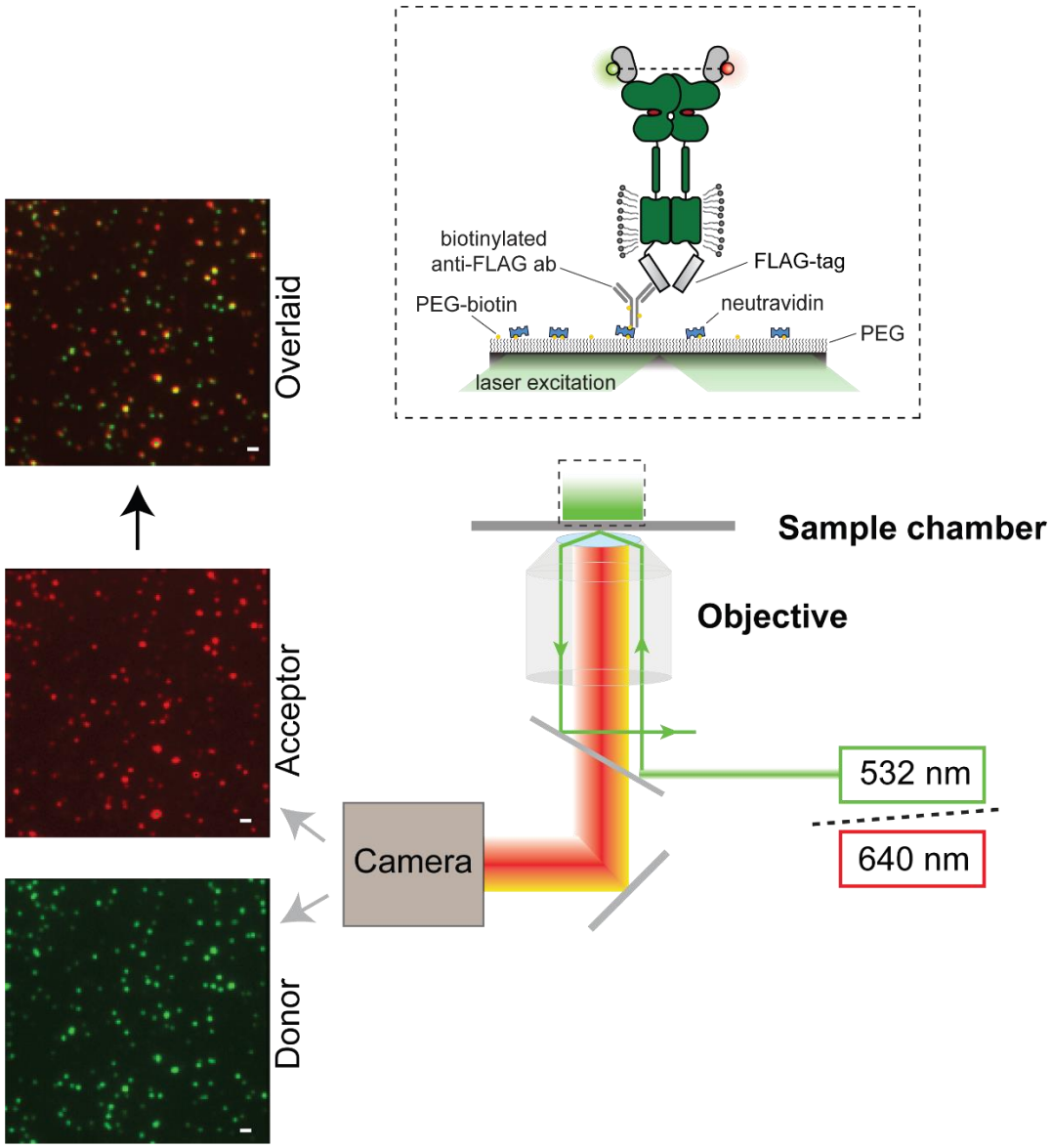

Figure 1.7 smFRET experimental setup
Objective-based total internal reflection (OTIR) fluorescence microscopy was used to acquire the data presented within this thesis. mGluRs were immune-purified onto the PEG passivated surface using a FLAG-tag antibody. FRET was then initiated via excitation by a 532nm laser, followed by excitation by a 640nm laser to ensure single donor-acceptor labeling. Fluorescence intensity of donor and acceptor from hundreds of individual molecules were measured simultaneously using an electron-multiplying charge-coupled device (EM-CCD) camera. (figure created by Banerjee, C. et al. 2022)

As the popularity of smFRET grew, several software packages have been developed for data acquisition and analysis that include SPARTAN (Juette et al., 2016), DeepFRET (Thomsen et al., 2020), and smCamera (http://ha.med.jhmi.edu/resources/). Furthermore, smFRET experiments can now be conducted in different formats such as confocal microscopy (Ha et al., 1997; Sabanayagam et al., 2004) or via FCS (Yu et al., 2021). In conclusion, this technique which probes protein rearrangement with high spatiotemporal resolution is ideal for characterizing the conformational dynamics underlying mGluR activation and modulation (Gopich & Szabo, 2010; Ha, 2001; Schuler, 2013).

1.7 Specific Aims

Aim 1 – Characterize mechanisms of mGluR2 activation. We hypothesize that mGluR2 activation requires the progression through multiple intermediate states and that domains are loosely coupled. Using single-molecule fluorescence resonance energy transfer (smFRET) microscopy, the structural dynamics of mGluR2 can be measured with high spatial and temporal resolution. By adopting and optimizing an unnatural amino acid (UAA) incorporation strategy, we can generate conformational FRET sensors of mGluR2.

Aim 2 – Identify mechanisms for mGluR2 allosteric modulation. We hypothesize that allosteric modulators affect receptor activity by modulating the occupancy and stability of intermediate conformational states. Furthermore, we hypothesize that allosteric modulators affect the conformation of each domain of mGluR2. Using UAA incorporation, we can generate sensors to

probe conformational rearrangement of each structural domain of mGluR2 using total internal reflection fluorescence (TIRF) microscopy.

Aim 3 – Characterize modulatory effects of lipids, cholesterol, and detergents on mGluR2. We hypothesize that choice of solubilizing scaffold shapes mGluR2 conformational dynamics. Using smFRET microscopy and conformational sensors developed for mGluR2, we will be able to quantify the effects of different detergents, lipids, and cholesterol on receptor structural dynamics.

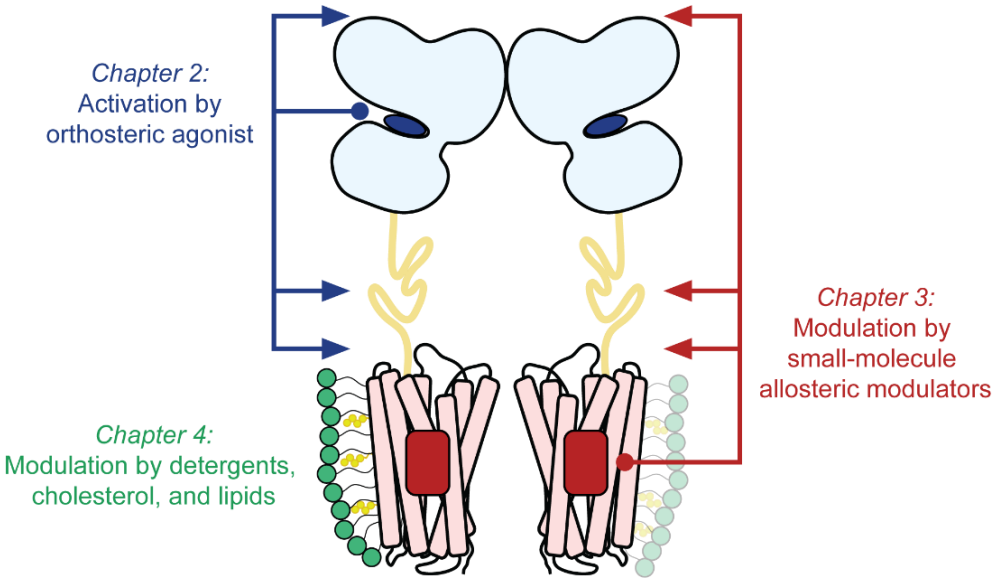

Figure 1.8 Schematic outline of thesis
This thesis consists of three major sections that address the topic of metabotropic glutamate receptor (mGluR) activation and modulation in response to both endogenous and synthetic compounds. **Chapter 2** describes the activation mechanism of mGluRs that is dependent on the loose allosteric coupling of structural domains. **Chapter 3** builds upon the activation framework established in Chapter 2 to describe novel mechanisms of mGluR modulation by allosteric modulators. Finally, **Chapter 4** dissects the contributions of the hydrophobic environment on mGluR structural dynamics by examining the effects of different detergents, lipids, and cholesterol.

1.8 Description of Thesis

Metabotropic glutamate receptors (mGluRs) are multidomain dimeric G protein-coupled receptors (GPCRs) that require complex and coordinated coupling of three spatially separated but conformationally linked domains to function. While the recent influx in structures for full-length receptors has been invaluable in delineating the structure-function relationship in mGluRs, these static representations are insufficient in describing the activation and modulation processes of these highly dynamic receptors. This thesis is composed of 5 chapters that describe mechanisms for mGluR activation and modulation.

At the outset of this thesis work, little was known about how structural changes were propagated from the Venus flytrap (VFT) domains to the 7 transmembrane (7TM) domains. In **Chapter 2**, I describe a novel activation mechanism for the cysteine-rich domain (CRD) of mGuR2. I find that the CRD is intrinsically dynamic and transitions in a sequential manner between four conformational states, including two novel intermediate states. In addition, this chapter provides a detailed protocol for unnatural amino acid (UAA) incorporation and labeling. This protocol was essential for the site-specific and non-perturbative labeling of the mGluR2 CRDs and can be broadly applied to a range of proteins to introduce novel chemical moieties. The activation framework established in this chapter is applied in **Chapter 3** to provide mechanistic insight on mGluR allosteric modulation.

mGluR allosteric modulators are challenging to study due to their unique mechanisms of action, lack of intrinsic functional effects, and the inherent complexity of the mGluR activation mechanism relative to other GPCRs. In **Chapter 3**, I describe the effects of different positive (PAM) and negative (NAM) allosteric modulators on each mGluR2 domain conformation.

Allosteric modulators were found to have a conserved effect on receptor structure based on their characterization as PAMs or NAMs. In addition, novel mechanisms for positive and negative modulation are described and found to function within the novel 4-state activation model.

In addition to pharmacological agents, the hydrophobic environments in which mGluRs reside also have the potential to regulate receptor structural dynamics. **Chapter 4** describes the effects of detergents with distinct hydrophobic moieties, lipids, and cholesterol on mGluR conformational dynamics. Receptor conformation was found to be highly dependent on the detergent of choice. The digitonin derivative, glycol-diosgenin (GDN), was found to function as a potent NAM of mGluR2. In contrast, cholesterol demonstrated a biphasic effect on mGluR2 conformation, functioning as a NAM at low concentrations and PAM at high concentrations. Lastly, the conformational profile and function of lipid-solubilized mGluR2 could be recapitulated using an optimized detergent-cholesterol mixture. Collectively, these findings emphasize the importance of the hydrophobic environment in shaping membrane protein structure and dynamics.

Finally, **Chapter 5** describes the conclusions and implications of this work along with a general outlook of the field. It is accepted that the complex pharmacology of GPCRs generally and mGluRs specifically are dependent on their ability to dynamically sample a diverse ensemble of conformations. However, compared to the wealth of structural information made available in recent years, our collective understanding of GPCR dynamics is relatively small, especially for large multidomain receptors. This thesis provides a robust and dynamic structural framework, consisting of multiple intermediate states, for interpreting mGluR activation and modulation by various therapeutic compounds and solubilizing agents.

Central question – What are mechanisms for mGluR activation and modulation?

Motivation - mGluRs are promising targets for treating a range of neurological and psychiatric disorders. However, due to their complex structure we have a poor understanding of how mGluRs are activated and modulated, making the design of effective therapeutics challenging.

Hypothesis – mGluR function is dependent on its structural dynamics and ability to sample an ensemble of distinct conformations.

Chapter 2: Characterizing mGluR2 conformational dynamics during activation

A previous version of this chapter has been published as:

Liauw, B.W.*, Afsari, H.S.*, Vafabakhsh, R. *Nature Chemical Biology*. **2021**.

2.1 Abstract

G protein-coupled receptors (GPCRs) relay information across cell membranes through conformational coupling between the ligand-binding domain and cytoplasmic signaling domain. In dimeric class C GPCRs, the mechanism of this process, which involves propagation of local ligand-induced conformational changes over 12 nm through three distinct structural domains, is unknown. Here, we used single-molecule FRET (smFRET) and live-cell imaging and found that metabotropic glutamate receptor 2 (mGluR2) interconverts between four conformational states, two of which were previously unknown, and activation proceeds through the conformational selection mechanism. Furthermore, the conformation of the ligand-binding domains and downstream domains are weakly coupled. We show that the intermediate states act as

conformational checkpoints for activation and control allosteric modulation of signaling. Our results demonstrate a mechanism for activation of mGluRs where ligand binding controls the proximity of signaling domains, analogous to some receptor kinases. This design principle may be generalizable to other biological allosteric sensors.

2.2 Introduction

Cells use membrane receptors to dynamically sense and interpret chemical and physical signals from their environment (Smock & Gierasch, 2009). A key design principle of many membrane receptors is that sensing is energetically passive, and no external energy is required. That is, the energetics of ligand binding is converted to a local conformational change and into the output signal. This process is often allosteric in nature and involves coupling of conformational dynamics between the ligand binding "sensory domain" and the cytoplasmic "signaling interface" (Changeux & Christopoulos, 2016).

In humans, G protein-coupled receptors (GPCRs) are the largest family of membrane receptors and have become key targets for drug development due to their involvement in nearly all physiological processes (Thal et al., 2018; Dorsam & Gutkind, 2007). A deeper understanding of the activation and modulatory mechanisms used by GPCRs would be invaluable for developing new therapeutics as well as designing synthetic receptors and sensors. Significant advances in structural methods have identified ligand and ion binding sites in many GPCRs (Thal et al., 2018; Zarzycka et al., 2019) as well as atomic-level details of different steps of signal transduction by GPCR complexes (Hilger et al., 2018; Latorraca et al., 2017). Moreover, improved understanding of the conformational dynamics of GPCRs by computational, nuclear magnetic resonance (NMR)

spectroscopy, double electron-electron resonance (DEER) spectroscopy and fluorescent based assays demonstrated that the two-state on–off model of GPCRs cannot account for their signaling versatility and complex pharmacology and GPCRs are highly dynamic proteins that sample multiple conformational states (Vafabakhsh et al., 2015; Ye et al., 2016; Nygaard et al., 2013a; Wingler et al., 2019a). Collectively, these approaches have started to provide a structural framework to understand multiple facets of GPCR pharmacology such as basal activity, partial agonism, biased signaling and allosteric modulation (Latorraca et al., 2017; Gusach et al., 2020; Gregorio et al., 2017a; Suomivuori et al., 2020). However, how large-scale conformational changes propagate during the activation process of GPCRs and ligands modify the structure and dynamics of GPCRs to tune their functional outcomes, especially for many large multidomain GPCRs is poorly understood.

Among all GPCRs, class C GPCRs are structurally unique in that they are multi-domain with a large extracellular domain and function as obligate dimers. Metabotropic glutamate receptors (mGluRs) are class C GPCRs that are responsible for the slow neuromodulatory effects of glutamate that are essential for tuning synaptic transmission and excitability (Niswender & Conn, 2010; Pin & Bettler, 2016). Structural (Kunishima et al., 2000; Wu et al., 2014; Koehl et al., 2019b) and spectroscopic studies (Hlavackova et al., 2012; Doumazane et al., 2013b) have shown that unlike the activation process of most class A GPCRs which is associated with subtle motions in the extracellular domain (ECD) of the receptor, the activation of mGluRs involves local and global conformational changes that propagate through the three structural domains of the receptor, over 12 nm, to reach the intracellular G protein-binding interface (signaling interface) (Vafabakhsh et

al., 2015; Hlavackova et al., 2012; Koehl et al., 2019b) (Figure 2.1A). The molecular details, timescales and sequence of conformational changes during this process are unclear.

Here, we used single-molecule FRET (smFRET) (Roy et al., 2008) and *in vivo* FRET imaging to visualize the propagation of conformational changes during the activation of mGluR2. To circumvent limitations of common site-specific fluorescent labeling approaches that requires generation of cysteine-less mutants or insertion of large protein tag, we adopted and optimized an unnatural amino acid incorporation strategy (Noren, Anthonycahill, et al., 1989). Using this assay, we found that the dimeric arrangement of mGluR2 adopts four distinct conformational states that are visited sequentially, in contrast to the two-state model deduced from the atomic structures (Kunishima et al., 2000; Koehl et al., 2019b). Using mutations and crosslinking approaches, we characterized the functional property and significance of the conformational states for the receptor signaling and modulation. This sequential four-state activation model provides a structural framework for understanding ligand efficacy and allosteric modulation of mGluRs and possibly other class C GPCRs.

2.3 Results

According to the current activation model for mGluRs, glutamate binding at the Venus flytrap (VFT) domain (sensory domain) closes the VFT lobes and results in the rearrangement of the VFT domains' dimer interface from "relaxed" to "active" (Kunishima et al., 2000; Vafabakhsh et al., 2015) (Figure 2.1A). Next, this conformational change is thought to bring the adjacent cysteine-rich domains (CRDs) closer together to activate the G protein-binding interface (Hlavackova et al., 2012; Koehl et al., 2019b) (Figure 2.1A). The CRD is the allosteric structural link that relays

the incoming signal (that is the conformation of the VFT domains) to the signaling site (7TM domains) (Figure 2.1A). We therefore hypothesized that the arrangement of the CRDs in the dimer reports how the VFT domains allosterically regulate the conformation of the 7TM domains, independent of intradomain movement of transmembrane helices. To test this, we applied smFRET and live-cell ensemble FRET imaging to visualize the conformational changes of the CRD of mGluR2 during activation, in real-time (Vafabakhsh et al., 2015; Roy et al., 2008; Doumazane et al., 2013b).

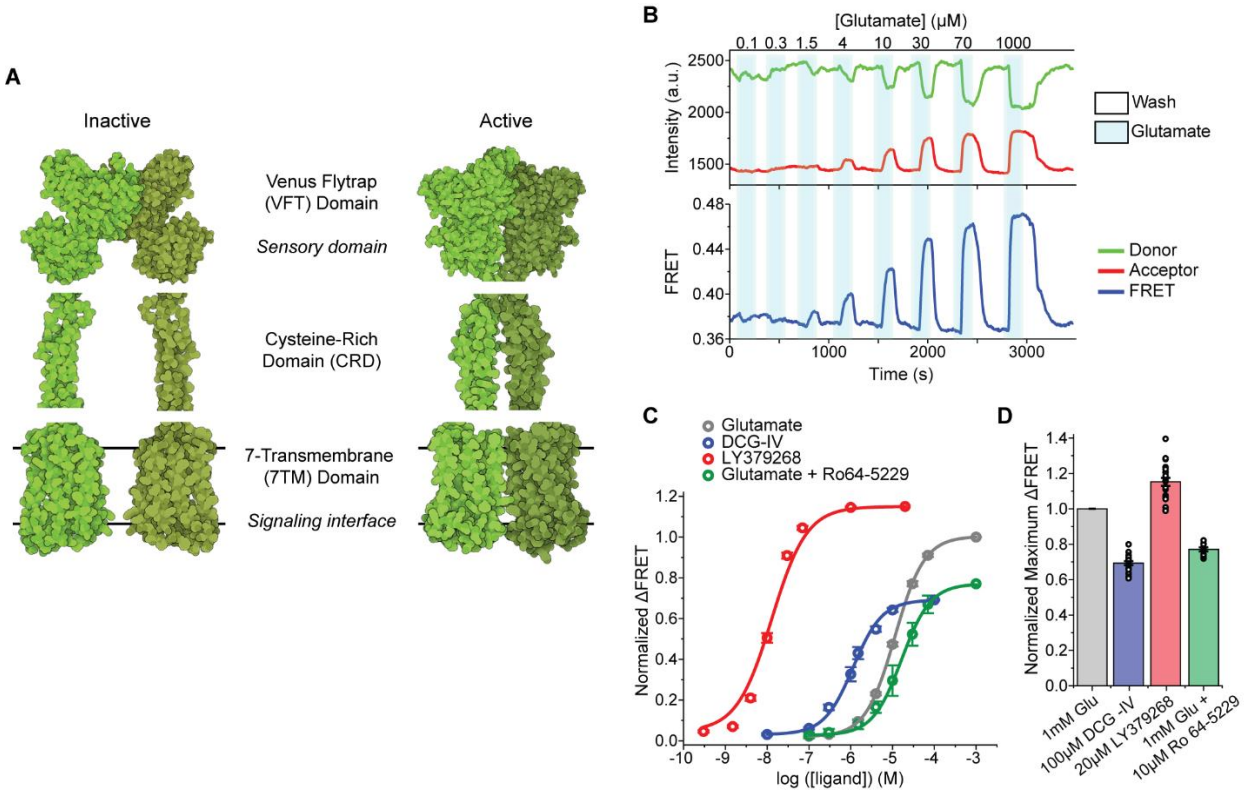

Figure 2.1 Design and characterization of the FRET-based CRD conformational sensor
(A) Cartoon illustrating the arrangement of the three structural domains of mGluR5 in the inactive (RCSB Protein Data Bank (PDB) accession 6N52) and active (PDB accession 6N51) states. (B) Representative donor and acceptor intensities and corresponding FRET signal from a cell in response to glutamate application. (C) Dose-response curves from live-cell FRET titration experiments for glutamate (grey), LY379268 (red), DCG-IV (blue) or glutamate +10 μM Ro64-5229 (green) in HEK293T cells. Each titration curve is normalized to the 1 mM glutamate response. Data represent mean ± s.e.m. of N=26, 20, 10 and 13 cells for glutamate, LY379268, DCG-IV and glutamate +10 μM Ro64-5229, respectively, examined over 3 independent experiments. (D) Maximum FRET change in the presence of saturating LY379268 (red), DCG-IV (blue) and glutamate +10 μM Ro64-5229 (green) normalized to the 1 mM glutamate response (grey) in HEK293T cells. Data represent mean ± s.e.m. of N=21, 19 and 9 cells for LY379268, DCG-IV and glutamate +10 μM Ro64-5229, respectively, examined over 3 independent experiments.

2.3.1 Design and validation of CRD conformational FRET sensor

To site-specifically attach donor and acceptor fluorophores, with minimal perturbation to the receptor structure, we adopted and optimized an unnatural amino acid incorporation strategy (Serfling & Coin, 2016; Huber et al., 2013b) and introduced a 4-azido-L-phenylalanine at amino acid 548 of mouse mGluR2 (hereafter, 548UAA) (Figure S2.1A-B). We expressed 548UAA in HEK293T cells and site-specifically labeled the cell-surface population of receptors with FRET donor (Cy3) and acceptor (Cy5) fluorophores, through a copper-catalyzed azide-alkyne click reaction (Presolski et al., 2011a) (Figure S2.1A-B). Because mGluRs are strict dimers any FRET signal is exclusively from the receptors that are labeled with a single donor and a single acceptor fluorophore. Total cell lysate from labeled cells on a non-reducing polyacrylamide gel showed a single band corresponding to the size of the full-length dimeric mGluR2 (Figure S2.1C), verifying that the receptor population on the plasma membrane are full-length.

We observed that glutamate induced a concentration-dependent increase in the FRET signal in labeled cells expressing 548UAA (Figure 2.1B, S2.1D), confirming a general decrease in the distance between the CRD domains upon activation and consistent with previous structural and crosslinking experiments (Koehl et al., 2019b; Muto et al., 2007b; S. L. Huang et al., 2011). This glutamate-dependent increase in ensemble FRET had an EC50 of 11.8 ± 0.5 μM (Figure 2.1C), consistent with the concentration-dependence of GIRK current activation in HEK293T cells (Vafabakhsh et al., 2015). Similar dose-dependent increase in the FRET efficiency was obtained with other orthosteric agonists LY379268 (hereafter, LY37) and DCG-IV with respective EC50 of 12.8 ± 0.5 nM and 1.2 ± 0.2 μM (Figure 2.1C, S2.2A), matching the published range for mGluR2 (Doumazane et al., 2013b). On the other hand, the mGluR2-specific negative allosteric modulator

(NAM) Ro64-5229 reduced the glutamate efficacy (max response 77% ± 1% of glutamate) (**Fig. 1d**) and potency (EC50 = 17.2 ± 1.1 μM) (Figure 2.1C, S2.2A), consistent with the notion that the CRD is the allosteric linker between ligand binding and signaling. Therefore, the 548UAA FRET sensor allows unperturbed quantitative analysis of ligand-induced conformational changes of the CRD in live cells. Importantly, the efficacy of ligands as characterized by signaling assays or VFT domain FRET sensors (Vafabakhsh et al., 2015; Doumazane et al., 2013b) correlate with the ligand-induced FRET change at the CRD with DCG-IV being a partial agonist and LY37 > glutamate > DCG-IV (Figure 2.1D, S2.2B).

2.3.2 CRD is in dynamic equilibrium between 4 states

To perform smFRET imaging, cells expressing 548UAA with a C-terminal FLAG tag were labeled with donor and acceptor fluorophores and then lysed. The cell lysate was applied onto a polyethylene glycol (PEG) passivated coverslip functionalized with anti-FLAG tag antibody to immunopurify the receptors (SiMPull) (Vafabakhsh et al., 2015; Jain et al., 2011) for total internal reflection fluorescence imaging (Figure S2.3A). In the absence of glutamate (inactive receptor), the CRD of individual mGluR2 receptors displayed rapid transitions between multiple FRET states (Figure 2.2A, S2.3B), in stark contrast to the previously reported behavior of the VFT domains that were stable in a single conformation (Vafabakhsh et al., 2015) (Figure S2.3C). Histogram of smFRET data from many single receptors revealed four conformations with smFRET efficiency peaks at: 0.31, 0.51, 0.71 and 0.89 (labeled as states 1-4) (Figure 2.2B, top histogram). The smFRET histogram was unchanged in the presence of saturating competitive antagonist LY341495 (Figure 2.2B), confirming that the observed dynamics is independent of the orthosteric agonist binding.

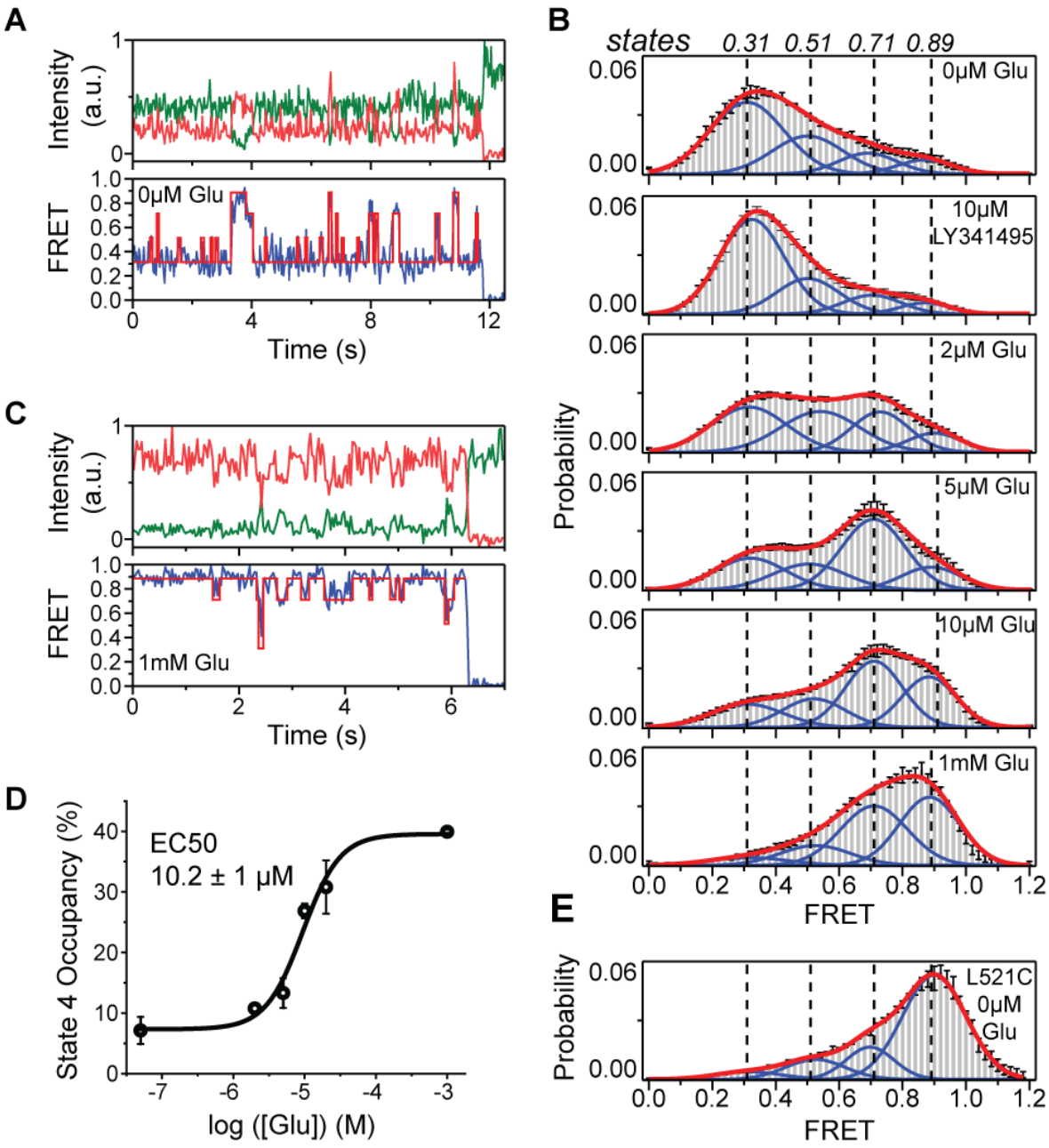

Figure 2.2 Single-molecule FRET reveals four conformational states of mGluR2 CRD
(A) Example single-molecule time trace of 548UAA in the absence of glutamate showing donor (green) and acceptor (red) intensities. Corresponding FRET (blue) is overlaid with predicted state sequence (red, bottom). (B) smFRET population histograms in the presence of competitive antagonist (LY341495) and a range of glutamate concentrations. Data represent mean ± s.e.m. of N=3 independent experiments. Total molecules examined for LY341495 and 0 μM, 2 μM, 5 μM,

10 μM and 1 mM glutamate conditions were 440, 250, 378, 879, 726 and 152, respectively. Histograms were fitted (red) to 4 Gaussian distributions (blue) centered around 0.31 (state 1), 0.51 (state 2), 0.71 (state 3) and 0.89 (state 4), denoted with dashed lines. (C) Example single-molecule time trace of 548UAA in the presence of 1 mM glutamate showing donor (green) and acceptor (red) intensities. Corresponding FRET (blue) is overlaid with predicted state sequence (red, bottom). (D)Glutamate dose-response curve of state 4 occupancy. State 4 occupancy is defined as area of Gaussian distribution centered at 0.89 as a fraction of total area. Data represent mean ± s.e.m. of N=3 independent experiments. Total molecules examined as in (B) (216 total molecules for 20 μM glutamate). (E) smFRET population histogram of the cross-linked constitutively active 548UAA (L521C; 176 total molecules) construct in the absence of glutamate. Data represent mean ± s.e.m. of N=3 independent experiments. Four FRET states are denoted with dashed lines.

In the presence of glutamate, receptors remained dynamic and showed transitions between the same four FRET states but with shifted occupancy to the higher states, in a glutamate-dependent manner (Figure 2.2B, S2.4A), and in qualitative agreement with the live-cell FRET experiment (Figure 2.1B). Notably, even at saturating glutamate (1 mM) receptors showed significant dynamics between states 3 and 4 (Figure 2.2C, S2.4B). A similar overall behavior was observed when examining mouse mGluR3 at the analogous position (A557) (Figure S2.5). The atomic structures of the inactive conformations of mGluR5 and mGluR3 have resolved the CRDs at a large distance apart (68.3 Å at position D560 in human mGluR5) (Koehl et al., 2019b; Muto et al., 2007b). Therefore, the lowest FRET peak at 0.31 (state 1), which is the predominant population in the absence of an agonist, corresponds to the crystallographic inactive conformation of the mGluR2. In this conformation the VFT domain lobes are “open” (oo) and the dimer interface is in the “relaxed” (R) state (R/oo) (Kunishima et al., 2000; Doumazane et al., 2013b). On the other hand, the highest FRET peak at 0.89 (state 4) corresponds to an approximate distance of 38 Å which agrees with the distance at our labeling position based on the recent structure of the ligand bound mGluR5 (Koehl et al., 2019b) (35.9 Å at position D560 in human mGluR5). The occupancy of this FRET peak showed a glutamate concentration-dependence with the EC50 of 10.2 ± 1 μM

(Figure 2.2D), matching the EC50 measured from signaling assays in live cells. Therefore, we hypothesized that the FRET state 4 is the crystallographic active CRD conformation of mGluR2. To test this, we performed a smFRET experiment on the intersubunit CRD cross-linked mGluR2(L521C) construct which was previously shown to result in a constitutively signaling active receptor (S. L. Huang et al., 2011).

Consistent with this, live-cell measurements with this construct showed no FRET change upon application of glutamate (Figure S2.6). smFRET experiments with this construct in the absence of glutamate showed a dominant peak at FRET 0.89 (Figure 2.2E). Together, these results confirm the assignment of state 4 as the active CRD conformation of mGluR2.

In the presence of other mGluR2 orthosteric agonists LY37 and DCG-IV, the CRD populated the same four FRET states (Figure 2.3A, S2.7A). Importantly, at saturating concentrations, LY37 showed 21% higher occupancy of the active state conformation than glutamate while DCG-IV showed 23% lower occupancy, consistent with their respective efficacy (Figure 2.3B, S2.7B). We further examined the nature and time-ordering of transitions using a four-state hidden Markov Model (HMM) (Bronson et al., 2009a; Zhang et al., 2018). The results of HMM analysis as a transition density plot (TDP) at different glutamate concentrations demonstrate three distinct sets of bidirectional transitions between the four FRET states (Figure 2.3C). Importantly, this analysis showed that transitions are sequential, happening between adjacent FRET peaks ($0.31 \leftrightarrow 0.51 \leftrightarrow 0.71 \leftrightarrow 0.89$). Together, these findings confirm the existence of four CRD conformations in the presence or absence of orthosteric agonists and support a stepwise compaction of mGluR2 during activation, consistent with a conformational selection mechanism(Nussinov et al., 2014).

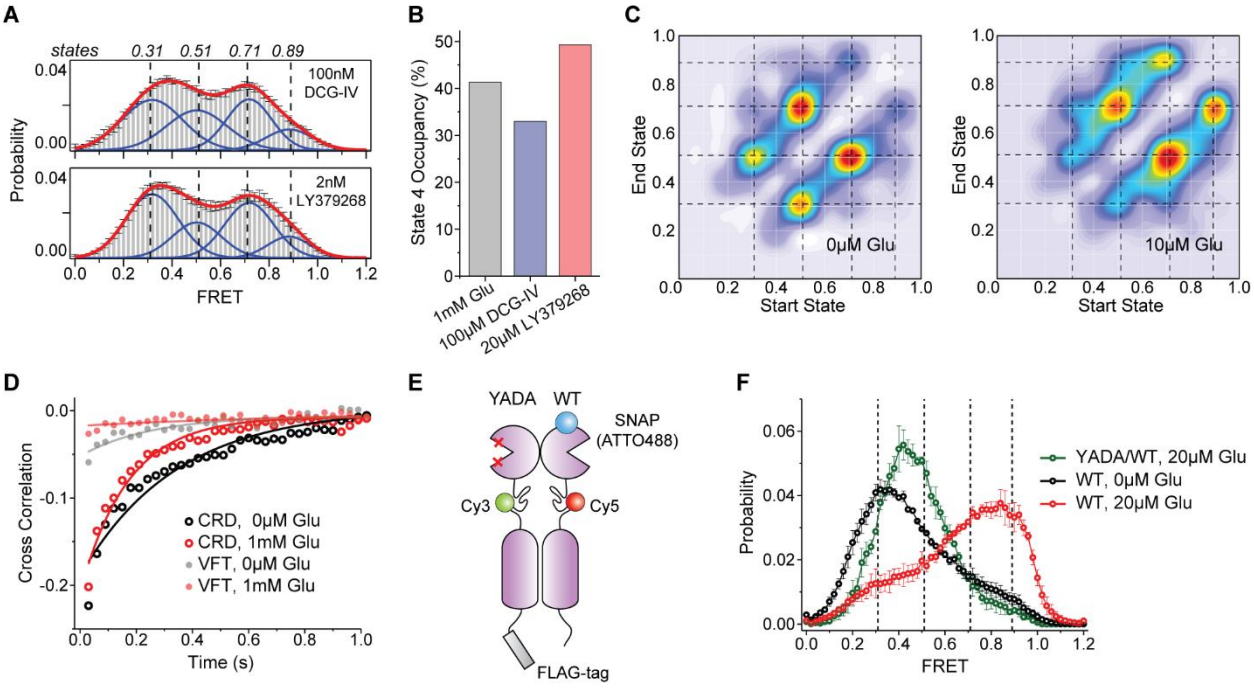

Figure 2.3 Activation of mGluR2 is a stepwise process

(A) smFRET population histogram of 548UAA sensor in the presence of intermediate concentrations of orthosteric agonists DCG-IV (top; 166 total molecules) and LY379268 (bottom; 220 total molecules). Data represent mean ± s.e.m. of N=3 independent experiments. Histograms are fitted (red) to 4 Gaussian distributions (blue) centered on 0.31 (state 1), 0.51 (state 2), 0.71 (state 3) and 0.89 (state 4), as denoted by dashed lines. (B) State 4 (active state) occupancy at saturating concentrations of mGluR2 orthosteric agonists. State 4 occupancy is defined as area of Gaussian distribution centered at 0.89 as the fraction of total area. FRET peak fitting and area calculations were performed on average histograms. (C) Transition density plots (TDPs) of 548UAA. Dashed lines represent 4 distinct FRET states. Transitions are from two independent measurements. (D) Cross-correlation plots comparing the dynamics of the CRDs and VFT domains of mGluR2 at 0 and 1 mM glutamate. Data are from three independent measurements. Data was fitted to a single exponential decay function. (E) Schematic of mGluR2 receptor constructs for the 548UAA YADA/WT heterodimer experiment. (F) smFRET population histogram of 548UAA YADA/WT heterodimer in the presence of 20 μM glutamate (55 total molecules), compared to 548UAA WT (250 and 216 total molecules for 0 μM and 20uM glutamate). Data represent mean ± s.e.m. of N=3 independent experiments. Dashed lines represent 4 distinct FRET states. Heterodimer data was acquired at 100 ms time resolution.

2.3.3 Conformations of CRDs and VFT domains are loosely coupled

Our observation that in the presence of saturating full agonist (1 mM glutamate) or absence of ligand the CRD is dynamic (Figure 2.2A,C, S2.8), is in stark contrast with the behavior of the VFT domains of mGluR2 which adopt a distinct stable conformation in these conditions (Vafabakhsh et al., 2015) (Figure S2.3C). Quantification of receptor dynamics using the cross-correlation of donor and acceptor signals also showed similar contrast between the dynamic behavior of the two adjacent domains (Figure 2.3D). Consistent with the reduction of VFT domains' dynamics in zero or saturating glutamate (1 mM), the amplitude of anti-correlation between donor and acceptor fluorophores for the VFT domain sensor (Figure S2.3C) vanished (Figure 2.3D). However, the CRD sensor showed strong amplitude in both these conditions (Figure 2.3D). Together, these results indicate that the conformation of the VFT domains and CRD are allosterically loosely coupled. Such loose coupling was previously observed in molecular dynamics (MD) simulations and nuclear magnetic resonance (NMR) experiments of beta2-adrenergic receptor (β2AR) (Manglik et al., 2015; Dror et al., 2011). Our findings extend this notion to the multi-domain class C GPCRs suggesting that loose allosteric coupling might be a more general feature of GPCRs and allosteric receptors as a whole, and is consistent with observations of distinct inter and intradomain rearrangement timescales in mGluR1 (Grushevskyi et al., 2019). Finally, the loose allosteric coupling that we uncovered here suggests that the CRD conformation, and not VFT domain conformation, is the more accurate metric to report the activation of mGluRs and perhaps class C GPCRs.

2.3.4 State 2 results from the closure of a single VFT domain

We further examined the correlation between the VFT domain lobe closure and the CRD conformation by performing smFRET experiments on receptors with a single glutamate-binding defective monomer (Kniazeff, Bessis, Maurel, Ansanay, Prezeau, et al., 2004) (548UAA-YADA with Y216A and D295A mutations). This was achieved by co-expressing the C-terminal FLAG tagged 548UAA-YADA construct and a N-terminal SNAP tagged 548UAA construct (Figure 2.3E). Following the expression, the cell surface population was labeled with BG-ATTO488 (SNAP-tag substrate) as well as Cy3 and Cy5 as before (supplementary materials and methods). Particles that were pulled down with the anti-FLAG antibody and showed the ATTO488 signal plus FRET donor and acceptor signals were analyzed. smFRET analysis showed that at 20 μM glutamate the CRD of the YADA/WT heterodimer predominantly occupies state 2 (Figure 2.3F, S2.9) with brief visits to higher FRET states, supporting the assignment of state 2 to a configuration in which one VFT domain is “closed” and the other is “open”(co) with the VFT domain interface in the “relaxed” (R) form and the receptor in the inactive state (R/co).

2.3.5 State 3 represents a pre-active receptor conformation

To investigate the identity of state 3 in mGluR2 activation we quantified the occupancy of all 4 states as a function of increasing glutamate (Figure 2.4A). While the occupancy of the active state 4 continuously increased with increasing glutamate concentration, state 3 occupancy initially increased and then plateaued around the EC50 concentration of glutamate. This observation and the fact that in saturating agonist the VFT domains are locked in a single active (Acc) conformation (Figure S2.3C), while the CRDs dynamically transition mostly between states 3 and 4 (Figure 2.2B-C, S2.8), suggest that state 3 represents a pre-active conformation of the receptor. In this

conformation the VFT domains are in the active arrangement (A/cc) (Vafabakhsh et al., 2015), yet the receptor is inactive. Existence of such pre-active state could be the consequence of a rate limiting step during the activation process such as intrasubunit conformational changes that contribute to formation of the active receptor. This interpretation is consistent with recent experiments which showed that activation of mGluR1 involves a fast and a slow time constant (Grushevskyi et al., 2019). Finally, cross linking and structural studies have shown that in the active state of mGluRs, the 7TM domains interact along the TM6 helix(Xue et al., 2015b). Thus, it is likely that the pre-active state 3 is a conformation in which the 7TM domains are brought into close proximity through the VFT domain closure (Acc conformation of the VFT domains) yet have not adopted the signaling competent configuration of the 7TM domain. Consistent with this interpretation, the active state 4 is transient (Figure 2.2C, S2.4).

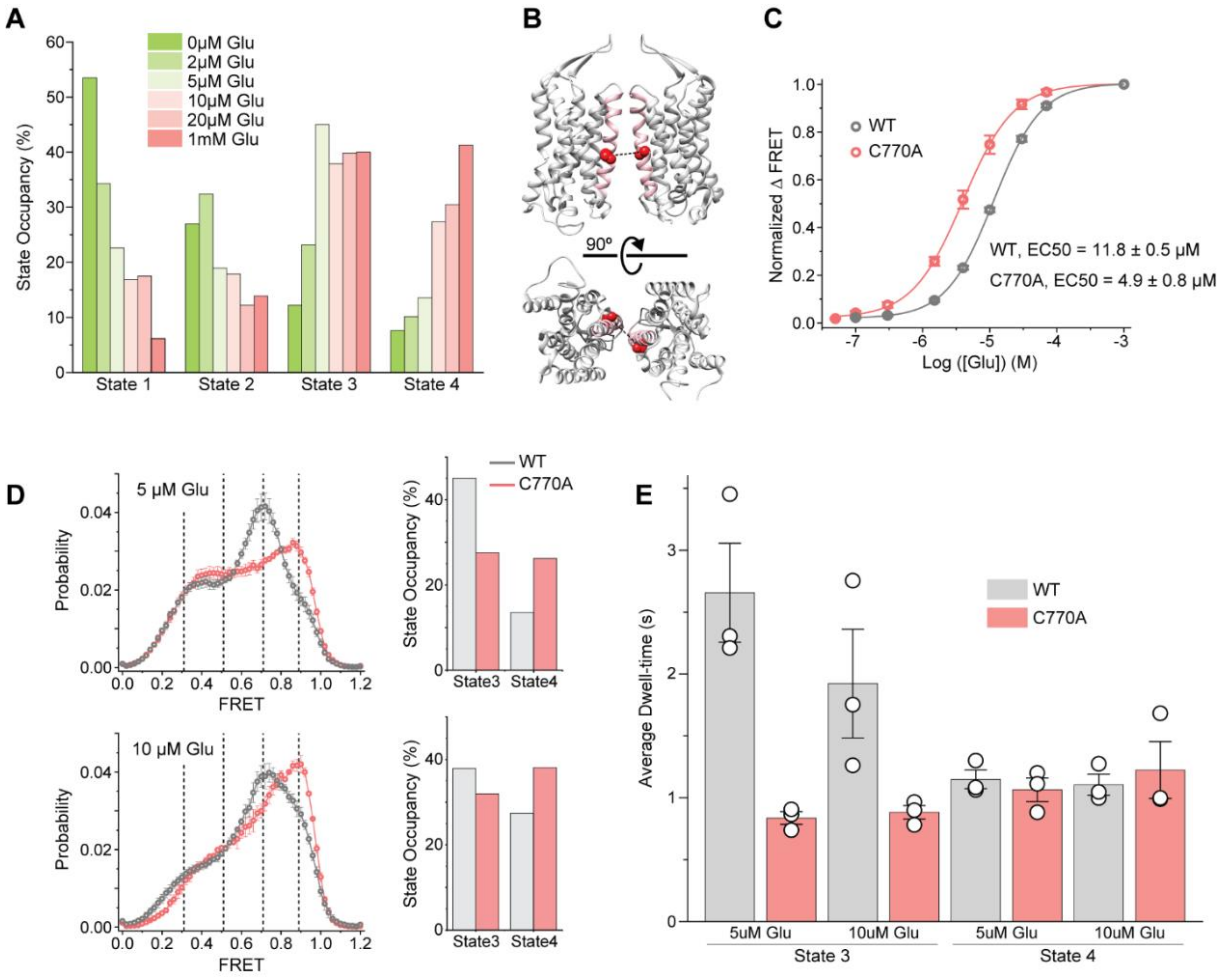

Figure 2.4 Conformational state 3 is a pre-active conformation of mGluR2
(A) Occupancy of the 4 conformational states of the CRD in the presence of increasing glutamate concentrations. Values represent area under each FRET peak from smFRET population histograms, centered at 0.31 (state 1), 0.51 (state 2), 0.71 (state 3) and 0.89 (state 4) and as the fraction of total area. (B) The PAM mutation (C770A, red spheres) on the structure of mGluR5 (PDB accession 6N61). TM6 is colored in pink. (C) Dose-response curves from live-cell FRET glutamate titration experiments for the 548UAA WT and C770A PAM receptor. Each curve is normalized to the 1 mM glutamate response. Data represent mean ± s.e.m. of N=26 and 13 cells expressing 548UAA WT or C770A PAM receptors, respectively, examined over 3 independent experiments. (D) smFRET population histograms of 548UAA WT receptors (grey) at 5 μM (879 total molecules) and 10 μM glutamate (726 total molecules) and C770A PAM receptors (red) at 5 μM (689 total molecules) and 10 μM glutamate (370 total molecules). Data represent mean ± s.e.m. of N=3 independent experiments. Dashed lines represent the 4 FRET states. Bar graphs represent area of FRET states 3 (FRET=0.71) and state 4 (FRET=0.89) as the fraction of total area for WT and PAM mutant receptor. (E) Dwell-times of states 3 and 4 for the WT receptor at 5 μM (147 total molecules) and 10 μM glutamate (140 total molecules) and PAM mutant receptor at 5

μM (128 total molecules) and 10 μM glutamate (142 total molecules). Average dwell-time was calculated by fitting a single exponential decay function to dwell-time histograms for each condition. Dwell-times represent mean ± s.e.m. of N=3 independent experiments at 100 ms. FRET peak fitting and area calculations were performed on averaged histograms.

To investigate the significance of the pre-active state 3 for receptor signaling, we studied the conformational dynamics of mGluR2 containing mutation C770A (Figure 2.4B). This mutation is shown to enhance mGluR signaling in a manner similar to a positive allosteric modulator (PAM) (Doumazane et al., 2013b; Yanagawa et al., 2009). Live-cell ensemble experiments for 548UAA with this PAM mutation showed increased mGluR2 sensitivity to glutamate (EC50 = 4.9 ± 0.8 μM compared to 11.8 ± 0.5 μM for the WT receptor) suggesting that the PAM effect of this mutation in the TMD is allosterically detectable at the CRD (Figure 2.4C). We next performed smFRET analysis of this construct and observed the same 4 states as the wildtype receptor (Figure S2.10A). However, at each glutamate concentration tested, the occupancy of the active state (state 4) was increased for the mutant compared to the wildtype receptor (Figure 2.4D), consistent with the expected response from a PAM and further confirming that the immobilized receptors retain functional properties of the TMD. To test whether this effect is due to increased lifetime of the active state or increased visits to the active state, we performed dwell-time analysis of states 3 and 4 with the PAM construct. Remarkably, while the lifetime of active state 4 was similar between WT and the PAM mutant, the lifetime of state 3 was reduced about 3-fold for the PAM mutant (Figure 2.4E, S2.10B). TDP analysis revealed that there were more transitions from state 3 to state 4 for the PAM mutant compared to the WT (Figure S2.10C).

Considering that only state 3 exhibits a substantially altered lifetime for the PAM mutant while the lifetimes of other states remain mostly unchanged (Figure S2.10D) and the fact that the major

FRET histogram population change is the shift from state 3 to state 4 occupancy, our results show that the C770A PAM mutation confers its modulatory effect allosterically by increasing transitions from the pre-active state 3 to the active state 4. Therefore, the stability of the pre-active state 3 is a critical tuner for setting the receptor activation threshold.

2.4 Discussion

GPCRs are evolved to transduce signals across the membrane through energetically passive allosteric mechanisms that involve communication between spatially separated and conformationally linked domains of the receptor (Thal et al., 2018). For many multi-domain GPCRs the mechanism of such conformational coupling and the dynamic interaction of the receptor domains during the allosteric process of activation are generally unknown. In this study, we successfully applied a novel smFRET and live-cell ensemble FRET approach to visualize the temporal sequence of conformational changes of the cysteine-rich domain in mGluR2. The CRD is a unique semi-rigid structural domain, conserved among class C GPCRs (except $GABA_B$ receptors) that relay the conformational information of the ligand binding domain to the 7TM domains. The CRD has a compact structural fold with nine cysteines. Therefore, conventional site-specific labeling approaches such as cycteine labeling (Gregorio et al., 2017a) or insertion of genetic tags (Vafabakhsh et al., 2015) are not applicable. We adopted an unanatural amino acid labeling approach (Serfling & Coin, 2016) combined with the single-molecule pulldown (Jain et al., 2011) to cirvumvent this limitatoin. We found that the CRD in mGluR2 is in equilibrium between four conformations. An agonist “loosely” controls the conformation of the ectodomains of the receptor that in turn results in redistribution of the conformational ensemble and the

compaction of the receptor in a stepwise manner (Figure 2.5). We observed the same 4-state model for mGluR3, suggesting that this model could be general for all mGluRs (Figure S2.5). A recent cryo-electron microscopy study identified four conformations of the $GABA_B$ receptor (Shaye et al., 2020), further suggesting that this four-state model could be the general activation model for all class C GPCRs. More broadly, other bi-lobed, clamshell LBD-containing proteins, such as the ionotropic neurotransmitter receptors (NMDA, AMPA), may have evolved to utilize a similar activation mechanism.

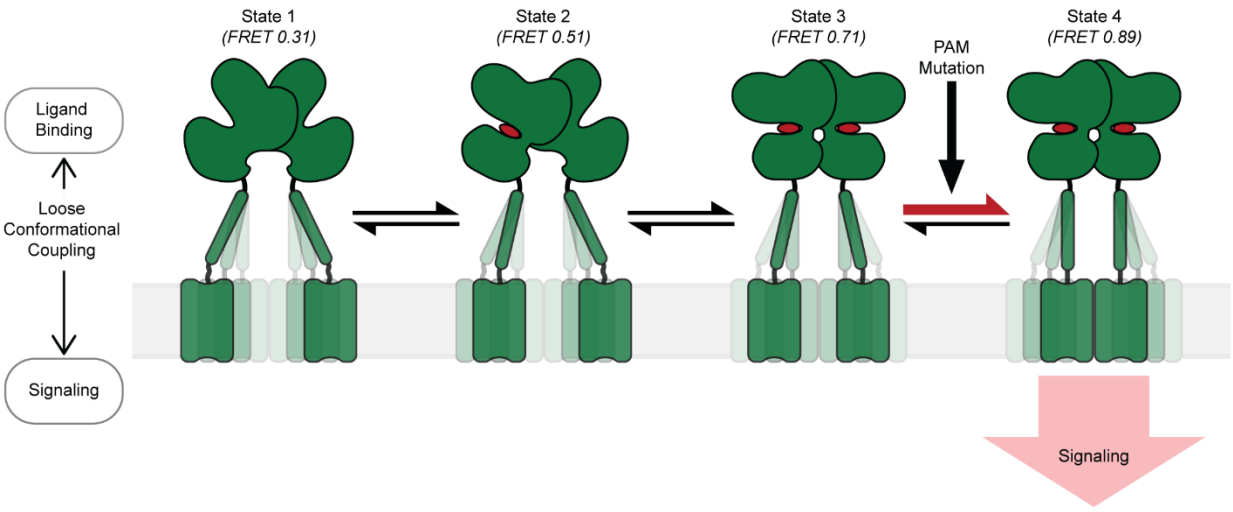

Figure 2.5 Schematic of the stepwise activation model for mGluR2
Four-state stepwise model for the mechanism of allosteric activation of mGluRs with receptors shown in green and ligand in red. Darker shading of CRDs and TMDs represent greater occupancy of a given conformation. State 1 (FRET=0.31) represents the most common CRD conformation of an unliganded receptor, where the CRDs are farthest apart. State 2 (FRET=0.51) represents the CRD conformation resulting from ligand binding to a single VFT domain. State 3 (FRET=0.71) represents the CRD conformation resulting from ligand binding to both VFT domains and prior to the formation of a stabilizing TMD interaction. State 4 (FRET=0.89) represents the CRD conformation resulting from ligand binding to both VFT domains and a stabilizing TMD interaction. State 4 is the active conformation of the receptor. PAM mutations can function by increasing transitions from state 3 to 4.

Our model (Figure 2.5) has several implications for the activation and modulation of mGluRs. First, we demonstrated that the activation proceeds through a conformational state where the LBD of only one subunit is active (state 2). Stalling the receptor in this state, which we achieved by mutations in the LBD of one subunit within the dimer, significantly hinders the progression of conformational changes of the receptor towards activation. Second, signaling of GPCRs in general and mGluRs specifically can be modulated by endogenous or exogenous allosteric modulators (such as lipids or PAMs and NAMs) (Thal et al., 2018; Foster & Conn, 2017). While synthetic allosteric modulators are attractive therapeutic approaches, due to their superior specificity and tunability (Foster & Conn, 2017), their mechanism of action in class C GPCRs is unknown. Our analysis revealed that the PAM mutation, C770A, confers positive allosteric modulation by decreasing the lifetime of the novel state 3 and by increasing transitions from state 3 to the active state 4, resulting in a greater overall occupancy of the active state (Figure 2.4D-E, S2.10B,D). Due to the stepwise compaction required for mGluR activation, several energetic barriers must be overcome to achieve receptor signaling. While each of these transitions may be modulable, we show that the C770A mutation specifically functions to reduce the barrier between states 3 and 4. Furthermore, the location of this mutation in TM6, the active TMD interface (Koehl et al., 2019b; Xue et al., 2015b), supports the possibility that a stabilizing TMD interaction is necessary for the active receptor conformation (state 4). Together, the novel intermediate states act as critical conformational checkpoints for regulating mGluR activation and signaling. These insights have the potential to accelerate development of drugs and modulators for mGluRs.

Third, we found that the active conformation of the receptor at the CRD is transient and dynamic, even in the presence of saturating full agonist (Figure 2.2C, 3D, S2.4B). This is in contrast to the

behavior of the ligand-binding domain of the receptor which is very stable in saturating agonist (Vafabakhsh et al., 2015) (Figure 2.3D, S2.3C). This could explain why while there are several active structures of the extracellular domain of class C GPCRs available (Kunishima et al., 2000; Koehl et al., 2019b; Muto et al., 2007b), obtaining the active structure of the TMD in intact mGluRs has been challenging (Koehl et al., 2019b). Finally, our results collectively suggest that mGluRs adopt a single active conformation, the stability of which is determined not only by ligand binding and closure of the VFT domains, but also by the propensity of the TMDs to interact within the dimer.

GPCR dimerization and oligomerization *in vivo* and in a ligand-dependent manner has been a subject of extensive research (Mijares et al., 2000; Stoneman et al., 2019) and formation of GPCR dimers are shown to be transient and depend on agonist binding (Hern et al., 2010; Calebiro et al., 2013; Moller et al., 2020). Our model raises the interesting possibility that class C GPCRs are evolved to use this intrinsic property to control their activation. In this framework, agonist binding effectively brings the 7TMs into close proximity to facilitate their interaction and promote formation of the signaling active configuration of the G protein binding interface. This mechanism is in essence similar to many receptor tyrosine kinases (RTKs) (Endres et al., 2013), where ligand binding effectively controls the proximity of signaling or enzymatic domains and may be the design principle underlying many biological allosteric switches.

2.5 Materials and Methods

2.5.1 Molecular cloning

The C-terminal FLAG-tagged mouse mGluR2 and mGluR3 constructs in pcDNA3.1(+) expression vector were purchased from GenScript (ORF clone: OMu19627D and OMu17682D) and verified by sequencing (ACGT Inc). The mutation of amino acid A548 in mGluR2 and A557 in mGluR3 to an amber codon (TAG) was performed using the QuikChange site-directed mutagenesis kit (Qiagen). The same approach was used to introduce point mutations in mGluR2 (Y216A, D295A, C770A, and L521C) for other experiments. For the YADA/WT mGluR2 (548UAA) heterodimer experiment, a SNAP-tag ($pSNAP_f$, NEB) was inserted at position 19, flanked by GGS linkers, using HiFi DNA Assembly Master Mix (NEB). Finally, site directed mutagenesis was done to remove the C-terminal FLAG-tag on this construct. All plasmids were sequence verified (ACGT Inc). DNA restriction enzymes, DNA polymerase and DNA ligase were from New England Biolabs. Plasmid preparation kits were purchased from Macherey-Nagel.

2.5.2 Cell culture conditions

HEK293T cells were purchased from Sigma and were maintained in DMEM (Corning) supplemented with 10% (v/v) fetal bovine serum (GE Healthcare), 100 unit/mL penicillin-streptomycin (Gibco) and 15 mM HEPES (pH=7.4, Gibco) at 37 °C under 5% CO_2. The cells were passaged with 0.05% trypsin-EDTA (Gibco). For unnatural amino acid-containing protein expression, the growth media was supplemented with 0.6 mM 4-azido-L-phenylalanine (Chem-Impex International). All media was filtered by 0.2 μM PES filters (Fisher Scientific).

2.5.3 Transfection and protein expression

24 hours before transfection, HEK293T cells were cultured in 10 cm cell culture dishes (Corning) or polylysine-coated 18 mm glass coverslips (VWR). One hour before transfection, media was changed to growth media supplemented with 0.6 mM 4-azido-L-phenylalanine. mGluR plasmids as described above and pIRE4-Azi plasmid (pIRE4-Azi was a gift from Irene Coin, Addgene plasmid # 105829) were co-transfected (1:1 w/w) into cells using Transporter 5 (Polysciences) or Lipofectamine 3000 (Invitrogen) (total plasmid: 1.5 µg/18 mm coverslip). For YADA/WT heterodimer experiments, SNAP-548UAA(WT), pIRE4-Azi and 548UAA-YADA were co-transfected (1:1:1 w/w/w) using Transporter 5 (Polysciences) (total plasmid: 2 µg/18 mm coverslip). The growth media containing 0.6 mM 4-azido-L-phenylalanine was refreshed after 24 hours and the cells were grown for another 24 hours (total 48 hours expression). On the day of the experiment, 10 minutes before labeling, supplemented growth media was removed and cells were washed twice by extracellular buffer solution containing (in mM): 128 NaCl, 2 KCl, 2.5 $CaCl_2$, 1.2 $MgCl_2$, 10 sucrose, 10 HEPES, pH=7.4 and were kept in growth medium without 4-azido-L-phenylalanine. Before the addition of labeling solution (below), cells were washed once with extracellular buffer solution.

2.5.4 SNAP-tag labeling in live cells

SNAP labeling of the N-terminus VFT domain (Figure S2.3C) was done by incubating the cells with 4 µM of benzylguanine Alexa-647 (NEB) and 4 µM of benzylguanine DY-549P1 (NEB) in extracellular buffer for 30 minutes at 37 °C. SNAP labeling for the WT/YADA heterodimer experiments (Figure 2.3E-F, S2.9) was done at 37 °C with 4 µM of SNAP-Surface ATTO488

(NEB) in extracellular buffer for 30 minutes. After labeling, coverslip was gently washed twice in extracellular buffer to remove excess dye.

2.5.5 Unnatural amino acid labeling in live cells by azide-alkyne click chemistry

A modified version of previously reported protocols (Serfling & Coin, 2016; Hong et al., 2010) was used to fluorescently label the incorporated 4-azido-L-phenylalanine in live cells. Stock solutions were made as follows: Cy3 and Cy5 alkyne dyes (Click Chemistry Tools) 10 mM in DMSO, BTTES (Click Chemistry Tools) 50 mM, copper sulfate (Millipore Sigma) 20 mM, aminoguanidine (Cayman Chemical) 100 mM, and (+)-sodium L-ascorbate (Millipore Sigma) 100 mM in ultrapure distilled water (Invitrogen). In 656 µL of extracellular buffer solution, Cy3 and Cy5 alkyne dyes were mixed to a final concentration of 18 µM of each dye. To this mixture, a fresh pre-mixed solution of copper sulfate and BTTES (1:5 molar ratio) was added at the final concentration of 150 µM and 750 µM, respectively. Next, aminoguanidine was added to the final concentration of 1.25 mM and (+)-sodium L-ascorbate was added to the mixture to a final concentration of 2.5 mM. Total labeling volume was 0.7 mL. The labeling mixture was kept at 4 °C for 8 minutes followed by 2 minutes at room temperature before addition to cells. Cells were washed prior to addition of labeling mixture. During labeling, cells were kept in the dark at 37 °C and 5% CO_2. After 10 minutes, L-glutamate (Sigma) was added to the cells to a final concentration of 0.5 mM and cells were incubated for an additional 5 minutes. After labelling, cells were washed twice by extracellular buffer. For the gel electrophoresis experiment, only Cy5 alkyne dye was used with the final concentration of 35 µM.

2.5.6 Gel electrophoresis

After labelling, cells from three 10 cm dishes were washed by extracellular buffer and detached from the plates by incubating with Ca^{2+}-free DPBS (Thermo Scientific) buffer followed by a gentle pipetting. Cells were then pelleted by a 4,000 *g* centrifugation at 4 °C for 10 minutes. The pellet was lysed in 1.5 mL lysis buffer (pH=7.2) consisting of 200 mM NaCl, 50 mM HEPES, 1 mM EDTA, protease inhibitor tablet (Thermo Fisher Scientific) and 1% DDM-CHS (10:1, Anatrace). After 1 hour of gentle mixing at 4 °C, cells were centrifuged at 20,000 *g* at 4°C for 20 minutes and the supernatant was collected and concentrated to 150 µL by 100kDa centrifugal filters (Millipore) at 4 °C. 10 µL of this solution was mixed with 10 µL of 50% glycerol and loaded into a precast 4-20 % gradient non-reducing polyacrylamide gel (Biorad) and ran at 100 V for 45 minutes. 2 µL of precision plus protein standard (Biorad) was used as a ladder. The gel was washed two times in ultrapure water and the image was captured using a Typhoon 9400 fluorimager (GE Healthcare) with 633 nm excitation wavelength and 670-BP30 emission filter.

2.5.7 Confocal microscopy

Live-cell images were acquired using an inverted confocal microscope (Zeiss, LSM-800) with a 40X oil-immersion objective, equipped with 561 and 640 nm lasers, with 2 GaAsP-PMT detectors with detection wavelengths of 540-617 nm and 645-700 nm for Cy3 and Cy5 channels respectively.

2.5.8 Live-cell FRET measurements

After labeling, coverslip was assembled in a flow chamber (Innova Plex) and attached to a gravity flow control system (ALA Scientific Instruments) to control buffer application during experiments. Buffers were applied at the rate of 5 mL/min. Labeled cells were imaged on a home-

built total internal reflection fluorescence (TIRF) microscope equipped with a 20X objective (Olympus, oil-immersion) in the oblique illumination mode and using an excitation filter set with a quad-edge dichroic mirror (Di03-R405/488/532/635, Semrock) and a long-pass filter (ET542lp, Chroma).

Cy3 (donor) was excited with a 532 nm laser (RPMC Lasers) and emissions from Cy3 and Cy5 fluorophores were simultaneously recorded with an electron multiplying charge-coupled device (EMCCD, iXon Ultra, Andor). All data was recorded at 4500 ms time resolution. In the emission path a quad-notch filter (NF01-405/488/532/635, Semrock) was used to block lasers and a dichroic beamsplitter (FF640-FDi01, Semrock) was used to split the emission into donor and acceptor signals.

Movies were analyzed in Fiji (Schindelin et al., 2012) by manually drawing an ROI around the membrane of each analyzed cell. Built-in Fiji functions were used to calculate the mean grey intensity within the ROIs in both donor and acceptor channels and over all the frames. Donor and acceptor intensities were corrected for background which was measured from a region in the same field of view and without cells. The acceptor intensity was corrected for bleed-through of the Cy3 donor signal into the Cy5 acceptor channel which we measured to be 8.8% of Cy3 intensity in our setup. Apparent FRET efficiency was calculated as $FRET = (I_A - 0.088 \times I_D) / (I_D + I_A)$, where I_D and I_A are the background-corrected donor and acceptor intensities. Cells and ROIs were inspected for lack of substantial drift, lateral movement, and the presence of anti-correlated behavior of donor and acceptor signals.

During the titration experiments the wash buffer or buffers containing the specified ligand were continuously applied long enough for the FRET curve to stabilize and plateau. To calculate the

FRET change (ΔFRET) for each ligand application, the average of FRET efficiency for 6 datapoints before the application of ligand was calculated and assigned as FRET_before. The average FRET efficiency for 6 datapoints after the application of ligand and after the FRET curve has plateaued was calculated and assigned as FRET_after. FRET change (ΔFRET) was calculated as ΔFRET = FRET_after - FRET_before. Dose response equation $y\,(x) = A1 + \frac{A2-A1}{1+\,10^{(Logx0-x)P}}$ was used for fitting ΔFRET data to calculate EC50.

DCG-IV and Ro64-5229 were purchased from Tocris. LY379268 was purchased from Cayman Chemical. All curve fittings were done in Origin Pro (OriginLab).

2.5.9 Structural analysis

Distances were measured in Chimera (Pettersen et al., 2004). Based on the spectral overlap of Cy3 alkyne and Cy5 alkyne, a Förster radius (R_0) of 55 Å was used to convert raw FRET efficiency (F) to an approximate distance using $FRET=1/(1+(R/\ R_0)^6)$. Figure 1a was created using Illustrate (Goodsell et al., 2019).

2.5.10 Single-molecule FRET measurements

Single-molecule FRET experiments were done in flow cells that were prepared using glass coverslips (VWR) and slides (Thermo Fisher Scientific) passivated with mPEG (Laysan Bio) and 1% (w/w) biotin-PEG to prevent unspecific protein adsorption, as previously described (Vafabakhsh et al., 2015; Jain et al., 2012). Prior to experiments, flow cells were first incubated with 500 nM NeutrAvidin (Thermo Fisher Scientific) for 2 minutes followed by 20 μM biotinylated FLAG antibody (A01429, GenScript) for 30 minutes. Unbound NeutrAvidin and

biotinylated FLAG antibody were removed by washing. Washes and protein dilutions were done with T50 buffer (50 mM NaCl, 10 mM Tris, pH 7.4).

After labeling, cells were recovered from a single 10 cm plate by incubating with Ca^{2+}-free DPBS followed by a gentle pipetting. Cells were then pelleted by a 4000 *g* centrifugation at 4 °C for 10 minutes. The cell pellet was lysed in 350 µL lysis buffer consisting of 200 mM NaCl, 50 mM HEPES, 1 mM EDTA, protease inhibitor tablet (Thermo Fisher Scientific) and 1% DDM-CHS (10:1, Anatrace), pH 7.2. After 1 hour of gentle mixing at 4 °C, lysate was centrifuged at 20,000 *g* for 20 min at 4 °C. The supernatant was collected and diluted (5 to 10-fold dilution depending on the concentration) and was then added to the flow chamber to achieve sparse surface immobilization of labeled receptors by their C-terminal FLAG-tag. Sample dilution and washes were done using a dilution buffer consisting of 200 mM NaCl, 50 mM HEPES and 0.1% DDM-CHS (10:1, Anatrace), pH 7.2. After optimal receptor coverage was achieved, flow chamber was washed extensively with dilution buffer to remove unbound proteins (> 20× chamber volume). Finally, labeled receptors were imaged in imaging buffer consisting of (in mM) 4 Trolox, 128 NaCl, 2 KCl, 2.5 $CaCl_2$, 1.2 $MgCl_2$, 40 HEPES, 0.05% DDM-CHS (10:1) and an oxygen scavenging system consisting of 4 protocatechuic acid (Sigma) and 1.6 U/mL bacterial protocatechuate 3,4-dioxygenase (rPCO) (Oriental Yeast Co.), pH 7.35. All reagents were prepared from ultrapure-grade chemicals (purity > 99.99%) and were purchased from Sigma. All buffers were made using ultrapure distilled water (Invitrogen).

Samples were imaged with a 100X objective (Olympus, 1.49 NA, Oil-immersion) on a total internal reflection fluorescence (TIRF) microscope, as described above, with 30 ms time resolution unless stated otherwise (Figure S2.3A). 532 nm and 638 nm lasers (RPMC Lasers) were used for

donor and acceptor excitation, respectively. For the YADA/WT mGluR2 heterodimer experiments, a 488 nm laser was used to excite receptors labeled by SNAP (BG-ATTO488), prior to excitation with lasers 532 nm and 638 nm (Figure S2.9).

2.5.11 smFRET data analysis

Analysis of single molecule fluorescence data was performed using smCamera (http://ha.med.jhmi.edu/resources/), custom MATLAB (MathWorks) scripts and OriginPro (OriginLab). Particle selection and generation of raw FRET traces were done automatically within the smCamera software (Figure S2.3A). For the selection, particles that showed acceptor signal upon donor excitation, with acceptor brightness greater than 10% above background and had a Gaussian intensity profile, were automatically selected and donor and acceptor intensities were measured over all the frames. Out of this pool, particles that showed a single donor and a single acceptor bleaching step during the acquisition time, stable total intensity (ID + IA), anti-correlated donor and acceptor intensity behavior without blinking events and lasted for more than 4 seconds were manually selected for further analysis (~20-30% of total molecules per movie). All data was analyzed by three individuals independently and the results were compared and showed to be identical. In addition, a subset of data was blindly analyzed to ensure no bias in analysis. Apparent FRET efficiency was calculated as $(IA - 0.088 \times ID) / (ID + IA)$, where ID and IA are raw donor and acceptor intensities, respectively. For the YADA/WT mGluR2 heterodimer experiments, identity of heterodimers was confirmed by observing a single photobleaching event upon 488 nm laser excitation. All experiments were repeated at least three times independently to ensure reproducibility of the results. Population smFRET histograms were generated by compiling at least 200 FRET traces from individual molecules unless otherwise stated. Before compiling traces,

FRET histograms of individual molecules were normalized to 1 to ensure that each trace contributes equally, regardless of trace length. Error bars on histograms represent the standard error of at least six independent movies.

Peak fitting on population smFRET histograms was performed using OriginPro and using four Gaussian distributions as $\boldsymbol{y(x)} = \sum_{\boldsymbol{i=1}}^{\boldsymbol{4}} \frac{\boldsymbol{A_i}}{\boldsymbol{w_i}\sqrt{\frac{\pi}{2}}} \boldsymbol{e}^{-2\frac{(x-xc_i)^2}{w_i^2}}$, where *A* is the peak area, *xc* is the FRET peak center and *w* is the peak width for each peak. Peak centers (*xc*) were constrained as mean FRET efficiency of a conformational state ± 0.02. The mean FRET efficiencies of the four conformations were determined based on the most frequent FRET states observed in transition density plots. This analysis is further described below. Peak widths were constrained as $0.1 \leq w \leq 0.24$. Peak areas were constrained as $A > 0$. Probability of state occupancy was calculated as area of specified peaks relative to the total area which is defined as the sum of all four individual peak areas.

Raw donor, acceptor and FRET traces were idealized by fitting with a Hidden Markov Model using vbFRET software (Zhang et al., 2018; Bronson et al., 2009b). Transition density plots were then generated by extracting all the transitions where ΔFRET > 0.1, from the idealized traces. Occasional traces for which the HMM fit did not converge (for example due to long blinking events or large non anti-correlated intensity fluctuations) were omitted from downstream analysis. The idealized FRET traces were also used to calculate the dwell times for each of the four states. 147, 140, 128 and 142 molecules from three independent measurements were used for dwell-time analysis of states 3 and 4 for UAA548 (5uM and 10uM glutamate) and mGluR2 C770A (5uM and 10uM glutamate), respectively. 86, 83, 91 and 72 molecules from two independent measurements

were used for dwell-time analysis of states 1 and 2 for the same respective constructs and conditions. Reported values represent mean and error bars represent s.e.m. At least 350 transitions were analyzed for each condition. The dwell times were plotted as cumulative count histograms and were fit with a single-exponential decay function $y(x) = y_0 + A_1 e^{-x/\tau}$ by OriginPro (OriginLab).

The cross-correlation (CC) of donor and acceptor intensity traces at time τ is defined as $CC(\tau) = \delta I_D(t)\delta I_A(t + \tau)/(\langle I_D(t)\rangle + \langle I_A(t)\rangle)$, where $\delta I_D(t) = I_D(t) - \langle I_D(t)\rangle$, and $\delta I_A(t) = I_A(t) - \langle I_A(t)\rangle$. $\langle I_D(t)\rangle$ and $\langle I_D(t)\rangle$ are time average donor and acceptor intensities, respectively. Cross-correlation calculations were performed on the same traces used to generate the histograms. Cross-correlation data were fit to a single exponential function.

2.6 Acknowledgements

We thank M.R. Schamber, D. Badong, D. May and A. Y. Pen for technical assistance, M. Gallio, J. Marko, A. Mondragon and K. Ragunathan for critical reading of the manuscript, J. Fei (University of Chicago) for providing MATLAB scripts. **Funding:** This work was supported by the National Institutes of Health grant R01GM140272 (to R.V.) and by The Searle Leadership Fund for the Life Sciences at Northwestern University and by the Chicago Biomedical Consortium with support from the Searle Funds at The Chicago Community Trust (to R.V.). B.W.L. was supported by National Institute of General Medical Sciences (NIGMS) Training Grant T32GM-008061. This work used resources of the Keck Biophysics Facility supported in part by the NCI CCSG P30 CA060553 grant awarded to the Robert H. Lurie Comprehensive Cancer Center of Northwestern University. **Author contributions:** B.W.L., H.S.A. and R.V. conceived the project

and designed the experiments. B.W.L. and H.S.A. performed the experiments. B.W.L., H.S.A. and R.V. analyzed the experimental data and wrote the paper.

Chapter 3: Identifying mechanisms for mGluR2 allosteric modulation

A previous version of this chapter has been published as:

Liauw, B.W., Foroutan, A., Schamber, M.R., Lu, W., Afsari, H.S., Vafabakhsh, R. *eLife*. **2022**.

3.1 Abstract

Activation of G protein-coupled receptors (GPCRs) is an allosteric process. It involves conformational coupling between the orthosteric ligand binding site and the G protein binding site. Factors that bind at non-cognate ligand binding sites to alter the allosteric activation process are classified as allosteric modulators and represent a promising class of therapeutics with distinct modes of binding and action. For many receptors, how modulation of signaling is represented at the structural level is unclear. Here, we developed FRET sensors to quantify receptor modulation at each of the three structural domains of metabotropic glutamate receptor 2 (mGluR2). We identified the conformational fingerprint for several allosteric modulators in live cells. This approach enabled us to derive a receptor-centric representation of allosteric modulation and to

correlate structural modulation to the standard signaling modulation metrics. Single-molecule FRET analysis revealed that a NAM increases the occupancy of one of the intermediate states while a PAM increases the occupancy of the active state. Moreover, we found that the effect of allosteric modulators on the receptor dynamics is complex and depend on the orthosteric ligand. Collectively, our findings provide a structural mechanism of allosteric modulation in mGluR2 and suggest possible strategies for design of future modulators.

3.2 Introduction

G protein-coupled receptors (GPCRs) are the largest family of membrane receptors in humans and are key drug targets due to their role in nearly all physiological processes (Thal et al., 2018; Dorsam & Gutkind, 2007). Compounds that bind to the defined, endogenous ligand binding pocket in GPCRs are called orthosteric ligands. Many such orthosteric agonists or antagonists have been developed as successful therapies (Lindsley et al., 2016). Despite this success, achieving target specificity in closely related receptors has been a long-standing challenge due to high conservation of the orthosteric binding site. Moreover, tolerability and safety of orthosteric drugs in therapeutic applications have been difficult to achieve for some GPCRs (Lindsley et al., 2016).

Recently, allosteric modulators have emerged as a promising class of therapeutic compounds for fine-tuning physiological response of GPCRs with high receptor specificity and pathway specificity. Allosteric modulators bind to allosteric sites which are structurally distinct from the orthosteric pocket, to indirectly tune the response to the orthosteric ligand (Foster & Conn, 2017). Major advances in design, synthesis, and screening of small molecule compounds have produced multiple selective and potent allosteric modulators for many GPCRs (Lindsley et al., 2016). In

addition, improvements in techniques for measuring GPCR activity have helped reveal the complex pharmacological properties of allosteric modulators (Christopoulos, 2014; Leach & Gregory, 2017) such as probe and cell-type context dependence (Sengmany et al., 2019), biased allosteric agonism, and biased modulation (Sengmany et al., 2017; Makita et al., 2007). Generally, functional characterization of allosteric modulators is done using assays that quantify changes at specific steps of the signaling cascade, downstream of receptor, such as intracellular Ca2+ levels, IP1 accumulation, cellular cAMP levels, ERK1/2 phosphorylation levels, or using energy transfer methods to quantify dissociation of signaling proteins. Collectively, these approaches have provided a pharmacological framework for characterizing and profiling allosteric modulators. However, as functional assays measure the effect of modulators downstream of the receptor, they are unable to provide direct mechanistic insight on allosteric modulation at the receptor level.

Advances in methods for structure determination of membrane proteins have yielded atomic structures of many GPCRs bound to different allosteric modulators and provided insight into different ligand binding modalities and distinct modulator-induced conformations (Seven et al., 2021; Shaye et al., 2020; Bueno et al., 2020; Kruse et al., 2013; Liu et al., 2019; Srivastava et al., 2014). However, despite these advances, for many receptors, structures of only a small subset of receptor-modulator combinations have been determined. Moreover, receptor activation and modulation are dynamic processes, and dynamic information is not achievable by structural representations alone. While progress has been made towards understanding the dynamics of allosteric modulation in class A GPCRs (Wootten et al., 2013; Thal et al., 2018; Gentry et al., 2015), more comprehensive mechanisms, especially for large multi-domain GPCRs, are lacking.

Among all GPCRs, the class C GPCRs are distinct as they are structurally modular, possessing a large extracellular domain and functioning as obligate dimers. Notably, the orthosteric ligand-binding site that is typically found within the 7 transmembrane (7TM) domain bundle in class A GPCRs is in the extracellular Venus flytrap (VFT) domain of class C GPCRs. The VFT domain is linked to the 7TM domain via the cysteine-rich domain (CRD) which is a semi-rigid linker domain. Thus, receptor activation is inherently an allosteric process that involves inter-subunit and inter-domain cooperativity. In the class C family, metabotropic glutamate receptors (mGluRs) are responsible for mediating the slow neuromodulatory effects of glutamate to tune synaptic excitability and transmission (Niswender & Conn, 2010; Pin & Bettler, 2016), making them promising therapeutic targets for treating a range of neurological and psychiatric disorders (Foster & Conn, 2017; Conn, Christopoulos, et al., 2009; Mantas et al., 2021). Based on structural (Wu et al., 2014; Doré et al., 2014; Seven et al., 2021; Du et al., 2021) and mutagenesis (Farinha et al., 2015; Lundström et al., 2011; Gregory & Conn, 2015) studies, the primary mGluR allosteric binding sites were determined to be located within the 7TM domain bundles. Previous work examining allosteric modulation of mGluR conformational dynamics generally used ensemble methods and was focused on the dimeric rearrangement of either the 7TM domain (Gutzeit et al., 2019; Nasrallah et al., 2021) or the extracellular ligand-binding domain (Cao et al., 2021). While these studies of individual domains provide insights into how allosteric modulators affect mGluR structure and dynamics, they are not conducive for the broader fingerprinting of the modulator effect across multiple domains of the receptor. Specifically, how key pharmacological parameters such as efficacy and potency of different orthosteric and allosteric ligands, are manifested

structurally at different domains and how positive and negative allosteric modulators achieve their modulatory effect through modifying the receptor's energy landscape are not known.

Here, we used live-cell fluorescence resonance energy transfer (FRET) and single-molecule FRET (smFRET) imaging with non-perturbing site-specific labeling, to explicitly examine and quantify the effects of orthosteric agonists and allosteric modulators on mGluR2 conformation and dynamics at the three structural domains of the receptor (Figure 3.1A). Comparing live-cell imaging results between the domains, we found that the effect of positive or negative allosteric modulators is represented at every domain of the receptor, but to different levels. The effect of modulators on the glutamate efficacy and potency as quantified by the compaction and rearrangement at each receptor domain via the FRET sensors matches with the known functional classification of the compounds. Interestingly, positive allosteric modulators (PAMs) generally increased glutamate efficacy to a greater extent when measured at the CRD and 7TM domains compared to the VFT domain. A similar trend was observed for orthosteric agonists. Our results illustrate that the conformation of the CRD and 7TM domain are more accurate metrics for quantifying ligand efficacy than that of the VFT domain, possibly due to the loose conformational coupling between mGluR2 domains (Grushevskyi et al., 2019; Liauw et al., 2021). Further examination of the CRD sensor by smFRET revealed that the PAM compound BINA, biases more compact intermediate CRD conformations even in the absence of glutamate and further stabilizes the intrinsic CRD dynamics in the presence of glutamate. In contrast, we found that MNI-137 which is a NAM, blocked receptor activation by impeding CRD progression to the active conformation and preventing glutamate-induced stabilization of the domain. Collectively, the

work presented here provides a dynamic receptor centric model of allosteric modulator effects on mGluR2 conformation and dynamics as well as mechanisms for positive and negative modulation.

3.3 Results

3.3.1 CRD and 7TM domain conformation are sensitive measures of mGluR2 activation

According to the general model for mGluR activation, binding of an orthosteric agonist induces a local conformational change that causes global receptor rearrangement to activate the G protein-binding interface 10 nm away, through stabilization of an asymmetric 7TM domain interface (Seven et al., 2021). Therefore, activation involves coordinated conformational coupling of the three receptor domains. Structurally, the VFT domain, CRD, and 7TM domain undergo unique dynamics during receptor activation (Cao et al., 2021; Grushevskyi et al., 2019; Liauw et al., 2021). Moreover, how each domain within mGluRs contribute to the overall receptor regulation and activation is now better understood (S. Huang et al., 2011; Thibado et al., 2021; Goudet et al., 2004). Thus, the three domains can be viewed as modular units that are linked to form a complex and conformationally coupled signaling machine. To gain further insight into mGluR activation and allostery, a better understanding of the dynamics of individual domains and their relation to one another is essential.

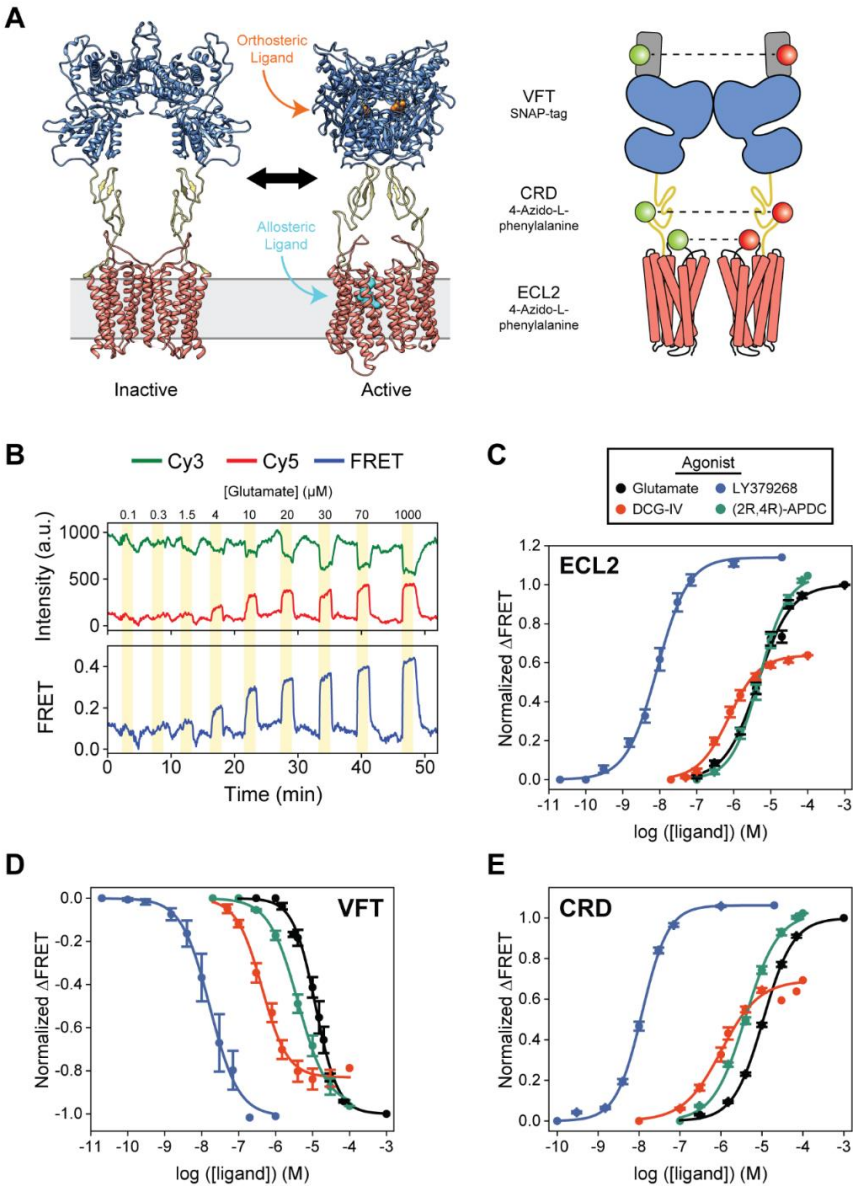

Figure 3.1 Agonist-induced structural change measured at each domain using conformational FRET sensors

(A) Full-length cryo-EM structures of inactive (7EPA) and fully active (7E9G) mGluR2 (human) and schematic illustrating fluorophore placement for each inter-domain sensor. (B) Representative normalized live-cell FRET trace from glutamate titration experiment on HEK293T cells expressing azi-ECL2. Data was acquired at 4.5 s time resolution. Dose-response curves from live-cell FRET orthosteric agonist titration experiments using (C) azi-ECL2, (D) SNAP-m2, and (E) azi-CRD. Data is acquired from individual cells and normalized to 1 mM glutamate response. Data represents mean ± s.e.m. of responses from individual cells from at least three independent experiments. Total number of cells examined, mean EC_{50}, mean max response, and errors are listed in Table 1-2.

Here, we used inter-subunit FRET sensors to measure the dimeric rearrangement of each structural domain within full-length mGluR2 in real-time and *in vivo* to obtain a more comprehensive picture of receptor activation (Figure 3.1A). Specifically, to study inter-7TM domain conformational change, we created a novel sensor based on an unnatural amino acid (UAA) incorporation strategy (Huber et al., 2013a; Noren, Anthony-Cahill, et al., 1989; Serfling & Coin, 2016; Liauw et al., 2021) to site-specifically label extracellular loop 2 (ECL2). We also utilized well established conformational sensors to examine the VFT domain and CRD (Doumazane et al., 2011; Vafabakhsh et al., 2015; Liauw et al., 2021). To generate the inter-7TM domain sensor, we inserted an amber codon between E715 and V716 which, after expression in HEK293T cells, was labeled with 4-azido-L-phenylalanine (hereafter, azi-ECL2). This sensor allowed us to precisely probe conformational changes at ECL2, which have been shown to be essential in coordinating structural transitions between the VFT domain and 7TM domain of not only mGluR2 (Seven et al., 2021; Du et al., 2021), but other class C GPCRs as well (Koehl et al., 2019a; Shen et al., 2021). We observed a glutamate concentration-dependent increase in FRET signal in cells expressing azi-ECL2, confirming a general reduction in distance between ECL2s during mGluR2 activation and consistent with structural studies (Seven et al., 2021; Du et al., 2021) (Figure 3.1B, S3.1A).

This glutamate-dependent increase in ensemble FRET had a half-maximum effective concentration (EC_{50}) of 5.1 ± 0.6 μM, consistent with the concentration-dependent activation of GIRK currents (Vafabakhsh et al., 2015) (Figure 3.1C, Table 3.1). These results validate the sensitivity and accuracy of this new FRET sensor. Next, we measured the concentration-dependent increases in ensemble FRET signals for other orthosteric ligands DCG-IV, LY379268, and (2R,4R)-APDC and measured EC_{50} values of 0.9 ± 0.1 μM, 10.2 ± 2.4 nM, and 6.7 ± 1.3 μM,

respectively, in agreement with the published range of EC_{50} values for these compounds (Doumazane et al., 2013a) (Figure 3.1C, S3.1B, Table 3.1). Importantly, azi-ECL2 accurately reports that DCG-IV is less efficacious than glutamate, consistent with its characterization as a partial agonist. Likewise, this sensor was able to accurately report on LY379268 and (2R,4R)-APDC which are known to be more efficacious agonists than glutamate (Figure 3.1C, S3.2, Table 3.2).

Sensor	Ligand	N	Mean EC_{50}	S.E.M.	Hill Slope	Standard Error
SNAP-m2	Glutamate	9	11.9	1.5	-1.44	0.08
SNAP-m2	DCG-IV	6	0.4	0.1	-1.26	0.11
SNAP-m2	LY379268	6	30.6	9.3	-1.12	0.07
SNAP-m2	(2R,4R)-APDC	6	6.9	3.1	-1.10	0.05
SNAP-m2	Glutamate + 10μM BINA	23	1.2	0.4	-1.24	0.09
SNAP-m2	Glutamate + 5μM LY487379	4	3.8	0.9	-1.43	0.11
SNAP-m2	Glutamate + 0.5μM JNJ-42153605	5	4.2	1.9	-0.95	0.05
SNAP-m2	Glutamate + 10μM MNI-137	4	17.2	2.8	-1.61	0.06
SNAP-m2	Glutamate + 10μM Ro 64-5229	3	19.6	2.6	-1.52	0.04
azi-CRD	Glutamate	26	11.6	0.5	1.19	0.03
azi-CRD	DCG-IV	10	1.1	0.2	0.94	0.10
azi-CRD	LY379268	20	12.1	0.5	1.36	0.05
azi-CRD	(2R,4R)-APDC	36	6.5	1.2	1.10	0.05
azi-CRD	Glutamate + 10μM BINA	10	1.6	0.3	1.16	0.05
azi-CRD	Glutamate + 5μM LY487379	22	4.5	0.6	0.91	0.04
azi-CRD	Glutamate + 0.5μM JNJ-42153605	10	4.7	1.3	0.84	0.03
azi-CRD	Glutamate + 10μM MNI-137	27	13.8	0.7	1.10	0.04
azi-CRD	Glutamate + 10μM Ro 64-5229	13	16.9	1.2	1.05	0.06
azi-ECL2	Glutamate	15	5.1	0.6	0.96	0.07
azi-ECL2	DCG-IV	24	0.9	0.1	1.05	0.06
azi-ECL2	LY379268	9	10.2	2.4	1.03	0.04
azi-ECL2	(2R,4R)-APDC	13	6.7	1.3	1.14	0.05
azi-ECL2	Glutamate + 10μM BINA	16	2.5	0.2	1.06	0.07
azi-ECL2	Glutamate + 5μM LY487379	22	3.5	0.2	0.98	0.05
azi-ECL2	Glutamate + 0.5μM JNJ-42153605	17	2.2	0.1	0.97	0.06
azi-ECL2	Glutamate + 10μM MNI-137	8	14.4	1.7	1.32	0.06
azi-ECL2	Glutamate + 10μM Ro 64-5229	5	17.4	2.4	1.07	0.09

*All EC50s and errors values are in micromolar, except for LY379268 (nanomolar).

Table 3.1 Live-cell FRET titration experiment data and statistics

Sensor	Ligand	N	Mean Max Response	S.E.M.
SNAP-m2	Glutamate	-	1	-
SNAP-m2	DCG-IV	25	0.79	0.01
SNAP-m2	LY379268	23	1.01	0.01
SNAP-m2	(2R,4R)-APDC	14	0.96	0.01
SNAP-m2	Glutamate + 10μM BINA	7	1.02	0.01
SNAP-m2	Glutamate + 5μM LY487379	14	1.07	0.01
SNAP-m2	Glutamate + 0.5μM JNJ-42153605	22	1.01	0.01
SNAP-m2	Glutamate + 10μM MNI-137	22	0.85	0.02
SNAP-m2	Glutamate + 10μM Ro 64-5229	35	0.87	0.01
azi-CRD	Glutamate	-	1	-
azi-CRD	DCG-IV	19	0.69	0.01
azi-CRD	LY379268	25	1.06	0.02
azi-CRD	(2R,4R)-APDC	13	1.02	0.01
azi-CRD	Glutamate + 10μM BINA	9	1.12	0.05
azi-CRD	Glutamate + 5μM LY487379	19	1.56	0.07
azi-CRD	Glutamate + 0.5μM JNJ-42153605	8	1.43	0.08
azi-CRD	Glutamate + 10μM MNI-137	18	0.86	0.02
azi-CRD	Glutamate + 10μM Ro 64-5229	18	0.59	0.03
azi-ECL2	Glutamate	-	1	-
azi-ECL2	DCG-IV	25	0.64	0.02
azi-ECL2	LY379268	22	1.14	0.04
azi-ECL2	(2R,4R)-APDC	56	1.05	0.01
azi-ECL2	Glutamate + 10μM BINA	14	1.42	0.07
azi-ECL2	Glutamate + 5μM LY487379	7	1.25	0.09
azi-ECL2	Glutamate + 0.5μM JNJ-42153605	13	0.99	0.02
azi-ECL2	Glutamate + 10μM MNI-137	58	0.78	0.03
azi-ECL2	Glutamate + 10μM Ro 64-5229	8	0.84	0.05

*All max response values are normalized to 1mM glutamate.

Table 3.2 Live-cell FRET max normalization experiment data and statistics

Receptor rearrangement and activation requires local ligand-induced structural change to propagate from the VFT domain through the CRD to the 7TM domain. Thus, we next compared the orthosteric agonist-induced FRET change of azi-ECL2 with that of the VFT domain FRET sensor (N-terminal SNAP-tag labeled mGluR2; hereafter, SNAP-m2) and CRD FRET sensor (labeled via 4-azido-L-phenylalanine insertion at position 548; hereafter, azi-CRD). We found that all three sensors accurately predict the relative efficacy of tested orthosteric ligands (Figure 3.1C-E, S3.2A, Table 3.2). Specifically, the three sensors rank the four agonists from most to least efficacious as LY379268 > (2R,4R)-APDC > glutamate > DCG-IV. However, the maximum response by highly efficacious agonists LY379268 and (2R,4R)-APDC are larger when measured at the CRD and 7TM domain compared to the VFT domain (Figure S3.2, Table 3.2). In contrast, maximum response by partial agonist DCG-IV is smaller at the CRD and 7TM domain as compared to measurements at the VFT domain. These findings are consistent with results from our functional calcium imaging assay that utilizes a chimeric G protein (Conklin et al., 1993) (Figure S3.3). For example, DCG-IV shows 79% of glutamate efficacy via the VFT domain FRET sensor, while it shows 69% efficacy via CRD sensor and 64% efficacy via the ECL2 sensor, compared to 69% efficacy via the functional assay. Collectively, the results show that the novel ECL2 sensor accurately report the activation of mGluR2. Moreover, conformation of the CRD and 7TM domain are a more sensitive measures of receptor activation compared to the VFT domain and consistent with the loose coupling between mGluR domains (Grushevskyi et al., 2019; Liauw et al., 2021).

3.3.2 Allosteric ligands modulate glutamate potency and efficacy at each structural domain

Establishing general principles to predict physiological outcome of mGluR allosteric modulators has been challenging due to their high context dependence and variability in functional measurements (Thal et al., 2018; Leach & Gregory, 2017). For example, many mGluR5 PAMs exhibit biased agonism when used in a panel of different functional assays and tested mGluR5 NAMs showed different effects between heterologous and endogenous systems (Sengmany et al., 2019; Sengmany et al., 2017). To overcome the inherent limitations due to convolution of responses of multiple components in the signaling pathway, we directly quantified the effects of a series of modulators on glutamate-induced rearrangement of mGluR2 using the three FRET sensors described above. This unique approach provides a conformational fingerprint of allosteric modulators, complementing available pharmacological and structural data.

We focused on three PAMs, BINA (Bonnefous et al., 2005), LY487379 (Johnson et al., 2003), and JNJ-42153605 (Cid et al., 2012), and two NAMs, MNI-137 (Hemstapat et al., 2007) and Ro 64-5229 (Kolczewski et al., 1999). We examined the ability of these compounds to modulate glutamate-induced FRET change of SNAP-m2, azi-CRD, and azi-ECL2 FRET sensors. Specifically, to quantify modulation of glutamate potency (EC_{50}), we performed glutamate titrations using each sensor in the presence of a different allosteric modulator. Next, in separate experiments, we derived maximum responses (efficacy) to 1 mM glutamate with and without each of the modulators (Figure S3.4-6, Table 3.2). First, glutamate titrations in the presence of all tested PAMs resulted in increased glutamate potency and efficacy at every domain, as measured via FRET (Figure 3.2A, C, D, F, G, I, Table 3.1-2). Therefore, the positive and negative allosteric modulation, which is defined through signaling assays, are generally manifested consistently at

every structural domain of mGluR2. We found that PAMs generally increase glutamate efficacy to a greater extent as probed at the CRD and 7TM domain compared to the VFT domain (Figure 3.2J, Table 3.2). This is similar to the effects we observed for highly efficacious orthosteric agonists LY379268 and (2R,4R)-APDC. Specifically, glutamate efficacy in the presence 10 μM BINA as reported by azi-CRD and azi-ECL2 and not SNAP-m2 are more consistent with our functional analysis, suggesting that the CRD and 7TM domain are better metrics of ligand efficacy (Figure S3.7). Interestingly, JNJ-42153605 showed no change in efficacy as quantified by the FRET signal at ECL2 while it showed changes at VFT domain and CRD (Figure 3.2G, I, J, Table 3.2). The ability of different mGluR2 PAMs to alter glutamate potency and efficacy as probed at each domain and to different degrees suggests that PAMs may utilize distinct mechanisms to achieve allosteric modulation of mGluR2, with each domain distinctly affected by each PAM.

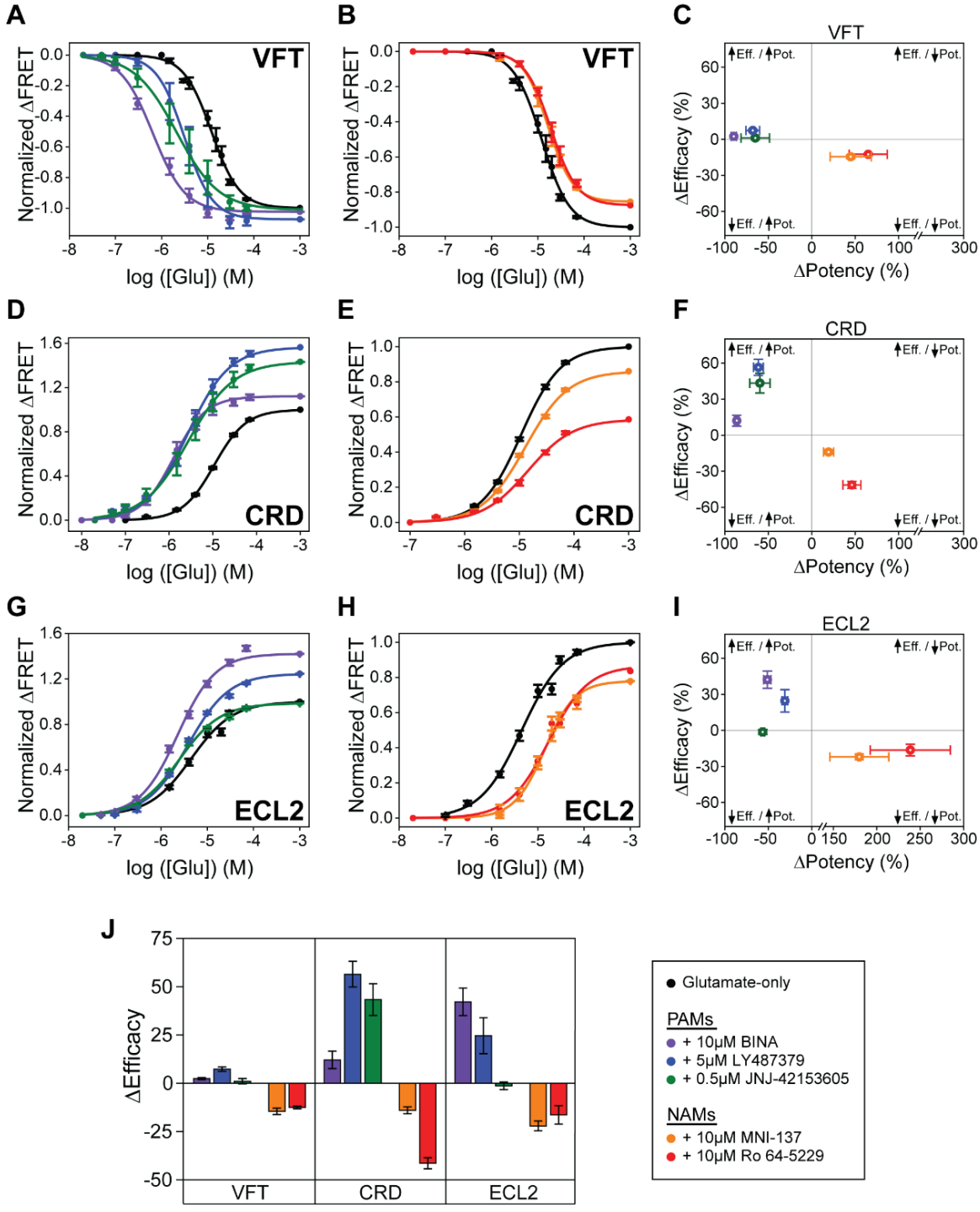

Figure 3.2 Positive and negative allosteric modulation of mGluR2 structural domains
SNAP-m2 glutamate dose-response curves in the presence of (A) PAMs or (B) NAMs. (C) Changes in glutamate potency and efficacy for SNAP-m2. azi-CRD glutamate dose-response curves in the presence of (D) PAMs or (E) NAMs. (F) Changes in glutamate potency and efficacy

for azi-CRD. azi-ECL2 glutamate dose-response curves in the presence of (G) PAMs or (H) NAMs. (I) Changes in glutamate potency and efficacy for azi-ECL2. (J) Changes in glutamate efficacy in response to PAMs and NAMs as measured by each conformational sensor. ΔPotency defined as (([modulator + glutamate]$_{EC50}$ − [glutamate] $_{EC50}$)/[glutamate] $_{EC50}$) × 100. ΔEfficacy defined as ([1 mM glutamate + modulator] - [1 mM glutamate]) × 100. Data is acquired from individual cells and normalized to 1 mM glutamate response. Data represents mean ± s.e.m. of responses from individual cells from at least three independent experiments. Total number of cells examined for titration and normalization experiments, mean EC_{50}, mean max response, and errors are listed in Table 1-2.

Next, glutamate titration in the presence of NAMs resulted in the overall reduction of glutamate potency and efficacy probed at each of the three domains, as expected for a NAM (Figure 3.2B, C, E, F, H, I, Table 3.1-2). These results are consistent with our functional calcium imaging assay as well (Figure S3.7). Interestingly, at NAM concentration used for FRET imaging (10 μM) we observed robust glutamate-induced conformational change (Figure 3.2B, E, H, S3.4-6) but could not detect receptor activation in the presence of glutamate, consistent with previous reports that high concentration of NAMs block mGluR2 signaling. (Hemstapat et al., 2007; Kolczewski et al., 1999). This shows that MNI-137 and Ro 64-5229 can block receptor activation without blocking glutamate-induced conformational change at every domain, even at the 7TM domain where the NAMs bind. Whether this is due to induction of novel conformational states upon NAM binding or due to interruption in existing conformational changes that precede receptor activation, cannot be addressed using ensemble assays.

Together, the results show that the tested allosteric modulators affect glutamate-induced compaction and activation of mGluR2 in a manner consistent with their functional characterization. Interestingly, while having overlapping binding pockets that share key residues, PAMs and NAMs modulate glutamate-induced conformational change in different ways (Figure S3.8). Despite the overall trend for PAMs and NAMs, the general variability in the change of

glutamate potency and efficacy between domains in response to individual modulators provides evidence for the existence of multiple pathways to achieve allosteric modulation of mGluR2.

3.3.3 BINA can function independently of glutamate and stabilizes receptor during activation

Live-cell FRET experiments revealed the general conformational fingerprint of mGluR2 modulators, which are defined as changes in glutamate potency and efficacy as measured by rearrangement of different domains. However, the ensemble method cannot provide mechanistic information such as receptor conformation, state occupancy, and state transitions. For example, whether the modulators stabilize novel states or alter transition rates between existing states is not directly deducible from the ensemble characterization. To overcome this limitation, we performed single-molecule FRET (smFRET) using the CRD FRET sensor. We selected azi-CRD because our live-cell FRET analysis showed that quantification of modulator effects on the CRD was very consistent with our functional results. Moreover, we previously showed azi-CRD to be a sensitive reporter of mGluR2 allosteric modulation via smFRET analysis (Liauw et al., 2021).

To perform smFRET imaging, HEK293T cells expressing azi-CRD containing a C-terminal FLAG-tag were labeled using mixture of donor (Cy3) and acceptor (Cy5) fluorophores, then lysed. Cell lysate was then applied to a polyethylene glycol (PEG) passivated coverslip, functionalized with anti-FLAG-tag antibody to immunopurify the receptors (SiMPull) for total internal reflection fluorescence (TIRF) imaging (Jain et al., 2011; Liauw et al., 2021) (Figure 3.3A). In the absence of glutamate, the CRD primarily occupied the inactive state and intermediate state 1, corresponding to open and inactive conformations of the VFT domains or the conformation where an individual VFT domain is closed, respectively (Liauw et al., 2021) (Figure 3.3B, H, S3.9A,

Table 3.3). Importantly, the receptor showed dynamics between these states. A glutamate scavenging system was added for 0 μM glutamate conditions to ensure no glutamate contamination. Interestingly, in the absence of glutamate and presence of 10 μM BINA, we detected a small increase in FRET, primarily through increased occupancy of intermediate state 2, a conformation in which the 7TM domains are hypothesized to have not formed a stabilizing interaction with one another that is necessary for receptor activation (Liauw et al., 2021) (Figure 3.3E, H, S3.10A, Table 3.3). Upon the addition of intermediate (15 μM) and saturating (1 mM) concentrations of glutamate, a concentration-dependent increase in the active state occupancy was observed (Figure 3.3C, D, H, S3.9, Table 3.3). The four conformational states and glutamate-dependent increase in FRET agree with previous work (Liauw et al., 2021). Specifically, addition of 15 μM glutamate in the presence of 10 μM BINA resulted in a FRET distribution similar to saturating glutamate alone (1 mM), consistent with the effect of PAM on increasing glutamate potency. Finally, 1 mM glutamate plus 10 μM BINA resulted in a further increase in active conformation occupancy, consistent with the effect of PAM on increasing glutamate efficacy (Figure 3.3F, G, H, S3.10, Table 3.3). Interestingly, examination of CRD dynamics, as measured by cross-correlation between donor and acceptor intensities, showed that in the presence of intermediate (15 μM) and saturating (1mM) glutamate concentrations, addition of 10 μM BINA reduced receptor dynamics (Figure 3.3I). Together, these observations suggests that PAMs may increase agonist efficacy by effectively increasing occupancy of the active conformation of the receptor. Moreover, these single-molecule measurements demonstrated that the effect of BINA on mGluR2 conformation and dynamics depends on the presence or absence of glutamate. In the absence of glutamate, BINA increased receptor dynamics and FRET by increasing the occupancy

of intermediate state 2 (Figure 3.3E, H, S3.10, Table 3.3). While in the presence of intermediate (15 μM) and saturating (1 mM) glutamate, BINA reduced the dynamics of the CRD and increased the occupancy of the active state (Figure 3.3F, G, H, I, S3.10, Table 3.3). Interestingly, even in the presence of 1 mM glutamate and BINA, the receptors remained dynamic with the CRDs not fully stabilized in a single conformation.

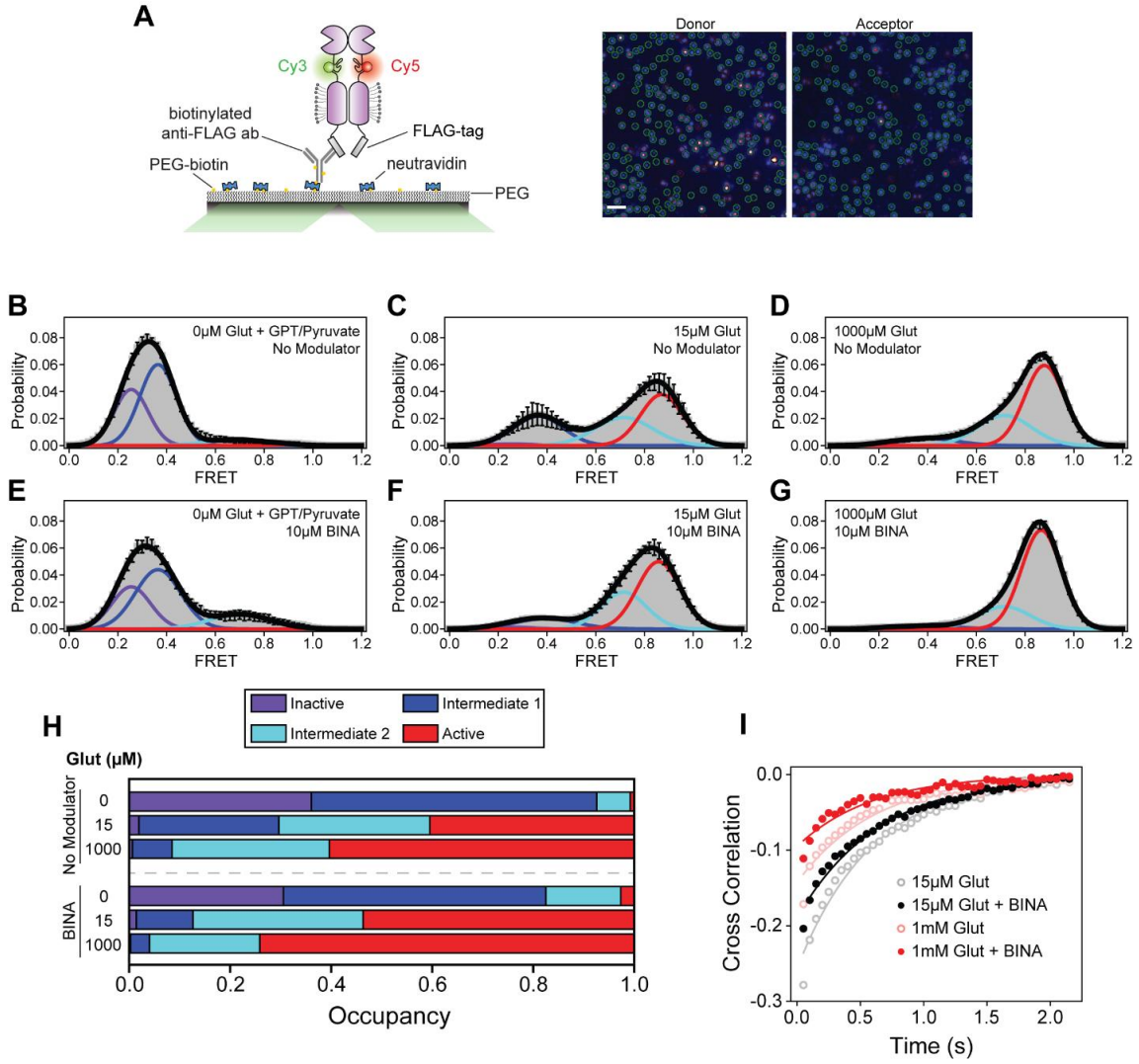

Figure 3.3 smFRET analysis of BINA effects on CRD conformational dynamics
(A) Schematic of SiMPull assay (left) and representative image of donor and acceptor channels during data acquisition (right). Green circles indicate molecules selected by software for analysis. Scale bar, 3 μm. smFRET population histograms of azi-CRD in the presence of 0 μM, 15 μM, and 1 mM glutamate without (B-D) or with (E-G) 10 μM BINA. Histograms were fitted (black) to four Gaussian distributions centered around 0.24 (inactive; purple), 0.38 (intermediate 1; blue), 0.70 (intermediate 2; cyan), and 0.87 (active; red) FRET. Error bars represent s.e.m. Histograms (B-G) were generated from 332, 366, 253, 252, 418, and 367 individual particles, respectively. (H) Mean occupancy of four conformational states of azi-CRD in varying ligand conditions. Values represent area under each FRET peak from smFRET histogram as a fraction of total area. Mean and s.e.m. values are reported in Table 3. (I) Mean cross-correlation of donor and acceptor intensities in the presence of intermediate (15 μM) and saturating (1 mM) glutamate with and without 10 μM BINA. Data was acquired at 50 ms time resolution. All data represents mean from three independent experiments.

Modulator	Glut (μM)	State (#)	Mean Occupancy	S.E.M.
None	0	1	0.36067	0.048
None	0	2	0.56526	0.02692
None	0	3	0.06615	0.02385
None	0	4	0.00792	0.00792
None	15	1	0.01932	0.01049
None	15	2	0.27699	0.06688
None	15	3	0.29899	0.01579
None	15	4	0.4047	0.09147
None	1000	1	0.00642	0.00292
None	1000	2	0.07841	0.01209
None	1000	3	0.31131	0.02404
None	1000	4	0.60386	0.01743
10μM BINA	0	1	0.30527	0.02468
10μM BINA	0	2	0.51994	0.04492
10μM BINA	0	3	0.14826	0.04699
10μM BINA	0	4	0.02653	0.01748
10μM BINA	15	1	0.01424	0.00761
10μM BINA	15	2	0.11217	0.01526
10μM BINA	15	3	0.3367	0.07918
10μM BINA	15	4	0.53688	0.07621
10μM BINA	1000	1	0.00296	0.00154
10μM BINA	1000	2	0.03751	0.00782
10μM BINA	1000	3	0.21791	0.01663
10μM BINA	1000	4	0.74162	0.01093
5μM MNI-137	0	1	0.74861	0.02014
5μM MNI-137	0	2	0.22198	0.01316
5μM MNI-137	0	3	0.02038	0.01004
5μM MNI-137	0	4	0.00903	0.00541
5μM MNI-137	15	1	0.10387	0.02484
5μM MNI-137	15	2	0.74937	0.01688
5μM MNI-137	15	3	0.12724	0.01026
5μM MNI-137	15	4	0.01952	0.00254
5μM MNI-137	1000	1	0.00207	0.000954
5μM MNI-137	1000	2	0.5597	0.02561
5μM MNI-137	1000	3	0.33098	0.03204
5μM MNI-137	1000	4	0.10725	0.00734

Table 3.3 smFRET state occupancy data and statistics

3.3.4 MNI-137 prevents CRD progression to the active conformation and glutamate-induced stabilization

Some mGluR2 NAMs that bind at the 7TM domain function as non-competitive antagonists and can prevent glutamate-dependent activation of the receptor (Hemstapat et al., 2007). To investigate the molecular mechanism underlying this phenomenon, we next performed smFRET analysis to directly visualize the effect of MNI-137 on the CRD sensor. In the absence of glutamate, 5 μM MNI-137 resulted in a decrease in FRET and increase in occupancy of the inactive conformation of the CRD as compared to unliganded receptor (Figure 3.4A, D, S3.11A, Table 3.3). The increase in inactive state occupancy was accompanied by a stabilization of the CRD, demonstrating that MNI-137 reduces intrinsic CRD dynamics in the absence of glutamate, which contrasts with the effects of BINA alone (Figure S3.12A). Upon the addition of intermediate (15 μM) and saturating (1 mM) glutamate concentrations and in the presence of 5 μM MNI-137, occupancy of intermediate states 1 and 2 substantially increased with minimal change in the active conformation observed (Figure 3.4B-D, S3.11, Table 3.3). To examine which specific state transitions are being hindered by MNI-137, we performed Hidden Markov modeling analysis on the smFRET time traces. Examination of the transition density plots (TDPs) obtained from this analysis showed that at 1mM glutamate alone the dominant transitions occur between intermediate state 2 and the active conformation for the CRD (Figure 3.4E). This is consistent with the intermediate state 2 being the "pre-active" conformation (Liauw et al., 2021). In contrast, in the presence of both 1 mM glutamate and MNI-137, the CRD primarily transitions between intermediate states 1 and 2, with few transitions to the active state. This suggests that MNI-137 effectively prevents the formation of the stabilizing 7TM domain interaction necessary for mGluR2 activation. Together, these results

directly show that MNI-137 prevents receptor activation by blocking the last step towards receptor activation and effectively trapping the receptor in constant transition between the existing intermediate states.

Interestingly, examination of the CRD dynamics by cross-correlation analysis revealed that the effect of MNI-137 on receptor dynamics is dependent on whether glutamate is present or not. In the absence of glutamate, MNI-137 reduced CRD dynamics (Figure S3.11A). In contrast, when glutamate and MNI-137 were both present, we observed a glutamate concentration-dependent increase in the CRD dynamics (Figure 3.4F). This effect is the opposite to the effect of BINA, a PAM (Figure 3.3I, S3.12B). Thus, in addition to impeding progression of the CRD to the active conformation, MNI-137 also effectively prevents glutamate-induced stabilization of the 7TM domain. Together, these results provide a mechanistic understanding of how MNI-137, a NAM, can block receptor activation. This reduction of CRD stability and blocking of entry into the active conformation also provides insight into why glutamate-induced conformational change can still be observed, both in live-cell and single-molecule imaging, despite the presence of inhibiting MNI-137 concentrations. Finally, the mechanisms of action for both MNI-137 and BINA highlights the importance of structural dynamics for mGluR activation and modulation.

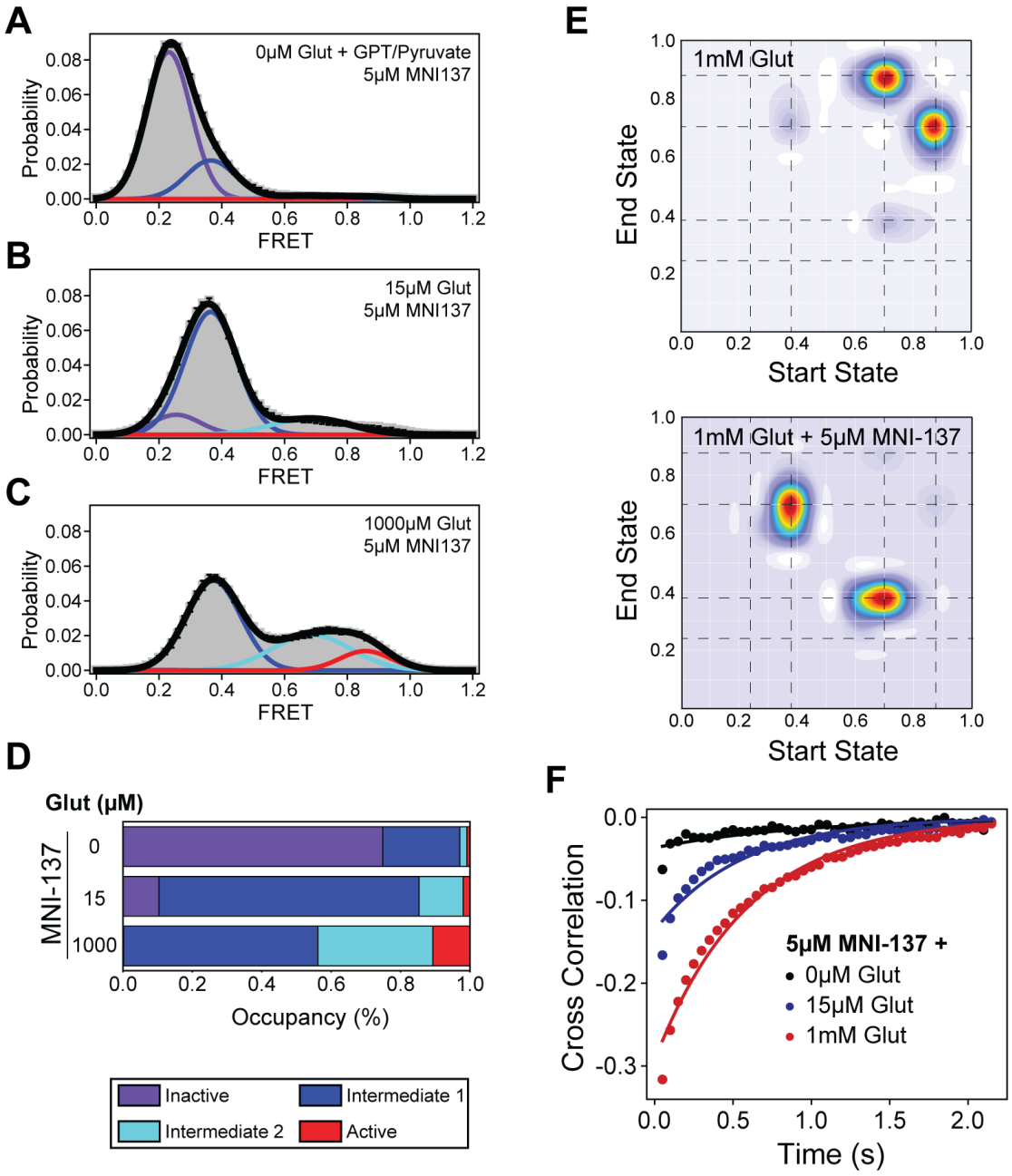

Figure 3.4 smFRET analysis of MNI-137 effects on CRD conformational dynamics
(A-C) smFRET population histograms of azi-CRD sensor in the presence of 0 μM (372 particles), 15 μM (560 particles), and 1 mM (479 particles) glutamate and 5 μM MNI-137. Histograms were fitted (black) to four Gaussian distributions centered around 0.24 (inactive; purple), 0.38 (intermediate 1; blue), 0.70 (intermediate 2; cyan), and 0.87 (active; red) FRET. Error bars represent s.e.m. (D) Mean occupancy of four conformational states of azi-CRD in varying ligand conditions. Values represent area under each FRET peak from smFRET histogram as a fraction of total area. Mean and s.e.m. values are reported in Table 3. (E) Transition density plots of azi-CRD

at 1 mM glutamate with and without MNI-137. Dashed lines represent four distinct FRET states. (F) Mean cross-correlation of donor and acceptor intensities in the presence of 0 μM, 15 μM, and 1 mM glutamate and 5 μM MNI-137. Data was acquired at 50 ms time resolution. Data represents mean from three independent experiments.

3.4 Discussion

A fundamental design principle for many receptors is that activation is allosteric in nature. Moreover, ligand "sensing" and receptor activation is driven by the energy from ligand binding and cellular energy cost in the form of ATP or GTP hydrolysis occurs after sensing and receptor activation. In GPCRs, activation involves conformational coupling between the ligand binding domain and the G protein binding interface. Recent experiments have shown that GPCRs are dynamic (Nygaard et al., 2013b) and undergo transition between multiple conformational states, including multiple intermediate states. For class A GPCRs, studies using conformational biosensors based on nuclear magnetic resonance (NMR) spectroscopy (Huang et al., 2021), double electron-electron resonance (DEER) spectroscopy (Wingler et al., 2019b), smFRET (Gregorio et al., 2017b), and fluorescent enhancement (Wei et al., 2022) have revealed the importance of conformational dynamics for receptor activation, ligand efficacy, and biased signaling. Specifically, activation of mGluRs involves coordinated movement between three structural domains. In this case, local conformational changes result in major conformational rearrangement that propagate from the ligand binding site to the active site, consistent with the "domino" model of allosteric signal transduction. Within this framework, allosteric modulators act on sites that are distinct from the orthosteric ligand binding site and affect the function of the receptor. Due to their potential to achieve subtype specificity, allosteric modulators have become a major focus for drug development. Common physiological characterization of GPCR allosteric modulators is often

pathway specific and rely on the use of functional assays that quantify the output of the receptor along the signaling cascade. In this work we aimed to develop a receptor-centric view of allosteric modulation by quantifying the relationship between allosteric modulation and protein structural dynamics. Potential sources of heterogeneity arising from differences in post-translational modifications or differences in the local lipid environment, may affect receptor conformation. Therefore, our results represent the average of a heterogeneous population of such receptors. We identified the *in vivo* conformational fingerprint of multiple allosteric modulators of mGluR2 at three structural domains by using novel non-perturbing FRET sensors. This *in vivo* approach established a direct connection between the effect of allosteric modulators on receptor conformation at each domain and the physiological metrics of the modulator (i.e., efficacy and potency). Specifically, we found that modulators consistently affect the general trend of glutamate-induced conformational change underlying activation at every structural domain of mGluR2 (Figure 3.2). This result demonstrates the existence of a long-range allosteric pathway along the receptor and over a 10 nm distance. Interestingly, for the same modulator, the degree of conformational change was different among different domains (Figure 3.2J). In fact, we determined that the CRD and 7TM domain conformations are more accurate predictors of ligand efficacy as compared to the VFT domain conformation.

Previous research showed that the activation of mGluR2 is a stepwise process with transitions between four states, including two intermediate states (Liauw et al., 2021). Our smFRET analysis with a PAM and NAM showed that allosteric modulators do not induce a new conformational state, within the resolution of smFRET measurements. Instead, they produce their modulatory effect by employing the inherent conformational flexibility of receptors to modify receptor

occupancy of the intermediate states. In the case of the PAM, BINA increases the efficacy and potency of glutamate by increasing the transitions from the intermediate state to the active state (Figure 3.3). On the other hand, previous work had shown that the mGluR2 NAM MNI-137 can block receptor signaling. Our analysis provides a mechanism for this observation where MNI-137 blocks entry into the active conformation and increases the transitions into the intermediate states, thereby increasing the occupancy of the intermediate states (Figure 3.4). As a result, the receptor is effectively trapped in the intermediate states. Further studies are necessary to determine the atomic structure of these intermediate states. Interestingly, the regulation of intermediate state occupancy has recently been shown to be a mechanism of allosteric modulation for other classes of GPCRs as well. NMR studies on the μ-opioid receptor (Kaneko et al., 2022) and cannabinoid receptor 1 (Wang et al., 2021) revealed that PAMs and NAMs regulate receptor function by acting on intermediate conformations in a manner similar to our findings for BINA and MNI-137. Collectively, these results suggest that designing compounds that regulate intermediate state occupancy is a plausible strategy for the development of allosteric modulators for mGluR2 and other families of GPCRs.

Protein allostery is intimately related to protein dynamics. Our results show that the effect of modulator binding at the 7TM domain on the receptor dynamics probed at the CRD, depends on the orthosteric agonist. In the absence of an orthosteric agonist, NAM stabilize the overall receptor dynamics while PAM increase receptor dynamics (Figure S3.12A). On the other hand, in the presence of saturating agonist, the PAM reduced receptor dynamics while the NAM increased receptor dynamics (Figure S3.12B). These results further highlight the roles of conformational dynamics in allosteric regulation.

In summary, our study provides a conformational fingerprint of diverse allosteric modulators of mGluR2 at different domains of the receptor. Classically receptors were thought of as two-state switches undergoing transition between on and off states. However, it is now clear that GPCRs' ability to dynamically sample a repertoire of conformations is central to their overall function. Our findings highlight the significance of intermediate states in GPCRs for receptor modulation. Furthermore, our findings suggest that designing compounds that modulate the stability of intermediate states could be a promising direction for developing allosteric drugs. The tools we developed and applied here are not limited to mGluRs and can be extended to the study of other complex multi-domain proteins.

3.5 Materials and Methods

3.5.1 Molecular cloning

The C-terminal FLAG-tagged mouse mGluR2 construct in pcDNA3.1(+) expression vector was purchased from GenScript (ORF clone: OMu19627D) and verified by sequencing (ACGT Inc). Full length mGluR2 construct with an amber codon (TAG) mutation of amino acid A548 (azi-CRD) or N-terminal SNAP-tag (SNAP-mGluR2) were generated as previously reported (Liauw et al., 2021). The insertion of an amber codon (TAG) between E715 and V716 in mGluR2 (azi-ECL2) was performed using the QuikChange site-directed mutagenesis kit (Agilent). SNAP-mGluR2 constructs used for calcium imaging had C-terminal FLAG-tag removed by PCR-based deletion using phosphorylated primers. All plasmids were sequence verified (ACGT Inc). DNA restriction enzymes, DNA polymerase and DNA ligase were from New England Biolabs. Plasmid preparation kits were purchased from Macherey-Nagel.

3.5.2 Cell culture

HEK293T cells (Sigma) were authenticated (ATCC) and tested for mycoplasma contamination (Lonza). HEK293T cells were maintained in DMEM (Corning) supplemented with 10% (v/v) fetal bovine serum (Fisher Scientific), 100 unit/mL penicillin-streptomycin (Gibco) and 15 mM HEPES (pH=7.4, Gibco) at 37 °C and 5% CO_2. The cells were passaged with 0.05% trypsin-EDTA (Gibco). For unnatural amino acid-containing protein expression, the growth media was supplemented with 0.6 mM 4-azido-L-phenylalanine (Chem-Impex International). All media was filtered by 0.2 μM PES filter (Fisher Scientific).

3.5.3 Transfection and Protein Expression

24 hours before transfection, HEK293T cells were cultured on poly-L-lysine-coated 18 mm glass coverslips (VWR). For SNAP-mGluR2 used in FRET experiments, media was refreshed with standard growth media and transfected using Lipofectamine 3000 (Fisher Scientific) (total plasmid: 1 μg/18 mm coverslip). Growth media was refreshed after 24 hours and cells were grown for an additional 24 hours.

For unnatural amino acid-containing protein expression, one hour before transfection, media was changed to the growth media supplemented with 0.6 mM 4-azido-L-phenylalanine. mGluR2 plasmids with an amber codon (azi-CRD or azi-ECL2) and pIRE4-Azi plasmid (pIRE4-Azi was a gift from Irene Coin, Addgene plasmid # 105829) were co-transfected (1:1 w/w) into cells using Lipofectamine 3000 (Fisher Scientific) (total plasmid: 2 μg/18 mm coverslip). The growth media containing 0.6 mM 4-azido-L-phenylalanine was refreshed after 24 hours and cells were grown for an additional 24 hours. On the day of the experiment, 30 minutes before labeling, supplemented growth media was removed and cells were washed by extracellular buffer solution containing (in

mM): 128 NaCl, 2 KCl, 2.5 $CaCl_2$, 1.2 $MgCl_2$, 10 sucrose, 10 HEPES, pH=7.4 and were kept in growth medium without 4-azido-L-phenylalanine.

For calcium imaging experiments, media was refreshed with standard growth media and cells were co-transfected with SNAP-mGluR2 (no FLAG-tag) and chimeric G protein (Gqo5, Addgene plasmid #24500) (1:2 w/w) using Lipofectamine 3000 (Fisher Scientific) (total plasmid: 1.5 µg/18 mm coverslip). For calcium imaging using unnatural amino acid containing proteins (azi-CRD or azi-ECL2), we followed the transfection and growth protocol described above and included an additional 1 µg of chimeric G protein (Gqo5). Growth media was refreshed after 24 hours, and cells were grown for an additional 24 hours. Before the addition of labeling solutions, cells were washed with extracellular buffer solution.

3.5.4 SNAP-tag labeling for FRET measurements

SNAP-tag labeling of SNAP-mGluR2 was done by incubating cells with 2 µM of SNAP-Surface Alexa Fluor 549 (NEB) and 2 µM of SNAP-Surface Alexa Fluor 647 (NEB) in extracellular buffer for 30 minutes at 37 °C. After labelling, cells were washed by extracellular buffer solution to remove excess dye.

3.5.5 Unnatural amino acid labeling by azide-alkyne click chemistry

Unnatural amino acid labeling by azide-alkyne click chemistry was performed as previously reported (Liauw et al., 2021). Stock solutions were made as follows: Cy3 and Cy5 alkyne dyes (Click Chemistry Tools) 10 mM in DMSO, BTTES (Click Chemistry Tools) 50 mM, copper (II) sulfate (Sigma) 20 mM, aminoguanidine (Cayman Chemical) 100 mM, and (+)-sodium L-ascorbate (Sigma) 100 mM in ultrapure distilled water (Invitrogen). In 656 µL of extracellular buffer solution, Cy3 and Cy5 alkyne dyes were mixed to a final concentration of 18 µM for each

dye. To this mixture, a fresh pre-mixed solution of copper (II) sulfate and BTTES (1:5 molar ratio) was added at the final concentration of 150 µM and 750 µM, respectively. Next, aminoguanidine was added to the final concentration of 1.25 mM. Lastly, (+)-sodium L-ascorbate was added to the mixture to a final concentration of 2.5 mM. Total labeling volume was 0.7 mL. The labeling mixture was incubated at 4 °C for 8 minutes, followed by a 2 minute incubation at room temperature before addition to cells. Cells were washed with extracellular buffer solution prior to addition of labeling mixture. During labeling, cells were kept in the dark at 37 °C and 5% CO_2. After 10 minutes, L-glutamate (Sigma) was added to the cells to a final concentration of 0.5 mM and cells were incubated for an additional 5 minutes. After labelling, cells were washed by the extracellular buffer solution to remove excess dye.

3.5.6 Labeling for calcium imaging

Cells used for calcium imaging experiments were labeled using 1 µM SNAP-Surface Alexa Fluor 647 (NEB) and 4 µM Oregon Green 488 BAPTA-1 (Fisher Scientific) in extracellular buffer for 30 minutes at 37 °C. For cells expressing unnatural amino acid containing proteins, we labeled the cells with 4 µM Oregon Green 488 BAPTA-1. After labelling, cells were washed by extracellular buffer solution to remove excess dye.

3.5.7 Live-cell FRET measurements

The microscope and flow system setup used were as previously reported (Liauw et al., 2021). After labeling, coverslip was assembled in the flow chamber (Innova Plex) and attached to a gravity flow control system (ALA Scientific Instruments). Extracellular buffer solution was used as imaging buffer and applied at the rate of 5 ml min^{-1}. Labeled cells were imaged on a home-built microscope equipped with a ×20 objective (Olympus, oil-immersion) and using an excitation filter

set with a quad-edge dichroic mirror (Di03-R405/488/532/635, Semrock) and a long-pass filter (ET542lp, Chroma). All data were recorded at 4.5 second time resolution for unnatural amino acid containing constructs and 4 seconds for SNAP-tag containing constructs. All experiments were performed at room temperature. Donor fluorophores were excited with a 532 nm laser (RPMC Lasers) and emissions from donor and acceptor fluorophores were simultaneously recorded.

Analysis of live-cell FRET data was performed using smCamera (http://ha.med.jhmi.edu/resources/), ImageJ (http://imagej.nih.gov/ij/), and OriginPro (OriginLab). Movies were corrected for bleed-through of the donor signal into the acceptor channel. Donor bleed-through correction was done by measuring signals from 50 ROIs of Cy3 labeled cells in both the donor and acceptor channels and was calculated to be 8.8%. ROIs used for analysis included the whole cell membrane for individual cells. Apparent FRET efficiency was calculated as FRET=($I_A - 0.088\times I_D$) / ($I_D + (I_A - 0.088\times I_D)$), where I_D and I_A are the donor and acceptor intensity after buffer-only background subtraction. ΔFRET was calculated as the difference between FRET signal during treatment condition and FRET signal before treatment. In each case, the fluorescence was averaged over 6 datapoints once the signal was stable. Dose-response equation $y(x) = A1 + \frac{A_2 - A_1}{1+10^{(\log x_0 - x)P}}$ was used for fitting FRET response to calculate EC_{50} values, where A1 is the lower asymptote, A2 is the upper asymptote, P is the Hill slope, and x_0 is the EC_{50}. Maximal responses were normalized to 1 mM glutamate response. All data is from at least three independent biological replicates.

As analysis was limited to relative FRET changes between drug treatments rather than absolute FRET values, no further corrections, aside from the 8.8% bleed-through subtraction, were applied. A small artifact in Cy3 signal (decrease in fluorescence) was observed in response to modulator

application for donor-only labeled cells. However, this response showed the same relative amplitude and kinetics as FRET responses and were similar among all modulators tested, thus, was not corrected for. All analyzed FRET changes were verified showing anti-correlated behavior. Furthermore, analysis of acceptor signal in response to different modulator treatment qualitatively recapitulated results of FRET data.

3.5.8 Calcium imaging

After labeling, sample was assembled in the flow chamber (Innova Plex) and attached to the flow control system (ALA Scientific Instruments) in an identical manner to live-cell FRET experiments. Labeled cells were imaged using an inverted confocal microscope (Zeiss, LSM-800) with a ×40 oil-immersion objective (Plan-Apochromat ×40/1.3oil DIC(UV) VIS-IR M27). Sample was illuminated using a 488 nm laser and fluorescence from Oregon Green 488 was measured by a GaAsP-PMT detector with detection wavelengths set to 410-617 nm. For cells expressing SNAP-mGluR2 (no FLAG-tag), samples were excited using the 488 nm laser and a 640 nm laser simultaneously, and Cy5 fluorescence was measured with detection wavelengths set to 648-700 nm. All calcium imaging data were recorded at 3 second time resolution and at room temperature. Analysis of functional calcium imaging data was performed using ImageJ (http://imagej.nih.gov/ij/) and OriginPro (OriginLab). All cells showing agonist-induced calcium response were selected for initial analysis, with those showing significant drift or photobleaching being omitted from downstream analysis. Fluorescence signal was measured for individual cells from a given movie, normalized from 0 to 1, and averaged. Changes in calcium signal were calculated from these averaged responses as the difference between max response during treatment and response before treatment. Baseline signal intensity was the average over 6 datapoints prior to

treatment application. Dose-response equation $y(x) = A1 + \frac{A_2 - A_1}{1+10^{(\log x_0 - x)P}}$ was used for fitting calcium response to calculate EC_{50} values, where *A1* is the lower asymptote, *A2* is the upper asymptote, *P* is the Hill slope, and x_0 is the EC_{50}. Maximal responses were calculated as a fraction of 10 μM ionomycin-induced response, then normalized to 1 mM glutamate response. Direct activation of mGluR2 and subsequent intracellular calcium flux caused by the positive allosteric modulators LY487379 and JNJ-42153605 precluded analysis of the compounds ability to affect glutamate potency and efficacy. All data are from three independent biological replicates.

3.5.9 Single-molecule FRET measurements

Single-molecule experiments were conducted using custom flow cells prepared from glass coverslips (VWR) and slides (Fisher Scientific) passivated with mPEG (Laysan Bio) and 1% (w/w) biotin-PEG to prevent unspecific protein adsorption, as previously described (Vafabakhsh et al., 2015; Jain et al., 2011). Prior to experiments, flow cells were functionalized with FLAG-tag antibody. This was achieved by first incubating flow cells with 500 nM NeutrAvidin (Fisher Scientific) for 2 minutes followed by 20 μM biotinylated FLAG-tag antibody (A01429, GenScript) for 30 minutes. Unbound NeutrAvidin and biotinylated FLAG-tag antibody were removed by washing between each incubation step. Washes and protein dilutions were done using T50 buffer (50 mM NaCl, 10 mM Tris, pH 7.4).

After labeling, cells were recovered from an 18 mm poly-L-lysine coverslip by incubating with Ca^{2+}-free DPBS followed by a gentle pipetting. Cells were then pelleted by a 4000 *g* centrifugation at 4 °C for 10 minutes. The supernatant was removed and cells were resuspended in 100 μL lysis buffer consisting of 200 mM NaCl, 50 mM HEPES, 1 mM EDTA, protease inhibitor tablet (Fisher Scientific), and 0.1 w/v% LMNG-CHS (10:1, Anatrace), pH 7.4. Cells were allowed to lyse with

gentle mixing at 4 °C for 1 hour. Cell lysate was then centrifuged for 20 min at 20,000 *g* and 4 °C. The supernatant was collected and immediately diluted 10-fold with dilution buffer consisting of 200 mM NaCl, 50 mM HEPES, 1 mM EDTA, protease inhibitor tablet, and 0.0004 w/v% GDN (Anatrace), pH 7.4. The diluted sample was then added to the flow chamber to achieve sparse surface immobilization of labeled receptors by their C-terminal FLAG-tag. After optimal receptor coverage was achieved, flow chamber was washed extensively (> 20× chamber volume) to remove unbound proteins and excess detergent with wash buffer consisting of 200 mM NaCl, 50 mM HEPES, 0.005 w/v% LMNG-CHS (10:1, Anatrace), and 0.0004 w/v% GDN, pH 7.4. Finally, labeled receptors were imaged in imaging buffer consisting of (in mM) 128 NaCl, 2 KCl, 2.5 $CaCl_2$, 1.2 $MgCl_2$, 40 HEPES, 4 Trolox, 0.005 w/v% LMNG-CHS (10:1), 0.0004 w/v% GDN, and an oxygen scavenging system consisting of protocatechuic acid (Sigma) and 1.6 U/mL bacterial protocatechuate 3,4-dioxygenase (rPCO) (Oriental Yeast Co.), pH 7.35. For glutamate-free conditions, imaging buffer contained 2 U/mL glutamic-pyruvic transaminase (Sigma) and 2 mM sodium pyruvate (Gibco) and was incubated at 37 °C for 10 minutes. All reagents were prepared from ultrapure-grade chemicals (purity > 99.99%) and were purchased from Sigma. All buffers were made using ultrapure distilled water (Invitrogen). Samples were imaged with a 100× objective (Olympus, 1.49 NA, Oil-immersion) on a custom-built microscope with 50 ms time resolution unless stated otherwise. 532 nm and 638 nm lasers (RPMC Lasers) were used for donor and acceptor excitation, respectively.

3.5.10 smFRET data analysis

Analysis of single-molecule fluorescence data was performed using smCamera (http://ha.med.jhmi.edu/resources/), custom MATLAB (MathWorks) scripts, and OriginPro

(OriginLab). Particle selection and generation of raw FRET traces were done automatically within the smCamera software. For the selection, particles that showed acceptor signal upon donor excitation, with acceptor brightness greater than 10% above background and had a Gaussian intensity profile, were automatically selected and donor and acceptor intensities were measured over all frames. Out of this pool, particles that showed a single donor and a single acceptor bleaching step during the acquisition time, stable total intensity ($I_D + I_A$), anti-correlated donor and acceptor intensity behavior without blinking events, and lasted for more than 4 seconds were manually selected for further analysis (~20-30% of total molecules per movie). All data was analyzed by three individuals independently and the results were compared and showed to be identical. In addition, a subset of data was blindly analyzed to ensure no bias in analysis. Apparent FRET efficiency was calculated as $(I_A - 0.088 \times I_D) / (I_D + (I_A - 0.088 \times I_D))$, where I_D and I_A are raw donor and acceptor intensities, respectively. Experiments were conducted on three independent biological replicates, to ensure reproducibility of the results. Population smFRET histograms were generated by compiling at least 250 total FRET traces of individual molecules from all replicates. Before compiling traces, FRET histograms of individual molecules were normalized to 1 to ensure that each trace contributes equally, regardless of trace length. Error bars on histograms represent the standard error of data from three independent biological replicates.

Peak fitting analysis on population smFRET histograms was performed with OriginPro and used four Gaussian distributions as $y(x) = \sum_{i=1}^{4} \frac{A_i}{w_i\sqrt{\frac{\pi}{2}}} e^{-2\frac{(x-xc_i)^2}{w_i^2}}$,where *A* is the peak area, *w* is the peak width, and *xc* is the peak center. Peak areas were constrained to $A > 0$. Peak widths were constrained to $0.1 \leq w \leq 0.25$. Peak centers were constrained to ± 0.015 of mean FRET efficiency

of each conformational state. The mean FRET efficiencies of the inactive state, intermediate state 1, intermediate state 2, and the active state were assigned to 0.24, 0.38, 0.70, and 0.87, respectively, based on the most common FRET states observed in transition density plots. This analysis is described in further detail below. State occupancy probability was calculated as area of specified peak relative to total area, which is defined as the sum of all four individual peak areas.

Raw donor, acceptor, and FRET traces were idealized with a hidden Markov model (HMM) using vbFRET software (Zhang et al., 2018; Bronson et al., 2009b). Transitions, defined as ΔFRET > 0.1, were extracted from idealized fits and used to generate transition density plots. In situations where the HMM fit does not converge to the data (for example, due to long fluorophore blinking events

or large non-anticorrelated intensity fluctuations), traces were omitted from downstream analysis. The cross-correlation (CC) of donor and acceptor intensity traces at time τ is defined as $CC(\tau) = \frac{\delta I_D(t)\delta I_A(t+\tau)}{<I_D(t)>+<I_A(t)>}$, where $\delta I_D(t) = I_D(t) - < I_D(t) >$, and $\delta I_A(t) = I_A(t) - < I_A(t) >$. $< I_D(t) >$ and $< I_A(t) >$ are time average donor and acceptor intensities, respectively. Cross-correlation calculations were performed on the same traces used to generate the histograms and fit to a single exponential function, $y(x) = Ae^{\frac{-x}{\tau}} + y_0$.

3.5.11 Structural representation of allosteric binding site by Chimera

Pairwise sequence alignment for PDB:7MTS, 7MTR, 7E9G, 7EPE, and 7EPF was performed using PDB:7MTS as the reference sequence. Alignment was based on best-aligning pair of chains and used the Needleman-Wunsch alignment algorithm. Unbound subunits and extracellular domains of mGluR2 were excluded prior to structure alignment. Specifically, residues L556-I816

(PDB: 7MTS, 7MTR, 7E9G) and G564-V825 (PDB:7EPE and 7EPF) were used for alignment. Allosteric pocket forming residues are from interacting residues in PDB:7MTS and previous mutagenesis studies (Seven et al., 2021; Farinha et al., 2015).

3.5.12 Data availability

All data generated or analyzed during this study are included in the manuscript and supporting files. The PDB accession codes for human mGluR2 structures used are 7MTS, 7MTR, 7E9G, 7EPE, and 7EPF.

3.6 Acknowledgements

We thank all members of the Reza Lab for thoughtful discussions and J. Fei (University of Chicago) for providing MATLAB scripts. This work was supported by the National Institutes of Health grant R01GM140272 (to R.V.) and by The Searle Leadership Fund for the Life Sciences at Northwestern University and by the Chicago Biomedical Consortium with support from the Searle Funds at The Chicago Community Trust (to R.V.). B.W.L. was supported in part by the National Institute of General Medical Sciences (NIGMS) Training Grant T32GM-008061.

Chapter 4: Characterizing modulatory effects of lipids and detergents on mGluR2

The following people acquired and analyzed data used in this chapter:

Chiranjib Banerjee, PhD: Figures 4.3, 4.4, 4.6, 4.7, 4.8, 4.9

4.1 Introduction

The lipid bilayer is a complex and heterogeneous environment that is essential for maintaining membrane protein integrity and native function (Ingólfsson et al., 2014). However, biophysical analysis of membrane proteins often requires their isolation and solubilization from the cellular environment. Thus, tools enabling membrane protein manipulation *in vitro*, such as detergents and membrane mimetics, have been developed and improved rapidly over time (Anandan & Vrielink, 2016). Although many of these tools have shown the ability to conserve native protein function, how they do so remains unclear.

Detergents primarily function to shield the hydrophobic domains of membrane proteins from the aqueous environment while serving as a scaffold that supports native-like protein function

(Anandan & Vrielink, 2016). Detergents can form micelles with a range of morphologies (Goyal & Aswal, 2001; Lichtenberg et al., 2013). The major parameters determining micelle morphology are detergent shape and packing ability, which is a function of detergent volume (v), hydrocarbon chain length (l), optimal area per molecule (a).

$$P = \frac{v}{l\,a}$$

These parameters are also important determinants of a detergent's ability to maintain protein integrity and function, as they dictate the degree of water penetration into the hydrophobic core of the protein and lateral pressure exerted by the micelle (Anglin & Conboy, 2008). Here, I examine the effects of three non-ionic detergents, that are commonly used in membrane protein biophysical studies, on the conformational dynamics of metabotropic glutamate receptor 2 (mGluR2).

I specifically focus on Dodecyl-ß-D-maltoside (DDM), Lauryl Maltose Neopentyl Glycol (LMNG), and Glyco-diosgenin (GDN) (VanAken et al., 1986; Chae et al., 2010; Chae et al., 2012) (Figure 4.1). DDM has functioned as the gold standard in membrane protein research for decades and is composed of a maltose headgroup and a single 12 carbon saturated alkyl tail (VanAken et al., 1986). While DDM has proven invaluable in structural and biophysical studies of a wide range of membrane proteins, its successful application to G protein-coupled receptors (GPCRs) is limited. In contrast, the two chain DDM analog, LMNG, has been essential in the structure determination and biophysical characterization of several GPCRs in recent years (Chae et al., 2010). This success is attributed to LMNG's two chain structure that shifts individual detergent molecules towards a cylindrical shape and increases the overall volume of the detergent (Anglin & Conboy, 2008; Bae et al., 2015). This more planar shape and increased volume results in reduced micelle curvature, increased lateral pressure, reduced detergent diffusion, and reduced solvent

penetration. Lastly, GDN is a synthetic digitonin derivative that possesses a di-maltose headgroup identical to LMNG and a steroidal moiety as the hydrophobic domain. Like LMNG, GDN has also shown recent success in the structure determination of GPCRs (Chae et al., 2012).

In addition to detergents, this chapter also aims to examine the effects of cholesterol on mGluR2 conformational dynamics. It has been established that cholesterol is important for the function of mGluRs and GPCRs in general. Previous studies on mGluR1 and the *drosophila* mGluR homolog (dmGluR) showed that cholesterol was essential for mGluR localization to lipid rafts and activation (Kumari et al., 2013; Eroglu et al., 2003). Further computational studies have also identified up to seven transient cholesterol interacting sites on mGluR2 (Kurth et al., 2020). In this chapter, I describe the direct effect of a cholesterol analog, cholesterol hemisuccinate (CHS), on mGluR2 structural dynamics to develop a receptor-centric understanding of cholesterol modulation (Figure 4.1). Moreover, this chapter will briefly discuss both detergent-dependent and concentration-dependent effects of cholesterol.

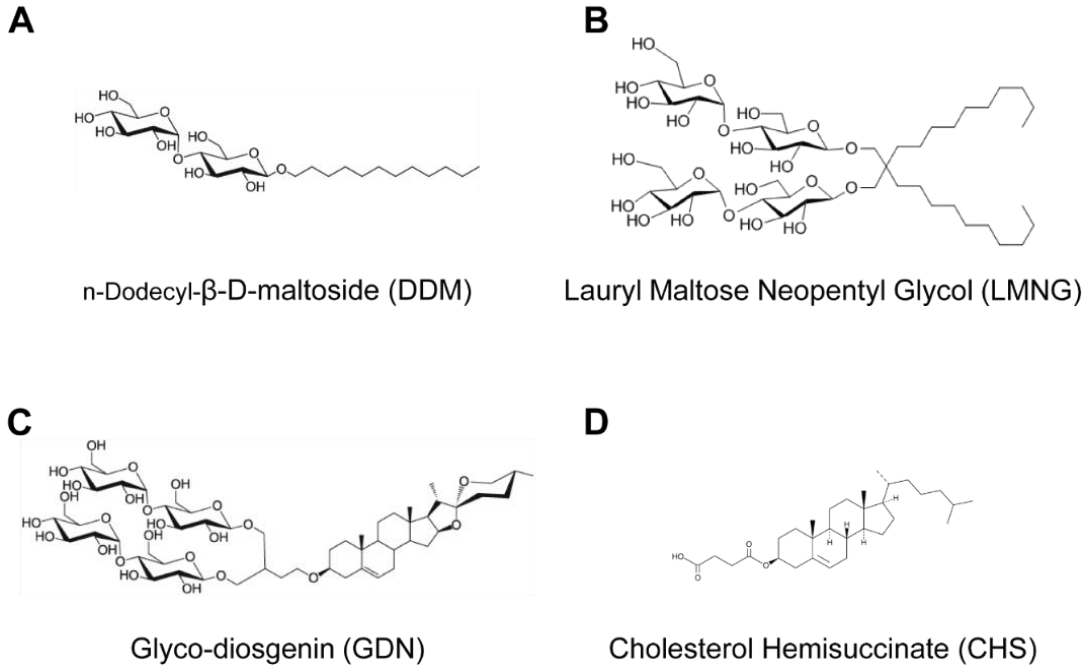

Figure 4.1 Solubilizing detergents and cholesterol analog
Structure of solubilizing detergents used in mGluR2 studies discussed in thesis that include (A) n-Dodecyl-ß-D-maltoside (DDM), (B) Lauryl Maltose Neopentyl Glycol (LMNG), (C) Glyco-diosgenin (GDN), and (D) Cholesterol Hemiscuccinate (CHS).

4.2 Results

4.2.1 Conformational dynamics of lipid solubilized mGluR2

smFRET experiments described in previous chapters examined detergent solubilized mGluR2. Although multiple detergent types yielded qualitatively similar results, whether the data accurately reflects the behavior of the mGluR2 CRD in the native lipidic environment is still unclear. To validate the conclusions drawn from detergent solubilized receptors, I examined lipid solubilized mGluR2 conformational dynamics using styrene maleic acid lipid particles (SMALPs). SMA is a self-assembling copolymer that spontaneously inserts into the plasma membrane to extract and solubilize receptors without detergents (S. C. Lee et al., 2016). SMA enables lipid solubilized

mGluR2 structural dynamics to be studied without the need for protein purification and reconstitution.

In the absence of glutamate, SMALP solubilized mGluR2 CRD sensor, azi-CRD, showed a broad conformational profile with a dominant peak at ~0.25 FRET (Figure 4.2A). This broad distribution is in agreement with the intrinsic dynamics observed for the CRDs in detergent solubilized mGluR2 (Liauw et al., 2021; Liauw et al., 2022). Upon stimulation with intermediate (10 μM) and saturating (1 mM) glutamate, the conformational distribution shifts towards higher FRET, aligned with the compaction of the CRD with receptor activation (Figure 4.2B-C). Furthermore, a dominant peak at ~0.90 FRET is observed at 1 mM glutamate conditions which is well aligned with the putative active conformation defined in previous chapters.

To test the integrity of the 7 transmembrane (7TM) domain, I treated SMALP solubilized mGluR2 with saturating (10 μM) positive allosteric modulator (PAM) BINA. In the absence of glutamate, BINA increases occupancy of higher FRET states with dominant peaks at ~0.70 and ~0.90 FRET (Figure 4.2A). This qualitatively matches the results for detergent solubilized mGluR2 reported in Chapter 3. The addition of BINA to intermediate (10 μM) and saturating (1 mM) glutamate also resulted in a general shift towards higher FRET relative to untreated conditions, again verifying BINA's ability to increase both glutamate potency and efficacy (Liauw et al., 2022) (Figure 4.2B-C). Collectively, the FRET profile of SMALP solubilized mGluR2 corroborate the conclusions drawn from detergent solubilized receptor data.

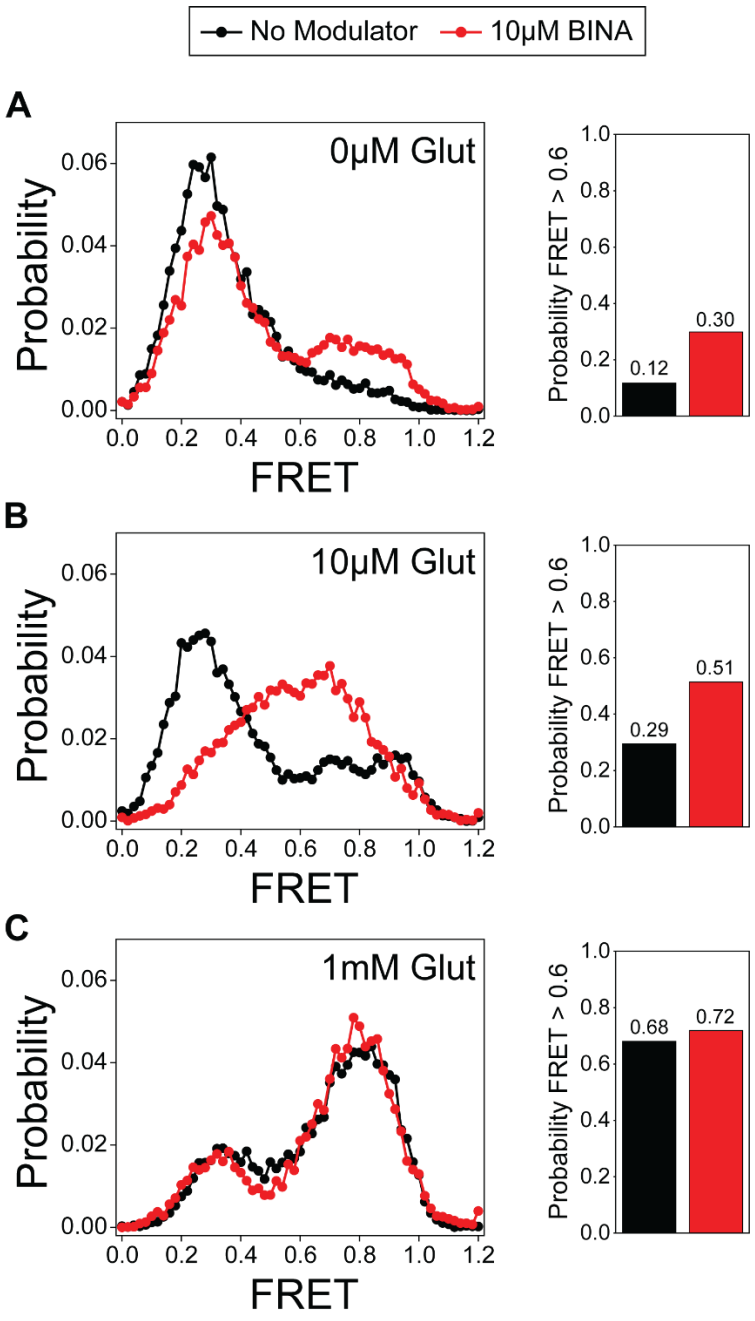

Figure 4.2 CRD conformation of SMALP solubilized mGluR2
SMALP solubilized azi-CRD conformational sensor demonstrates sensitivity to BINA and compaction in response to glutamate. Population smFRET histograms of azi-CRD in the presence of (A) no glutamate, (B) intermediate glutamate, and (C) saturating glutamate in the absence (black) or presence (red) of 10 μM BINA. Area under each histogram for FRET > 0.60 was calculated. Data was acquired at 50 ms time resolution. Data is from one independent experiment.

4.2.2 Detergent effects on mGluR2 structural dynamics

The choice of solubilizing detergent is an important decision when working with membrane proteins. Fortunately, there is a growing number of chemically diverse detergent options that can maintain the integrity and function of a wide range of proteins (Kotov et al., 2019). However, whether these detergents interact with and stabilize proteins in a similar manner is unclear. Here, I examine the effects of DDM, LMNG, and GDN solubilization on mGluR2 conformational dynamics.

In the presence of antagonist, azi-CRD shows a broad conformational distribution and dominant low FRET state when solubilized with each detergent (Figure 4.3A). However, GDN solubilized azi-CRD shows a substantially left shifted low FRET peak and general reduction in high FRET conformations relative to DDM and LMNG that are associated with receptor activation. This suggests that GDN may preferentially stabilize a less compact conformation of the CRD and may function as a negative allosteric modulator (NAM) of mGluR2. The NAM-like effect of GDN becomes more apparent at intermediate (10 μM) and saturating (1 mM) glutamate conditions (Figure 4.3B-C). While DDM and LMNG FRET profiles appear almost identical, demonstrating a gradual shift from low FRET to high FRET in a glutamate-dependent manner, GDN effectively prevents receptor compaction and entry into the active conformation defined as 0.89 FRET in Chapter 2.

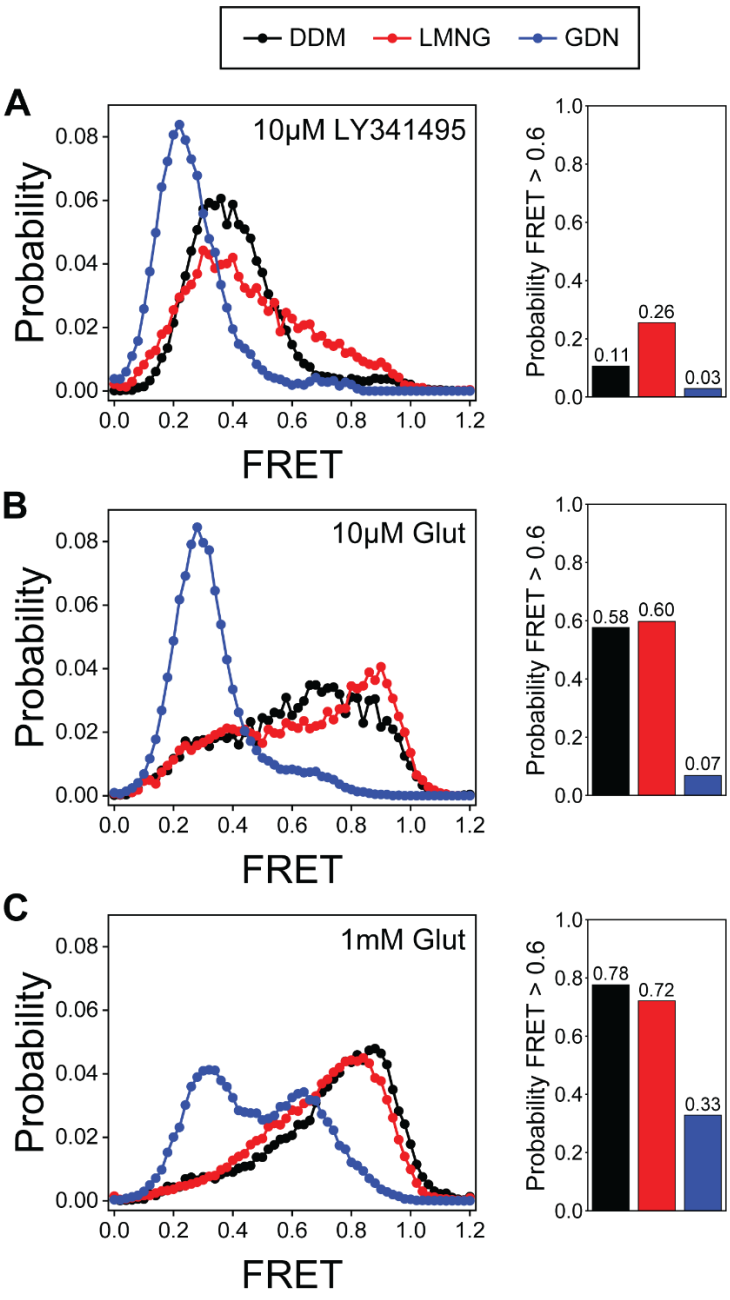

Figure 4.3 Detergent effects on CRD conformation
Detergents differentially modulate ligand-induced conformational change of the CRDs. Population smFRET histograms of the azi-CRD conformational sensor in the presence of (A) antagonist, (B) intermediate glutamate, and (C) saturating glutamate and DDM (black), LMNG (red), or GDN (blue). Area under each histogram for FRET > 0.60 was calculated. Data was acquired at 50 ms time resolution. Data is from one independent experiment.

Despite the separation of the ligand binding site from the 7TM domain, GDN's NAM effects extend to the VFT domains (Figure 4.4). In both inactive and active conditions, GDN solubilized VFT domain sensors, mGluR2 possessing N-terminal SNAP-tags (henceforth SNAP-m2), show reduced occupancy of lower FRET states associated with VFT domain closure, reorientation, and activation. Interestingly, active low FRET peak positions are well aligned among detergents while inactive peaks are more variable, suggesting a conserved active conformation and detergent-dependent inactive states.

Based on the similarity in conformational dynamics between DDM and LMNG solubilized mGluR2 FRET sensors, I hypothesized that these detergents would maintain receptor integrity and function with equal efficacy (Figure 4.3, 4.4). However, previous work that demonstrated DDM is unable to maintain mGluR2 function for extended periods while LMNG and GDN can (Cao et al., 2021). This discrepancy in conformational dynamics and receptor function raises questions regarding which detergent most accurately recapitulates the lipid environment. Comparison of each detergent sample with SMALP solubilized mGluR2 indicates that no detergent alone fully mimics the lipid environment (Figure 4.2).

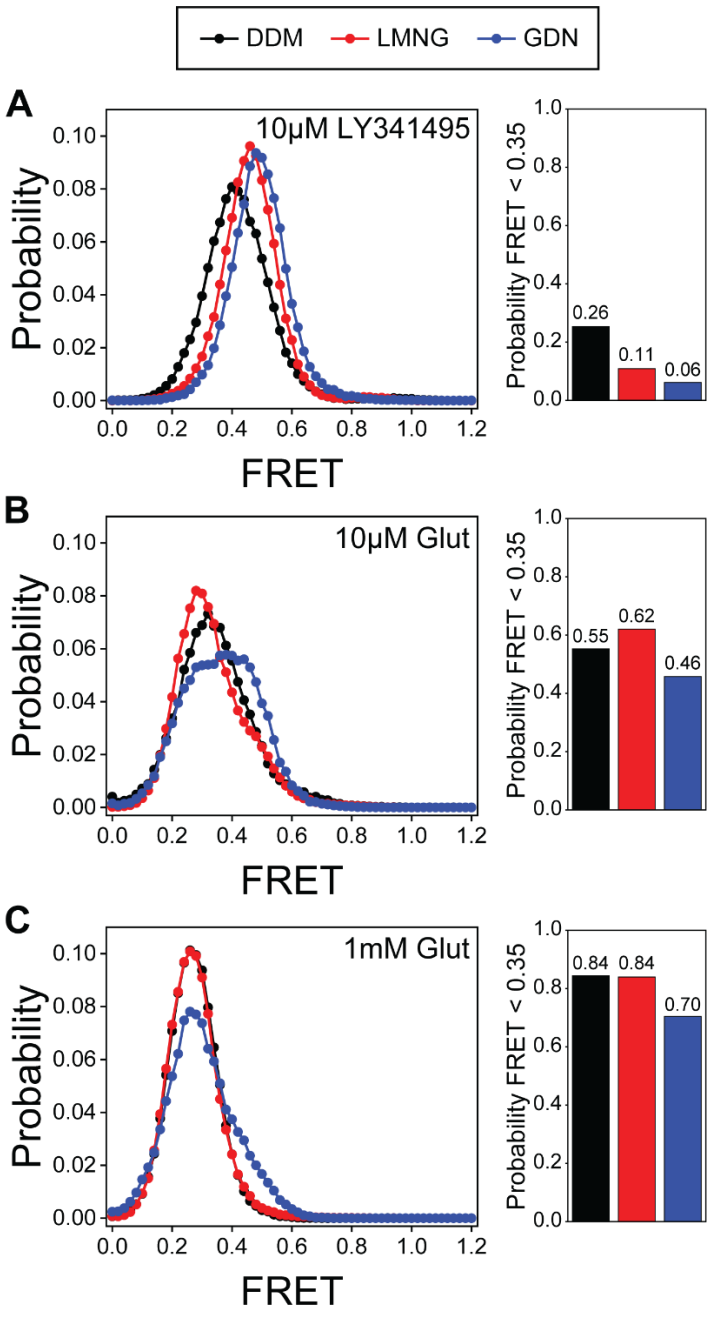

Figure 4.4 Detergent effects on VFT domain conformation
Detergents differentially modulate ligand-induced conformational change of the VFT domains. Population smFRET histograms of the SNAP-m2 conformational sensor in the presence of (A) antagonist, (B) intermediate glutamate, and (C) saturating glutamate and DDM (black), LMNG (red), or GDN (blue). Area under each histogram for FRET < 0.35 was calculated. Data was acquired at 50 ms time resolution. Data is from one independent experiment.

Detergents usefulness as tools for membrane protein biophysical studies make the determination of an optimized detergent mixture a worthwhile goal. To identify an optimized detergent mixture for mGluR smFRET studies, I conducted a GDN titration in the presence of fixed concentrations of LMNG and cholesterol hemisuccinate (CHS), a cholesterol analog (Figure 4.5). Generally, a left shift in the FRET distribution and reduction in high FRET conformations occurs in a GDN concentration-dependent manner. GDN effects are not apparent below 0.0004 w/v%. In contrast, at high concentrations, 0.005 w/v%, GDN effects become dominant with the FRET profile becoming GDN-like (Figure 4.3). The SMALP solubilized mGluR2 distribution was best recapitulated by the addition of 0.0004 w/v% GDN (Figure 4.2). Interestingly, 0.0004 w/v% GDN was the threshold concentration necessary for allosteric modulator binding to occur, providing further evidence for this optimized mixture's more native-like characteristics. Collectively, GDN-induced stabilization of the inactive conformation was an unexpected finding and illustrated how detergent choice can substantially affect results of biophysical studies.

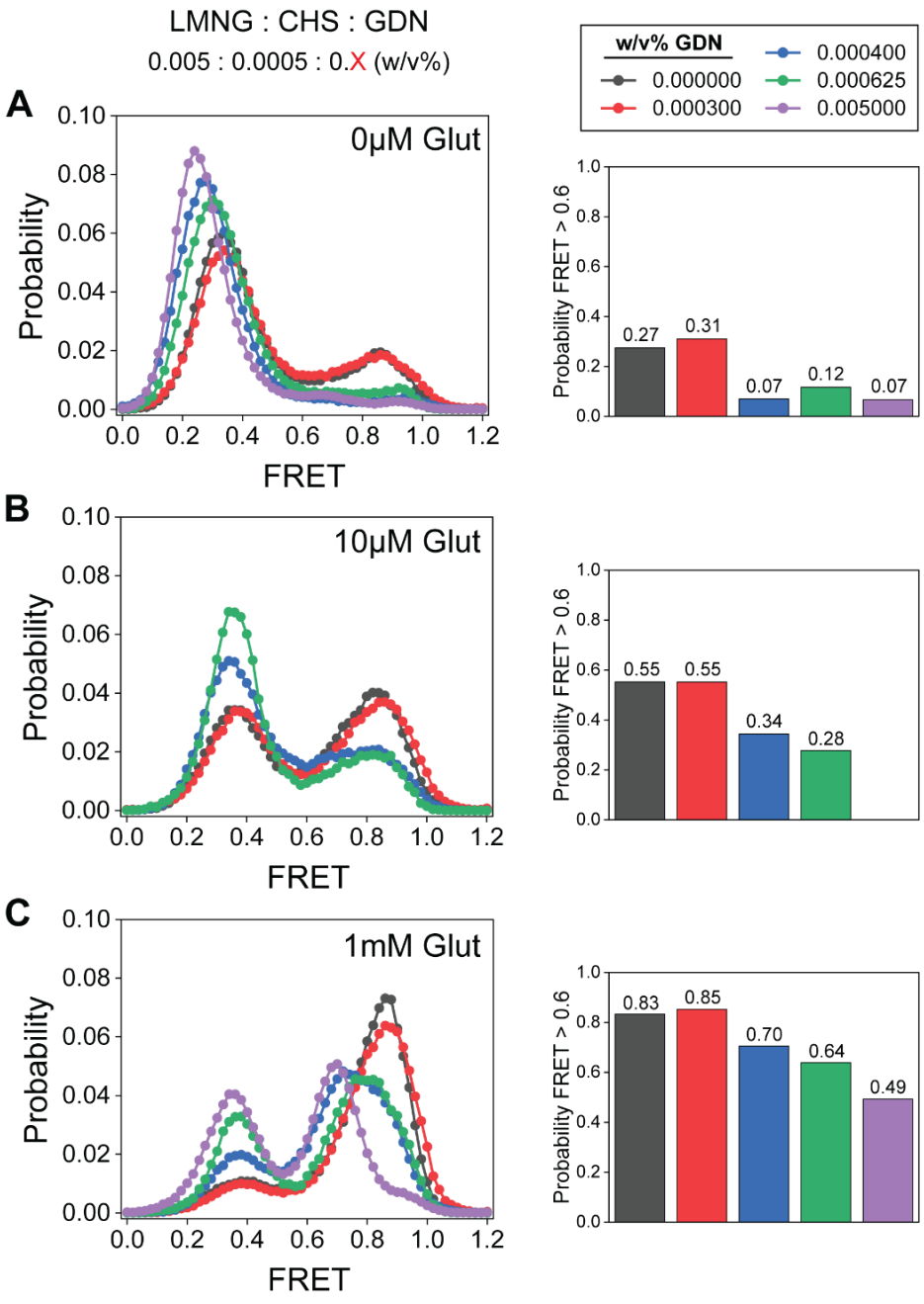

Figure 4.5 Optimized detergent mixture recapitulates lipid effects on CRD conformation
GDN titration on azi-CRD conformational sensor demonstrates its NAM function. Population smFRET histograms of the azi-CRD solubilized with LMNG, CHS, and variable concentrations of GDN in the presence of (A) no glutamate, (B) intermediate glutamate, and (C) saturating glutamate. Area under each histogram for FRET > 0.60 was calculated. Data was acquired at 50 ms time resolution. Data is from one independent experiment.

GDN's steroidal hydrophobic domain distinguishes it from DDM and LMNG (Figure 4.1). I next investigated whether the NAM-like effect of GDN was a conserved characteristic of sterols. I specifically focused on the effect of CHS on mGluR2 conformational dynamics. When solubilized by DDM, SNAP-m2 reported no substantial conformational difference in the presence (10:1 w/v% DDM:CHS) or absence of CHS when treated with antagonist, intermediate glutamate (10 μM), or saturating glutamate (1 mM) conditions (Figure 4.6A, C, E). In contrast, when adding CHS to LMNG solubilized mGluR2, the NAM-like effect is apparent, especially at intermediate (10 μM) and saturating (1 mM) glutamate conditions where the inactive peak at ~0.45 FRET is still pronounced (Figure 4.6B, D, F). This is aligned with previous findings that showed CHS to have no effect when solubilized with DDM (Cao et al., 2021).

The effect of CHS extends to the CRD as well. As with the VFT domain, the CRD conformation is nearly identical in the presence or absence of CHS when solubilized by DDM (Figure 4.7A, C, E). However, azi-CRD demonstrates a more complex phenotype when solubilized with LMNG and CHS, relative to the VFT domain. While a general left shift in the FRET profile occurs in the presence of LMNG and CHS (10:1 w/v%), a bimodal FRET distribution also emerges (Figure 4.7B, D, F). Interestingly, the dominant peaks are at FRET states associated with the ground inactive and active conformation previously defined in Chapter 2. This suggests that CHS does not simply impede receptor compaction but may modulate the energic profile in a way that disfavors intermediate conformations.

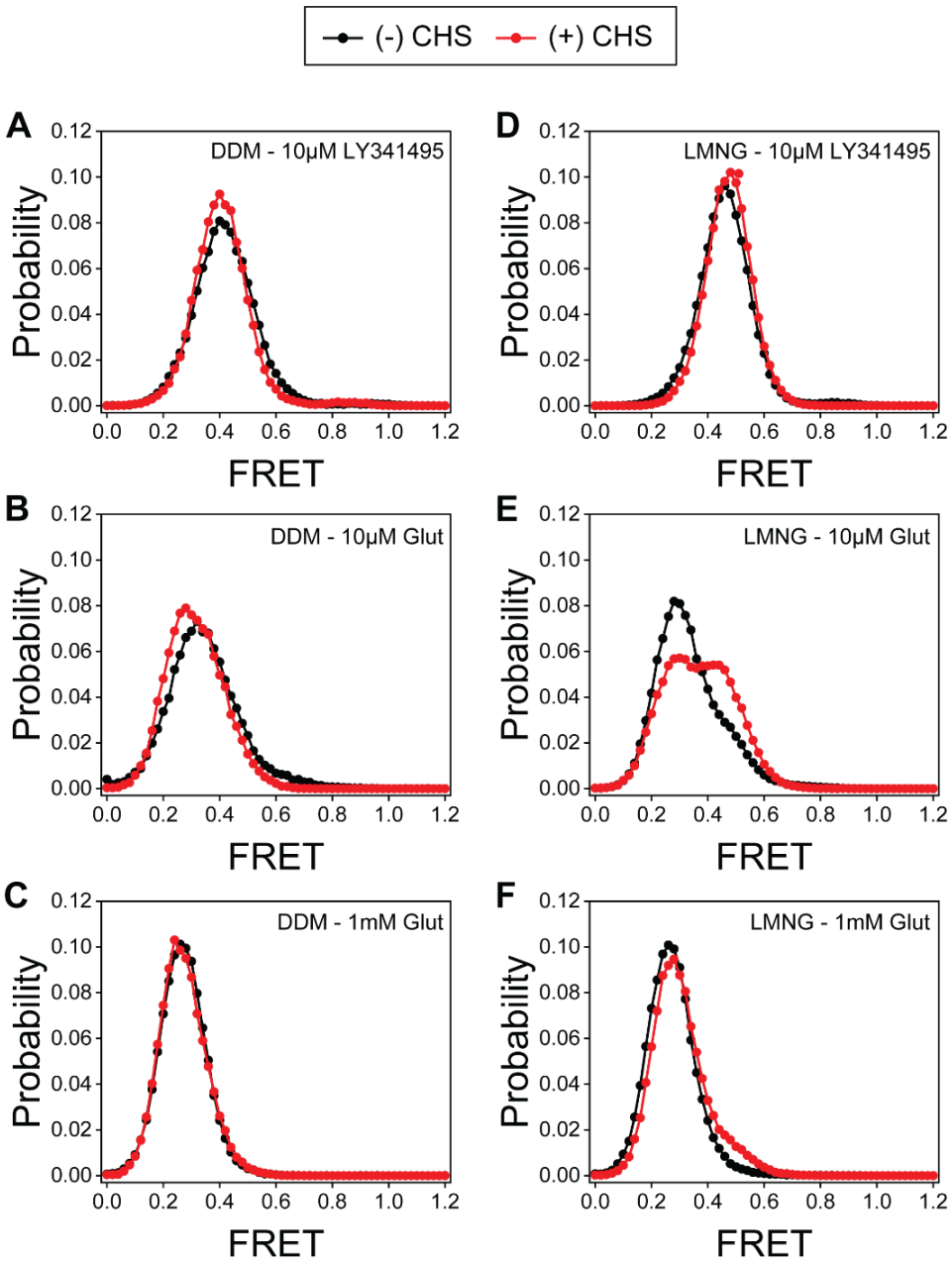

Figure 4.6 Cholesterol effects on VFT domain conformation
Cholesterol affects SNAP-m2 conformation in the presence of certain detergents. SNAP-m2 solubilized in (A-C) DDM or (D-F) LMNG with and without cholesterol (10:1 detergent: cholesterol w/v% ratio) and in the presence of (A,D) antagonist, (B,E) intermediate glutamate, and (C,F) saturating glutamate. Detergent-only conditions (black) and detergent + cholesterol conditions (red). Data was acquired at 50 ms time resolution. Data is from one independent experiment.

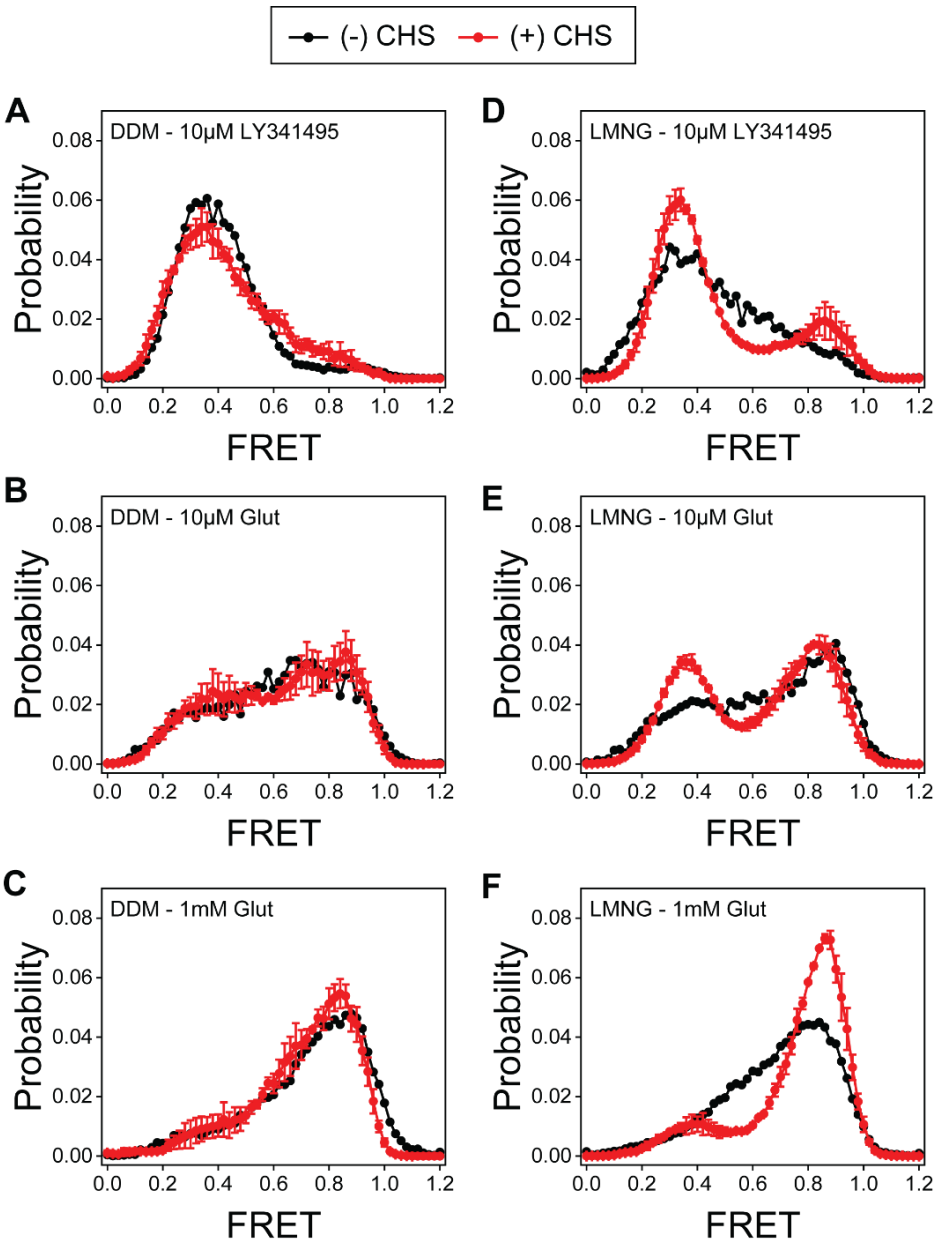

Figure 4.7 Cholesterol effects on CRD conformation
Cholesterol affects azi-CRD conformation in the presence of certain detergents. azi-CRD solubilized in (A-C) DDM or (D-F) LMNG with and without cholesterol (10:1 detergent: cholesterol w/v% ratio) and in the presence of (A,D) antagonist, (B,E) intermediate glutamate, and (C,F) saturating glutamate. Detergent-only conditions (black) and detergent + cholesterol conditions (red). Data was acquired at 50 ms time resolution. Detergent-only data is from one independent experiment while detergent + cholesterol data is from three independent experiment. Error bars represent s.e.m.

4.2.3 Cholesterol regulation of mGluR2 conformational dynamics

Previously, functional analyses of other mGluRs revealed that cholesterol was important for both receptor recruitment to lipid rafts and activation (Kumari et al., 2013; Eroglu et al., 2003). To verify if cholesterol played a similar role in mGluR2 function, I conducted single-cell functional calcium imaging experiments on HEK293T cells transiently expressing mGluR2 (Figure 4.8). Specifically, a glutamate titration was conducted on cells depleted of cholesterol by Methyl-β-cyclodextrin (MβCD) and untreated cells, resulting EC_{50}s of 12.9 μM and 5.5 μM, respectively. Although this reduced glutamate sensitivity is in direct conflict with my smFRET results, I hypothesized this discrepancy was the result of vastly different cholesterol concentrations present in cell membranes and lipid rafts versus smFRET experiments (10:1 w/v% LMNG:CHS) (Sezgin et al., 2017).

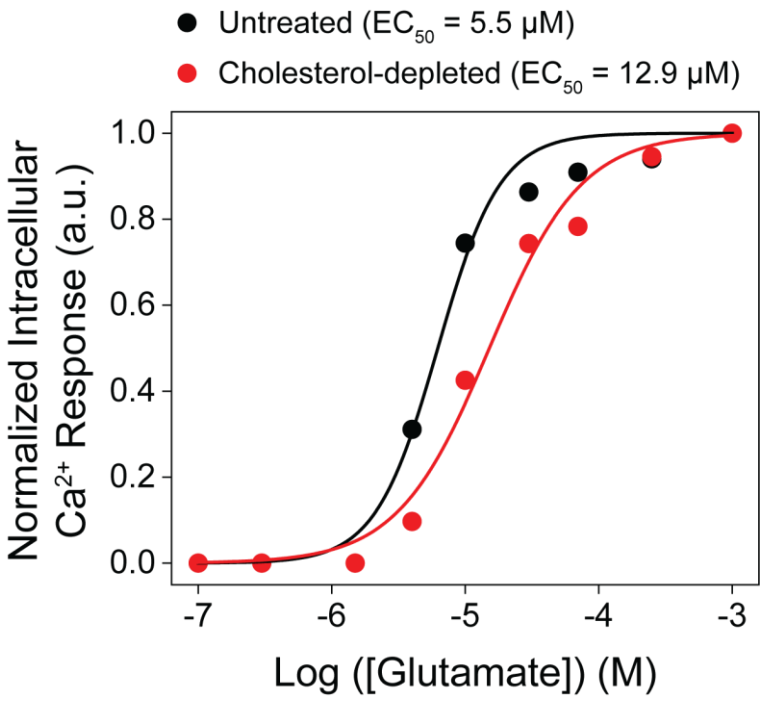

Figure 4.8 Cholesterol-depletion reduces mGluR2 glutamate sensitivity
Dose-response curves for SNAP-m2-induced calcium flux during glutamate titrations for (A) untreated HEK293T cells and (B) cholesterol-depleted HEK293T cells. The same region of interest was examined for both untreated and cholesterol-depleted conditions. Data is normalized to 1 mM glutamate response. Data represents results from one independent experiment.

To address this discrepancy, smFRET experiments were conducted on mGluR2 solubilized by a 1:1 w/v% LMNG:CHS mixture, an environment more representative of cholesterol-enriched lipid rafts (Figure 4.9). Unexpectedly, in the presence of increased CHS, the NAM-like effects of CHS were reversed. This concentration-dependent bimodal behavior of CHS is particularly apparent in inactive antagonist treated and intermediate glutamate treated conditions (Figure 4.9A-B). While these results are preliminary, they demonstrate a potentially novel mechanism for regulating membrane protein structure and function.

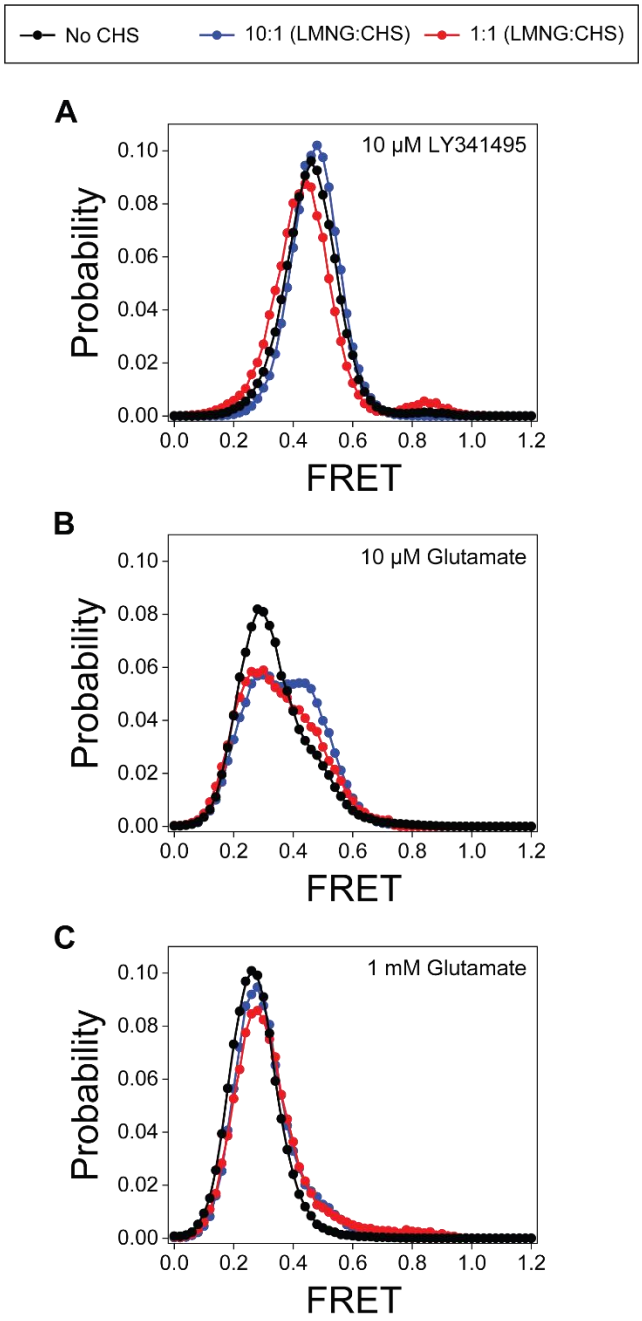

Figure 4.9 Cholesterol analog demonstrates concentration-dependent biphasic effect on mGluR2 conformation

Cholesterol hemisuccinate (CHS), a cholesterol analog, functions as a NAM when used at 10:1 w/v% (LMNG:CHS) and functions as a PAM at 1:1 w/v% (LMNG:CHS). No cholesterol (black), 10:1 w/v% cholesterol (blue), and 1:1 w/v% cholesterol (red) are shown in the presence of (A) antagonist, (B) intermediate glutamate, (C) and saturating glutamate conditions.

4.3 Conclusions and Discussion

The membrane bilayer is a mosaic of lipidic and proteinaceous components that form a complex and heterogeneous physiochemical environment (Ingólfsson et al., 2014). Strategies have emerged that enable biophysical analysis of membrane proteins within their native environment, however, these approaches are technically challenging and are not widely available (Asher et al., 2021; Lučič et al., 2013). To support membrane protein studies, a broad array of surfactants and membrane mimetic scaffolds have been developed that enable effective extraction, solubilization, and stabilization of membrane proteins *in vitro* (Anandan & Vrielink, 2016). While these tools have proven invaluable, the nuanced effects of detergent choice on membrane protein structure and dynamics is generally underappreciated.

The large size and multidomain architecture of mGluRs highlight the range of effects that detergent can have on membrane protein structure. Initial examination of the VFT domain and CRD revealed that DDM, LMNG, and GDN each shape mGluR conformational dynamics in a distinct manner (Figure 4.3, 4.4). Among the tested detergents, GDN demonstrated a unique and potent NAM-like effect, reducing CRD compaction and VFT domain closure and reorientation (Figure 4.5). Interestingly, although GDN solubilization of mGluR2 resulted in very distinct conformational profiles, GDN and LMNG are known to conserve mGluR function with similar efficacy (Seven et al., 2021; Lin et al., 2021). Typically, choice of detergent for membrane protein studies is governed by its ability to maintain protein function. This approach assumes that membrane protein function is maintained by stabilizing specific structural and dynamic properties *in vitro*. However, the discrepancy in GDN and LMNG conformational profiles suggest this may not be the case. This raises two questions. First, which conformational profile better reflects mGluR behavior on the

plasma membrane? Second, how does one select a solubilizing detergent, considering that they may differentially stabilize membrane proteins?

To answer both these questions, the use of membrane mimetics is essential. Using SMALP solubilized mGluR2, I was able to identify an optimized detergent mixture that not only recapitulated the conformational profile of lipid solubilized receptors but also conserved the integrity of the allosteric ligand binding site (Figure 4.2, 4.5). Membrane mimetics effectively provide a baseline of comparison for different detergents. Furthermore, hydrophobic copolymer assemblies have emerged as a powerful tool for this purpose as their application bypasses membrane protein purification or reconstitution (S. C. Lee et al., 2016). The primary drawback of SMALP solubilization is the heterogeneity in extracted lipids which precludes specific questions on lipid-protein interactions to be addressed.

In addition to revealing unique detergent-induced conformational fingerprints, smFRET experiments also uncovered concentration-dependent effects of cholesterol (Figure 4.9). Cell stiffness or deformability is highly dependent on membrane cholesterol content which regulates lipid ordering and ultimately membrane fluidity (Song et al., 2014; Lingwood & Simons, 2010; Sezgin et al., 2017). Cholesterol modulation of membrane fluidity is biphasic in nature and a function of temperature (Subczynski et al., 2017). Cholesterol's temperature dependence enables it to serve as a buffer and effectively maintain membrane fluidity. Here, I demonstrate that cholesterol modulates membrane protein structural dynamics and function in a concentration-dependent manner (Figure 4.9). While these results are still preliminary, this finding provides context on how cholesterol-enriched domains such as lipid rafts modulate membrane protein function.

4.4 Materials and Methods

4.4.1 Molecular cloning

The C-terminal FLAG-tagged mouse mGluR2 construct in pcDNA3.1(+) expression vector was purchased from GenScript (ORF clone: OMu19627D) and verified by sequencing (ACGT Inc). Full length mGluR2 construct with an amber codon (TAG) mutation of amino acid A548 (azi-CRD) or N-terminal SNAP-tag (SNAP-mGluR2) were generated as previously reported (Liauw et al., 2021). SNAP-mGluR2 constructs used for calcium imaging had C-terminal FLAG-tag removed by PCR-based deletion using phosphorylated primers. All plasmids were sequence verified (ACGT Inc). DNA restriction enzymes, DNA polymerase and DNA ligase were from New England Biolabs. Plasmid preparation kits were purchased from Macherey-Nagel.

4.4.2 Cell culture

HEK293T cells (Sigma) were authenticated (ATCC) and tested for mycoplasma contamination (Lonza). HEK293T cells were maintained in DMEM (Corning) supplemented with 10% (v/v) fetal bovine serum (Fisher Scientific), 100 unit/mL penicillin-streptomycin (Gibco) and 15 mM HEPES (pH=7.4, Gibco) at 37 °C and 5% CO_2. The cells were passaged with 0.05% trypsin-EDTA (Gibco). For unnatural amino acid-containing protein expression, the growth media was supplemented with 0.6 mM 4-azido-L-phenylalanine (Chem-Impex International). All media was filtered by 0.2 μM PES filter (Fisher Scientific).

4.4.3 Transfection and protein expression

24 hours before transfection, HEK293T cells were cultured on poly-L-lysine-coated 18 mm glass coverslips (VWR). For SNAP-mGluR2 used in FRET experiments, media was refreshed with

standard growth media and transfected using Lipofectamine 3000 (Fisher Scientific) (total plasmid: 1 µg/18 mm coverslip). Growth media was refreshed after 24 hours and cells were grown for an additional 24 hours.

For unnatural amino acid-containing protein expression, one hour before transfection, media was changed to the growth media supplemented with 0.6 mM 4-azido-L-phenylalanine. mGluR2 CRD sensor (azi-CRD) and pIRE4-Azi plasmid (pIRE4-Azi was a gift from Irene Coin, Addgene plasmid # 105829) were co-transfected (1:1 w/w) into cells using Lipofectamine 3000 (Fisher Scientific) (total plasmid: 2 µg/18 mm coverslip). The growth media containing 0.6 mM 4-azido-L-phenylalanine was refreshed after 24 hours and cells were grown for an additional 24 hours. On the day of the experiment, 30 minutes before labeling, supplemented growth media was removed and cells were washed by extracellular buffer solution containing (in mM): 128 NaCl, 2 KCl, 2.5 $CaCl_2$, 1.2 $MgCl_2$, 10 sucrose, 10 HEPES, pH=7.4 and were kept in growth medium without 4-azido-L-phenylalanine.

For calcium imaging experiments, media was refreshed with standard growth media and cells were co-transfected with SNAP-mGluR2 (no FLAG-tag) and chimeric G protein (Gqo5, Addgene plasmid #24500) (1:2 w/w) using Lipofectamine 3000 (Fisher Scientific) (total plasmid: 1.5 µg/18 mm coverslip). Growth media was refreshed after 24 hours, and cells were grown for an additional 24 hours. Before the addition of labeling solutions, cells were washed with extracellular buffer solution.

4.4.4 SNAP-tag labeling for FRET measurements

SNAP-tag labeling of SNAP-mGluR2 was done by incubating cells with 2 µM of SNAP-Surface Alexa Fluor 549 (NEB) and 2 µM of SNAP-Surface Alexa Fluor 647 (NEB) in extracellular buffer

for 30 minutes at 37 °C. After labelling, cells were washed by extracellular buffer solution to remove excess dye.

4.4.5 Unnatural amino acid labeling by azide-alkyne click chemistry

Unnatural amino acid labeling by azide-alkyne click chemistry was performed as previously reported (Liauw et al., 2021). Stock solutions were made as follows: Cy3 and Cy5 alkyne dyes (Click Chemistry Tools) 10 mM in DMSO, BTTES (Click Chemistry Tools) 50 mM, copper (II) sulfate (Sigma) 20 mM, aminoguanidine (Cayman Chemical) 100 mM, and (+)-sodium L-ascorbate (Sigma) 100 mM in ultrapure distilled water (Invitrogen). In 656 µL of extracellular buffer solution, Cy3 and Cy5 alkyne dyes were mixed to a final concentration of 18 µM for each dye. To this mixture, a fresh pre-mixed solution of copper (II) sulfate and BTTES (1:5 molar ratio) was added at the final concentration of 150 µM and 750 µM, respectively. Next, aminoguanidine was added to the final concentration of 1.25 mM. Lastly, (+)-sodium L-ascorbate was added to the mixture to a final concentration of 2.5 mM. Total labeling volume was 0.7 mL. The labeling mixture was incubated at 4 °C for 8 minutes, followed by a 2 minute incubation at room temperature before addition to cells. Cells were washed with extracellular buffer solution prior to addition of labeling mixture. During labeling, cells were kept in the dark at 37 °C and 5% CO_2. After 10 minutes, L-glutamate (Sigma) was added to the cells to a final concentration of 0.5 mM and cells were incubated for an additional 5 minutes. After labelling, cells were washed by the extracellular buffer solution to remove excess dye.

4.4.6 Labeling for calcium imaging

Cells used for calcium imaging experiments were labeled using 1 µM SNAP-Surface Alexa Fluor 647 (NEB) and 4 µM Oregon Green 488 BAPTA-1 (Fisher Scientific) in extracellular buffer for

30 minutes at 37 °C. After labelling, cells were washed by extracellular buffer solution to remove excess dye.

4.4.7 Calcium imaging

The microscope and flow system setup used were as previously reported (Liauw et al., 2022). After labeling, coverslip was assembled in the flow chamber (Innova Plex) and attached to a gravity flow control system (ALA Scientific Instruments). Extracellular buffer solution was used as imaging buffer and applied at the rate of 5 ml min^{-1}. Cells were imaged using an inverted confocal microscope (Zeiss, LSM-800) with a ×40 oil-immersion objective (Plan-Apochromat ×40/1.3oil DIC(UV) VIS-IR M27). Samples were excited using both a 488 nm and a 640 nm laser and Oregon Green 488 and Cy5 fluorescence were measured simultaneously with a GaAsP-PMT detector with detection wavelengths set to 410-617 nm and 648-700 nm. All calcium imaging data were recorded at 3 second time resolution and at room temperature.

Analysis of functional calcium imaging data was performed using ImageJ (http://imagej.nih.gov/ij/) and OriginPro (OriginLab). All cells showing agonist-induced calcium response were selected for initial analysis, with those showing significant drift or photobleaching being omitted from downstream analysis. Fluorescence signal was measured for individual cells from a given movie, normalized from 0 to 1, and averaged. Changes in calcium signal were calculated from these averaged responses as the difference between max response during treatment and response before treatment. Baseline signal intensity was the average over 6 datapoints prior to treatment application. Dose-response equation $y(x) = A1 + \frac{A_2 - A_1}{1+10^{(\log x_0 - x)P}}$ was used for fitting calcium response to calculate EC_{50} values, where *A1* is the lower asymptote, *A2* is the upper

asymptote, P is the Hill slope, and x_0 is the EC_{50}. All responses were normalized to 1 mM glutamate response.

The same sample and ROI imaged for the untreated condition was imaged after cholesterol depletion. Cells were washed with imaging buffer for 20 minutes upon completion of glutamate titration experiment on untreated cells. Cholesterol depletion of HEK293T cells was achieved by exchanging imaging buffer on samples with Opti-MEM containing 10 mM Methyl-β-cyclodextrin (MβCD) and incubating for 20 minutes at room temperature. Cholesterol depletion did not preclude glutamate-induced calcium release in a significant number of cells.

4.4.8 Single-molecule FRET measurements

Single-molecule experiments were conducted using custom flow cells prepared from glass coverslips (VWR) and slides (Fisher Scientific) passivated with mPEG (Laysan Bio) and 1% (w/w) biotin-PEG to prevent unspecific protein adsorption, as previously described (Vafabakhsh et al., 2015; Jain et al., 2011). Prior to experiments, flow cells were functionalized with FLAG-tag antibody. This was achieved by first incubating flow cells with 500 nM NeutrAvidin (Fisher Scientific) for 2 minutes followed by 20 μM biotinylated FLAG-tag antibody (A01429, GenScript) for 30 minutes. Unbound NeutrAvidin and biotinylated FLAG-tag antibody were removed by washing between each incubation step. Washes and protein dilutions were done using T50 buffer (50 mM NaCl, 10 mM Tris, pH 7.4).

After labeling, cells were recovered from an 18 mm poly-L-lysine coverslip by incubating with Ca^{2+}-free DPBS followed by a gentle pipetting. Cells were then pelleted by a 4000 *g* centrifugation at 4 °C for 10 minutes. The supernatant was removed and cells were resuspended in 100 μL lysis buffer consisting of 200 mM NaCl, 50 mM HEPES, 1 mM EDTA, protease inhibitor tablet (Fisher

Scientific), and the detergent or detergent mixture of choice (Table 4.1), pH 7.4. Cells were allowed to lyse with gentle mixing at 4 °C for 1 hour. Cell lysate was then centrifuged for 20 min at 20,000 *g* and 4 °C. The supernatant was collected and immediately diluted 10-fold with dilution buffer consisting of 200 mM NaCl, 50 mM HEPES, 1 mM EDTA, and protease inhibitor tablet, pH 7.4. The diluted sample was then added to the flow chamber to achieve sparse surface immobilization of labeled receptors by their C-terminal FLAG-tag. After optimal receptor coverage was achieved, flow chamber was washed extensively (> 20× chamber volume) to remove unbound proteins and excess detergent with wash buffer consisting of 200 mM NaCl, 50 mM HEPES, and the detergent or detergent mixture of choice (Table 4.1), pH 7.4. Finally, labeled receptors were imaged in imaging buffer consisting of (in mM) 128 NaCl, 2 KCl, 2.5 $CaCl_2$, 1.2 $MgCl_2$, 40 HEPES, 4 Trolox, the detergent or detergent mixture of choice (Table 4.1), and an oxygen scavenging system consisting of protocatechuic acid (Sigma) and 1.6 U/mL bacterial protocatechuate 3,4-dioxygenase (rPCO) (Oriental Yeast Co.), pH 7.35. For glutamate-free conditions, imaging buffer contained 2 U/mL glutamic-pyruvic transaminase (Sigma) and 2 mM sodium pyruvate (Gibco) and was incubated at 37 °C for 10 minutes. All reagents were prepared from ultrapure-grade chemicals (purity > 99.99%) and were purchased from Sigma. All buffers were made using ultrapure distilled water (Invitrogen). Samples were imaged with a 100× objective (Olympus, 1.49 NA, Oil-immersion) on a custom-built microscope with 50 ms time resolution unless stated otherwise. 532 nm and 638 nm lasers (RPMC Lasers) were used for donor and acceptor excitation, respectively.

Detergent-Cholesterol Mixture	Detergent #1 / (w/v%) lysis	Detergent #2 / (w/v%) lysis	Detergent #1 / (w/v%) imaging	Detergent #2 / (w/v%) imaging
DDM	DDM / 1	-	DDM / 0.05	-
LMNG	LMNG / 0.1	-	LMNG /0.005	-
GDN	GDN / 0.1	-	GDN / 0.005	-
DDM-CHS (10:1)	DDM / 1	-	DDM / 0.05	-
LMNG-CHS (10:1)	LMNG / 0.1	-	LMNG /0.005	-
GDN-CHS (10:1)	GDN / 0.1	-	GDN / 0.005	-
DDM-CHS (1:1)	DDM / 1	-	DDM / 0.05	-
LMNG-CHS (1:1)	LMNG / 0.1	-	LMNG /0.005	-
GDN-CHS (1:1)	GDN / 0.1	-	GDN / 0.005	-
LMNG-CHS-GDN (0.0003)	LMNG / 0.1	-	LMNG / 0.005	GDN / 0.0003
LMNG-CHS-GDN (0.0004)	LMNG / 0.1	-	LMNG / 0.005	GDN / 0.0004
LMNG-CHS-GDN (0.000625)	LMNG / 0.1	-	LMNG / 0.005	GDN / 0.000625
LMNG-CHS-GDN (0.005)	LMNG / 0.1	-	LMNG / 0.005	GDN / 0.005

Table 4.1 Detergent and cholesterol mixtures for smFRET experiments

4.4.9 Styrene maleic acid (SMA) extraction and solubilization of mGluR2

Styrene maleic acid lipid particle (SMALP) -based mGluR2 isolation was adapted from previously reported protocols (S. C. Lee et al., 2016; Routledge et al., 2020). Briefly, first express and label mGluR2 FRET sensors in HEK293T cells following previously described protocols. SMALP-based isolation of mGluR2 from HEK293T cells requires ~1E7 cells or a ~65 mg cell pellet. This is equivalent to 14 18 mm coverslips or 1 10 cm tissue culture dish with cells at 90% confluency. Detach and resuspend cells by gentle pipetting using 8 mL of lysis buffer consisting of 50 mM HEPES, 200 mM NaCl, and protease inhibitor tablet (Fisher Scientific), pH 7.4. Gently lyse cells by probe sonication for 2 minutes in total with a 1 minute cycle time of 30 seconds on and 30 seconds off (duty cycle = 50%). Adjust sonicator output as necessary based on lysis efficiency. Centrifuge sample at 750 *g* and 4 °C for 10 minutes to remove unlysed cells. Transfer supernatant to ultracentrifugation tubes and centrifuge at 100,000 *g* and 4 °C for 60 minutes. Weigh pellet

containing membrane fraction and resuspend using resuspension buffer at 40 mg/mL. Resuspension buffer consists of 300 mM NaCl, 50 mM HEPES, protease inhibitor tablet (Fisher Scientific), and 2.5 w/v% SMA-EA copolymer (Anatrace), pH 7.4. Mix thoroughly to break up membrane fraction pellet. Gently mix the solution in the dark at room temperature for 60 minutes. Centrifuge at 20,000 *g* and 4 °C for 10 minutes to remove insoluble fraction and store supernatant in fresh pre-chilled tube. Sample is ready to be imaged using detergent-free imaging buffer as previously described.

4.4.10 smFRET data analysis

Analysis of single-molecule fluorescence data was performed using smCamera (http://ha.med.jhmi.edu/resources/), custom MATLAB (MathWorks) scripts, and OriginPro (OriginLab). Particle selection and generation of raw FRET traces were done automatically within the smCamera software. For the selection, particles that showed acceptor signal upon donor excitation, with acceptor brightness greater than 10% above background and had a Gaussian intensity profile, were automatically selected and donor and acceptor intensities were measured over all frames. Out of this pool, particles that showed a single donor and a single acceptor bleaching step during the acquisition time, stable total intensity ($I_D + I_A$), anti-correlated donor and acceptor intensity behavior without blinking events, and lasted for more than 4 seconds were manually selected for further analysis (~20-30% of total molecules per movie). All data was analyzed by three individuals independently and the results were compared and showed to be identical. In addition, a subset of data was blindly analyzed to ensure no bias in analysis. Apparent FRET efficiency was calculated as $(I_A - 0.088 \times I_D) / (I_D + (I_A - 0.088 \times I_D))$, where I_D and I_A are raw donor and acceptor intensities, respectively. Population smFRET histograms were generated

by compiling at least 25 total FRET traces of individual molecules. Before compiling traces, FRET histograms of individual molecules were normalized to 1 to ensure that each trace contributes equally, regardless of trace length. Error bars on histograms represent the standard error of data from three independent biological replicates.

Chapter 5: Conclusions and prospectus

5.1 Conclusions

In this thesis dissertation, live-cell FRET, smFRET, and functional calcium imaging techniques were used to probe the conformational dynamics of mGluR2 activation and modulation. This work revealed that mGluR2 activation is a dynamic process and requires the coordinated coupling of the three structural domains to occur. In addition, the work here provides a dynamic structural framework to interpret and describe mechanisms of allosteric modulation by both pharmaceutical agents and endogenous modulators. The concepts underlying mGluR2 activation and modulation likely extend not only to other class C GPCRs, but also to other multidomain membrane receptors.

5.1.1 mGluR2 activation is an ordered and stepwise process

At the beginning of this thesis work, the molecular details of mGluR rearrangement during activation were generally fragmented and incomplete. No full-length mGluR structures were available and biophysical characterization predominantly focused on the ligand binding VFT domain. In **Chapter 2**, I addressed this by focusing my attention on the CRD. The CRD's role as an allosteric linker between the glutamate binding VFT domain and G protein-coupling 7TM

domain made it an ideal structural domain to study mGluR activation. However, due to its compact and flexible structure, the CRD is not amenable to traditional fluorescent labeling strategies. To circumvent this obstacle, we adapted and optimized a method to site-specifically incorporate UAAs into the CRD enabling non-perturbative labeling via a copper-catalyzed click reaction (Noren, Anthony-Cahill, et al., 1989; Presolski et al., 2011b).

Using this novel CRD conformational FRET sensor, we identified four distinct and ordered conformations that included two novel intermediates states. These findings confirmed the general compaction that occurred during mGluR activation (Koehl et al., 2019a). By coupling our novel CRD sensor with a range of pharmacological, mutagenesis, and crosslinking strategies, we determined that the CRD had a single active conformation and that the intermediate states effectively functioned as conformational checkpoints towards activation. The identification and characterization of these different states highlight the strength of smFRET as a technique that enables one to bypass conformational heterogeneity in a way that traditional biophysical tools cannot.

In addition, comparison of the CRD and VFT domain revealed that receptor dynamics are highly variable across different domains. While the VFT domain was stable in inactive or fully active conditions, the CRD demonstrated substantial intrinsic dynamics regardless of ligand present. This result clearly illustrates loose coupling between mGluR2 structural domains. Collectively, these findings clearly illustrate the importance of dynamics and the conformational ensemble in receptor function. The four-state activation model established in **Chapter 2** serves as the framework for interpreting and describing mechanisms of allosteric modulation in **Chapter 3** and **Chapter 4**.

5.1.2 Allosteric modulators have a distinct conformational fingerprint

Allosteric modulators are a promising class of therapeutics that enable improved mGluR subtype specificity through the targeting of evolutionary distinct binding sites and leveraging of a broader array of binding modalities (Foster & Conn, 2017). While subtype specificity is a key strength of allosteric modulators, their distinct mechanisms of action impede efficient clinical translation. Furthermore, the lack of intrinsic effect and context-dependence of many allosteric modulators make them difficult to characterize. To bypass this inherent complexity, we developed a receptor-centric interpretation of allosteric modulators in **Chapter 3**.

Using our UAA-incorporation strategy, we developed sensors for each mGluR2 domain, allowing us to define a "conformational fingerprint" for each modulator. All tested modulators regulated each domain in a manner consistent with their functional characterization, suggesting some conserved modulatory mechanism. However, substantial variation in ΔPotency and ΔEfficacy among domains and modulators provided evidence for distinct "conformational pathways". We hypothesize that these "pathways" may achieve some net modulatory effect by eliciting differential contributions from each mGluR2 structural domain. A systematic analysis using a broader range of modulators and sensors will be necessary to verify this hypothesis.

To gain mechanistic insight on mGluR2 allosteric modulation, I conducted smFRET experiments on prototypical PAM and NAM, BINA and MNI-137, respectively. I found that BINA, a pure PAM with no intrinsic agonist effect, served to prime mGluR2 in the pre-active intermediate conformation in the absence of glutamate, while increasing entry into the active conformation with glutamate present. In contrast, MNI-137 generally reduced mGluR2 compaction and prevented entry into the active conformation. Interestingly, receptor dynamics was an important parameter

regulated by both these modulators, further emphasizing the importance of structural dynamics in GPCR function. Collectively, these smFRET experiments validated and expanded upon the activation framework described in **Chapter 2**.

5.1.3 The hydrophobic environment shapes receptor structure and function

During the process of characterizing mechanisms of BINA and MNI-137 modulation, studies found that the choice of solubilizing detergent was essential for conserving the integrity of the allosteric binding pocket (Cao et al., 2021). As a result, a systematic analysis of detergents, detergent mixtures, and cholesterol effects on mGluR2 conformational dynamics was underway. The goal of this study was to not only determine which combination of surfactants best conserved the allosteric pocket, but also to determine which best reflected native mGluR2 conformation.

Using SMALP-based mGluR2 isolation, I showed that no individual detergent effectively recapitulated the conformation of lipid solubilized mGluR2. Fortunately, recognizing GDN's unique NAM-like behavior enabled me to determine the optimal detergent-cholesterol mixture that reflected the conformation of lipid solubilized mGluR2 while conserving the allosteric pocket integrity. This optimization process highlights the importance of testing multiple detergents when conducting *in vitro* biophysical studies on membrane proteins.

The distinct NAM-like behavior of GDN raised questions regarding the conservation of this property among steroidal molecules. The role of cholesterol in modulating lipid bilayer fluidity and its dependence on temperature and concentration have been thoroughly reported (Subczynski et al., 2017). However, minimal work has been done examining the non-linear effects of cholesterol on membrane protein structure and dynamics (Serdiuk et al., 2022). Leveraging the high spatial resolution of smFRET, we provided direct evidence of cholesterol's biphasic

modulatory effects on mGluR2 structural dynamics. This finding provides mechanistic insight on how membrane receptor function may be regulated by cholesterol-enriched microdomains on the cell membrane.

5.2 Prospectus

5.2.1 Intramolecular and intradomain mGluR structural dynamics

The work described in this thesis focuses primarily on symmetrical intermolecular rearrangement between mGluR monomers. This was in part due to the technical challenges of efficiently selecting heterodimeric receptors with a single labeling competent monomer and poor expression of UAA-containing heterodimeric receptors. However, improved methods for bio-orthogonal amino acid incorporation (Elsässer et al., 2016), a growing library of UAAs with orthogonal chemistries (Lang & Chin, 2014), and improved heterodimerization selection tools make designing intramolecular FRET sensors a more straightforward process (Margeta-Mitrovic et al., 2000). A recent study has already applied UAA incorporation to probe the closure of an individual VFT domain of mGluR2 by labeling both LB1 and LB2 (Lecat-Guillet et al., 2022). These advances will enable us to examine a broader array of structural rearrangements, better define conformational coupling of spatially separated domains, and build a more comprehensive picture of mGluR activation.

5.2.2 Defining structure-function relationship of mGluR heterodimers

mGluR heterodimerization significantly expands the potential functionality of the receptor family by including up to 11 heterodimers with unique physiological properties (Doumazane et al., 2011). Cell-based and single-molecule studies have already revealed that mGluR heterodimerization can result in transactivation (Liu et al., 2017), basal activity (Habrian et al., 2019), and altered

cooperativity (Levitz et al., 2016). These studies only begin to describe the functional diversity made possible by heterodimeric mGluRs. Although the presence and localization of heterodimeric mGluRs in native tissues are poorly defined and remain an active area of research, defining their unique physiological and structural properties will likely be vital to their clinical application as homo- and heterodimers have been shown to colocalize, further complicating the challenge of subtype selectivity (Meng et al., 2022; Moreno Delgado et al., 2017). Fortunately, advances in tools for labeling and heterodimer selection have laid the groundwork for the straightforward characterization of mGluR heterodimers.

5.2.3 Mechanisms of allosteric modulation by other allosteric ligand and regulatory proteins

Allosteric modulators are promising therapeutic agents that enable mGluR subtype selectivity (Lindsley et al., 2016). However, the mechanism of action for most allosteric modulators is poorly understood, slowing the optimization and clinical translation of these therapeutics (Thal et al., 2018). In **Chapter 3**, I was able to define mechanisms for the pure PAM BINA and NAM MNI-137 in great detail using smFRET. By combining smFRET, our library of conformational sensors, and the activation framework established in **Chapter 2**, defining mechanisms of action for other mGluR modulators should be a reasonably straightforward process. For instance, this strategy can be applied to identify mechanisms utilized by agonist-PAMs, neutral allosteric modulators, and biased allosteric modulators or more generally to define different modes of positive and negative allosteric modulation. Furthermore, this workflow can also be adapted to study protein-protein interactions between mGluRs and other intracellular regulatory proteins.

5.2.4 Lipid modulation of mGluR conformational dynamics

SMALP-based mGluR2 isolation enabled preliminary analysis of lipid solubilized mGluR2 conformation dynamics. However, it is known that lipids and lipid mixtures may differentially affect membrane proteins through either direct binding or modulation of bilayer biophysical properties (Gimpl, 2016; Sarkar & Chattopadhyay, 2020; Sejdiu & Tieleman, 2020). As SMA non-specifically isolates mGluR2 and surrounding lipids from the cell membrane, the lipid composition of SMALPs is heterogeneous (Teo et al., 2019). Thus, in-depth analysis of specific lipid effects is not possible using SMALP scaffolds. To study the effects of specific lipids on mGluRs, nanodiscs, liposomes, or any lipidic scaffold that enables strict control of the lipid environment should be used.

Appendix A: Supplemental data for chapter 2

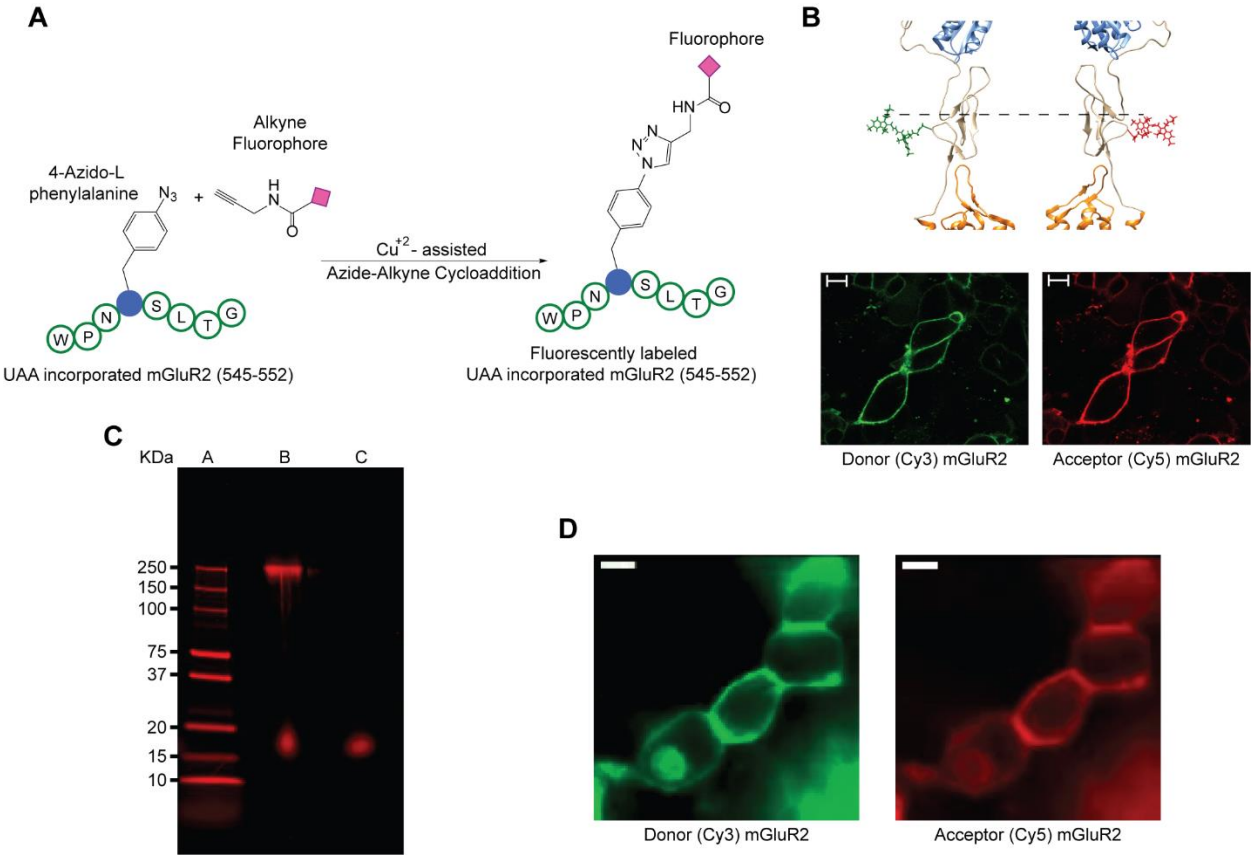

Figure S2.1 Site-specific labeling of mGluR2 by click chemistry
(A) Schematic showing site-specific fluorescent labeling of mGluR2, with the unnatural amino acid 4-azido-L-phenylalanine at residue 548, by copper catalyzed azide-alkyne click reaction. (B) Donor (green: Cy3) and acceptor (red: Cy5) fluorophores conjugated to the CRD of inactive mGluR5 at the position corresponding to residue 548 in mGluR2 (top). Representative confocal microscope image of HEK293T cells expressing 548UAA with the cell surface population labeled with donor (green: Cy3) and acceptor (red: Cy5) fluorophores through click chemistry (bottom). Scale bars, 10 µm. (C) Unprocessed image of non-reducing 4-20% polyacrylamide gel electrophoresis of cell lysate from HEK293T cells expressing 548UAA and labeled by Cy5-alkyne. The gel is imaged with 633 nm excitation wavelength and 670-BP30 emission filter. Lane A: protein ladder; lane B: cell lysate; lane C: Cy5-alkyne dye. Results are representative of an individual experiment. (D) Image of HEK293T cells expressing 548UAA and labeled with donor (green: Cy3) and acceptor (red: Cy5) fluorophores through click chemistry during live-cell FRET experiments. Scale bars, 10 µm. Results are representative of all titration and max response experiments for the 548UAA construct (N=21 independent experiments).

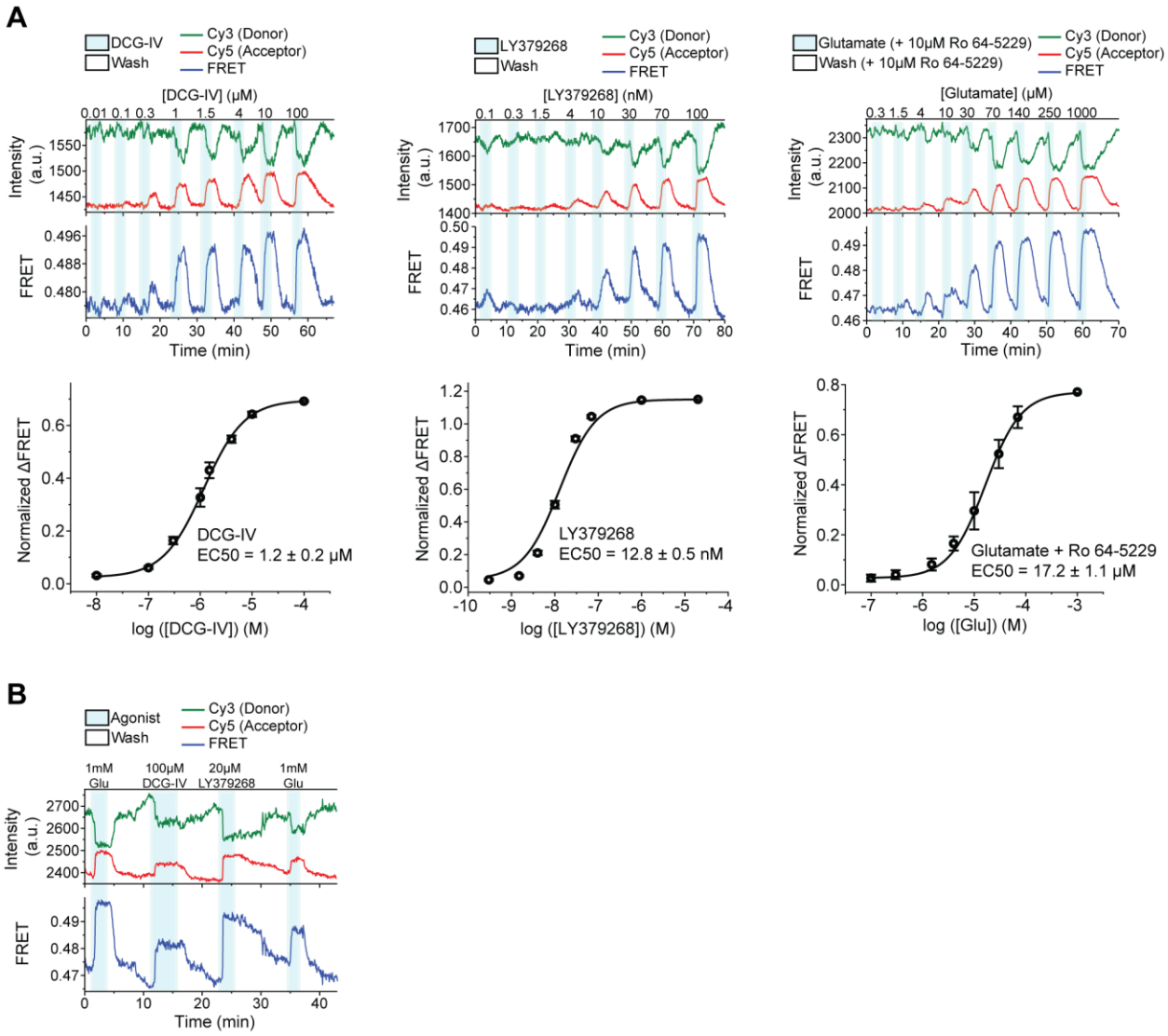

Figure S2.2 Live-cell ensemble FRET response to orthosteric ligands and a negative allosteric modulator

(A) Representative donor and acceptor intensities and corresponding FRET signal from live-cell FRET titration experiments for DCG-IV, LY379268 and Glutamate +10 μM Ro64-5229 measured using HEK293T cells expressing 548UAA (top) and corresponding dose-response curves (bottom). Each titration curve is normalized to the 1 mM glutamate response. Data represent mean ± s.e.m. of N=20, 10 and 13 cells for LY379268, DCG-IV and glutamate +10 μM Ro64-5229, respectively, examined over 3 independent experiments. (B) Donor and acceptor intensities and corresponding FRET signal in response to saturating concentrations of glutamate (1 mM), DCG-IV (100 μM) and LY37 (20 μM) in HEK293T cells expressing 548UAA.

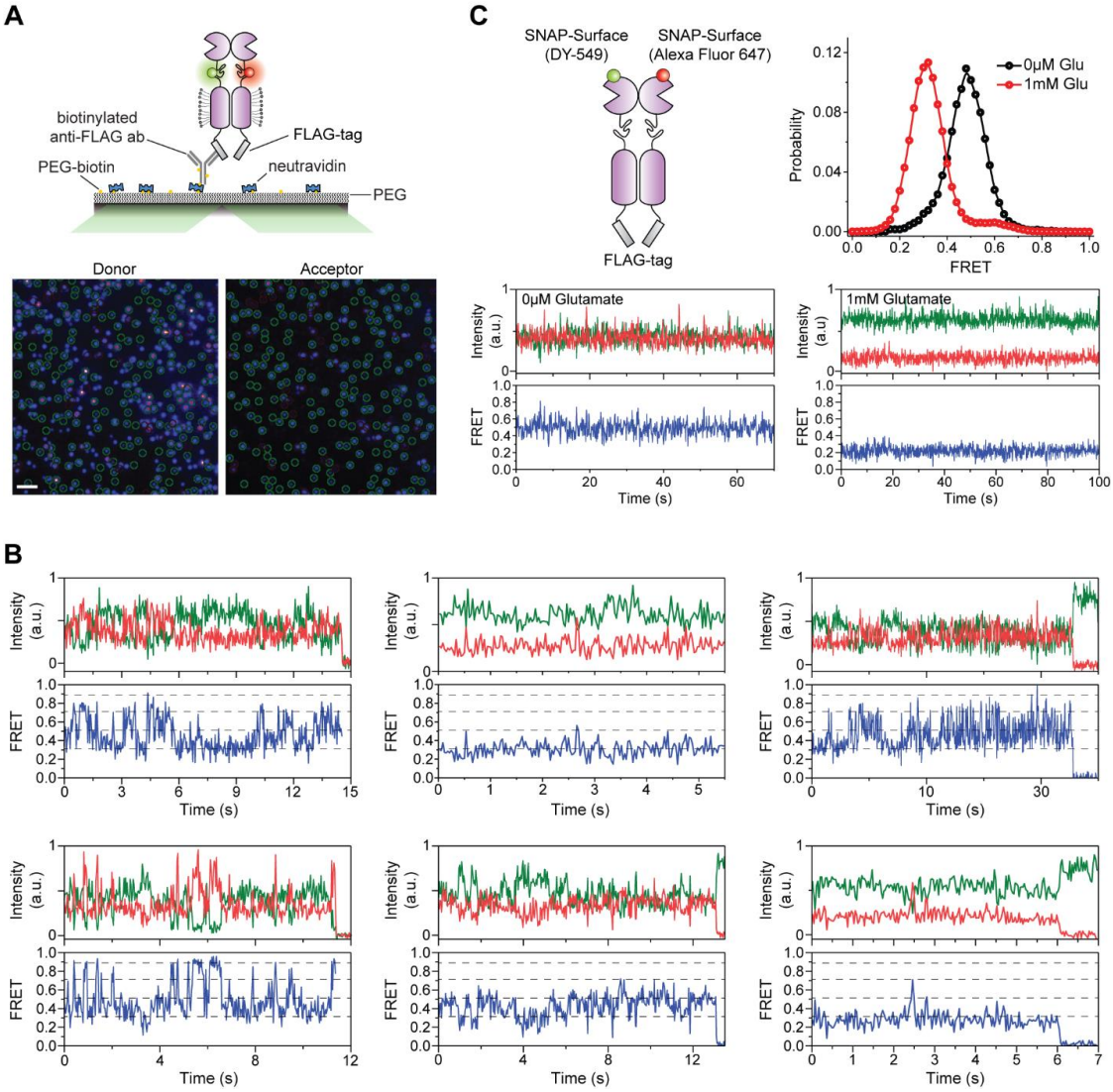

Figure S2.3 Example single-molecule time traces of CRD and VFT domain sensors
(A) Schematic of the single-molecule experiments (top). Representative frame from a single-molecule movie with the donor channel (Cy3) on the left and acceptor channel (Cy5) on the right (bottom). Molecules selected by analysis software for downstream processing are indicated by green circles. Scale bar, 3 μm. (B) Example single-molecule time traces of the 548UAA in the absence of glutamate (0 μM) showing donor (green) and acceptor (red) intensities and corresponding FRET (blue). Dashed lines represent 4 distinct FRET states. (C) Schematic of the VFT domain conformational sensor (left). Example single-molecule time traces of VFT domain sensor in the absence of glutamate and presence of saturating glutamate showing donor (green) and acceptor (red) intensities and corresponding FRET (blue) (bottom). smFRET population histogram of VFT domain mGluR2 sensor in the inactive (0 μM glutamate; 36 total molecules) and active (1 mM glutamate; 24 total molecules) conditions (top right). Data represent mean of N=2 independent experiments.

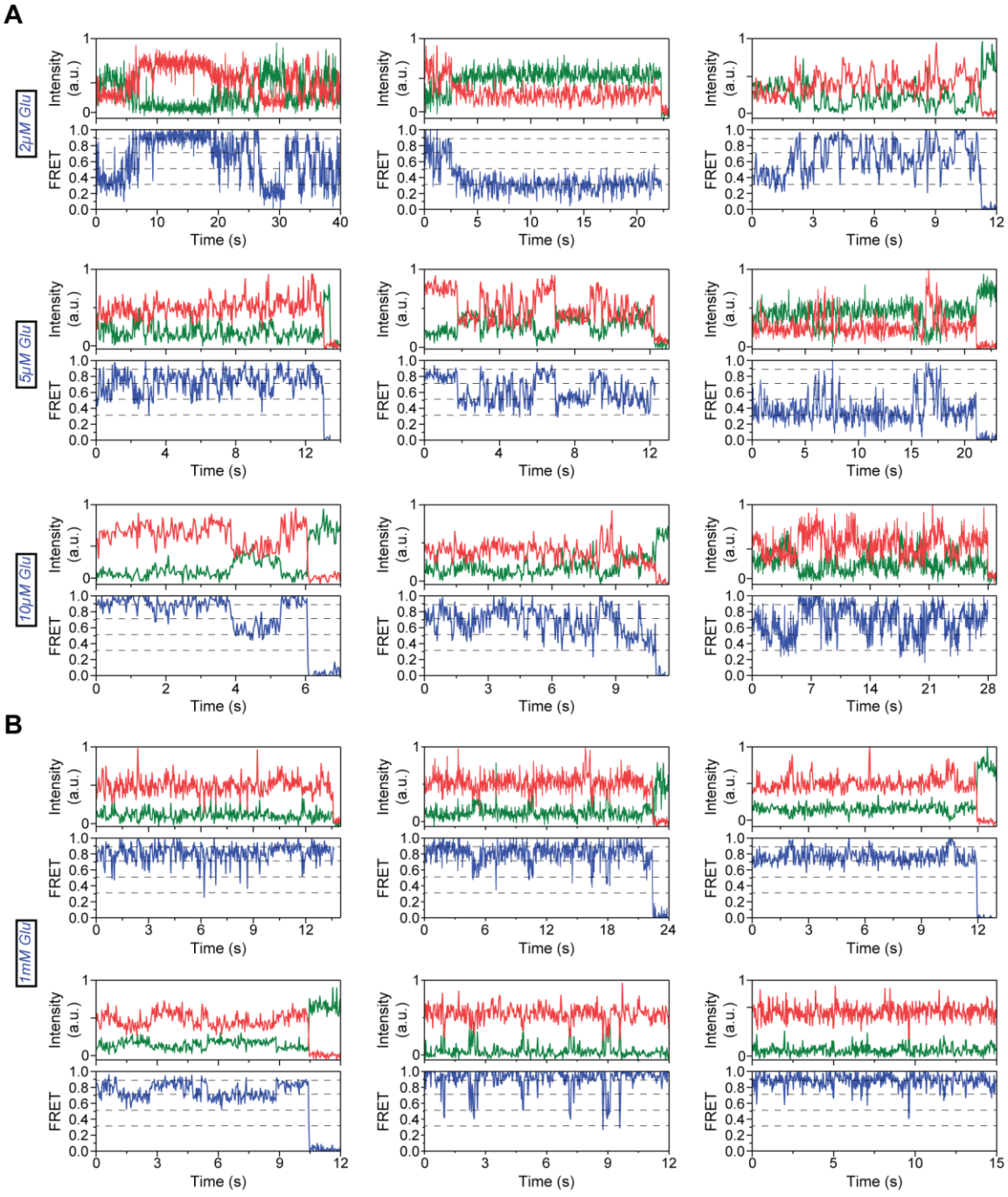

Figure S2.4 Example single-molecule time traces of CRD at different glutamate concentrations

(A) Example single-molecule time traces of the 548UAA at intermediate glutamate concentrations. (B) Example single-molecule time traces of the 548UAA in saturating (1 mM) glutamate. Donor (green) and acceptor (red) intensities and corresponding FRET (blue) are shown. Dashed lines represent 4 distinct FRET states.

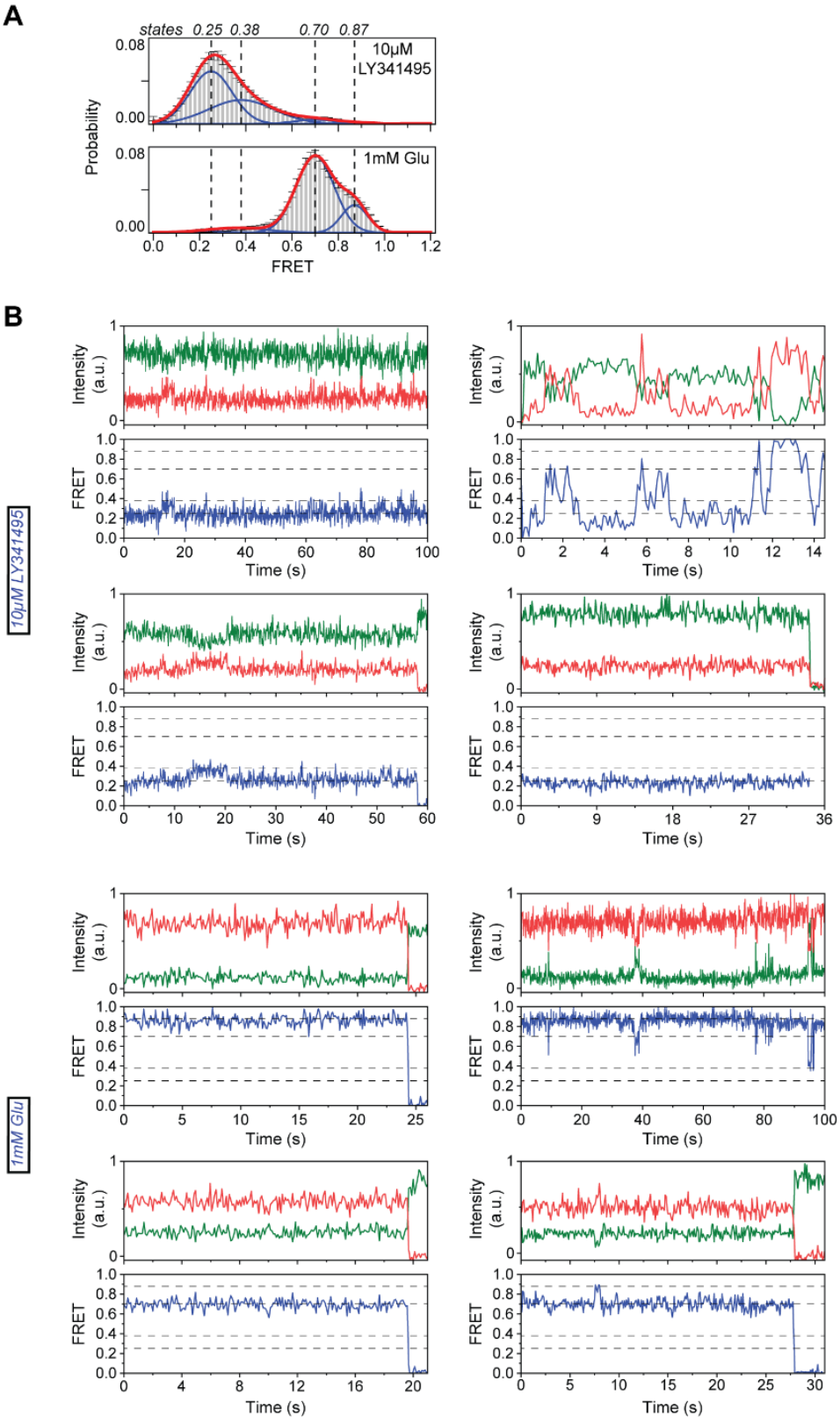
A
states 0.25 0.38 0.70 0.87
10μM LY341495
1mM Glu
Probability
FRET
B
10μM LY341495
1mM Glu
Intensity (a.u.)
FRET
Time (s)

Figure S2.5 mGluR3 undergoes a 4-state activation process
(A) smFRET population histograms of mGluR3 CRD sensor (labeled at residue 557) in the presence of competitive antagonist (LY341495; 221 total molecules) or saturating glutamate (290 total molecules). Data represent mean ± s.e.m. of N=3 independent experiments. Histograms are fitted (red) to 4 Gaussian distributions (blue) centered around 0.25 (state 1), 0.38 (state 2), 0.7 (state 3) and 0.87 (state 4), denoted with dashed lines. (B) Example single-molecule time traces of mGluR3 CRD sensor in the presence of antagonist (LY341495) or saturating glutamate showing donor (green) and acceptor (red) intensities and corresponding FRET (blue). Dashed lines represent 4 distinct FRET states. Data was acquired at 100 ms time resolution.

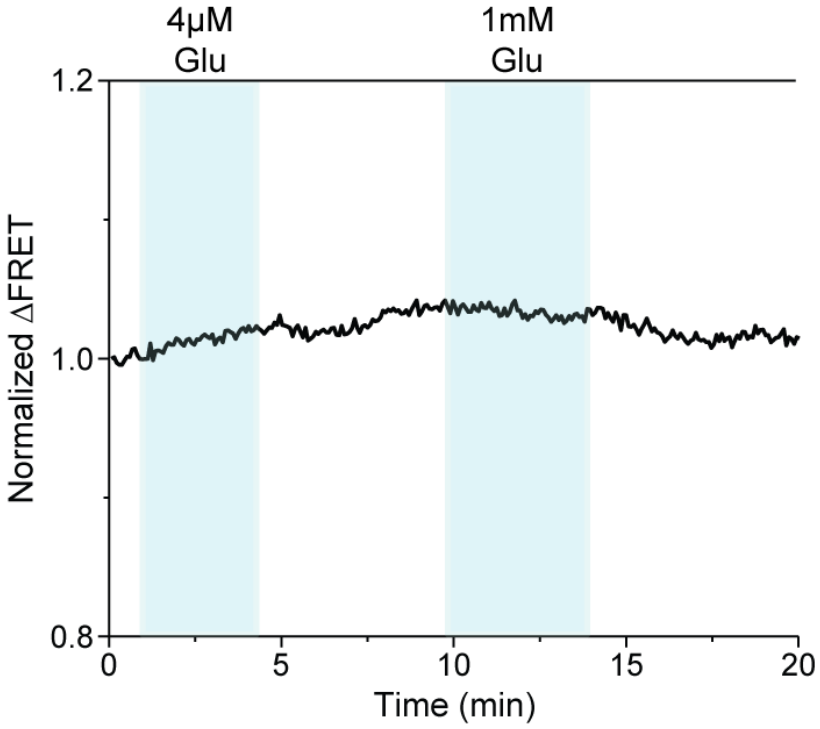

Figure S2.6 Effect of intersubunit crosslinking on the CRD conformation
Representative live-cell FRET measurement using HEK293T cells expressing 548UAA with the crosslinking mutation L521C upon application of intermediate and saturating glutamate. FRET signal is normalized using initial FRET at time = 0.

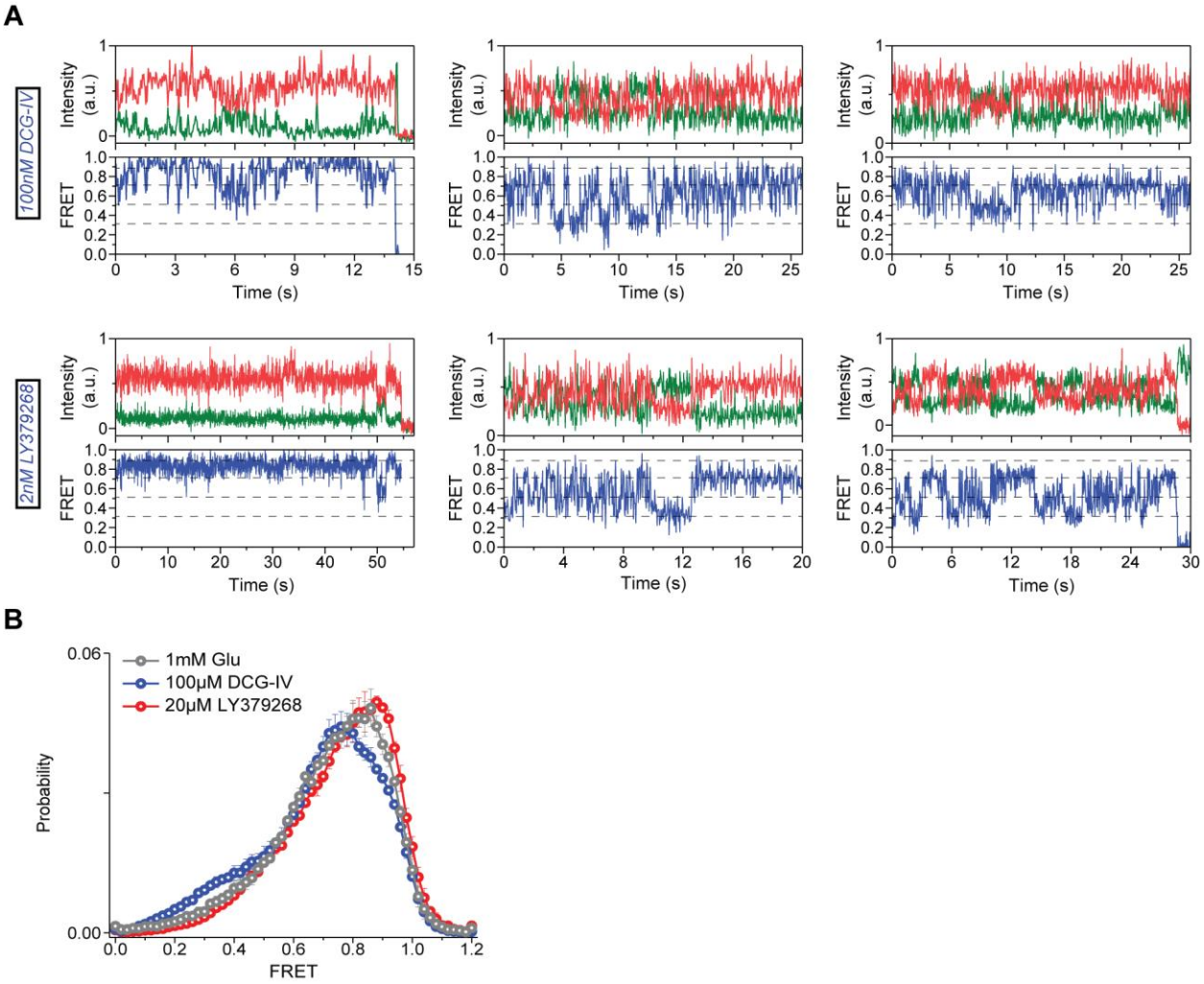

Figure S2.7 smFRET analysis of CRD in the presence of orthosteric agonists
(A) Example single-molecule time traces of 548UAA at intermediate concentrations of DCG-IV (100 nM, top) and LY379268 (2 nM, bottom) showing donor (green) and acceptor (red) intensities and corresponding FRET (blue). Dashed lines represent 4 distinct FRET states. (B) smFRET population histograms for 548UAA in the presence of saturating glutamate (1 mM; 152 total molecules), DCG-IV (100 μM; 470 total molecules) and LY379268 (20 μM; 356 total molecules). Data represent mean ± s.e.m. of N=3 independent experiments.

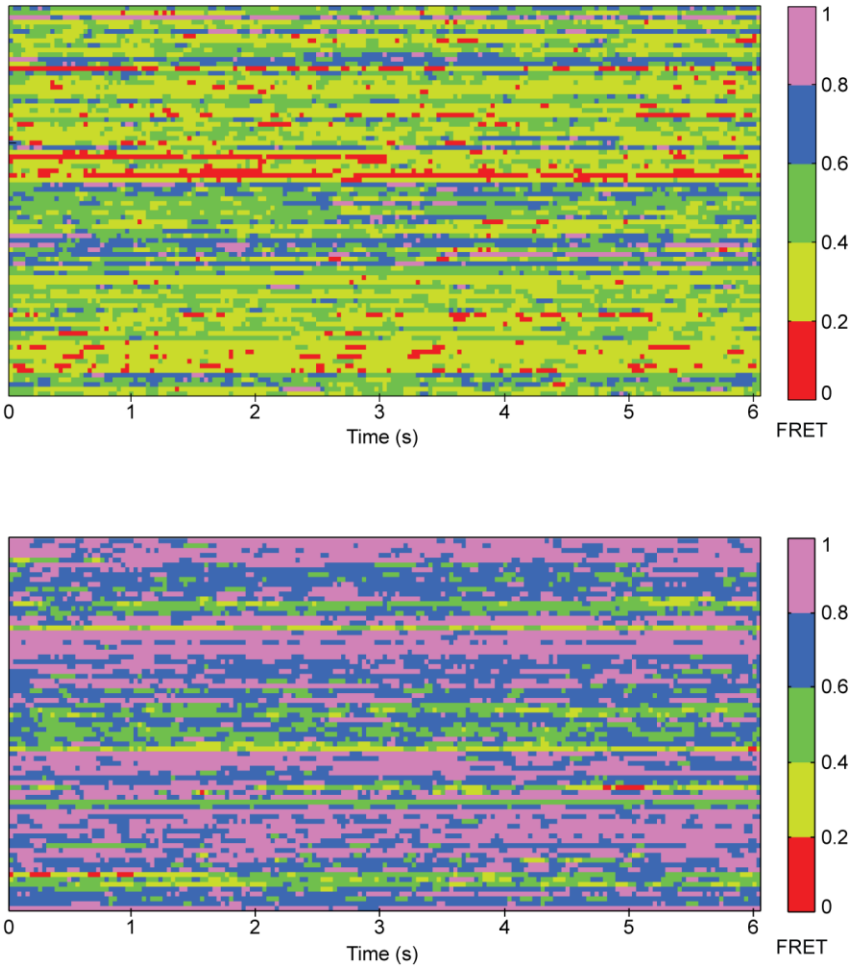

Figure S2.8 CRDs of mGluR2 are dynamic
Heatmap illustrating the FRET values sampled by individual 548UAA receptors in the inactive (0 μM glutamate, top) and fully active (1 mM glutamate, bottom) conditions. Each row is the smFRET time trace of a single molecule over 6 seconds. The smFRET traces were smoothed using a 3-point moving average filter. 100 independent molecules are shown for each condition.

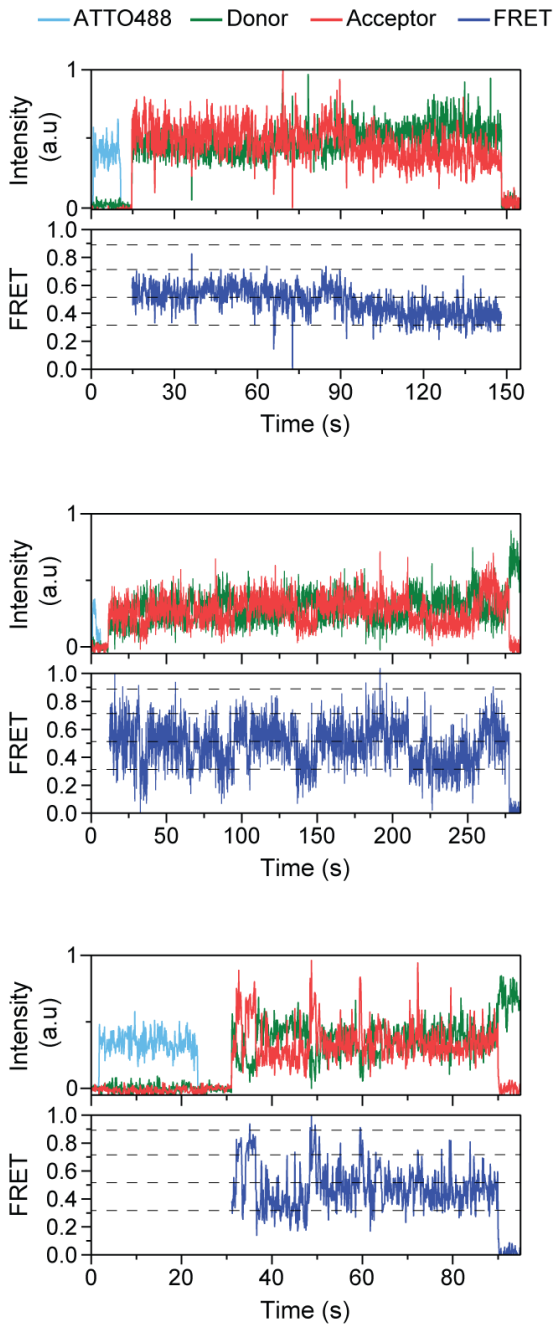

Figure S2.9 Analysis of conformational state 2 and state 4
Example single-molecule time traces of 548UAA YADA/WT heterodimers at 20 µM glutamate. ATTO488 (light blue), donor (green) and acceptor (red) intensities and the corresponding FRET (blue) are shown. Dashed lines represent 4 distinct FRET states. Data was acquired at 100 ms time resolution.

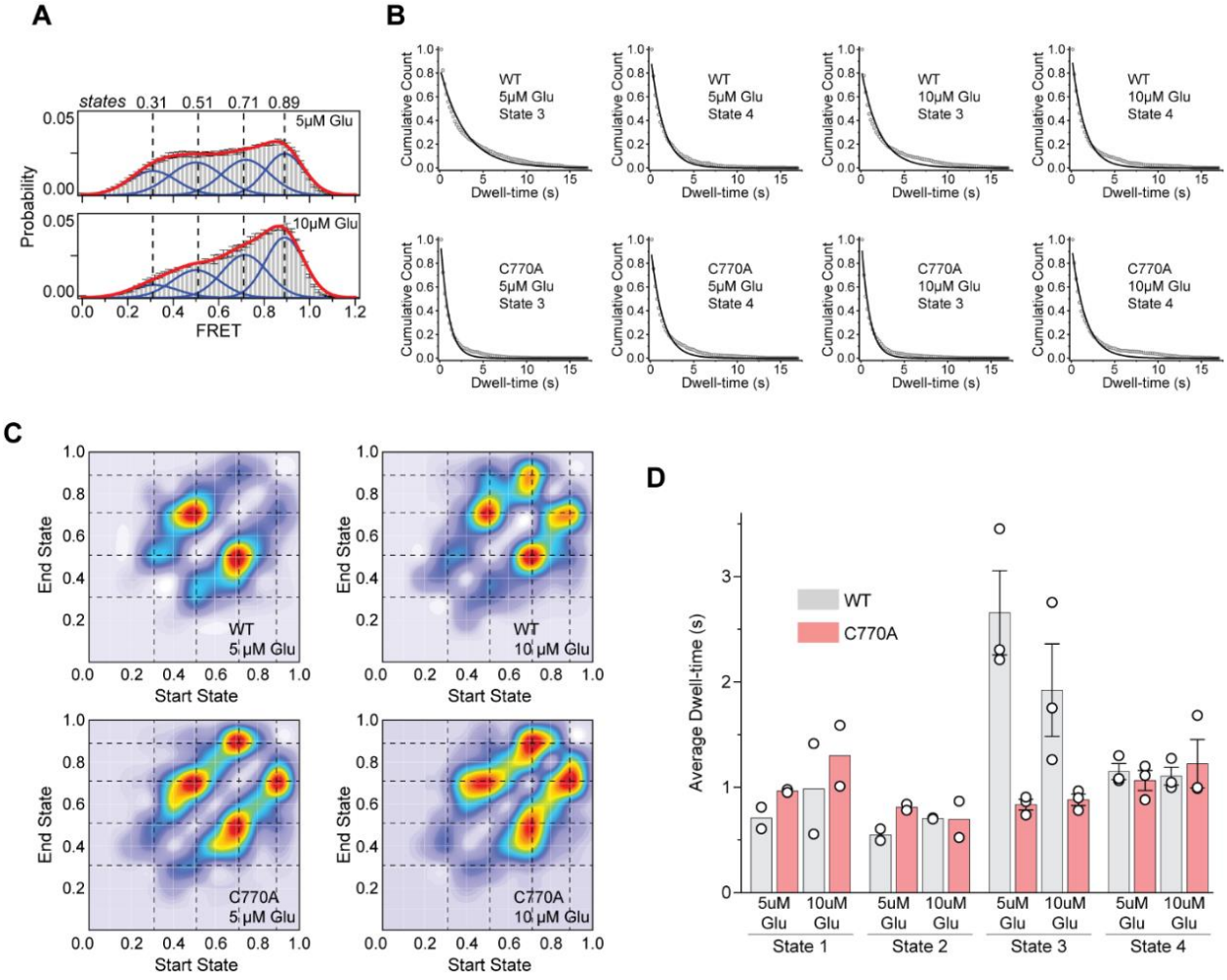

Figure S2.10 Characterization of the mGluR2 PAM mutant conformational dynamics
(A) smFRET population histograms of 548UAA PAM mutant (C770A) in the presence of 5 μM (689 total molecules) or 10 μM (370 total molecules) glutamate. Histograms are fitted (red) to 4 Gaussian distributions (blue) centered around 0.31 (state 1), 0.51 (state 2), 0.71 (state 3) and 0.89 (state 4), denoted with dashed lines. Data represent mean ± s.e.m. of N=3 independent experiments. (B) Normalized histograms of state 3 (pre-active) and state 4 (active) dwell-times (cumulative count) in the presence of 5 or 10 μM glutamate for 548UAA and 548UAA PAM mutant (C770A). Data is fit to a single exponential decay function. Dwell-times are from > 80 total molecules per condition from two independent experiments. (C) Transition density plots (TDPs) of 548UAA and 548UAA PAM mutant (C770A) at 5 or 10 μM glutamate. Dashed lines represent 4 distinct FRET states. Transitions are compiled from two independent experiments. (D) Dwell-times of states 1-4 for 548UAA and 548UAA PAM mutant (C770A) in the presence of 5 or 10 μM glutamate. Average dwell-time was calculated by fitting a single exponential decay function to dwell-time histograms for each condition. Dwell-times of states 1 and 2 represent the mean of

N=2 independent experiments with 86, 83, 91 and 72 total molecules examined for WT (5 μM), WT (10 μM), C770A (5 μM) and C770A (10 μM), respectively. Dwell-times of states 3 and 4 represent the mean ± s.e.m. of N=3 independent experiments with 147, 140, 128 and 142 total molecules examined for WT (5 μM), WT (10 μM), C770A (5 μM) and C770A (10 μM), respectively. Transition and dwell-time analysis were performed on 100 ms data.

Appendix B: Supplemental data for chapter 3

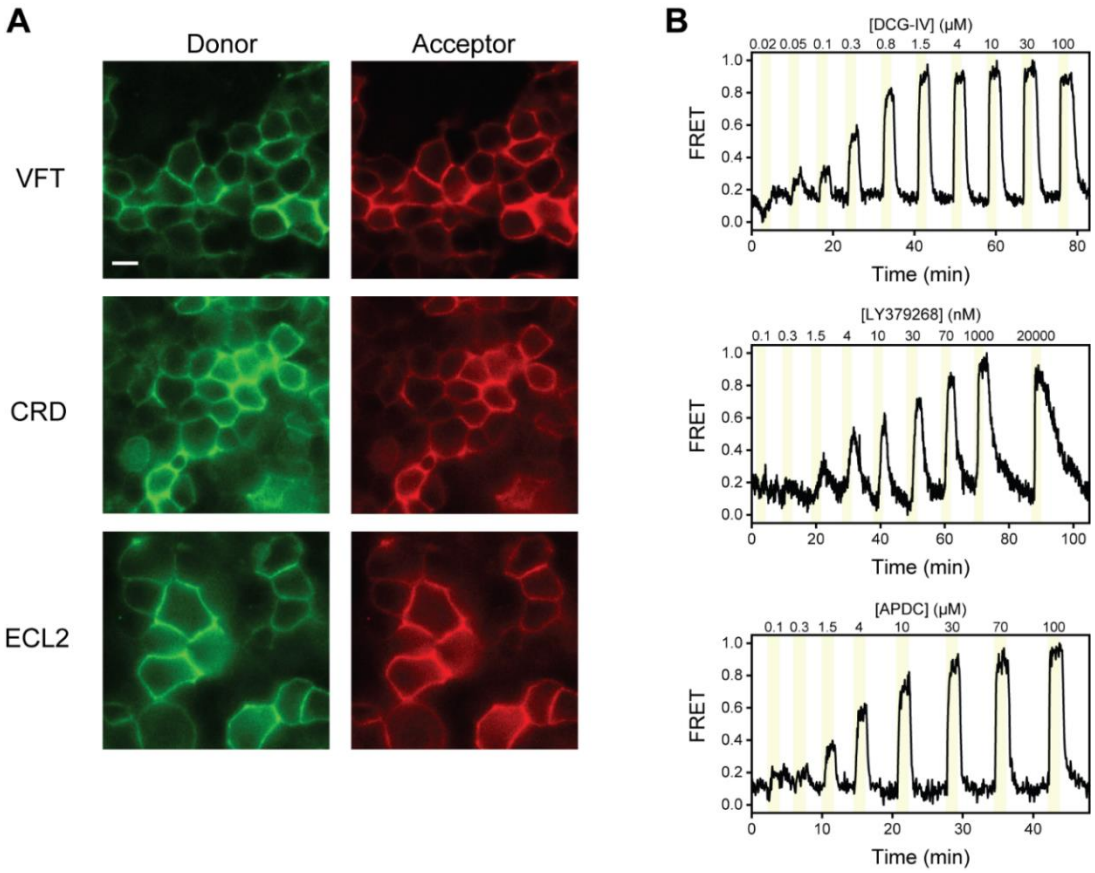

Figure S3.1 Representative images and FRET traces from live-cell FRET experiments
(A) Representative image of HEK293T cells expressing SNAP-m2, azi-CRD, or azi-ECL2 labeled with donor (left) and acceptor (right) fluorophores used for live-cell FRET experiments. Scale bar, 10 μM. (B) Representative normalized live-cell FRET traces of DCG-IV, LY379268, and (2R,4R)-APDC titration experiments on HEK293T cells expressing azi-ECL2. Data was acquired at 4.5 s time resolution.

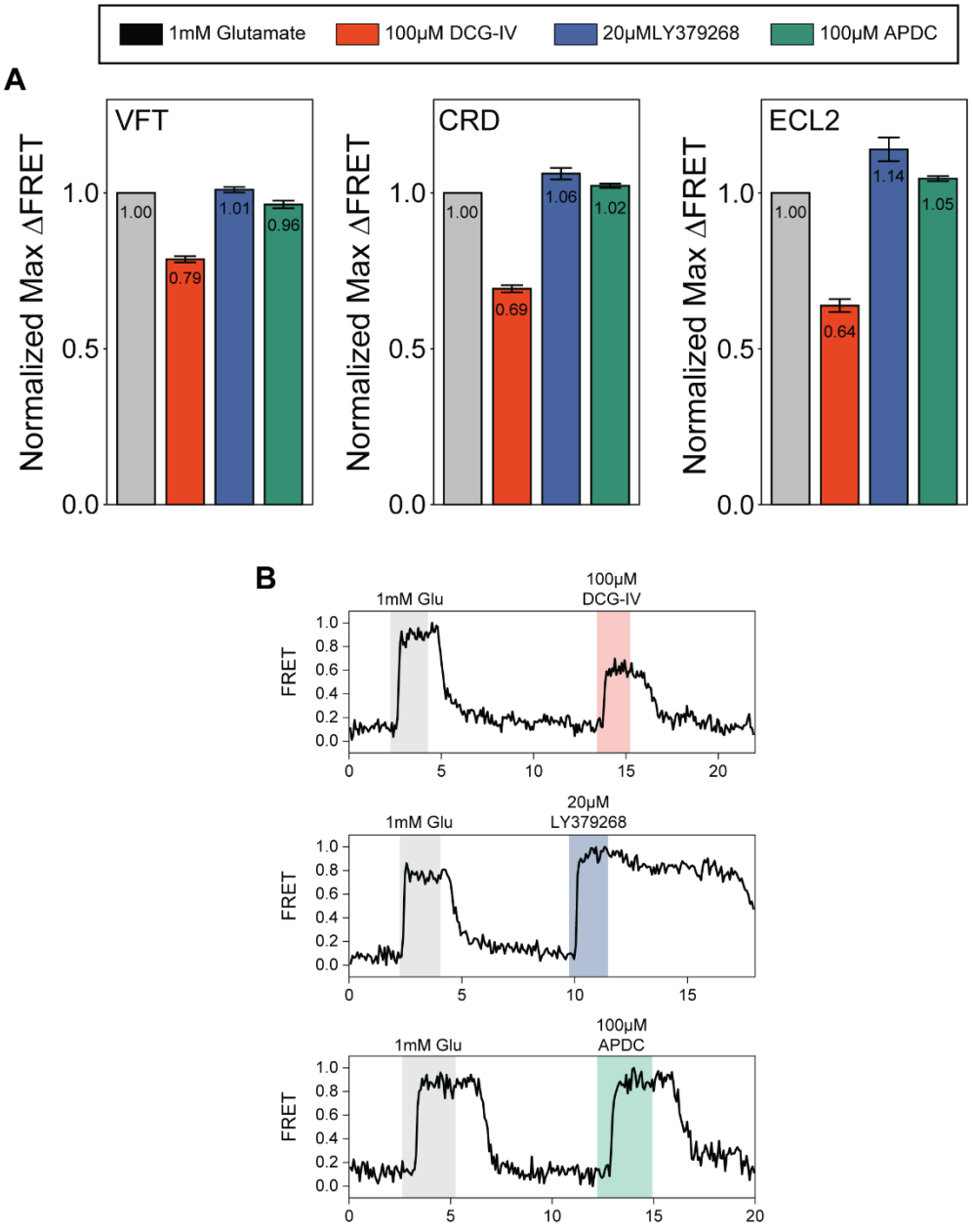

Figure S3.2 Quantification of orthosteric agonist efficacy
(A) Normalized maximal agonist-induced FRET change for SNAP-m2, azi-CRD, and azi-ECL2 sensors. Data represents mean ± s.e.m. of responses from individual cells from at least three independent experiments. Total number of cells examined for normalization experiments, mean max response, and errors are listed in Table 2. (B) Representative normalized live-cell FRET traces from DCG-IV, LY379268, and (2R,4R)-APDC normalization experiments of azi-ECL2. Data is normalized to 1 mM glutamate response and collected at 4.5 s time resolution.

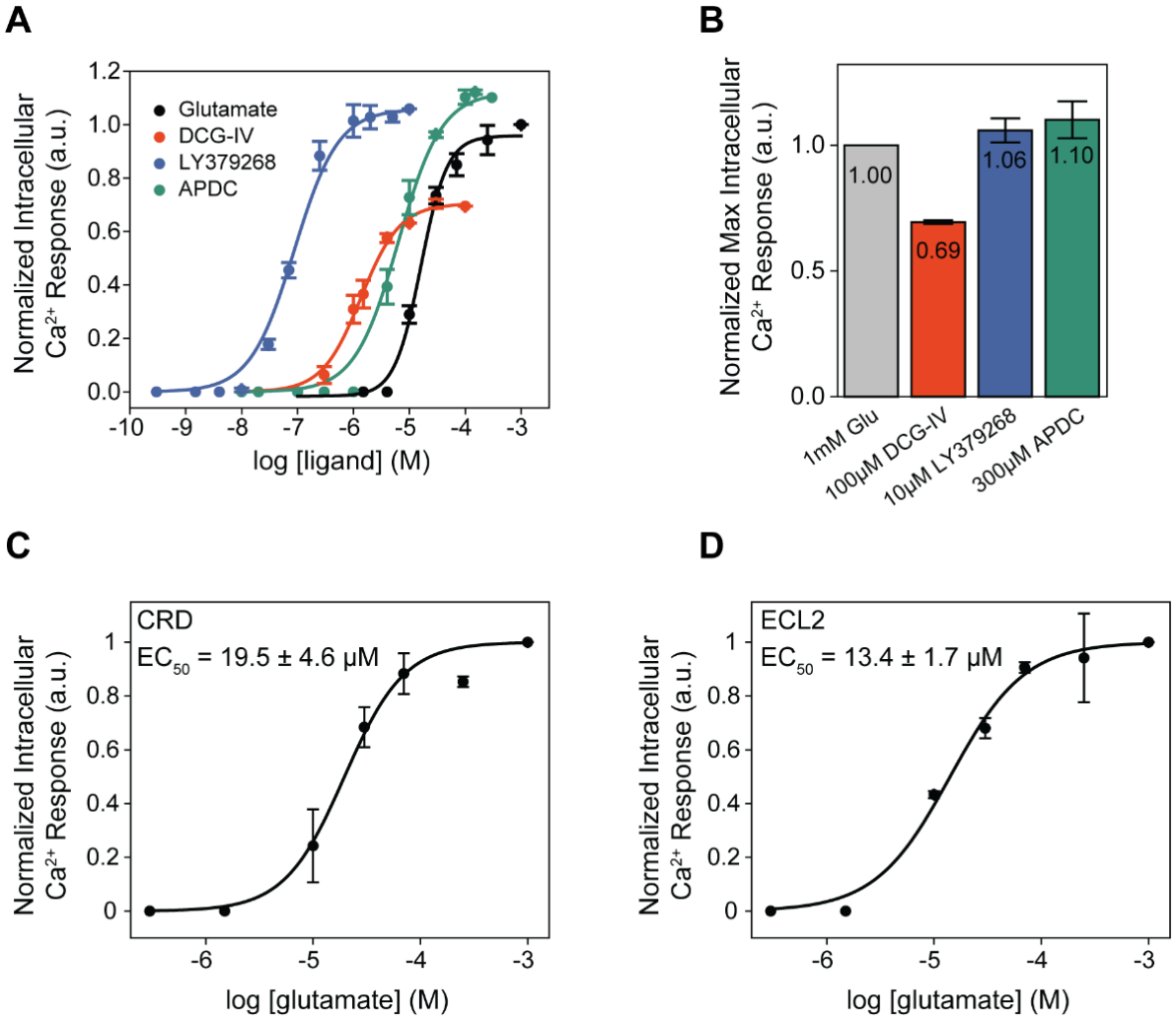

Figure S3.3 Orthosteric agonists examined by functional calcium imaging
(A) Dose-response curves for mGluR2-induced calcium flux during orthosteric agonist titrations. (B) Normalized maximal agonist-induced intracellular calcium levels. Glutamate dose-response curves for calcium flux induced by (C) azi-CRD and (D) azi-ECL2. Data is normalized to 1 mM glutamate response. Data represents mean ± s.e.m. of results from three independent experiments.

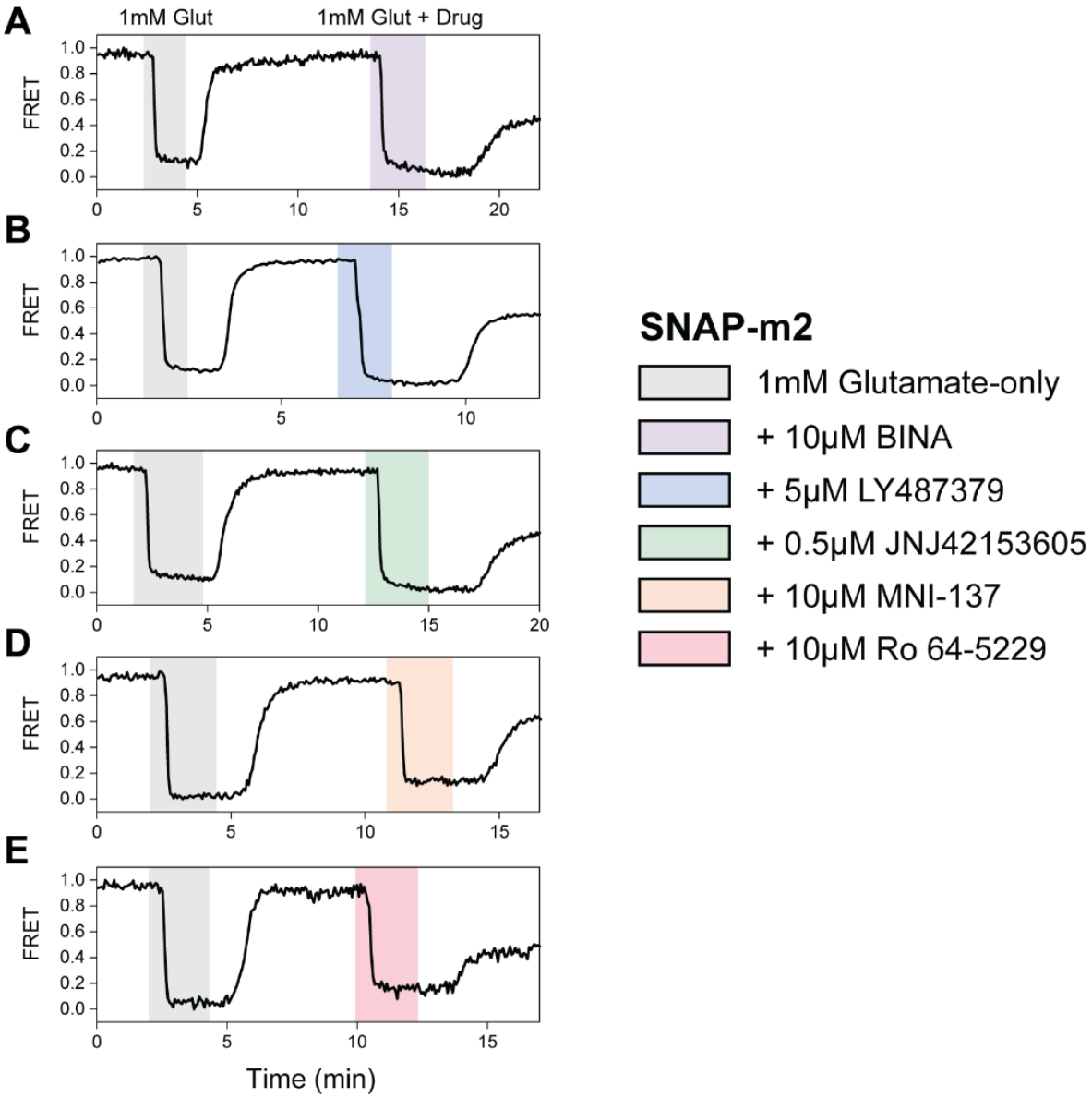

Figure S3.4 Max normalization of ΔFRET for SNAP-m2
(A-E) Representative normalized live-cell FRET traces of SNAP-m2 normalization experiments for all PAMs and NAMs tested. Data was acquired at 4 s time resolution.

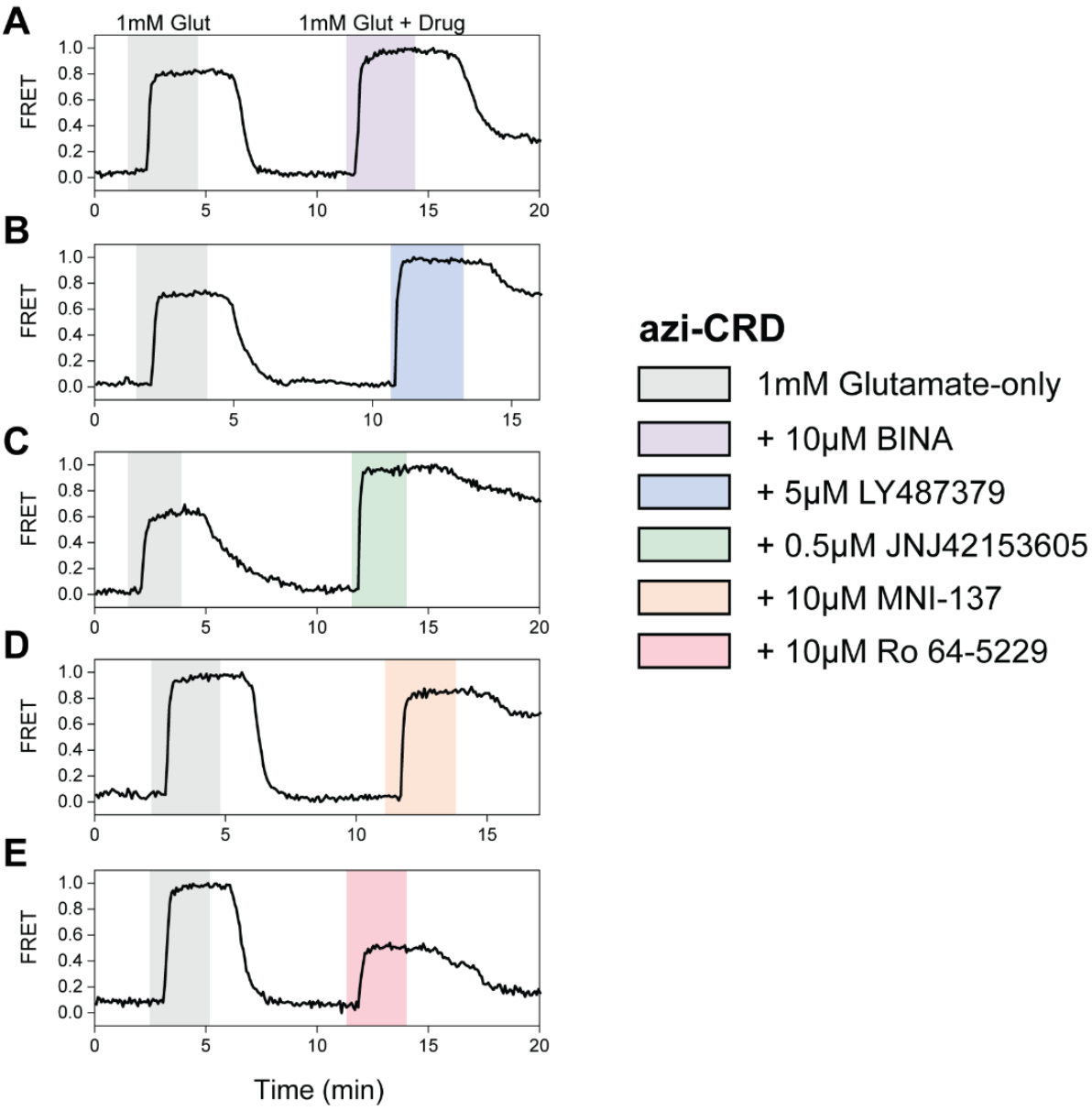

Figure S3.5 Max normalization of ΔFRET for azi-CRD
(A-E) Representative normalized live-cell FRET traces of azi-CRD normalization experiments for all PAMs and NAMs tested. Data was acquired at 4.5 s time resolution.

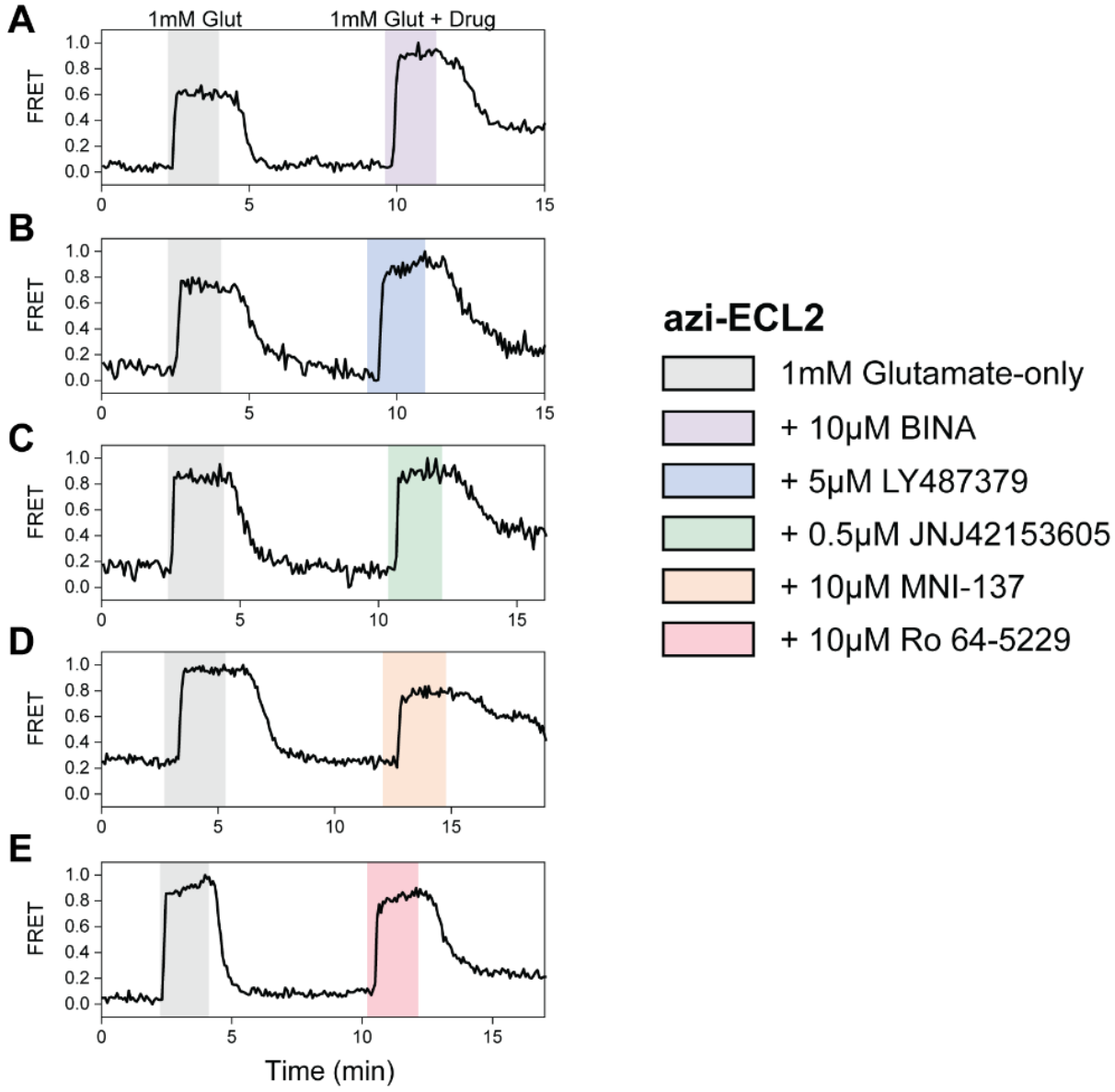

Figure S3.6 Max normalization of ΔFRET for azi-ECL2
(A-E) Representative normalized live-cell FRET traces of azi-ECL2 normalization experiments for all PAMs and NAMs tested. Data was acquired at 4.5 s time resolution.

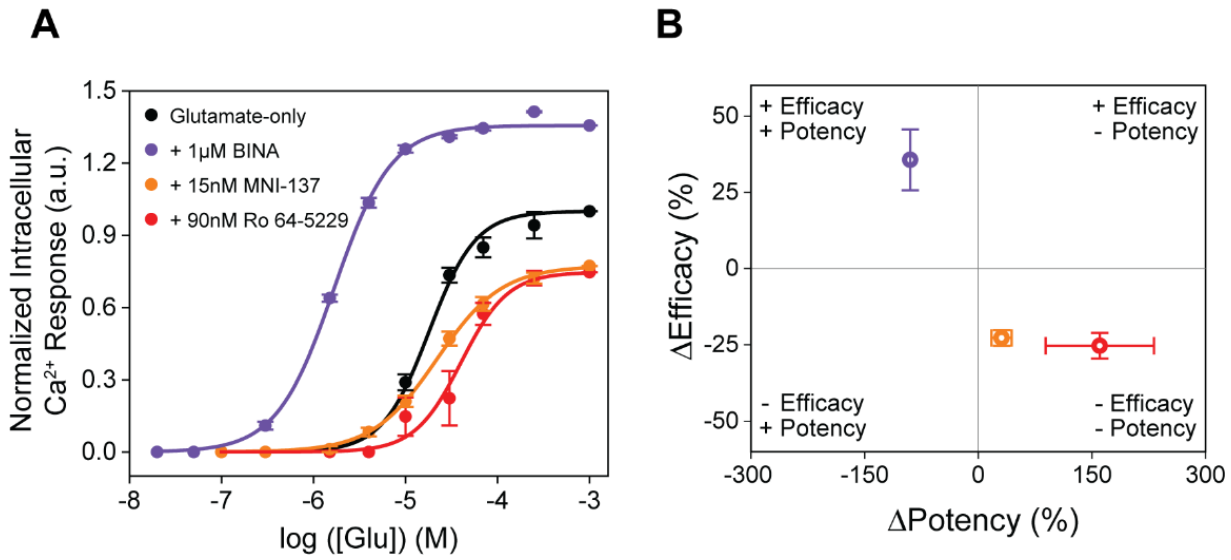

Figure S3.7 Allosteric modulators examined by functional calcium imaging
(A) Glutamate dose-response curves with and without allosteric modulators for mGluR2-induced calcium flux. (B) Changes in glutamate potency and efficacy in response to allosteric modulator treatment, measured by intracellular calcium levels. ΔPotency defined as (([modulator + glutamate]$_{EC50}$ – [glutamate]$_{EC50}$)/[glutamate]$_{EC50}$) × 100. ΔEfficacy defined as ([1 mM glutamate + modulator] - [1 mM glutamate]) × 100. Data is normalized to 1 mM glutamate response. Data represents mean ± s.e.m. of results from three independent experiments.

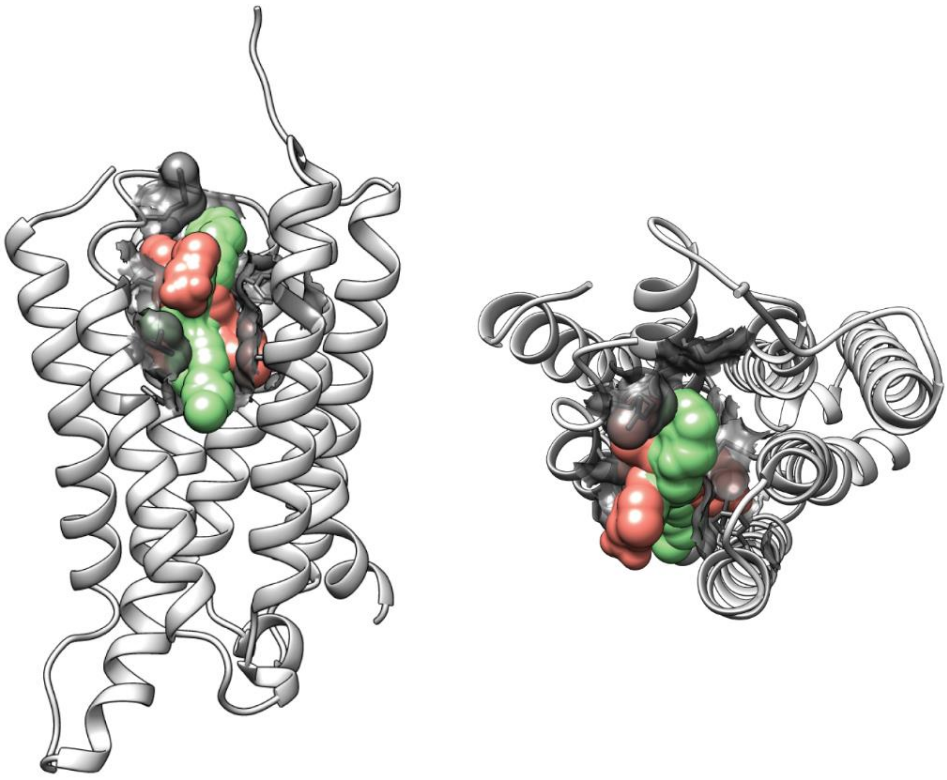

Figure S3.8 Structural representation of allosteric modulator binding pocket
7TM domain (white) is from PAM bound subunit of mGluR2 (PDB:7MTS). Lateral view (left) and top view (right). Residues found to interact with PAM in structure (PDB: 7MTS) and from mutagenesis studies are shown with surface representations (grey). Ligands bound are superimposed volumes of PAMs (green; PDB: 7MTR, 7MTS, 7E9G) and NAMs (pink; PDB: 7EPE, 7EPF) solved in complex with mGluR2.

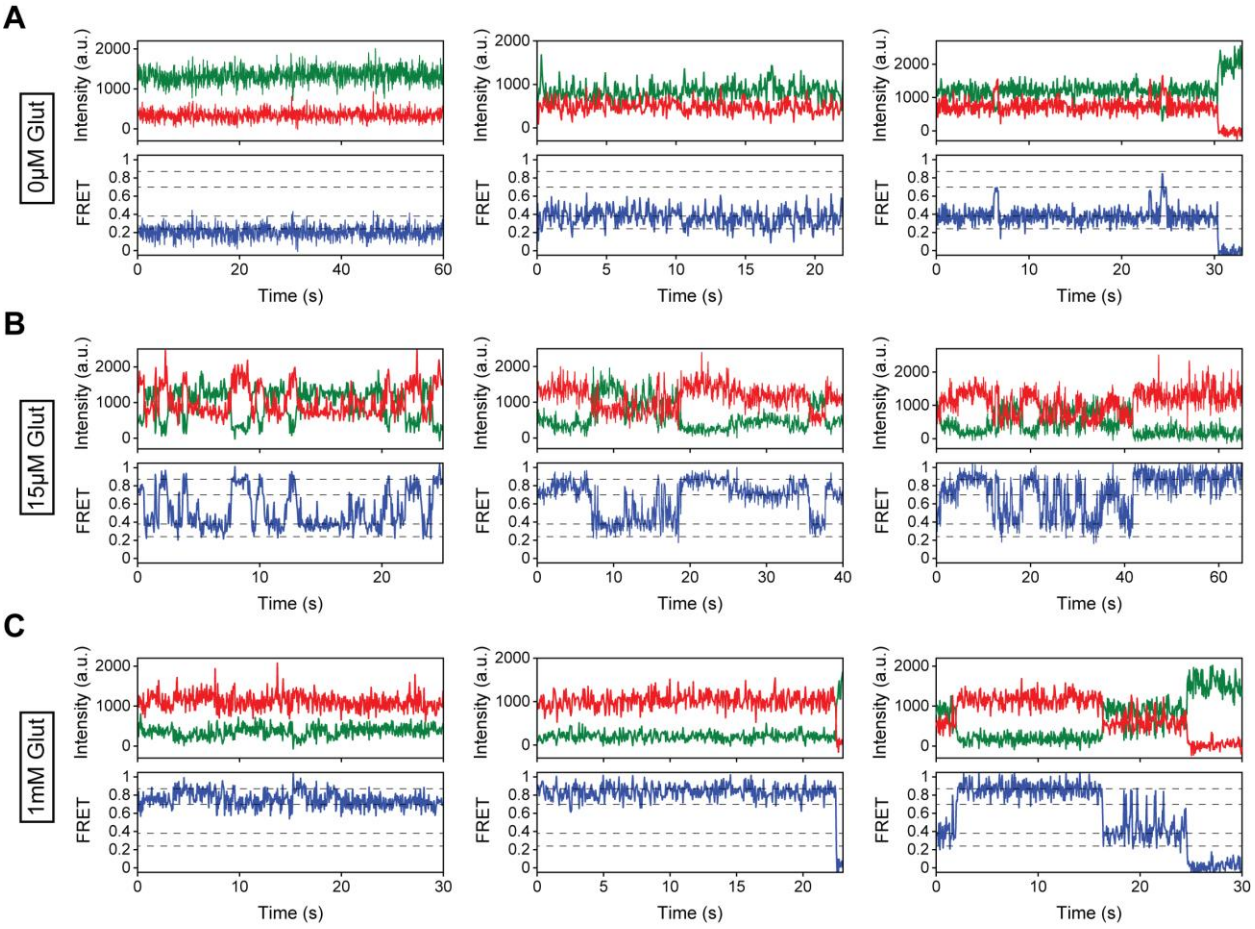

Figure S3.9 Representative smFRET traces for modulator-free conditions
(A-C) Representative smFRET traces of azi-CRD in the presence of (A) 0 μM, (B) 15 μM, and (C) 1 mM glutamate showing donor (green) and acceptor (red) and corresponding FRET (blue). Dashed lines represent 4 distinct FRET states. Data was acquired at 50 ms time resolution.

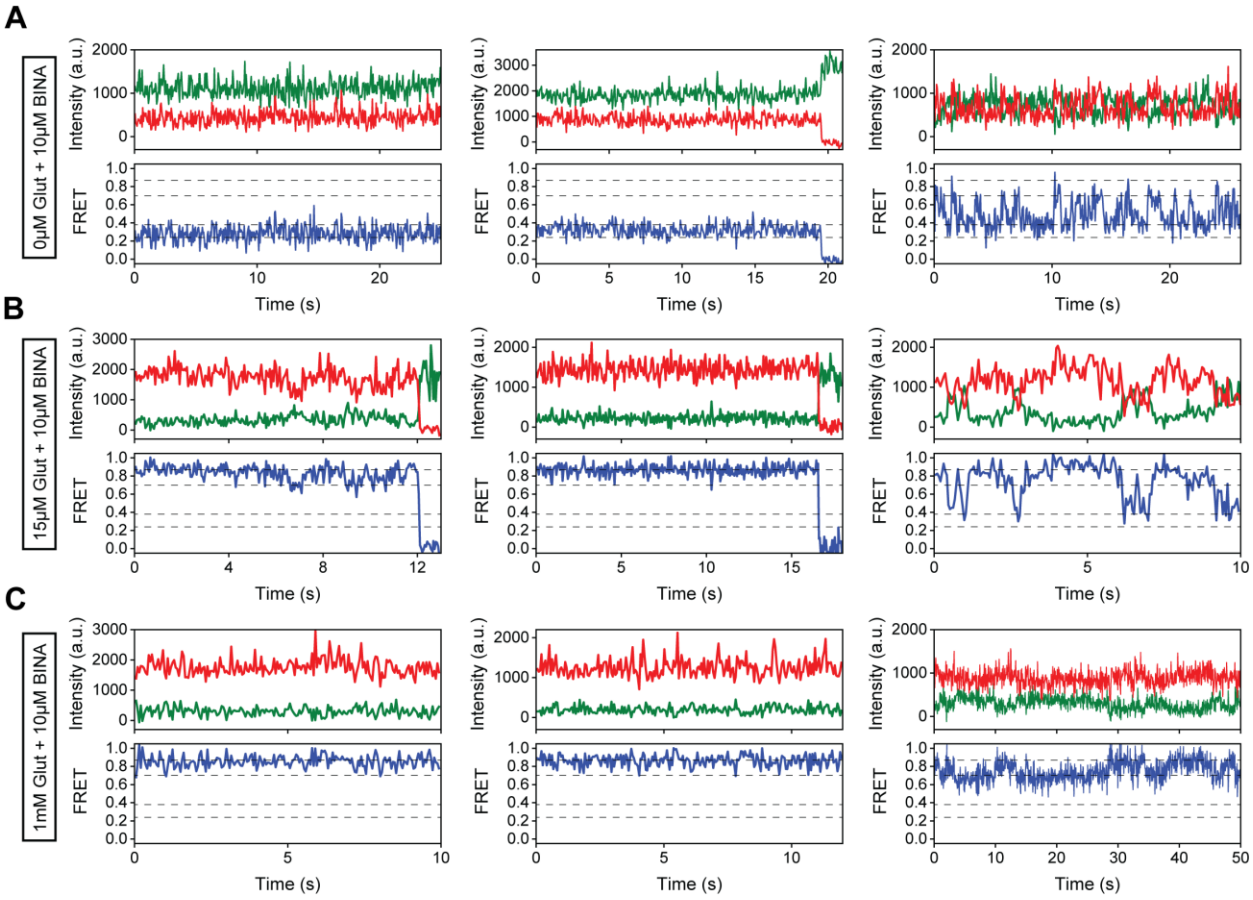

Figure S3.10 Representative smFRET traces for 10 μM BINA conditions
(A-C) Representative smFRET traces of azi-CRD in the presence of 10 μM BINA and (A) 0 μM, (B) 15 μM, and (C) 1 mM glutamate showing donor (green) and acceptor (red) and corresponding FRET (blue). Dashed lines represent 4 distinct FRET states. Data was acquired at 50 ms time resolution.

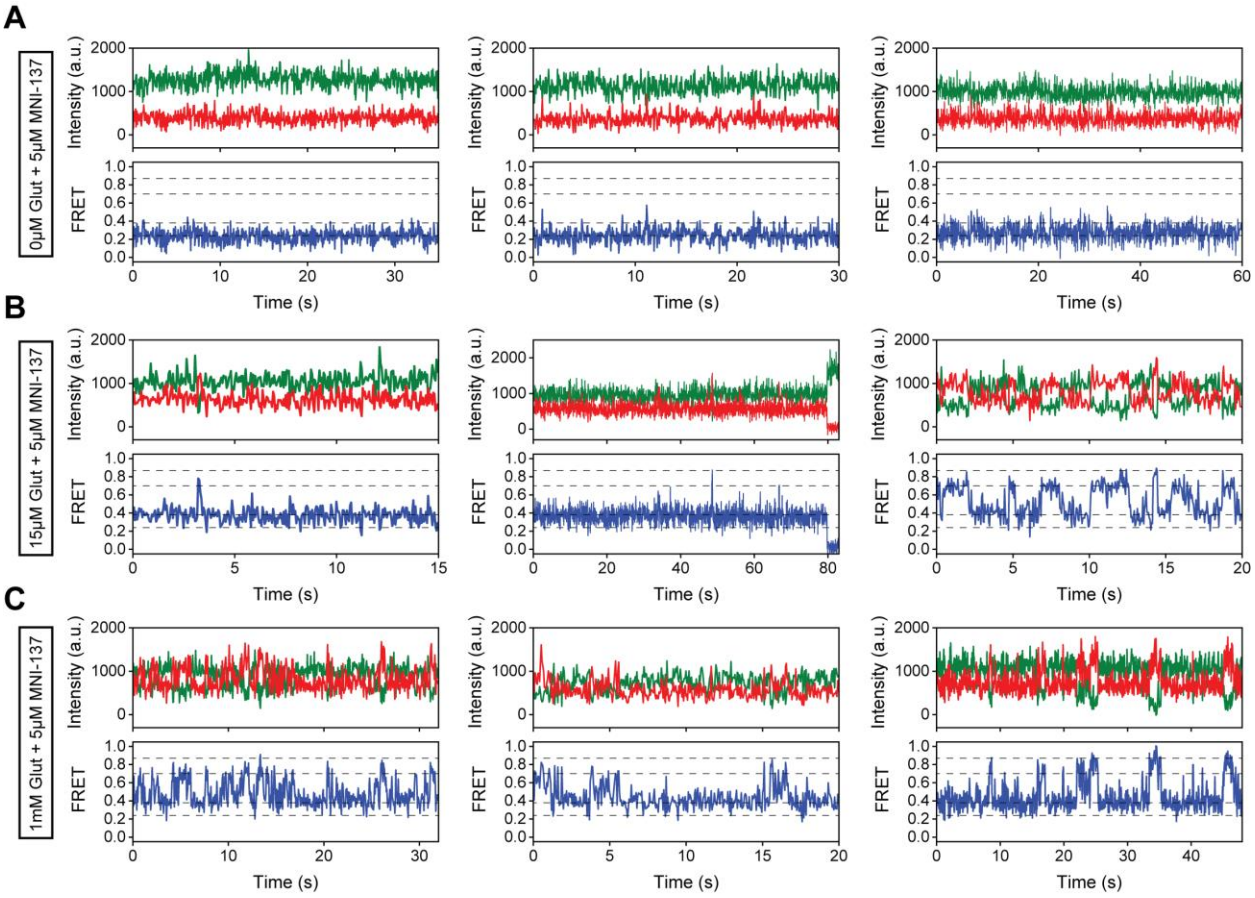

Figure S3.11 Representative smFRET traces for 5 μM MNI-137 conditions
(A-C) Representative smFRET traces of azi-CRD in the presence of 5 μM MNI-137 and (A) 0 μM, (B) 15 μM, and (C) 1 mM glutamate showing donor (green) and acceptor (red) and corresponding FRET (blue). Dashed lines represent 4 distinct FRET states. Data was acquired at 50 ms time resolution.

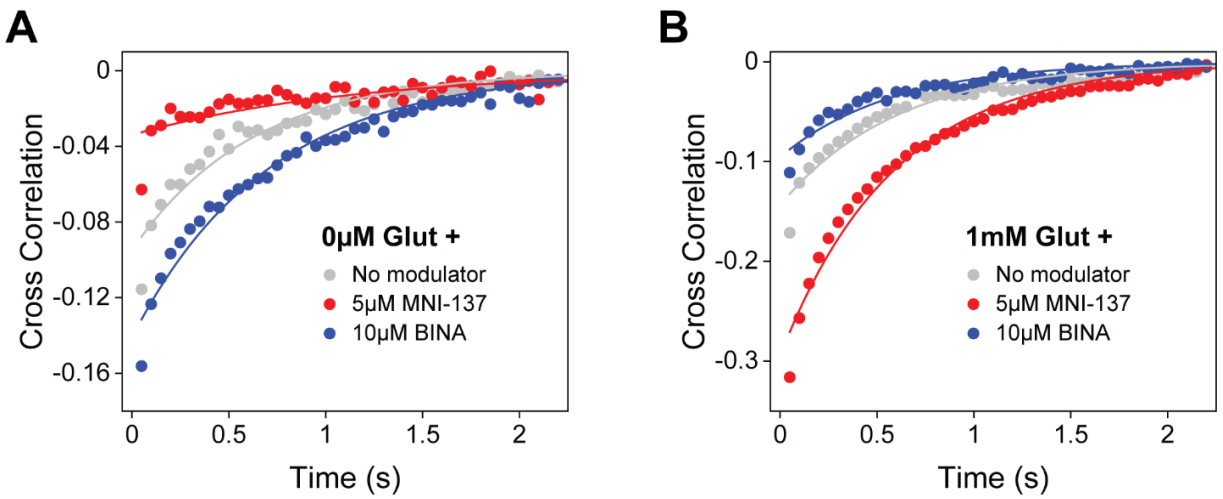

Figure S3.12 Allosteric modulator effects on azi-CRD cross correlation
(A) Cross-correlation of azi-CRD donor and acceptor intensities in the presence of 0 μM glutamate alone and with 5 μM MNI-137 or 10 μM BINA. (B) Cross-correlation of azi-CRD donor and acceptor intensities in the presence of 1 mM glutamate alone and with 5 μM MNI-137 or 10 μM BINA. Data was acquired at 50 ms time resolution.

References

Smock, R. G., & Gierasch, L. M. (2009). Sending signals dynamically. *Science, 324*(5924), 198-203. https://doi.org/10.1126/science.1169377

Regard, J. B., Sato, I. T., & Coughlin, S. R. (2008). Anatomical profiling of G protein-coupled receptor expression. *Cell, 135*(3), 561-571. https://doi.org/10.1016/j.cell.2008.08.040

Niswender, C. M., & Conn, P. J. (2010). Metabotropic glutamate receptors: physiology, pharmacology, and disease. *Annu Rev Pharmacol Toxicol, 50*, 295-322. https://doi.org/10.1146/annurev.pharmtox.011008.145533

Wootten, D., Christopoulos, A., Marti-Solano, M., Babu, M. M., & Sexton, P. M. (2018). Mechanisms of signalling and biased agonism in G protein-coupled receptors. *Nat Rev Mol Cell Biol, 19*(10), 638-653. https://doi.org/10.1038/s41580-018-0049-3

Hauser, A. S., Attwood, M. M., Rask-Andersen, M., Schiöth, H. B., & Gloriam, D. E. (2017). Trends in GPCR drug discovery: new agents, targets and indications. *Nat Rev Drug Discov, 16*(12), 829-842. https://doi.org/10.1038/nrd.2017.178

Ciancetta, A., Sabbadin, D., Federico, S., Spalluto, G., & Moro, S. (2015). Advances in computational techniques to study GPCR–ligand recognition. *Trends in pharmacological sciences, 36*(12), 878-890.

Lee, Y., Basith, S., & Choi, S. (2018). Recent advances in structure-based drug design targeting class AG protein-coupled receptors utilizing crystal structures and computational simulations. *Journal of Medicinal Chemistry, 61*(1), 1-46.

Rasmussen, S. G., DeVree, B. T., Zou, Y., Kruse, A. C., Chung, K. Y., Kobilka, T. S., Thian, F. S., Chae, P. S., Pardon, E., Calinski, D., Mathiesen, J. M., Shah, S. T., Lyons, J. A., Caffrey, M., Gellman, S. H., Steyaert, J., Skiniotis, G., Weis, W. I., Sunahara, R. K., & Kobilka, B. K. (2011). Crystal structure of the β2 adrenergic receptor-Gs protein complex. *Nature, 477*(7366), 549-555. https://doi.org/10.1038/nature10361

Flock, T., Ravarani, C. N. J., Sun, D., Venkatakrishnan, A. J., Kayikci, M., Tate, C. G., Veprintsev, D. B., & Babu, M. M. (2015). Universal allosteric mechanism for Gα activation by GPCRs. *Nature, 524*(7564), 173-179. https://doi.org/10.1038/nature14663

Zhou, Q., Yang, D., Wu, M., Guo, Y., Guo, W., Zhong, L., Cai, X., Dai, A., Jang, W., Shakhnovich, E. I., Liu, Z. J., Stevens, R. C., Lambert, N. A., Babu, M. M., Wang, M. W., & Zhao, S. (2019). Common activation mechanism of class A GPCRs. *Elife, 8*. https://doi.org/10.7554/eLife.50279

Basith, S., Cui, M., Macalino, S. J. Y., Park, J., Clavio, N. A. B., Kang, S., & Choi, S. (2018). Exploring G Protein-Coupled Receptors (GPCRs) Ligand Space via Cheminformatics Approaches: Impact on Rational Drug Design. *Front Pharmacol, 9*, 128. https://doi.org/10.3389/fphar.2018.00128

Boulter, J., Hollmann, M., O'Shea-Greenfield, A., Hartley, M., Deneris, E., Maron, C., & Heinemann, S. (1990). Molecular cloning and functional expression of glutamate receptor subunit genes. *Science, 249*(4972), 1033-1037. https://doi.org/10.1126/science.2168579

Moriyoshi, K., Masu, M., Ishii, T., Shigemoto, R., Mizuno, N., & Nakanishi, S. (1991). Molecular cloning and characterization of the rat NMDA receptor. *Nature, 354*(6348), 31-37. https://doi.org/10.1038/354031a0

Hollmann, M., O'Shea-Greenfield, A., Rogers, S. W., & Heinemann, S. (1989). Cloning by functional expression of a member of the glutamate receptor family. *Nature*, *342*(6250), 643-648. https://doi.org/10.1038/342643a0

Nicoletti, F., Wroblewski, J. T., Novelli, A., Alho, H., Guidotti, A., & Costa, E. (1986). The activation of inositol phospholipid metabolism as a signal-transducing system for excitatory amino acids in primary cultures of cerebellar granule cells. *J Neurosci*, *6*(7), 1905-1911. https://doi.org/10.1523/jneurosci.06-07-01905.1986

Sladeczek, F., Pin, J. P., Récasens, M., Bockaert, J., & Weiss, S. (1985). Glutamate stimulates inositol phosphate formation in striatal neurones. *Nature*, *317*(6039), 717-719. https://doi.org/10.1038/317717a0

Sugiyama, H., Ito, I., & Hirono, C. (1987). A new type of glutamate receptor linked to inositol phospholipid metabolism. *Nature*, *325*(6104), 531-533. https://doi.org/10.1038/325531a0

Houamed, K. M., Kuijper, J. L., Gilbert, T. L., Haldeman, B. A., O'Hara, P. J., Mulvihill, E. R., Almers, W., & Hagen, F. S. (1991). Cloning, expression, and gene structure of a G protein-coupled glutamate receptor from rat brain. *Science*, *252*(5010), 1318-1321. https://doi.org/10.1126/science.1656524

Abe, T., Sugihara, H., Nawa, H., Shigemoto, R., Mizuno, N., & Nakanishi, S. (1992). Molecular characterization of a novel metabotropic glutamate receptor mGluR5 coupled to inositol phosphate/Ca2+ signal transduction. *J Biol Chem*, *267*(19), 13361-13368.

Duvoisin, R. M., Zhang, C., & Ramonell, K. (1995). A novel metabotropic glutamate receptor expressed in the retina and olfactory bulb. *J Neurosci*, *15*(4), 3075-3083. https://doi.org/10.1523/jneurosci.15-04-03075.1995

Nakanishi, S. (1992). Molecular diversity of glutamate receptors and implications for brain function. *Science*, *258*(5082), 597-603. https://doi.org/10.1126/science.1329206

Okamoto, N., Hori, S., Akazawa, C., Hayashi, Y., Shigemoto, R., Mizuno, N., & Nakanishi, S. (1994). Molecular characterization of a new metabotropic glutamate receptor mGluR7 coupled to inhibitory cyclic AMP signal transduction. *J Biol Chem*, *269*(2), 1231-1236.

Tanabe, Y., Masu, M., Ishii, T., Shigemoto, R., & Nakanishi, S. (1992). A family of metabotropic glutamate receptors. *Neuron*, *8*(1), 169-179. https://doi.org/10.1016/0896-6273(92)90118-w

Nakajima, Y., Iwakabe, H., Akazawa, C., Nawa, H., Shigemoto, R., Mizuno, N., & Nakanishi, S. (1993). Molecular characterization of a novel retinal metabotropic glutamate receptor mGluR6 with a high agonist selectivity for L-2-amino-4-phosphonobutyrate. *J Biol Chem*, *268*(16), 11868-11873.

Abreu, N., Acosta-Ruiz, A., Xiang, G., & Levitz, J. (2021). Mechanisms of differential desensitization of metabotropic glutamate receptors. *Cell Rep*, *35*(4), 109050. https://doi.org/10.1016/j.celrep.2021.109050

Eng, A. G., Kelver, D. A., Hedrick, T. P., & Swanson, G. T. (2016). Transduction of group I mGluR-mediated synaptic plasticity by β-arrestin2 signalling. *Nat Commun*, *7*, 13571. https://doi.org/10.1038/ncomms13571

Hermans, E., & Challiss, R. A. (2001). Structural, signalling and regulatory properties of the group I metabotropic glutamate receptors: prototypic family C G-protein-coupled receptors. *Biochem J*, *359*(Pt 3), 465-484. https://doi.org/10.1042/0264-6021:3590465

Iacovelli, L., Bruno, V., Salvatore, L., Melchiorri, D., Gradini, R., Caricasole, A., Barletta, E., De Blasi, A., & Nicoletti, F. (2002). Native group-III metabotropic glutamate receptors are coupled to the mitogen-activated protein kinase/phosphatidylinositol-3-kinase pathways. *J Neurochem, 82*(2), 216-223. https://doi.org/10.1046/j.1471-4159.2002.00929.x

Doumazane, E., Scholler, P., Zwier, J. M., Trinquet, E., Rondard, P., & Pin, J. P. (2011). A new approach to analyze cell surface protein complexes reveals specific heterodimeric metabotropic glutamate receptors. *Faseb j, 25*(1), 66-77. https://doi.org/10.1096/fj.10-163147

Habrian, C. H., Levitz, J., Vyklicky, V., Fu, Z., Hoagland, A., McCort-Tranchepain, I., Acher, F., & Isacoff, E. Y. (2019). Conformational pathway provides unique sensitivity to a synaptic mGluR. *Nat Commun, 10*(1), 5572. https://doi.org/10.1038/s41467-019-13407-8

Levitz, J., Habrian, C., Bharill, S., Fu, Z., Vafabakhsh, R., & Isacoff, E. Y. (2016). Mechanism of Assembly and Cooperativity of Homomeric and Heteromeric Metabotropic Glutamate Receptors. *Neuron, 92*(1), 143-159. https://doi.org/10.1016/j.neuron.2016.08.036

Liu, J., Zhang, Z., Moreno-Delgado, D., Dalton, J. A., Rovira, X., Trapero, A., Goudet, C., Llebaria, A., Giraldo, J., Yuan, Q., Rondard, P., Huang, S., Liu, J., & Pin, J. P. (2017). Allosteric control of an asymmetric transduction in a G protein-coupled receptor heterodimer. *Elife, 6*. https://doi.org/10.7554/eLife.26985

Lindsley, C. W., Emmitte, K. A., Hopkins, C. R., Bridges, T. M., Gregory, K. J., Niswender, C. M., & Conn, P. J. (2016). Practical Strategies and Concepts in GPCR Allosteric Modulator Discovery: Recent Advances with Metabotropic Glutamate Receptors. *Chem Rev, 116*(11), 6707-6741. https://doi.org/10.1021/acs.chemrev.5b00656

O'Hara, P. J., Sheppard, P. O., Thøgersen, H., Venezia, D., Haldeman, B. A., McGrane, V., Houamed, K. M., Thomsen, C., Gilbert, T. L., & Mulvihill, E. R. (1993). The ligand-binding domain in metabotropic glutamate receptors is related to bacterial periplasmic binding proteins. *Neuron, 11*(1), 41-52. https://doi.org/10.1016/0896-6273(93)90269-w

Okamoto, T., Sekiyama, N., Otsu, M., Shimada, Y., Sato, A., Nakanishi, S., & Jingami, H. (1998). Expression and purification of the extracellular ligand binding region of metabotropic glutamate receptor subtype 1. *J Biol Chem, 273*(21), 13089-13096. https://doi.org/10.1074/jbc.273.21.13089

Hampson, D. R., Huang, X. P., Pekhletski, R., Peltekova, V., Hornby, G., Thomsen, C., & Thøgersen, H. (1999). Probing the ligand-binding domain of the mGluR4 subtype of metabotropic glutamate receptor. *J Biol Chem, 274*(47), 33488-33495. https://doi.org/10.1074/jbc.274.47.33488

Kunishima, N., Shimada, Y., Tsuji, Y., Sato, T., Yamamoto, M., Kumasaka, T., Nakanishi, S., Jingami, H., & Morikawa, K. (2000). Structural basis of glutamate recognition by a dimeric metabotropic glutamate receptor. *Nature, 407*(6807), 971-977. https://doi.org/10.1038/35039564

Mølck, C., Harpsøe, K., Gloriam, D. E., Mathiesen, J. M., Nielsen, S. M., & Bräuner-Osborne, H. (2014). mGluR5: exploration of orthosteric and allosteric ligand binding pockets and their applications to drug discovery. *Neurochem Res, 39*(10), 1862-1875. https://doi.org/10.1007/s11064-014-1248-8

Ray, K., & Hauschild, B. C. (2000). Cys-140 is critical for metabotropic glutamate receptor-1 dimerization. *J Biol Chem*, *275*(44), 34245-34251. https://doi.org/10.1074/jbc.M005581200

Romano, C., Miller, J. K., Hyrc, K., Dikranian, S., Mennerick, S., Takeuchi, Y., Goldberg, M. P., & O'Malley, K. L. (2001). Covalent and noncovalent interactions mediate metabotropic glutamate receptor mGlu5 dimerization. *Mol Pharmacol*, *59*(1), 46-53.

Romano, C., Yang, W. L., & O'Malley, K. L. (1996). Metabotropic glutamate receptor 5 is a disulfide-linked dimer. *J Biol Chem*, *271*(45), 28612-28616. https://doi.org/10.1074/jbc.271.45.28612

Tsuji, Y., Shimada, Y., Takeshita, T., Kajimura, N., Nomura, S., Sekiyama, N., Otomo, J., Usukura, J., Nakanishi, S., & Jingami, H. (2000). Cryptic dimer interface and domain organization of the extracellular region of metabotropic glutamate receptor subtype 1. *J Biol Chem*, *275*(36), 28144-28151. https://doi.org/10.1074/jbc.M003226200

Vafabakhsh, R., Levitz, J., & Isacoff, E. Y. (2015). Conformational dynamics of a class C G-protein-coupled receptor. *Nature*, *524*(7566), 497-501. https://doi.org/10.1038/nature14679

Kniazeff, J., Bessis, A. S., Maurel, D., Ansanay, H., Prézeau, L., & Pin, J. P. (2004). Closed state of both binding domains of homodimeric mGlu receptors is required for full activity. *Nat Struct Mol Biol*, *11*(8), 706-713. https://doi.org/10.1038/nsmb794

Liu, X., He, Q., Studholme, D. J., Wu, Q., Liang, S., & Yu, L. (2004). NCD3G: a novel nine-cysteine domain in family 3 GPCRs. *Trends Biochem Sci*, *29*(9), 458-461. https://doi.org/10.1016/j.tibs.2004.07.009

Muto, T., Tsuchiya, D., Morikawa, K., & Jingami, H. (2007a). Structures of the extracellular regions of the group II/III metabotropic glutamate receptors. *Proc Natl Acad Sci U S A*, *104*(10), 3759-3764. https://doi.org/10.1073/pnas.0611577104

Rondard, P., Liu, J., Huang, S., Malhaire, F., Vol, C., Pinault, A., Labesse, G., & Pin, J. P. (2006). Coupling of agonist binding to effector domain activation in metabotropic glutamate-like receptors. *J Biol Chem*, *281*(34), 24653-24661. https://doi.org/10.1074/jbc.M602277200

Doumazane, E., Scholler, P., Fabre, L., Zwier, J. M., Trinquet, E., Pin, J. P., & Rondard, P. (2013a). Illuminating the activation mechanisms and allosteric properties of metabotropic glutamate receptors. *Proc Natl Acad Sci U S A*, *110*(15), E1416-1425. https://doi.org/10.1073/pnas.1215615110

Koehl, A., Hu, H., Feng, D., Sun, B., Zhang, Y., Robertson, M. J., Chu, M., Kobilka, T. S., Laeremans, T., Steyaert, J., Tarrasch, J., Dutta, S., Fonseca, R., Weis, W. I., Mathiesen, J. M., Skiniotis, G., & Kobilka, B. K. (2019a). Structural insights into the activation of metabotropic glutamate receptors. *Nature*, *566*(7742), 79-84. https://doi.org/10.1038/s41586-019-0881-4

Huang, S., Cao, J., Jiang, M., Labesse, G., Liu, J., Pin, J. P., & Rondard, P. (2011). Interdomain movements in metabotropic glutamate receptor activation. *Proc Natl Acad Sci U S A*, *108*(37), 15480-15485. https://doi.org/10.1073/pnas.1107775108

Tateyama, M., Abe, H., Nakata, H., Saito, O., & Kubo, Y. (2004). Ligand-induced rearrangement of the dimeric metabotropic glutamate receptor 1alpha. *Nat Struct Mol Biol*, *11*(7), 637-642. https://doi.org/10.1038/nsmb770

Wu, H., Wang, C., Gregory, K. J., Han, G. W., Cho, H. P., Xia, Y., Niswender, C. M., Katritch, V., Meiler, J., Cherezov, V., Conn, P. J., & Stevens, R. C. (2014). Structure of a class C GPCR metabotropic glutamate receptor 1 bound to an allosteric modulator. *Science*, *344*(6179), 58-64. https://doi.org/10.1126/science.1249489

Doré, A. S., Okrasa, K., Patel, J. C., Serrano-Vega, M., Bennett, K., Cooke, R. M., Errey, J. C., Jazayeri, A., Khan, S., Tehan, B., Weir, M., Wiggin, G. R., & Marshall, F. H. (2014). Structure of class C GPCR metabotropic glutamate receptor 5 transmembrane domain. *Nature*, *511*(7511), 557-562. https://doi.org/10.1038/nature13396

Xu, F., Wu, H., Katritch, V., Han, G. W., Jacobson, K. A., Gao, Z. G., Cherezov, V., & Stevens, R. C. (2011). Structure of an agonist-bound human A2A adenosine receptor. *Science*, *332*(6027), 322-327. https://doi.org/10.1126/science.1202793

Seven, A. B., Barros-Álvarez, X., de Lapeyrière, M., Papasergi-Scott, M. M., Robertson, M. J., Zhang, C., Nwokonko, R. M., Gao, Y., Meyerowitz, J. G., Rocher, J. P., Schelshorn, D., Kobilka, B. K., Mathiesen, J. M., & Skiniotis, G. (2021). G-protein activation by a metabotropic glutamate receptor. *Nature*, *595*(7867), 450-454. https://doi.org/10.1038/s41586-021-03680-3

Du, J., Wang, D., Fan, H., Xu, C., Tai, L., Lin, S., Han, S., Tan, Q., Wang, X., Xu, T., Zhang, H., Chu, X., Yi, C., Liu, P., Wang, X., Zhou, Y., Pin, J. P., Rondard, P., Liu, H., . . . Zhao, Q. (2021). Structures of human mGlu2 and mGlu7 homo- and heterodimers. *Nature*, *594*(7864), 589-593. https://doi.org/10.1038/s41586-021-03641-w

Thibado, J. K., Tano, J. Y., Lee, J., Salas-Estrada, L., Provasi, D., Strauss, A., Marcelo Lamim Ribeiro, J., Xiang, G., Broichhagen, J., Filizola, M., Lohse, M. J., & Levitz, J. (2021). Differences in interactions between transmembrane domains tune the activation of metabotropic glutamate receptors. *Elife*, *10*. https://doi.org/10.7554/eLife.67027

Xue, L., Rovira, X., Scholler, P., Zhao, H., Liu, J., Pin, J. P., & Rondard, P. (2015a). Major ligand-induced rearrangement of the heptahelical domain interface in a GPCR dimer. *Nat Chem Biol*, *11*(2), 134-140. https://doi.org/10.1038/nchembio.1711

Lin, S., Han, S., Cai, X., Tan, Q., Zhou, K., Wang, D., Wang, X., Du, J., Yi, C., Chu, X., Dai, A., Zhou, Y., Chen, Y., Zhou, Y., Liu, H., Liu, J., Yang, D., Wang, M. W., Zhao, Q., & Wu, B. (2021). Structures of G(i)-bound metabotropic glutamate receptors mGlu2 and mGlu4. *Nature*, *594*(7864), 583-588. https://doi.org/10.1038/s41586-021-03495-2

Franke, R. R., König, B., Sakmar, T. P., Khorana, H. G., & Hofmann, K. P. (1990). Rhodopsin mutants that bind but fail to activate transducin. *Science*, *250*(4977), 123-125. https://doi.org/10.1126/science.2218504

Ohyama, K., Yamano, Y., Chaki, S., Kondo, T., & Inagami, T. (1992). Domains for G-protein coupling in angiotensin II receptor type I: studies by site-directed mutagenesis. *Biochem Biophys Res Commun*, *189*(2), 677-683. https://doi.org/10.1016/0006-291x(92)92254-u

Cotecchia, S., Ostrowski, J., Kjelsberg, M. A., Caron, M. G., & Lefkowitz, R. J. (1992). Discrete amino acid sequences of the alpha 1-adrenergic receptor determine the selectivity of coupling to phosphatidylinositol hydrolysis. *J Biol Chem*, *267*(3), 1633-1639.

Kobilka, B. K., Kobilka, T. S., Daniel, K., Regan, J. W., Caron, M. G., & Lefkowitz, R. J. (1988). Chimeric alpha 2-,beta 2-adrenergic receptors: delineation of domains involved in effector coupling and ligand binding specificity. *Science*, *240*(4857), 1310-1316. https://doi.org/10.1126/science.2836950

Francesconi, A., & Duvoisin, R. M. (1998). Role of the second and third intracellular loops of metabotropic glutamate receptors in mediating dual signal transduction activation. *J Biol Chem*, *273*(10), 5615-5624. https://doi.org/10.1074/jbc.273.10.5615

Gomeza, J., Joly, C., Kuhn, R., Knöpfel, T., Bockaert, J., & Pin, J. P. (1996). The second intracellular loop of metabotropic glutamate receptor 1 cooperates with the other intracellular domains to control coupling to G-proteins. *J Biol Chem*, *271*(4), 2199-2205. https://doi.org/10.1074/jbc.271.4.2199

Cao, A. M., Quast, R. B., Fatemi, F., Rondard, P., Pin, J. P., & Margeat, E. (2021). Allosteric modulators enhance agonist efficacy by increasing the residence time of a GPCR in the active state. *Nat Commun*, *12*(1), 5426. https://doi.org/10.1038/s41467-021-25620-5

Olofsson, L., Felekyan, S., Doumazane, E., Scholler, P., Fabre, L., Zwier, J. M., Rondard, P., Seidel, C. A., Pin, J. P., & Margeat, E. (2014). Fine tuning of sub-millisecond conformational dynamics controls metabotropic glutamate receptors agonist efficacy. *Nat Commun*, *5*, 5206. https://doi.org/10.1038/ncomms6206

Hlavackova, V., Zabel, U., Frankova, D., Bätz, J., Hoffmann, C., Prezeau, L., Pin, J. P., Blahos, J., & Lohse, M. J. (2012). Sequential inter- and intrasubunit rearrangements during activation of dimeric metabotropic glutamate receptor 1. *Sci Signal*, *5*(237), ra59. https://doi.org/10.1126/scisignal.2002720

Maurel, D., Comps-Agrar, L., Brock, C., Rives, M. L., Bourrier, E., Ayoub, M. A., Bazin, H., Tinel, N., Durroux, T., Prézeau, L., Trinquet, E., & Pin, J. P. (2008). Cell-surface protein-protein interaction analysis with time-resolved FRET and snap-tag technologies: application to GPCR oligomerization. *Nat Methods*, *5*(6), 561-567. https://doi.org/10.1038/nmeth.1213

Grushevskyi, E. O., Kukaj, T., Schmauder, R., Bock, A., Zabel, U., Schwabe, T., Benndorf, K., & Lohse, M. J. (2019). Stepwise activation of a class C GPCR begins with millisecond dimer rearrangement. *Proc Natl Acad Sci U S A*, *116*(20), 10150-10155. https://doi.org/10.1073/pnas.1900261116

Santos, R., Ursu, O., Gaulton, A., Bento, A. P., Donadi, R. S., Bologa, C. G., Karlsson, A., Al-Lazikani, B., Hersey, A., Oprea, T. I., & Overington, J. P. (2017). A comprehensive map of molecular drug targets. *Nat Rev Drug Discov*, *16*(1), 19-34. https://doi.org/10.1038/nrd.2016.230

Congreve, M., de Graaf, C., Swain, N. A., & Tate, C. G. (2020). Impact of GPCR Structures on Drug Discovery. *Cell*, *181*(1), 81-91. https://doi.org/10.1016/j.cell.2020.03.003

Conn, P. J., & Jones, C. K. (2009). Promise of mGluR2/3 activators in psychiatry. *Neuropsychopharmacology*, *34*(1), 248-249. https://doi.org/10.1038/npp.2008.156

Conn, P. J., Lindsley, C. W., & Jones, C. K. (2009). Activation of metabotropic glutamate receptors as a novel approach for the treatment of schizophrenia. *Trends Pharmacol Sci*, *30*(1), 25-31. https://doi.org/10.1016/j.tips.2008.10.006

Abd-Elrahman, K. S., Albaker, A., de Souza, J. M., Ribeiro, F. M., Schlossmacher, M. G., Tiberi, M., Hamilton, A., & Ferguson, S. S. G. (2020). Aβ oligomers induce pathophysiological mGluR5 signaling in Alzheimer's disease model mice in a sex-selective manner. *Sci Signal*, *13*(662). https://doi.org/10.1126/scisignal.abd2494

Kumar, A., Dhull, D. K., & Mishra, P. S. (2015). Therapeutic potential of mGluR5 targeting in Alzheimer's disease. *Front Neurosci*, *9*, 215. https://doi.org/10.3389/fnins.2015.00215

Hopkins, C. R., Lindsley, C. W., & Niswender, C. M. (2009). mGluR4-positive allosteric modulation as potential treatment for Parkinson's disease. *Future Med Chem*, *1*(3), 501-513. https://doi.org/10.4155/fmc.09.38

Renner, M., Lacor, P. N., Velasco, P. T., Xu, J., Contractor, A., Klein, W. L., & Triller, A. (2010). Deleterious effects of amyloid beta oligomers acting as an extracellular scaffold for mGluR5. *Neuron*, *66*(5), 739-754. https://doi.org/10.1016/j.neuron.2010.04.029

Aguilar-Valles, A., Matta-Camacho, E., Khoutorsky, A., Gkogkas, C., Nader, K., Lacaille, J. C., & Sonenberg, N. (2015). Inhibition of Group I Metabotropic Glutamate Receptors Reverses Autistic-Like Phenotypes Caused by Deficiency of the Translation Repressor eIF4E Binding Protein 2. *J Neurosci*, *35*(31), 11125-11132. https://doi.org/10.1523/jneurosci.4615-14.2015

Stoppel, D. C., McCamphill, P. K., Senter, R. K., Heynen, A. J., & Bear, M. F. (2021). mGluR5 Negative Modulators for Fragile X: Treatment Resistance and Persistence. *Front Psychiatry*, *12*, 718953. https://doi.org/10.3389/fpsyt.2021.718953

Li, S. H., Colson, T. L., Abd-Elrahman, K. S., & Ferguson, S. S. G. (2021). Metabotropic Glutamate Receptor 2/3 Activation Improves Motor Performance and Reduces Pathology in Heterozygous zQ175 Huntington Disease Mice. *J Pharmacol Exp Ther*, *379*(1), 74-84. https://doi.org/10.1124/jpet.121.000735

Griebel, G., Pichat, P., Boulay, D., Naimoli, V., Potestio, L., Featherstone, R., Sahni, S., Defex, H., Desvignes, C., Slowinski, F., Vigé, X., Bergis, O. E., Sher, R., Kosley, R., Kongsamut, S., Black, M. D., & Varty, G. B. (2016). The mGluR2 positive allosteric modulator, SAR218645, improves memory and attention deficits in translational models of cognitive symptoms associated with schizophrenia. *Sci Rep*, *6*, 35320. https://doi.org/10.1038/srep35320

Joffe, M. E., Santiago, C. I., Oliver, K. H., Maksymetz, J., Harris, N. A., Engers, J. L., Lindsley, C. W., Winder, D. G., & Conn, P. J. (2020). mGlu(2) and mGlu(3) Negative Allosteric Modulators Divergently Enhance Thalamocortical Transmission and Exert Rapid Antidepressant-like Effects. *Neuron*, *105*(1), 46-59.e43. https://doi.org/10.1016/j.neuron.2019.09.044

Woo, M. S., Ufer, F., Rothammer, N., Di Liberto, G., Binkle, L., Haferkamp, U., Sonner, J. K., Engler, J. B., Hornig, S., Bauer, S., Wagner, I., Egervari, K., Raber, J., Duvoisin, R. M., Pless, O., Merkler, D., & Friese, M. A. (2021). Neuronal metabotropic glutamate receptor 8 protects against neurodegeneration in CNS inflammation. *J Exp Med*, *218*(5). https://doi.org/10.1084/jem.20201290

Fisher, N. M., Seto, M., Lindsley, C. W., & Niswender, C. M. (2018). Metabotropic Glutamate Receptor 7: A New Therapeutic Target in Neurodevelopmental Disorders. *Front Mol Neurosci*, *11*, 387. https://doi.org/10.3389/fnmol.2018.00387

Palazzo, E., Marabese, I., de Novellis, V., Rossi, F., & Maione, S. (2016). Metabotropic Glutamate Receptor 7: From Synaptic Function to Therapeutic Implications. *Curr Neuropharmacol*, *14*(5), 504-513. https://doi.org/10.2174/1570159x13666150716165323

Pereira, M. S. L., Klamt, F., Thomé, C. C., Worm, P. V., & de Oliveira, D. L. (2017). Metabotropic glutamate receptors as a new therapeutic target for malignant gliomas. *Oncotarget*, *8*(13), 22279-22298. https://doi.org/10.18632/oncotarget.15299

Varin, J., Bouzidi, N., Dias, M. M. S., Pugliese, T., Michiels, C., Robert, C., Desrosiers, M., Sahel, J. A., Audo, I., Dalkara, D., & Zeitz, C. (2021). Restoration of mGluR6 Localization Following AAV-Mediated Delivery in a Mouse Model of Congenital Stationary Night Blindness. *Invest Ophthalmol Vis Sci*, *62*(3), 24. https://doi.org/10.1167/iovs.62.3.24

Mazzitelli, M., Palazzo, E., Maione, S., & Neugebauer, V. (2018). Group II Metabotropic Glutamate Receptors: Role in Pain Mechanisms and Pain Modulation. *Front Mol Neurosci*, *11*, 383. https://doi.org/10.3389/fnmol.2018.00383

Bräuner-Osborne, H., Wellendorph, P., & Jensen, A. A. (2007). Structure, pharmacology and therapeutic prospects of family C G-protein coupled receptors. *Curr Drug Targets*, *8*(1), 169-184. https://doi.org/10.2174/138945007779315614

Goudet, C., Vilar, B., Courtiol, T., Deltheil, T., Bessiron, T., Brabet, I., Oueslati, N., Rigault, D., Bertrand, H. O., McLean, H., Daniel, H., Amalric, M., Acher, F., & Pin, J. P. (2012). A novel selective metabotropic glutamate receptor 4 agonist reveals new possibilities for developing subtype selective ligands with therapeutic potential. *Faseb j*, *26*(4), 1682-1693. https://doi.org/10.1096/fj.11-195941

Wootten, D., Christopoulos, A., & Sexton, P. M. (2013). Emerging paradigms in GPCR allostery: implications for drug discovery. *Nat Rev Drug Discov*, *12*(8), 630-644. https://doi.org/10.1038/nrd4052

Farinha, A., Lavreysen, H., Peeters, L., Russo, B., Masure, S., Trabanco, A. A., Cid, J., & Tresadern, G. (2015). Molecular determinants of positive allosteric modulation of the human metabotropic glutamate receptor 2. *Br J Pharmacol*, *172*(9), 2383-2396. https://doi.org/10.1111/bph.13065

Lundström, L., Bissantz, C., Beck, J., Wettstein, J. G., Woltering, T. J., Wichmann, J., & Gatti, S. (2011). Structural determinants of allosteric antagonism at metabotropic glutamate receptor 2: mechanistic studies with new potent negative allosteric modulators. *Br J Pharmacol*, *164*(2b), 521-537. https://doi.org/10.1111/j.1476-5381.2011.01409.x

Feng, Z., Ma, S., Hu, G., & Xie, X. Q. (2015). Allosteric Binding Site and Activation Mechanism of Class C G-Protein Coupled Receptors: Metabotropic Glutamate Receptor Family. *Aaps j*, *17*(3), 737-753. https://doi.org/10.1208/s12248-015-9742-8

Thal, D. M., Glukhova, A., Sexton, P. M., & Christopoulos, A. (2018). Structural insights into G-protein-coupled receptor allostery. *Nature*, *559*(7712), 45-53. https://doi.org/10.1038/s41586-018-0259-z

Urwyler, S. (2011). Allosteric modulation of family C G-protein-coupled receptors: from molecular insights to therapeutic perspectives. *Pharmacol Rev*, *63*(1), 59-126. https://doi.org/10.1124/pr.109.002501

Foster, D. J., & Conn, P. J. (2017). Allosteric Modulation of GPCRs: New Insights and Potential Utility for Treatment of Schizophrenia and Other CNS Disorders. *Neuron*, *94*(3), 431-446. https://doi.org/10.1016/j.neuron.2017.03.016

Harpsøe, K., Isberg, V., Tehan, B. G., Weiss, D., Arsova, A., Marshall, F. H., Bräuner-Osborne, H., & Gloriam, D. E. (2015). Selective Negative Allosteric Modulation Of Metabotropic Glutamate Receptors – A Structural Perspective of Ligands and Mutants. *Sci Rep*, *5*, 13869. https://doi.org/10.1038/srep13869

Gregory, K. J., Malosh, C., Turlington, M., Morrison, R., Vinson, P., Daniels, J. S., Jones, C., Niswender, C. M., Conn, P. J., & Lindsley, C. W. (2015). Identification of a high affinity MPEP-site silent allosteric modulator (SAM) for the metabotropic glutamate subtype 5 receptor (mGlu5). *Probe Reports from the NIH Molecular Libraries Program [Internet]*.

Annoura, H., Fukunaga, A., Uesugi, M., Tatsuoka, T., & Horikawa, Y. (1996). A novel class of antagonists for metabotropic glutamate receptors, 7-(hydroxyimino) cyclopropa [b] chromen-1a-carboxylates. *Bioorganic & Medicinal Chemistry Letters*, *6*(7), 763-766.

Sengmany, K., Hellyer, S. D., Albold, S., Wang, T., Conn, P. J., May, L. T., Christopoulos, A., Leach, K., & Gregory, K. J. (2019). Kinetic and system bias as drivers of metabotropic glutamate receptor 5 allosteric modulator pharmacology. *Neuropharmacology*, *149*, 83-96. https://doi.org/10.1016/j.neuropharm.2019.02.005

Sengmany, K., Hellyer, S. D., Christopoulos, A., Lapinsky, D. J., Leach, K., & Gregory, K. J. (2020). Differential contribution of metabotropic glutamate receptor 5 common allosteric binding site residues to biased allosteric agonism. *Biochem Pharmacol*, *177*, 114011. https://doi.org/10.1016/j.bcp.2020.114011

Sengmany, K., Singh, J., Stewart, G. D., Conn, P. J., Christopoulos, A., & Gregory, K. J. (2017). Biased allosteric agonism and modulation of metabotropic glutamate receptor 5: Implications for optimizing preclinical neuroscience drug discovery. *Neuropharmacology*, *115*, 60-72. https://doi.org/10.1016/j.neuropharm.2016.07.001

Song, Y., Kenworthy, A. K., & Sanders, C. R. (2014). Cholesterol as a co-solvent and a ligand for membrane proteins. *Protein Sci*, *23*(1), 1-22. https://doi.org/10.1002/pro.2385

Allende, D., Vidal, A., & McIntosh, T. J. (2004). Jumping to rafts: gatekeeper role of bilayer elasticity. *Trends Biochem Sci*, *29*(6), 325-330. https://doi.org/10.1016/j.tibs.2004.04.002

Anishkin, A., Loukin, S. H., Teng, J., & Kung, C. (2014). Feeling the hidden mechanical forces in lipid bilayer is an original sense. *Proc Natl Acad Sci U S A*, *111*(22), 7898-7905. https://doi.org/10.1073/pnas.1313364111

Chini, B., & Parenti, M. (2009). G-protein-coupled receptors, cholesterol and palmitoylation: facts about fats. *J Mol Endocrinol*, *42*(5), 371-379. https://doi.org/10.1677/jme-08-0114

Gimpl, G. (2016). Interaction of G protein coupled receptors and cholesterol. *Chem Phys Lipids*, *199*, 61-73. https://doi.org/10.1016/j.chemphyslip.2016.04.006

Lingwood, D., & Simons, K. (2010). Lipid rafts as a membrane-organizing principle. *Science*, *327*(5961), 46-50. https://doi.org/10.1126/science.1174621

Brown, D. A. (2006). Lipid rafts, detergent-resistant membranes, and raft targeting signals. *Physiology (Bethesda)*, *21*, 430-439. https://doi.org/10.1152/physiol.00032.2006

Elson, E. L., Fried, E., Dolbow, J. E., & Genin, G. M. (2010). Phase separation in biological membranes: integration of theory and experiment. *Annu Rev Biophys*, *39*, 207-226. https://doi.org/10.1146/annurev.biophys.093008.131238

Mouritsen, O., & Bloom, M. (1984). Mattress model of lipid-protein interactions in membranes. *Biophysical journal*, *46*(2), 141-153.

Lundbaek, J., Andersen, O., Werge, T., & Nielsen, C. (2003). Cholesterol-induced protein sorting: an analysis of energetic feasibility. *Biophysical journal*, *84*(3), 2080-2089.

Rawicz, W., Olbrich, K. C., McIntosh, T., Needham, D., & Evans, E. (2000). Effect of chain length and unsaturation on elasticity of lipid bilayers. *Biophysical journal*, *79*(1), 328-339.

Needham, D., & Nunn, R. S. (1990). Elastic deformation and failure of lipid bilayer membranes containing cholesterol. *Biophysical journal*, *58*(4), 997-1009.

Gandhavadi, M., Allende, D., Vidal, A., Simon, S., & McIntosh, T. (2002). Structure, composition, and peptide binding properties of detergent soluble bilayers and detergent resistant rafts. *Biophysical journal*, *82*(3), 1469-1482.

Brown, D. A., & London, E. (2000). Structure and function of sphingolipid-and cholesterol-rich membrane rafts. *Journal of Biological Chemistry*, *275*(23), 17221-17224.

Hanson, M. A., Cherezov, V., Griffith, M. T., Roth, C. B., Jaakola, V. P., Chien, E. Y., Velasquez, J., Kuhn, P., & Stevens, R. C. (2008). A specific cholesterol binding site is established by the 2.8 A structure of the human beta2-adrenergic receptor. *Structure*, *16*(6), 897-905. https://doi.org/10.1016/j.str.2008.05.001

Sarkar, P., & Chattopadhyay, A. (2020). Cholesterol interaction motifs in G protein-coupled receptors: Slippery hot spots? *Wiley Interdiscip Rev Syst Biol Med*, *12*(4), e1481. https://doi.org/10.1002/wsbm.1481

Kumari, R., Castillo, C., & Francesconi, A. (2013). Agonist-dependent signaling by group I metabotropic glutamate receptors is regulated by association with lipid domains. *J Biol Chem*, *288*(44), 32004-32019. https://doi.org/10.1074/jbc.M113.475863

Eroglu, C., Brugger, B., Wieland, F., & Sinning, I. (2003). Glutamate-binding affinity of Drosophila metabotropic glutamate receptor is modulated by association with lipid rafts. *Proc Natl Acad Sci U S A*, *100*(18), 10219-10224. https://doi.org/10.1073/pnas.1737042100

Kurth, M., Lolicato, F., Sandoval-Perez, A., Amaya-Espinosa, H., Teslenko, A., Sinning, I., Beck, R., Brügger, B., & Aponte-Santamaría, C. (2020). Cholesterol Localization around the Metabotropic Glutamate Receptor 2. *J Phys Chem B*, *124*(41), 9061-9078. https://doi.org/10.1021/acs.jpcb.0c05264

Lee, A. G. (2019). Interfacial Binding Sites for Cholesterol on G Protein-Coupled Receptors. *Biophys J*, *116*(9), 1586-1597. https://doi.org/10.1016/j.bpj.2019.03.025

Sejdiu, B. I., & Tieleman, D. P. (2020). Lipid-Protein Interactions Are a Unique Property and Defining Feature of G Protein-Coupled Receptors. *Biophys J*, *118*(8), 1887-1900. https://doi.org/10.1016/j.bpj.2020.03.008

Jeong, E., Kim, Y., Jeong, J., & Cho, Y. (2021). Structure of the class C orphan GPCR GPR158 in complex with RGS7-Gβ5. *Nat Commun*, *12*(1), 6805. https://doi.org/10.1038/s41467-021-27147-1

Patil, D. N., Singh, S., Laboute, T., Strutzenberg, T. S., Qiu, X., Wu, D., Novick, S. J., Robinson, C. V., Griffin, P. R., Hunt, J. F., Izard, T., Singh, A. K., & Martemyanov, K. A. (2022). Cryo-EM structure of human GPR158 receptor coupled to the RGS7-Gβ5 signaling complex. *Science*, *375*(6576), 86-91. https://doi.org/10.1126/science.abl4732

Papasergi-Scott, M. M., Robertson, M. J., Seven, A. B., Panova, O., Mathiesen, J. M., & Skiniotis, G. (2020). Structures of metabotropic GABA(B) receptor. *Nature*, *584*(7820), 310-314. https://doi.org/10.1038/s41586-020-2469-4

Yang, M. Y., Kim, S. K., & Goddard, W. A., 3rd. (2022). G protein coupling and activation of the metabotropic GABA(B) heterodimer. *Nat Commun*, *13*(1), 4612. https://doi.org/10.1038/s41467-022-32213-3

Lin, S.-H., & Guidotti, G. (2009). Purification of membrane proteins. *Methods in enzymology*, *463*, 619-629.

le Maire, M., Champeil, P., & MÖller, J. V. (2000). Interaction of membrane proteins and lipids with solubilizing detergents. *Biochimica et Biophysica Acta (BBA)-Biomembranes*, *1508*(1-2), 86-111.

Charalambous, K., Miller, D., Curnow, P., & Booth, P. J. (2008). Lipid bilayer composition influences small multidrug transporters. *BMC biochemistry*, *9*(1), 1-12.

VanAken, T., Foxall-VanAken, S., Castleman, S., & Ferguson-Miller, S. (1986). Alkyl glycoside detergents: synthesis and applications to the study of membrane proteins. *Methods Enzymol*, *125*, 27-35. https://doi.org/10.1016/s0076-6879(86)25005-3

Newstead, S., Ferrandon, S., & Iwata, S. (2008). Rationalizing alpha-helical membrane protein crystallization. *Protein Sci*, *17*(3), 466-472. https://doi.org/10.1110/ps.073263108

Chae, P. S., Rasmussen, S. G., Rana, R. R., Gotfryd, K., Chandra, R., Goren, M. A., Kruse, A. C., Nurva, S., Loland, C. J., Pierre, Y., Drew, D., Popot, J. L., Picot, D., Fox, B. G., Guan, L., Gether, U., Byrne, B., Kobilka, B., & Gellman, S. H. (2010). Maltose-neopentyl glycol (MNG) amphiphiles for solubilization, stabilization and crystallization of membrane proteins. *Nat Methods*, *7*(12), 1003-1008. https://doi.org/10.1038/nmeth.1526

Lee, S., Ghosh, S., Jana, S., Robertson, N., Tate, C. G., & Vaidehi, N. (2020). How Do Branched Detergents Stabilize GPCRs in Micelles? *Biochemistry*, *59*(23), 2125-2134. https://doi.org/10.1021/acs.biochem.0c00183

Lee, S., Mao, A., Bhattacharya, S., Robertson, N., Grisshammer, R., Tate, C. G., & Vaidehi, N. (2016). How Do Short Chain Nonionic Detergents Destabilize G-Protein-Coupled Receptors? *J Am Chem Soc*, *138*(47), 15425-15433. https://doi.org/10.1021/jacs.6b08742

Chae, P. S., Rasmussen, S. G., Rana, R. R., Gotfryd, K., Kruse, A. C., Manglik, A., Cho, K. H., Nurva, S., Gether, U., Guan, L., Loland, C. J., Byrne, B., Kobilka, B. K., & Gellman, S. H. (2012). A new class of amphiphiles bearing rigid hydrophobic groups for solubilization and stabilization of membrane proteins. *Chemistry*, *18*(31), 9485-9490. https://doi.org/10.1002/chem.201200069

Frey, L., Lakomek, N. A., Riek, R., & Bibow, S. (2017). Micelles, Bicelles, and Nanodiscs: Comparing the Impact of Membrane Mimetics on Membrane Protein Backbone Dynamics. *Angew Chem Int Ed Engl*, *56*(1), 380-383. https://doi.org/10.1002/anie.201608246

Warschawski, D. E., Arnold, A. A., Beaugrand, M., Gravel, A., Chartrand, É., & Marcotte, I. (2011). Choosing membrane mimetics for NMR structural studies of transmembrane proteins. *Biochim Biophys Acta*, *1808*(8), 1957-1974. https://doi.org/10.1016/j.bbamem.2011.03.016

Akbarzadeh, A., Rezaei-Sadabady, R., Davaran, S., Joo, S. W., Zarghami, N., Hanifehpour, Y., Samiei, M., Kouhi, M., & Nejati-Koshki, K. (2013). Liposome: classification, preparation, and applications. *Nanoscale Res Lett*, *8*(1), 102. https://doi.org/10.1186/1556-276x-8-102

Dürr, U. H., Gildenberg, M., & Ramamoorthy, A. (2012). The magic of bicelles lights up membrane protein structure. *Chem Rev*, *112*(11), 6054-6074. https://doi.org/10.1021/cr300061w

Bayburt, T. H., Grinkova, Y. V., & Sligar, S. G. (2002). Self-assembly of discoidal phospholipid bilayer nanoparticles with membrane scaffold proteins. *Nano letters*, *2*(8), 853-856.

Denisov, I. G., Grinkova, Y. V., Lazarides, A. A., & Sligar, S. G. (2004). Directed self-assembly of monodisperse phospholipid bilayer Nanodiscs with controlled size. *Journal of the American Chemical Society*, *126*(11), 3477-3487.

Knowles, T. J., Finka, R., Smith, C., Lin, Y.-P., Dafforn, T., & Overduin, M. (2009). Membrane proteins solubilized intact in lipid containing nanoparticles bounded by styrene maleic acid copolymer. *Journal of the American Chemical Society*, *131*(22), 7484-7485.

Tonge, S., & Tighe, B. (2001). Responsive hydrophobically associating polymers: a review of structure and properties. *Advanced drug delivery reviews*, *53*(1), 109-122.

Lee, S. C., Knowles, T. J., Postis, V. L., Jamshad, M., Parslow, R. A., Lin, Y. P., Goldman, A., Sridhar, P., Overduin, M., Muench, S. P., & Dafforn, T. R. (2016). A method for detergent-free isolation of membrane proteins in their local lipid environment. *Nat Protoc*, *11*(7), 1149-1162. https://doi.org/10.1038/nprot.2016.070

Kopf, A. H., Lijding, O., Elenbaas, B. O. W., Koorengevel, M. C., Dobruchowska, J. M., van Walree, C. A., & Killian, J. A. (2022). Synthesis and Evaluation of a Library of Alternating Amphipathic Copolymers to Solubilize and Study Membrane Proteins. *Biomacromolecules*, *23*(3), 743-759. https://doi.org/10.1021/acs.biomac.1c01166

Yasuhara, K., Arakida, J., Ravula, T., Ramadugu, S. K., Sahoo, B., Kikuchi, J. I., & Ramamoorthy, A. (2017). Spontaneous Lipid Nanodisc Fomation by Amphiphilic Polymethacrylate Copolymers. *J Am Chem Soc*, *139*(51), 18657-18663. https://doi.org/10.1021/jacs.7b10591

Cleg, R. (2006). The history of FRET: from conception through the labors of birth. In (pp. 1): Springer, New York.

Jones, G. A., & Bradshaw, D. S. (2019). Resonance Energy Transfer: From Fundamental Theory to Recent Applications [Review]. *Frontiers in Physics*, *7*. https://doi.org/10.3389/fphy.2019.00100

Perrin, F. (1932). Théorie quantique des transferts d'activation entre molécules de même espèce. Cas des solutions fluorescentes. Annales de Physique,

Förster, T. (1948). Zwischenmolekulare energiewanderung und fluoreszenz. *Annalen der physik*, *437*(1-2), 55-75.

Förster, T. (1965). Delocalized excitation and excitation transfer, O. Sinanoglu (Ed.), Modern Quantum Chemistry. Istanbul Lectures 3. In: Academic Press, New York/London.

Latt, S., Cheung, H., & Blout, E. (1965). Energy transfer. A system with relatively fixed donor-acceptor separation. *Journal of the American Chemical Society*, *87*(5), 995-1003.

Sahoo, H. (2011). Förster resonance energy transfer–A spectroscopic nanoruler: Principle and applications. *Journal of Photochemistry and Photobiology C: Photochemistry Reviews*, *12*(1), 20-30.

Stryer, L., & Haugland, R. P. (1967). Energy transfer: a spectroscopic ruler. *Proc Natl Acad Sci U S A*, *58*(2), 719-726. https://doi.org/10.1073/pnas.58.2.719

Gopich, I. V., & Szabo, A. (2010). FRET efficiency distributions of multistate single molecules. *J Phys Chem B*, *114*(46), 15221-15226. https://doi.org/10.1021/jp105359z

Ha, T. (2001). Single-molecule fluorescence resonance energy transfer. *Methods*, *25*(1), 78-86. https://doi.org/10.1006/meth.2001.1217

Schuler, B. (2013). Single-molecule FRET of protein structure and dynamics - a primer. *J Nanobiotechnology*, *11 Suppl 1*(Suppl 1), S2. https://doi.org/10.1186/1477-3155-11-s1-s2

Ha, T., Enderle, T., Ogletree, D. F., Chemla, D. S., Selvin, P. R., & Weiss, S. (1996). Probing the interaction between two single molecules: fluorescence resonance energy transfer between a single donor and a single acceptor. *Proc Natl Acad Sci U S A*, *93*(13), 6264-6268. https://doi.org/10.1073/pnas.93.13.6264

Michalet, X., Weiss, S., & Jäger, M. (2006). Single-molecule fluorescence studies of protein folding and conformational dynamics. *Chem Rev*, *106*(5), 1785-1813. https://doi.org/10.1021/cr0404343

Sasmal, D. K., Pulido, L. E., Kasal, S., & Huang, J. (2016). Single-molecule fluorescence resonance energy transfer in molecular biology. *Nanoscale*, *8*(48), 19928-19944. https://doi.org/10.1039/c6nr06794h

Seidel, R., & Dekker, C. (2007). Single-molecule studies of nucleic acid motors. *Curr Opin Struct Biol*, *17*(1), 80-86. https://doi.org/10.1016/j.sbi.2006.12.003

Smiley, R. D., & Hammes, G. G. (2006). Single molecule studies of enzyme mechanisms. *Chem Rev*, *106*(8), 3080-3094. https://doi.org/10.1021/cr0502955

Weiss, S. (1999). Fluorescence spectroscopy of single biomolecules. *Science*, *283*(5408), 1676-1683. https://doi.org/10.1126/science.283.5408.1676

Zhuang, X. (2005). Single-molecule RNA science. *Annu Rev Biophys Biomol Struct*, *34*, 399-414. https://doi.org/10.1146/annurev.biophys.34.040204.144641

Joo, C., & Ha, T. (2012). Single-molecule FRET with total internal reflection microscopy. *Cold Spring Harb Protoc*, *2012*(12). https://doi.org/10.1101/pdb.top072058

Lerner, E., Barth, A., Hendrix, J., Ambrose, B., Birkedal, V., Blanchard, S. C., Börner, R., Sung Chung, H., Cordes, T., Craggs, T. D., Deniz, A. A., Diao, J., Fei, J., Gonzalez, R. L., Gopich, I. V., Ha, T., Hanke, C. A., Haran, G., Hatzakis, N. S., . . . Weiss, S. (2021). FRET-based dynamic structural biology: Challenges, perspectives and an appeal for open-science practices. *Elife*, *10*. https://doi.org/10.7554/eLife.60416

Roy, R., Hohng, S., & Ha, T. (2008). A practical guide to single-molecule FRET. *Nat Methods*, *5*(6), 507-516. https://doi.org/10.1038/nmeth.1208

Brasselet, S., Peterman, E. J., Miyawaki, A., & Moerner, W. (2000). Single-molecule fluorescence resonant energy transfer in calcium concentration dependent cameleon. *The Journal of Physical Chemistry B*, *104*(15), 3676-3682.

Hohng, S., & Ha, T. (2004). Near-complete suppression of quantum dot blinking in ambient conditions. *J Am Chem Soc*, *126*(5), 1324-1325. https://doi.org/10.1021/ja039686w

Hohng, S., & Ha, T. (2005). Single-molecule quantum-dot fluorescence resonance energy transfer. *Chemphyschem*, *6*(5), 956-960. https://doi.org/10.1002/cphc.200400557

Kapanidis, A. N., & Weiss, S. (2002). Fluorescent probes and bioconjugation chemistries for single-molecule fluorescence analysis of biomolecules. *The Journal of chemical physics*, *117*(24), 10953-10964.

Hohng, S., Joo, C., & Ha, T. (2004). Single-molecule three-color FRET. *Biophys J*, *87*(2), 1328-1337. https://doi.org/10.1529/biophysj.104.043935

Grimm, J. B., Brown, T. A., English, B. P., Lionnet, T., & Lavis, L. D. (2017). Synthesis of Janelia Fluor HaloTag and SNAP-Tag Ligands and Their Use in Cellular Imaging

Experiments. *Methods Mol Biol*, *1663*, 179-188. https://doi.org/10.1007/978-1-4939-7265-4_15

Hübner, C. G., Renn, A., Renge, I., & Wild, U. P. (2001). Direct observation of the triplet lifetime quenching of single dye molecules by molecular oxygen. *The Journal of chemical physics*, *115*(21), 9619-9622.

Benesch, R. E., & Benesch, R. (1953). Enzymatic removal of oxygen for polarography and related methods. *Science*, *118*(3068), 447-448. https://doi.org/10.1126/science.118.3068.447

Aitken, C. E., Marshall, R. A., & Puglisi, J. D. (2008). An oxygen scavenging system for improvement of dye stability in single-molecule fluorescence experiments. *Biophys J*, *94*(5), 1826-1835. https://doi.org/10.1529/biophysj.107.117689

Rasnik, I., McKinney, S. A., & Ha, T. (2006). Nonblinking and long-lasting single-molecule fluorescence imaging. *Nat Methods*, *3*(11), 891-893. https://doi.org/10.1038/nmeth934

Wu, P., & Brand, L. (1994). Resonance energy transfer: methods and applications. *Anal Biochem*, *218*(1), 1-13. https://doi.org/10.1006/abio.1994.1134

Cole, N. B. (2013). Site-specific protein labeling with SNAP-tags. *Curr Protoc Protein Sci*, *73*, 30.31.31-30.31.16. https://doi.org/10.1002/0471140864.ps3001s73

Los, G. V., Encell, L. P., McDougall, M. G., Hartzell, D. D., Karassina, N., Zimprich, C., Wood, M. G., Learish, R., Ohana, R. F., Urh, M., Simpson, D., Mendez, J., Zimmerman, K., Otto, P., Vidugiris, G., Zhu, J., Darzins, A., Klaubert, D. H., Bulleit, R. F., & Wood, K. V. (2008). HaloTag: a novel protein labeling technology for cell imaging and protein analysis. *ACS Chem Biol*, *3*(6), 373-382. https://doi.org/10.1021/cb800025k

Johnsson, N., George, N., & Johnsson, K. (2005). Protein chemistry on the surface of living cells. *Chembiochem*, *6*(1), 47-52. https://doi.org/10.1002/cbic.200400290

Guimaraes, C. P., Witte, M. D., Theile, C. S., Bozkurt, G., Kundrat, L., Blom, A. E., & Ploegh, H. L. (2013). Site-specific C-terminal and internal loop labeling of proteins using sortase-mediated reactions. *Nat Protoc*, *8*(9), 1787-1799. https://doi.org/10.1038/nprot.2013.101

Braman, J. (2002). *In vitro mutagenesis protocols* (Vol. 182). Springer.

Higuchi, R., Krummel, B., & Saiki, R. K. (1988). A general method of in vitro preparation and specific mutagenesis of DNA fragments: study of protein and DNA interactions. *Nucleic Acids Res*, *16*(15), 7351-7367. https://doi.org/10.1093/nar/16.15.7351

Lang, K., & Chin, J. W. (2014). Cellular incorporation of unnatural amino acids and bioorthogonal labeling of proteins. *Chem Rev*, *114*(9), 4764-4806. https://doi.org/10.1021/cr400355w

Elsässer, S. J., Ernst, R. J., Walker, O. S., & Chin, J. W. (2016). Genetic code expansion in stable cell lines enables encoded chromatin modification. *Nat Methods*, *13*(2), 158-164. https://doi.org/10.1038/nmeth.3701

Huber, T., Naganathan, S., Tian, H., Ye, S., & Sakmar, T. P. (2013a). Unnatural amino acid mutagenesis of GPCRs using amber codon suppression and bioorthogonal labeling. *Methods Enzymol*, *520*, 281-305. https://doi.org/10.1016/b978-0-12-391861-1.00013-7

Noren, C. J., Anthony-Cahill, S. J., Griffith, M. C., & Schultz, P. G. (1989). A general method for site-specific incorporation of unnatural amino acids into proteins. *Science*, *244*(4901), 182-188. https://doi.org/10.1126/science.2649980

Serfling, R., & Coin, I. (2016). Incorporation of Unnatural Amino Acids into Proteins Expressed in Mammalian Cells. *Methods Enzymol*, *580*, 89-107. https://doi.org/10.1016/bs.mie.2016.05.003

Axelrod, D. (1990). Total internal reflection fluorescence at biological surfaces. *Modern cell biology*, *9*, 93-127.

Axelrod, D. (2003). Total internal reflection fluorescence microscopy in cell biology. *Methods Enzymol*, *361*, 1-33. https://doi.org/10.1016/s0076-6879(03)61003-7

Michalet, X., Siegmund, O. H., Vallerga, J. V., Jelinsky, P., Millaud, J. E., & Weiss, S. (2007). Detectors for single-molecule fluorescence imaging and spectroscopy. *J Mod Opt*, *54*(2-3), 239. https://doi.org/10.1080/09500340600769067

Sofia, S. J., Premnath, V. V., & Merrill, E. W. (1998). Poly(ethylene oxide) Grafted to Silicon Surfaces: Grafting Density and Protein Adsorption. *Macromolecules*, *31*(15), 5059-5070. https://doi.org/10.1021/ma971016l

Cai, H., & Wind, S. J. (2016). Improved Glass Surface Passivation for Single-Molecule Nanoarrays. *Langmuir*, *32*(39), 10034-10041. https://doi.org/10.1021/acs.langmuir.6b02444

Heyes, C. D., Groll, J., Möller, M., & Nienhaus, G. U. (2007). Synthesis, patterning and applications of star-shaped poly(ethylene glycol) biofunctionalized surfaces. *Mol Biosyst*, *3*(6), 419-430. https://doi.org/10.1039/b700055n

Heyes, C. D., Kobitski, A. Y., Amirgoulova, E. V., & Nienhaus, G. U. (2004). Biocompatible surfaces for specific tethering of individual protein molecules. *The Journal of Physical Chemistry B*, *108*(35), 13387-13394.

Pan, H., Xia, Y., Qin, M., Cao, Y., & Wang, W. (2015). A simple procedure to improve the surface passivation for single molecule fluorescence studies. *Phys Biol*, *12*(4), 045006. https://doi.org/10.1088/1478-3975/12/4/045006

Hellenkamp, B., Schmid, S., Doroshenko, O., Opanasyuk, O., Kühnemuth, R., Rezaei Adariani, S., Ambrose, B., Aznauryan, M., Barth, A., Birkedal, V., Bowen, M. E., Chen, H., Cordes, T., Eilert, T., Fijen, C., Gebhardt, C., Götz, M., Gouridis, G., Gratton, E., . . . Hugel, T. (2018). Precision and accuracy of single-molecule FRET measurements-a multi-laboratory benchmark study. *Nat Methods*, *15*(9), 669-676. https://doi.org/10.1038/s41592-018-0085-0

Paul, T., & Myong, S. (2022). Protocol for generation and regeneration of PEG-passivated slides for single-molecule measurements. *STAR Protoc*, *3*(1), 101152. https://doi.org/10.1016/j.xpro.2022.101152

Juette, M. F., Terry, D. S., Wasserman, M. R., Altman, R. B., Zhou, Z., Zhao, H., & Blanchard, S. C. (2016). Single-molecule imaging of non-equilibrium molecular ensembles on the millisecond timescale. *Nat Methods*, *13*(4), 341-344. https://doi.org/10.1038/nmeth.3769

Thomsen, J., Sletfjerding, M. B., Jensen, S. B., Stella, S., Paul, B., Malle, M. G., Montoya, G., Petersen, T. C., & Hatzakis, N. S. (2020). DeepFRET, a software for rapid and automated single-molecule FRET data classification using deep learning. *Elife*, *9*. https://doi.org/10.7554/eLife.60404

Ha, T., Chemla, D., Enderle, T., & Weiss, S. (1997). Single molecule spectroscopy with automated positioning. *Applied Physics Letters*, *70*(6), 782-784.

Sabanayagam, C. R., Eid, J. S., & Meller, A. (2004). High-throughput scanning confocal microscope for single molecule analysis. *Applied Physics Letters*, *84*(7), 1216-1218.

Yu, L., Lei, Y., Ma, Y., Liu, M., Zheng, J., Dan, D., & Gao, P. (2021). A Comprehensive Review of Fluorescence Correlation Spectroscopy [Review]. *Frontiers in Physics, 9*. https://doi.org/10.3389/fphy.2021.644450

Changeux, J. P., & Christopoulos, A. (2016). Allosteric Modulation as a Unifying Mechanism for Receptor Function and Regulation. *Cell*, *166*(5), 1084-1102. https://doi.org/10.1016/j.cell.2016.08.015

Dorsam, R. T., & Gutkind, J. S. (2007). G-protein-coupled receptors and cancer. *Nat Rev Cancer*, *7*(2), 79-94. https://doi.org/10.1038/nrc2069

Zarzycka, B., Zaidi, S. A., Roth, B. L., & Katritch, V. (2019). Harnessing Ion-Binding Sites for GPCR Pharmacology. *Pharmacol Rev*, *71*(4), 571-595. https://doi.org/10.1124/pr.119.017863

Hilger, D., Masureel, M., & Kobilka, B. K. (2018). Structure and dynamics of GPCR signaling complexes. *Nat Struct Mol Biol*, *25*(1), 4-12. https://doi.org/10.1038/s41594-017-0011-7

Latorraca, N. R., Venkatakrishnan, A. J., & Dror, R. O. (2017). GPCR Dynamics: Structures in Motion. *Chem Rev*, *117*(1), 139-155. https://doi.org/10.1021/acs.chemrev.6b00177

Ye, L., Van Eps, N., Zimmer, M., Ernst, O. P., & Prosser, R. S. (2016). Activation of the A2A adenosine G-protein-coupled receptor by conformational selection. *Nature*, *533*(7602), 265-268. https://doi.org/10.1038/nature17668

Nygaard, R., Zou, Y., Dror, R. O., Mildorf, T. J., Arlow, D. H., Manglik, A., Pan, A. C., Liu, C. W., Fung, J. J., Bokoch, M. P., Thian, F. S., Kobilka, T. S., Shaw, D. E., Mueller, L., Prosser, R. S., & Kobilka, B. K. (2013a). The dynamic process of beta(2)-adrenergic receptor activation. *Cell*, *152*(3), 532-542. https://doi.org/10.1016/j.cell.2013.01.008

Wingler, L. M., Elgeti, M., Hilger, D., Latorraca, N. R., Lerch, M. T., Staus, D. P., Dror, R. O., Kobilka, B. K., Hubbell, W. L., & Lefkowitz, R. J. (2019a). Angiotensin Analogs with Divergent Bias Stabilize Distinct Receptor Conformations. *Cell*, *176*(3), 468-478 e411. https://doi.org/10.1016/j.cell.2018.12.005

Gusach, A., Maslov, I., Luginina, A., Borshchevskiy, V., Mishin, A., & Cherezov, V. (2020). Beyond structure: emerging approaches to study GPCR dynamics. *Curr Opin Struct Biol*, *63*, 18-25. https://doi.org/10.1016/j.sbi.2020.03.004

Gregorio, G. G., Masureel, M., Hilger, D., Terry, D. S., Juette, M., Zhao, H., Zhou, Z., Perez-Aguilar, J. M., Hauge, M., Mathiasen, S., Javitch, J. A., Weinstein, H., Kobilka, B. K., & Blanchard, S. C. (2017a). Single-molecule analysis of ligand efficacy in beta2AR-G-protein activation. *Nature*, *547*(7661), 68-73. https://doi.org/10.1038/nature22354

Suomivuori, C. M., Latorraca, N. R., Wingler, L. M., Eismann, S., King, M. C., Kleinhenz, A. L. W., Skiba, M. A., Staus, D. P., Kruse, A. C., Lefkowitz, R. J., & Dror, R. O. (2020). Molecular mechanism of biased signaling in a prototypical G protein-coupled receptor. *Science*, *367*(6480), 881-887. https://doi.org/10.1126/science.aaz0326

Pin, J. P., & Bettler, B. (2016). Organization and functions of mGlu and GABA(B) receptor complexes. *Nature*, *540*(7631), 60-68. https://doi.org/10.1038/nature20566

Koehl, A., Hu, H. L., Feng, D., Sun, B. F., Zhang, Y., Robertson, M. J., Chu, M., Kobilka, T. S., Laeremans, T., Steyaert, J., Tarrasch, J., Dutta, S., Fonseca, R., Weis, W. I., Mathiesen, J. M., Skiniotis, G., & Kobilka, B. K. (2019b). Structural insights into the activation of

metabotropic glutamate receptors. *Nature, 567*(7747), 79-84. <Go to ISI>://WOS:000461126600009

Doumazane, E., Scholler, P., Fabre, L., Zwier, J. M., Trinquet, E., Pin, J. P., & Rondard, P. (2013b). Illuminating the activation mechanisms and allosteric properties of metabotropic glutamate receptors. *Proc. Natl. Acad. Sci. USA*, *110*(15), E1416-1425. https://www.ncbi.nlm.nih.gov/pubmed/23487753

Noren, C. J., Anthonycahill, S. J., Griffith, M. C., & Schultz, P. G. (1989). A General-Method for Site-Specific Incorporation of Unnatural Amino-Acids into Proteins. *Science, 244*(4901), 182-188. https://doi.org/DOI 10.1126/science.2649980

Huber, T., Naganathan, S., Tian, H., Ye, S. X., & Sakmar, T. P. (2013b). Unnatural Amino Acid Mutagenesis of GPCRs Using Amber Codon Suppression and Bioorthogonal Labeling. *G Protein Coupled Receptors: Structure, 520*, 281-305. https://doi.org/10.1016/B978-0-12-391861-1.00013-7

Presolski, S. I., Hong, V. P., & Finn, M. G. (2011a). Copper-Catalyzed Azide-Alkyne Click Chemistry for Bioconjugation. *Curr. Protoc. Chem. Biol., 3*(4), 153-162. https://www.ncbi.nlm.nih.gov/pubmed/22844652

Muto, T., Tsuchiya, D., Morikawa, K., & Jingami, H. (2007b). Structures of the extracellular regions of the group II/III metabotropic glutamate receptors. *Proc. Natl. Acad. Sci. USA*, *104*(10), 3759-3764. https://www.ncbi.nlm.nih.gov/pubmed/17360426

Huang, S. L., Cao, J. H., Jiang, M., Labesse, G., Liu, J. F., Pin, J. P., & Rondard, P. (2011). Interdomain movements in metabotropic glutamate receptor activation. *Proc. Natl. Acad. Sci. USA, 108*(37), 15480-15485. <Go to ISI>://WOS:000294804900093

Jain, A., Liu, R., Ramani, B., Arauz, E., Ishitsuka, Y., Ragunathan, K., Park, J., Chen, J., Xiang, Y. K., & Ha, T. (2011). Probing cellular protein complexes using single-molecule pull-down. *Nature, 473*(7348), 484-488. https://doi.org/10.1038/nature10016

Bronson, J. E., Fei, J., Hofman, J. M., Gonzalez, R. L., Jr., & Wiggins, C. H. (2009a). Learning rates and states from biophysical time series: a Bayesian approach to model selection and single-molecule FRET data. *Biophys. J., 97*(12), 3196-3205. https://www.ncbi.nlm.nih.gov/pubmed/20006957

Zhang, J., Chetnani, B., Cormack, E. D., Alonso, D., Liu, W., Mondragón, A., & Fei, J. (2018). Specific structural elements of the T-box riboswitch drive the two-step binding of the tRNA ligand. *Elife, 7*. https://doi.org/10.7554/eLife.39518

Nussinov, R., Ma, B., & Tsai, C. J. (2014). Multiple conformational selection and induced fit events take place in allosteric propagation. *Biophys. Chem., 186*, 22-30. https://www.ncbi.nlm.nih.gov/pubmed/24239303

Manglik, A., Kim, T. H., Masureel, M., Altenbach, C., Yang, Z., Hilger, D., Lerch, M. T., Kobilka, T. S., Thian, F. S., Hubbell, W. L., Prosser, R. S., & Kobilka, B. K. (2015). Structural Insights into the Dynamic Process of beta2-Adrenergic Receptor Signaling. *Cell, 161*(5), 1101-1111. https://doi.org/10.1016/j.cell.2015.04.043

Dror, R. O., Arlow, D. H., Maragakis, P., Mildorf, T. J., Pan, A. C., Xu, H., Borhani, D. W., & Shaw, D. E. (2011). Activation mechanism of the beta2-adrenergic receptor. *Proc. Natl. Acad. Sci. USA, 108*(46), 18684-18689. https://www.ncbi.nlm.nih.gov/pubmed/22031696

Kniazeff, J., Bessis, A. S., Maurel, D., Ansanay, H., Prezeau, L., & Pin, J. P. (2004). Closed state of both binding domains of homodimeric mGlu receptors is required for full activity. *Nat. Struct. Mol. Biol., 11*(8), 706-713. https://www.ncbi.nlm.nih.gov/pubmed/15235591

Xue, L., Rovira, X., Scholler, P., Zhao, H., Liu, J., Pin, J. P., & Rondard, P. (2015b). Major ligand-induced rearrangement of the heptahelical domain interface in a GPCR dimer. *Nat. Chem. Biol., 11*(2), 134-140. https://www.ncbi.nlm.nih.gov/pubmed/25503927

Yanagawa, M., Yamashita, T., & Shichida, Y. (2009). Activation switch in the transmembrane domain of metabotropic glutamate receptor. *Mol Pharmacol, 76*(1), 201-207. https://doi.org/10.1124/mol.109.056549

Shaye, H., Ishchenko, A., Lam, J. H., Han, G. W., Xue, L., Rondard, P., Pin, J. P., Katritch, V., Gati, C., & Cherezov, V. (2020). Structural basis of the activation of a metabotropic GABA receptor. *Nature, 584*(7820), 298-303. https://doi.org/10.1038/s41586-020-2408-4

Mijares, A., Lebesgue, D., Wallukat, G., & Hoebeke, J. (2000). From agonist to antagonist: Fab fragments of an agonist-like monoclonal anti-beta2-adrenoceptor antibody behave as antagonists. *Mol. Pharmacol., 58*(2), 373-379. https://www.ncbi.nlm.nih.gov/pubmed/10908305

Stoneman, M. R., Biener, G., Ward, R. J., Pediani, J. D., Badu, D., Eis, A., Popa, I., Milligan, G., & Raicu, V. (2019). A general method to quantify ligand-driven oligomerization from fluorescence-based images. *Nat. Methods, 16*(6), 493-496. https://www.ncbi.nlm.nih.gov/pubmed/31110281

Hern, J. A., Baig, A. H., Mashanov, G. I., Birdsall, B., Corrie, J. E., Lazareno, S., Molloy, J. E., & Birdsall, N. J. (2010). Formation and dissociation of M1 muscarinic receptor dimers seen by total internal reflection fluorescence imaging of single molecules. *Proc. Natl. Acad. Sci. USA, 107*(6), 2693-2698. https://www.ncbi.nlm.nih.gov/pubmed/20133736

Calebiro, D., Rieken, F., Wagner, J., Sungkaworn, T., Zabel, U., Borzi, A., Cocucci, E., Zurn, A., & Lohse, M. J. (2013). Single-molecule analysis of fluorescently labeled G-protein-coupled receptors reveals complexes with distinct dynamics and organization. *Proc. Natl. Acad. Sci. USA, 110*(2), 743-748. https://www.ncbi.nlm.nih.gov/pubmed/23267088

Moller, J., Isbilir, A., Sungkaworn, T., Osberg, B., Karathanasis, C., Sunkara, V., Grushevskyi, E. O., Bock, A., Annibale, P., Heilemann, M., Schutte, C., & Lohse, M. J. (2020). Single-molecule analysis reveals agonist-specific dimer formation of micro-opioid receptors. *Nat Chem Biol*, *16*(9), 946-954. https://doi.org/10.1038/s41589-020-0566-1

Endres, N. F., Das, R., Smith, A. W., Arkhipov, A., Kovacs, E., Huang, Y., Pelton, J. G., Shan, Y., Shaw, D. E., Wemmer, D. E., Groves, J. T., & Kuriyan, J. (2013). Conformational coupling across the plasma membrane in activation of the EGF receptor. *Cell, 152*(3), 543-556. https://doi.org/10.1016/j.cell.2012.12.032

Hong, V., Steinmetz, N. F., Manchester, M., & Finn, M. G. (2010). Labeling live cells by copper-catalyzed alkyne--azide click chemistry. *Bioconjug Chem, 21*(10), 1912-1916. https://doi.org/10.1021/bc100272z

Schindelin, J., Arganda-Carreras, I., Frise, E., Kaynig, V., Longair, M., Pietzsch, T., Preibisch, S., Rueden, C., Saalfeld, S., Schmid, B., Tinevez, J. Y., White, D. J., Hartenstein, V., Eliceiri, K., Tomancak, P., & Cardona, A. (2012). Fiji: an open-source platform for biological-image analysis. *Nat Methods*, *9*(7), 676-682. https://doi.org/10.1038/nmeth.2019

Pettersen, E. F., Goddard, T. D., Huang, C. C., Couch, G. S., Greenblatt, D. M., Meng, E. C., & Ferrin, T. E. (2004). UCSF Chimera--a visualization system for exploratory research and analysis. *J Comput Chem*, *25*(13), 1605-1612. https://doi.org/10.1002/jcc.20084

Goodsell, D. S., Autin, L., & Olson, A. J. (2019). Illustrate: Software for Biomolecular Illustration. *Structure*, *27*(11), 1716-1720.e1711. https://doi.org/10.1016/j.str.2019.08.011

Jain, A., Liu, R., Xiang, Y. K., & Ha, T. (2012). Single-molecule pull-down for studying protein interactions. *Nat Protoc*, *7*(3), 445-452. https://doi.org/10.1038/nprot.2011.452

Bronson, J. E., Fei, J., Hofman, J. M., Gonzalez, R. L., Jr., & Wiggins, C. H. (2009b). Learning rates and states from biophysical time series: a Bayesian approach to model selection and single-molecule FRET data. *Biophys J*, *97*(12), 3196-3205. https://doi.org/10.1016/j.bpj.2009.09.031

Christopoulos, A. (2014). Advances in G protein-coupled receptor allostery: from function to structure. *Mol Pharmacol*, *86*(5), 463-478. https://doi.org/10.1124/mol.114.094342

Leach, K., & Gregory, K. J. (2017). Molecular insights into allosteric modulation of Class C G protein-coupled receptors. *Pharmacol Res*, *116*, 105-118. https://doi.org/10.1016/j.phrs.2016.12.006

Makita, N., Sato, J., Manaka, K., Shoji, Y., Oishi, A., Hashimoto, M., Fujita, T., & Iiri, T. (2007). An acquired hypocalciuric hypercalcemia autoantibody induces allosteric transition among active human Ca-sensing receptor conformations. *Proc Natl Acad Sci U S A*, *104*(13), 5443-5448. https://doi.org/10.1073/pnas.0701290104

Bueno, A. B., Sun, B., Willard, F. S., Feng, D., Ho, J. D., Wainscott, D. B., Showalter, A. D., Vieth, M., Chen, Q., Stutsman, C., Chau, B., Ficorilli, J., Agejas, F. J., Cumming, G. R., Jiménez, A., Rojo, I., Kobilka, T. S., Kobilka, B. K., & Sloop, K. W. (2020). Structural insights into probe-dependent positive allosterism of the GLP-1 receptor. *Nat Chem Biol*, *16*(10), 1105-1110. https://doi.org/10.1038/s41589-020-0589-7

Kruse, A. C., Ring, A. M., Manglik, A., Hu, J., Hu, K., Eitel, K., Hübner, H., Pardon, E., Valant, C., Sexton, P. M., Christopoulos, A., Felder, C. C., Gmeiner, P., Steyaert, J., Weis, W. I., Garcia, K. C., Wess, J., & Kobilka, B. K. (2013). Activation and allosteric modulation of a muscarinic acetylcholine receptor. *Nature*, *504*(7478), 101-106. https://doi.org/10.1038/nature12735

Liu, X., Masoudi, A., Kahsai, A. W., Huang, L. Y., Pani, B., Staus, D. P., Shim, P. J., Hirata, K., Simhal, R. K., Schwalb, A. M., Rambarat, P. K., Ahn, S., Lefkowitz, R. J., & Kobilka, B. (2019). Mechanism of β(2)AR regulation by an intracellular positive allosteric modulator. *Science*, *364*(6447), 1283-1287. https://doi.org/10.1126/science.aaw8981

Srivastava, A., Yano, J., Hirozane, Y., Kefala, G., Gruswitz, F., Snell, G., Lane, W., Ivetac, A., Aertgeerts, K., Nguyen, J., Jennings, A., & Okada, K. (2014). High-resolution structure of the human GPR40 receptor bound to allosteric agonist TAK-875. *Nature*, *513*(7516), 124-127. https://doi.org/10.1038/nature13494

Gentry, P. R., Sexton, P. M., & Christopoulos, A. (2015). Novel Allosteric Modulators of G Protein-coupled Receptors. *J Biol Chem*, *290*(32), 19478-19488. https://doi.org/10.1074/jbc.R115.662759

Conn, P. J., Christopoulos, A., & Lindsley, C. W. (2009). Allosteric modulators of GPCRs: a novel approach for the treatment of CNS disorders. *Nat Rev Drug Discov*, *8*(1), 41-54. https://doi.org/10.1038/nrd2760

Mantas, I., Saarinen, M., Xu, Z. D., & Svenningsson, P. (2021). Update on GPCR-based targets for the development of novel antidepressants. *Mol Psychiatry*. https://doi.org/10.1038/s41380-021-01040-1

Gregory, K. J., & Conn, P. J. (2015). Molecular Insights into Metabotropic Glutamate Receptor Allosteric Modulation. *Mol Pharmacol*, *88*(1), 188-202. https://doi.org/10.1124/mol.114.097220

Gutzeit, V. A., Thibado, J., Stor, D. S., Zhou, Z., Blanchard, S. C., Andersen, O. S., & Levitz, J. (2019). Conformational dynamics between transmembrane domains and allosteric modulation of a metabotropic glutamate receptor. *Elife*, *8*. https://doi.org/10.7554/eLife.45116

Nasrallah, C., Cannone, G., Briot, J., Rottier, K., Berizzi, A. E., Huang, C. Y., Quast, R. B., Hoh, F., Banères, J. L., Malhaire, F., Berto, L., Dumazer, A., Font-Ingles, J., Gómez-Santacana, X., Catena, J., Kniazeff, J., Goudet, C., Llebaria, A., Pin, J. P., . . . Lebon, G. (2021). Agonists and allosteric modulators promote signaling from different metabotropic glutamate receptor 5 conformations. *Cell Rep*, *36*(9), 109648. https://doi.org/10.1016/j.celrep.2021.109648

Liauw, B. W., Afsari, H. S., & Vafabakhsh, R. (2021). Conformational rearrangement during activation of a metabotropic glutamate receptor. *Nat Chem Biol*, *17*(3), 291-297. https://doi.org/10.1038/s41589-020-00702-5

Goudet, C., Gaven, F., Kniazeff, J., Vol, C., Liu, J., Cohen-Gonsaud, M., Acher, F., Prézeau, L., & Pin, J. P. (2004). Heptahelical domain of metabotropic glutamate receptor 5 behaves like rhodopsin-like receptors. *Proc Natl Acad Sci U S A*, *101*(1), 378-383. https://doi.org/10.1073/pnas.0304699101

Shen, C., Mao, C., Xu, C., Jin, N., Zhang, H., Shen, D. D., Shen, Q., Wang, X., Hou, T., Chen, Z., Rondard, P., Pin, J. P., Zhang, Y., & Liu, J. (2021). Structural basis of GABA(B) receptor-G(i) protein coupling. *Nature*, *594*(7864), 594-598. https://doi.org/10.1038/s41586-021-03507-1

Conklin, B. R., Farfel, Z., Lustig, K. D., Julius, D., & Bourne, H. R. (1993). Substitution of three amino acids switches receptor specificity of Gq alpha to that of Gi alpha. *Nature*, *363*(6426), 274-276. https://doi.org/10.1038/363274a0

Bonnefous, C., Vernier, J.-M., Hutchinson, J. H., Gardner, M. F., Cramer, M., James, J. K., Rowe, B. A., Daggett, L. P., Schaffhauser, H., & Kamenecka, T. M. (2005). Biphenyl-indanones: Allosteric potentiators of the metabotropic glutamate subtype 2 receptor. *Bioorganic & Medicinal Chemistry Letters*, *15*(19), 4354-4358. https://doi.org/https://doi.org/10.1016/j.bmcl.2005.06.062

Johnson, M. P., Baez, M., Jagdmann, G. E., Jr., Britton, T. C., Large, T. H., Callagaro, D. O., Tizzano, J. P., Monn, J. A., & Schoepp, D. D. (2003). Discovery of allosteric potentiators for the metabotropic glutamate 2 receptor: synthesis and subtype selectivity of N-(4-(2-methoxyphenoxy)phenyl)-N-(2,2,2- trifluoroethylsulfonyl)pyrid-3-ylmethylamine. *J Med Chem*, *46*(15), 3189-3192. https://doi.org/10.1021/jm034015u

Cid, J. M., Tresadern, G., Vega, J. A., de Lucas, A. I., Matesanz, E., Iturrino, L., Linares, M. L., Garcia, A., Andrés, J. I., Macdonald, G. J., Oehlrich, D., Lavreysen, H., Megens, A., Ahnaou, A., Drinkenburg, W., Mackie, C., Pype, S., Gallacher, D., & Trabanco, A. A. (2012). Discovery of 3-cyclopropylmethyl-7-(4-phenylpiperidin-1-yl)-8-trifluoromethyl[1,2,4]triazolo[4,3-a]pyridine (JNJ-42153605): a positive allosteric modulator of the metabotropic glutamate 2 receptor. *J Med Chem*, *55*(20), 8770-8789. https://doi.org/10.1021/jm3010724

Hemstapat, K., Da Costa, H., Nong, Y., Brady, A. E., Luo, Q., Niswender, C. M., Tamagnan, G. D., & Conn, P. J. (2007). A novel family of potent negative allosteric modulators of group II metabotropic glutamate receptors. *J Pharmacol Exp Ther*, *322*(1), 254-264. https://doi.org/10.1124/jpet.106.117093

Kolczewski, S., Adam, G., Stadler, H., Mutel, V., Wichmann, J., & Woltering, T. (1999). Synthesis of heterocyclic enol ethers and their use as group 2 metabotropic glutamate receptor antagonists. *Bioorg Med Chem Lett*, *9*(15), 2173-2176. https://doi.org/10.1016/s0960-894x(99)00346-7

Nygaard, R., Zou, Y., Dror, R. O., Mildorf, T. J., Arlow, D. H., Manglik, A., Pan, A. C., Liu, C. W., Fung, J. J., Bokoch, M. P., Thian, F. S., Kobilka, T. S., Shaw, D. E., Mueller, L., Prosser, R. S., & Kobilka, B. K. (2013b). The dynamic process of β(2)-adrenergic receptor activation. *Cell*, *152*(3), 532-542. https://doi.org/10.1016/j.cell.2013.01.008

Huang, S. K., Pandey, A., Tran, D. P., Villanueva, N. L., Kitao, A., Sunahara, R. K., Sljoka, A., & Prosser, R. S. (2021). Delineating the conformational landscape of the adenosine A(2A) receptor during G protein coupling. *Cell*, *184*(7), 1884-1894.e1814. https://doi.org/10.1016/j.cell.2021.02.041

Wingler, L. M., Elgeti, M., Hilger, D., Latorraca, N. R., Lerch, M. T., Staus, D. P., Dror, R. O., Kobilka, B. K., Hubbell, W. L., & Lefkowitz, R. J. (2019b). Angiotensin Analogs with Divergent Bias Stabilize Distinct Receptor Conformations. *Cell*, *176*(3), 468-478.e411. https://doi.org/10.1016/j.cell.2018.12.005

Gregorio, G. G., Masureel, M., Hilger, D., Terry, D. S., Juette, M., Zhao, H., Zhou, Z., Perez-Aguilar, J. M., Hauge, M., Mathiasen, S., Javitch, J. A., Weinstein, H., Kobilka, B. K., & Blanchard, S. C. (2017b). Single-molecule analysis of ligand efficacy in β(2)AR-G-protein activation. *Nature*, *547*(7661), 68-73. https://doi.org/10.1038/nature22354

Wei, S., Thakur, N., Ray, A. P., Jin, B., Obeng, S., McCurdy, C. R., McMahon, L. R., Gutiérrez-de-Terán, H., Eddy, M. T., & Lamichhane, R. (2022). Slow conformational dynamics of the human A(2A) adenosine receptor are temporally ordered. *Structure*, *30*(3), 329-337.e325. https://doi.org/10.1016/j.str.2021.11.005

Kaneko, S., Imai, S., Asao, N., Kofuku, Y., Ueda, T., & Shimada, I. (2022). Activation mechanism of the μ-opioid receptor by an allosteric modulator. *Proc Natl Acad Sci U S A*, *119*(16), e2121918119. https://doi.org/10.1073/pnas.2121918119

Wang, X., Liu, D., Shen, L., Li, F., Li, Y., Yang, L., Xu, T., Tao, H., Yao, D., Wu, L., Hirata, K., Bohn, L. M., Makriyannis, A., Liu, X., Hua, T., Liu, Z. J., & Wang, J. (2021). A Genetically Encoded F-19 NMR Probe Reveals the Allosteric Modulation Mechanism of Cannabinoid Receptor 1. *J Am Chem Soc*, *143*(40), 16320-16325. https://doi.org/10.1021/jacs.1c06847

Ingólfsson, H. I., Melo, M. N., van Eerden, F. J., Arnarez, C., Lopez, C. A., Wassenaar, T. A., Periole, X., de Vries, A. H., Tieleman, D. P., & Marrink, S. J. (2014). Lipid organization of the plasma membrane. *J Am Chem Soc*, *136*(41), 14554-14559. https://doi.org/10.1021/ja507832e

Anandan, A., & Vrielink, A. (2016). Detergents in Membrane Protein Purification and Crystallisation. *Adv Exp Med Biol*, *922*, 13-28. https://doi.org/10.1007/978-3-319-35072-1_2

Goyal, P., & Aswal, V. (2001). Micellar structure and inter-micelle interactions in micellar solutions: results of small angle neutron scattering studies. *CURRENT SCIENCE-BANGALORE-*, *80*(8), 972-979.

Lichtenberg, D., Ahyayauch, H., & Goñi, F. M. (2013). The mechanism of detergent solubilization of lipid bilayers. *Biophys J*, *105*(2), 289-299. https://doi.org/10.1016/j.bpj.2013.06.007

Anglin, T. C., & Conboy, J. C. (2008). Lateral pressure dependence of the phospholipid transmembrane diffusion rate in planar-supported lipid bilayers. *Biophys J*, *95*(1), 186-193. https://doi.org/10.1529/biophysj.107.118976

Bae, H. E., Gotfryd, K., Thomas, J., Hussain, H., Ehsan, M., Go, J., Loland, C. J., Byrne, B., & Chae, P. S. (2015). Deoxycholate-Based Glycosides (DCGs) for Membrane Protein Stabilisation. *Chembiochem*, *16*(10), 1454-1459. https://doi.org/10.1002/cbic.201500151

Liauw, B. W., Foroutan, A., Schamber, M. R., Lu, W., Samareh Afsari, H., & Vafabakhsh, R. (2022). Conformational fingerprinting of allosteric modulators in metabotropic glutamate receptor 2. *Elife*, *11*. https://doi.org/10.7554/eLife.78982

Kotov, V., Bartels, K., Veith, K., Josts, I., Subhramanyam, U. K. T., Günther, C., Labahn, J., Marlovits, T. C., Moraes, I., Tidow, H., Löw, C., & Garcia-Alai, M. M. (2019). High-throughput stability screening for detergent-solubilized membrane proteins. *Sci Rep*, *9*(1), 10379. https://doi.org/10.1038/s41598-019-46686-8

Sezgin, E., Levental, I., Mayor, S., & Eggeling, C. (2017). The mystery of membrane organization: composition, regulation and roles of lipid rafts. *Nat Rev Mol Cell Biol*, *18*(6), 361-374. https://doi.org/10.1038/nrm.2017.16

Asher, W. B., Geggier, P., Holsey, M. D., Gilmore, G. T., Pati, A. K., Meszaros, J., Terry, D. S., Mathiasen, S., Kaliszewski, M. J., McCauley, M. D., Govindaraju, A., Zhou, Z., Harikumar, K. G., Jaqaman, K., Miller, L. J., Smith, A. W., Blanchard, S. C., & Javitch, J. A. (2021). Single-molecule FRET imaging of GPCR dimers in living cells. *Nat Methods*, *18*(4), 397-405. https://doi.org/10.1038/s41592-021-01081-y

Lučič, V., Rigort, A., & Baumeister, W. (2013). Cryo-electron tomography: the challenge of doing structural biology in situ. *J Cell Biol*, *202*(3), 407-419. https://doi.org/10.1083/jcb.201304193

Subczynski, W. K., Pasenkiewicz-Gierula, M., Widomska, J., Mainali, L., & Raguz, M. (2017). High Cholesterol/Low Cholesterol: Effects in Biological Membranes: A Review. *Cell Biochem Biophys*, *75*(3-4), 369-385. https://doi.org/10.1007/s12013-017-0792-7

Routledge, S. J., Jamshad, M., Little, H. A., Lin, Y. P., Simms, J., Thakker, A., Spickett, C. M., Bill, R. M., Dafforn, T. R., Poyner, D. R., & Wheatley, M. (2020). Ligand-induced conformational changes in a SMALP-encapsulated GPCR. *Biochim Biophys Acta Biomembr*, *1862*(6), 183235. https://doi.org/10.1016/j.bbamem.2020.183235

Presolski, S. I., Hong, V. P., & Finn, M. G. (2011b). Copper-Catalyzed Azide-Alkyne Click Chemistry for Bioconjugation. *Curr Protoc Chem Biol*, *3*(4), 153-162. https://doi.org/10.1002/9780470559277.ch110148

Serdiuk, T., Manna, M., Zhang, C., Mari, S. A., Kulig, W., Pluhackova, K., Kobilka, B. K., Vattulainen, I., & Müller, D. J. (2022). A cholesterol analog stabilizes the human β(2)-adrenergic receptor nonlinearly with temperature. *Sci Signal*, *15*(737), eabi7031. https://doi.org/10.1126/scisignal.abi7031

Margeta-Mitrovic, M., Jan, Y. N., & Jan, L. Y. (2000). A trafficking checkpoint controls GABA(B) receptor heterodimerization. *Neuron*, *27*(1), 97-106. https://doi.org/10.1016/s0896-6273(00)00012-x

Lecat-Guillet, N., Quast, R. B., Liu, H., Møller, T. C., Rovira, X., Soldevila, S., Lamarque, L., Trinquet, E., Liu, J., Pin, J.-P., Rondard, P., & Margeat, E. (2022). Dissecting conformational rearrangements and allosteric modulation in metabotropic glutamate receptor activation. *bioRxiv*, 2022.2001.2007.474531. https://doi.org/10.1101/2022.01.07.474531

Meng, J., Xu, C., Lafon, P. A., Roux, S., Mathieu, M., Zhou, R., Scholler, P., Blanc, E., Becker, J. A. J., Le Merrer, J., González-Maeso, J., Chames, P., Liu, J., Pin, J. P., & Rondard, P. (2022). Nanobody-based sensors reveal a high proportion of mGlu heterodimers in the brain. *Nat Chem Biol*, *18*(8), 894-903. https://doi.org/10.1038/s41589-022-01050-2

Moreno Delgado, D., Møller, T. C., Ster, J., Giraldo, J., Maurel, D., Rovira, X., Scholler, P., Zwier, J. M., Perroy, J., Durroux, T., Trinquet, E., Prezeau, L., Rondard, P., & Pin, J. P. (2017). Pharmacological evidence for a metabotropic glutamate receptor heterodimer in neuronal cells. *Elife*, *6*. https://doi.org/10.7554/eLife.25233

Teo, A. C. K., Lee, S. C., Pollock, N. L., Stroud, Z., Hall, S., Thakker, A., Pitt, A. R., Dafforn, T. R., Spickett, C. M., & Roper, D. I. (2019). Analysis of SMALP co-extracted phospholipids shows distinct membrane environments for three classes of bacterial membrane protein. *Sci Rep*, *9*(1), 1813. https://doi.org/10.1038/s41598-018-37962-0